Preparations for the Spin-Filtering Experiments at COSY/Jülich

Inaugural-Dissertation

zur

Erlangung des Doktorgrades

der Mathematisch-Naturwissenschaftlichen Fakultät

der Universität zu Köln

vorgelegt von

Christian Weidemann

aus Jena

Jülich, 2011

Berichterstatter: Prof. Dr. H. Ströher

Prof. Dr. J. Jolie

Tag der mündlichen Prüfung: 21.10.2011

ABSTRACT

Polarized antiprotons allow unique access to a number of fundamental physics observables. One example is the transversity distribution which is the last missing piece to complete the knowledge of the nucleon partonic structure at leading twist in the QCD-based parton model. The transversity is directly measurable via Drell-Yan production in double polarized antiproton-proton collisions. This and a multitude of other findings, which are accessible via $\vec{p}\vec{p}$ scattering experiments, led the Polarized Antiproton eXperiments (PAX) collaboration to propose such investigations at the High Energy Storage Ring (HESR) of the Facility for Antiproton and Ion Research (FAIR).

Already the production of intense polarized antiproton beams is still an unsolved problem. The PAX anticipated time plan to experiments at HESR mainly consists of three phases. PAX@COSY, as first step, is aiming for an optimization of the polarization build-up in proton beams at the Cooler Synchrotron COSY Jülich. The spin-filtering method, where the originally unpolarized beam becomes polarized due to the spin-dependent part of the hadronic interaction with a Polarized Internal Target (PIT), will be applied. The feasibility of this method was shown to work for protons by the Filter Experiment (FILTEX) at the Test Storage Ring (TSR) in Heidelberg. PAX@CERN will determine the spin-dependent cross sections in $\vec{\bar{p}}\vec{p}$ scattering at beam energies of $50 - 450\,\mathrm{MeV}$ using the antiproton beam of the Antiproton Decelerator (AD) at CERN. PAX@FAIR constitutes the third phase where the antiproton beam will be polarized in a dedicated Antiproton Polarizer Ring (APR) at the HESR, converted into a double-polarized proton-antiproton collider, in order to study the transverse spin structure of nucleons.

The present thesis discusses the preparations for the spin-filtering experiments at COSY. This includes the successful installation and commissioning of the experimental equipment such as a low-β section, a dedicated pumping system, an Atomic Beam Source (ABS), a Breit-Rabi Polarimeter (BRP), and a target chamber with an openable storage cell. In addition, the accomplished investigations of the beam lifetime dependencies, resulting in significantly improved beam lifetimes, and relevant machine parameters, e.g., the machine acceptance, are described. The results are utilized to calculate the expected polarization build-up in a cooled and stored proton beam with a kinetic energy of $49.3\,\mathrm{MeV}$ using a target with an areal density of $5 \cdot 10^{13}\,\mathrm{atoms/cm^2}$. Simulations of the determination of the beam polarization using elastic proton-deuteron scattering and a polarimeter, that consists of silicon micro-strip detectors, allows one to estimate the achievable precision of the measurement of the spin-dependent total hadronic cross section. The presented results constitute the basis of a beam time request for transverse spin-filtering to the COSY Program Advisory Committee (PAC), which was approved in spring 2011.

ZUSAMMENFASSUNG

Gespeicherte polarisierte Antiprotonen ermöglichen eine Vielzahl von bedeutenden Experimenten im Bereich der Teilchenphysik. Hierzu gehört die direkte Messung der sogenannten Transversity, welche als letztes fehlendes Stück zur Beschreibung der partonischen Struktur des Nukleons im Rahmen der Quantenchromodynamik (QCD) angesehen wird. Mit Hilfe der Drell-Yan Produktion in doppeltpolarisierten Proton-Antiproton Streuexperimenten ist eine Untersuchung der transversalen Spinstruktur der Nukleonen möglich. Aufgrund dieser und einer Fülle weiterer möglicher wesentlicher Erkenntnisse wurden Untersuchungen doppeltpolarisierter Antiproton-Proton Kollissionen am High Energy Storage Ring (HESR) der Facility for Antiproton and Ion Research (FAIR) von der Polarized Antiproton eXperiments Kollaboration (PAX) vorgeschlagen.
Hierbei ist bereits die Erzeugung intensiver polarisierter Protonenstrahlen eine anspruchsvolle und bisher ungelöste Aufgabe. Der PAX Zeitplan hin zu Experimenten am HESR besteht im Wesentlichen aus drei Phasen. Im ersten Schritt wird PAX@COSY den Polarisationsaufbau mit Protonen am Cooler Synchrotron COSY in Jülich optimieren. Anwendung findet hierbei die Spinfilter Methode bei der ein anfangs unpolarisierte Strahl aufgrund der spinabhängigen hadronischen Wechselwirkung mit einem polarisierten Target polarisiert wird. Ein erfolgreicher Test dieser Methode wurde für Protonen bereits im Rahmen des Filter Experiments (FILTEX) am Test Storage Ring (TSR) in Heidelberg durchgeführt. PAX@CERN soll im zweiten Schritt mit dem Antiprotonenstrahl des Antiproton Decelerators (AD) am CERN zeigen, wie groß die spinabhängigen Wirkungsquerschnitte in der Proton-Antiproton Streuung sind. PAX@FAIR bildet die dritte Phase, in der die Antiprotonen in einem dedizierten Speicherring, dem Antiproton Polarizer Ring (APR), polarisiert werden. Mit Hilfe des polarisierten Antiprotonenstrahles soll in Streuexperimenten in einem doppeltpolarisierten Proton-Antiproton Collider die Vermessung der transversalen Spinstruktur des Protons erreicht werden.
Die vorliegende Arbeit erläutert die Vorbereitungen für das geplante Spinfilter Experiment an COSY. Im Rahmen dieser Vorbereitungsphase wurde unter anderem das notwendige experimentelle Equipment, bestehend aus einer sogenannten low-β Sektion, einem leistungsfähigen Vakuumsystem, einer Atomstrahlquelle, einem Breit-Rabi Polarimeter und einer Targetkammer mit auffahrbarer Speicherzelle, installiert und erfolgreich in Betrieb genommen. Des Weiteren wurden Messungen zur Abhängigkeit der Strahllebensdauer mit dem Resultat einer signifikanten Lebensdauererhöhung und detaillierte Studien zu relevanten Maschinenparametern, wie z.B. Akzeptanzwinkel, durchgeführt. Die Ergebnisse dieser Studien dienen als Grundlage zur Berechnung des erwarteten Polarisationsaufbaus in einem gespeicherten, gekühlten Protonenstrahl bei einer kinetischen Energie von $49.3\,\mathrm{MeV}$ und einer Targetdichte von $5 \cdot 10^{13}\,\mathrm{Atome/cm^2}$. Die weiterhin durchgeführten Simulationsrechnungen zur Messung dieser Polarisation mit Hilfe von elastischer Proton-Deuteron Streuung und eines Polarimeters, bestehend aus Siliziumstreifendetektoren, geben Aufschluss über die benötigte Messzeit und die erreichbare Genauigkeit der Messung des spinabhängigen totalen Wirkungsquerschnittes mit transversaler Strahlpolarisation. Auf der Basis der präsentierten Ergebnisse wurde ein Experimentantrag der PAX Kollaboration an das COSY Program Advisory Committee (PAC) eingereicht und vom PAC bewilligt.

CONTENTS

1. PHYSICS CASE

The QCD[1] description of the partonic structure of the nucleon is in leading twist based on three structure functions, namely the well studied quark distribution $q(x, Q^2)$, the helicity distribution $\Delta q(x, Q^2)$ and the largely unknown transversity distribution $\delta q(x, Q^2)$. A first direct measurement of this transversity distribution of the valence quarks in the proton has been proposed by the Polarized Antiproton eXperiments collaboration (PAX) at the High Energy Storage Ring (HESR) [1]. Since it is directly accessible uniquely via double polarized proton-antiproton scattering, polarized antiproton beams are a prerequisite to address this important topic. Therefore, in 2005 the PAX collaboration suggested to provide for the first time an intense polarized antiproton beam by the spin-filtering method, which is based on the spin-dependent part of the hadronic cross section.
The present description of the proton structure and how it was developed on the basis of scattering experiments is illustrated in Sec. 1.1. A detailed report on the planned experimental program of the PAX collaboration is given in Sec. 1.2.

1.1. Proton Structure

Since its very beginning, physics has pondered the question of what the fundamental building blocks of matter are. In the 19th century all matter was shown to be composed of atoms. After the discovery of the electron by Joseph John Thomson in 1897 [2], it was realized that there has to be a positively charged center within the atom to balance the negative electrons and create electrically neutral atoms. This center was found to be the atomic nucleus by Rutherford, Geiger and Mardsen [3, 4], whose alpha scattering experiments were the first experiments, in which individual particles were systematically scattered and detected. Since the beginning of atomic physics nothing has improved the understanding of the inner structure of matter more than scattering experiments. They led to the discovery of the proton in 1919 by Rutherford [5] and almost 50 years later it became clear, that this particle possesses a substructure.
The enhancement of the performance of particle accelerators over the past decades, led to a dramatic increase of the projectile energies and thus their power to resolve structures at small distances. Inclusive Deep Inelastic Scattering ($e + p \rightarrow e^{'} + X$) experiments at SLAC[2], where a proton breaks up, allowed for the verification of the existence of point-like sub-nucleonic particles (partons) by Bjørken and Feynman [6–8]. These spin-$\frac{1}{2}$ particles with fractional electric charge and a new degree of freedom called flavor, later identified as quarks, had been predicted earlier by Gell-Mann and Zweig [9, 10]. In the Quark Parton Model (QPM), which was developed at that time, two up quarks (u) with electrical charge $+\frac{2}{3}e$ and one down quark (d) with $-\frac{1}{3}e$ constitute one proton with a total charge of $+e$.
However, the discovery made in 1972 that roughly only $50\,\%$ of the nucleon momentum is carried by quarks [11] is in contradiction to this model. This discrepancy could be explained within the framework of QCD, the gauge theory of strong interactions. According to this

[1] Quantum Chromodynamics
[2] Stanford Linear Accelerator Center

theory, which requires the existence of color as an additional degree of freedom of the quarks, the missing momentum of the nucleon is carried by the gluons, the "massless" vector gauge bosons mediating the strong force. The gluons can split into a virtual quark-antiquark pair ($\bar{q}q$), called sea quarks [12], which can annihilate back into gluons.
In the following, the present understanding of the proton structure by means of the QPM and how it developed with the help of elastic and deep inelastic lepton-nucleon scattering is illuminated. This points out the substantial physics potential of double polarized $\bar{p}p$ scattering experiments proposed by the PAX collaboration.

1.1.1. Elastic Electron-Nucleon Scattering

In elastic scattering of electrons off protons ($e+p \rightarrow e+p$), which is assumed to be dominated by single-photon exchange (Fig. 1.1), the target proton stays intact and no new particles are created.

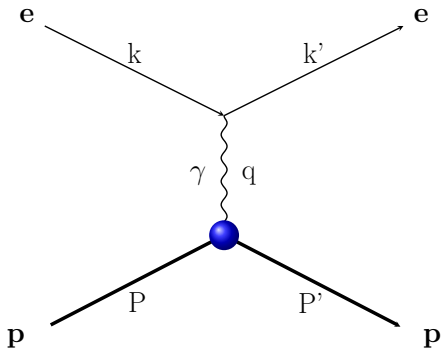

Fig. 1.1: Feynman diagram of elastic electron-proton scattering, here k, k' and P, P' are the four-momenta of the electron and proton before and after the collision, respectively, and $q = k - k' = P' - P$ is the four-momentum of the virtual photon (the four-momentum transfer from the electron to the proton).

The elastic electron-proton scattering cross section, also known as Rosenbluth formula [13], can be written in the form

$$\frac{d\sigma}{d\Omega} = \left(\frac{d\sigma}{d\Omega}\right)_{\text{Mott}} \cdot \left(\frac{G_{\text{E}}^2 + \tau G_{\text{M}}^2}{1+\tau} + 2\tau G_{\text{M}}^2 \tan^2(\Theta/2)\right), \tag{1.1}$$

where

$$\left(\frac{d\sigma}{d\Omega}\right)_{\text{Mott}} = \frac{\alpha^2 \cos^2(\Theta/2)}{4E_0^2 \cdot \sin^4(\Theta/2) \cdot [1 + (2E_0/M)\sin^2(\Theta/2)]} \tag{1.2}$$

is the Mott cross section, that describes the elastic scattering of a relativistic spin-$1/2$ particle off a spinless point-like particle. Here Θ is the electron scattering angle, M is the proton mass, E_0 is the incident electron energy, $\alpha = {}^{e^2}/_{4\pi}$ is the electromagnetic coupling constant and $\tau = {}^{q^2}/_{4M^2}$ with $q = k - k' = P' - P$ the four-momentum of the exchanged virtual photon. k, k' and P, P' are the four-momenta of the electron and the proton before and after the collision, respectively. G_{E} and G_{M} are the electric and magnetic proton form factors, where the former is associated with the charge distribution and the latter with the magnetic moment distribution of the proton. The measurement of the cross section and the subsequent extraction of G_{E} allows one to extract the root-mean-square charge radius r_{E} of the proton [14]:

$$r_{\text{E}}^2 = \int d^3x r^2 \rho(r) = -6 \frac{dG_{\text{E}}(q^2)}{dq^2}\bigg|_{q_0^2} = (0.81 \pm 0.04\,\text{fm})^2. \tag{1.3}$$

The same radius ($0.8\,\text{fm}$) was also obtained for the magnetic distribution.
The extraction of G_{E} and G_{M} was achieved by the Rosenbluth separation method [13], which involves measuring cross sections at constant Q^2 ($= -q^2$) and varying the beam energy and

scattering angle to separate the electric and magnetic contributions. The extracted value for $\mu G_{\mathrm{E}}/G_{\mathrm{M}}$ was shown to be Q^2-independent (see Fig. 1 in [15]). Q^2, the negative squared four momentum of the virtual photon $Q^2 := -q^2 \overset{\text{lab}}{=} 4EE' \sin^2(\Theta/2)$, is a measure of the spatial scale that can be resolved by a virtual photon with the wavelength $\lambda = {}^{1}/_{|q|}$, where $v := \frac{P \cdot q}{M} \overset{\text{lab}}{=} E - E'$ is the energy carried by the virtual photon. Since G_{M} in Eq. (1.1) is multiplied by τ, the cross section becomes dominated by G_{M} as Q^2 increases. Consequently, the extraction of G_{E} is more difficult above $Q^2 = 1\,\mathrm{GeV}$.
Recent experiments at the Jefferson laboratory using polarization observables indicate an unexpected Q^2-dependence of the ratio of the magnetic and electric form factors of the proton [15, 16]. Reasons for the discrepancy between the two methods have been indicated in two photon exchange [17, 18].

1.1.2. Deep Inelastic Scattering

In deep inelastic lepton-nucleon scattering (DIS), the nucleon N breaks up and forms a hadronic final state X, due to an increased lepton-beam energy and thus a larger momentum transfer:

$$l + N \rightarrow l' + X. \tag{1.4}$$

Since leptons do not interact via the strong force, they are used as an electromagnetic probe to measure a variety of parton distribution functions and related observables. Figure 1.2 shows a sketch of the DIS process in the one-photon exchange approximation.

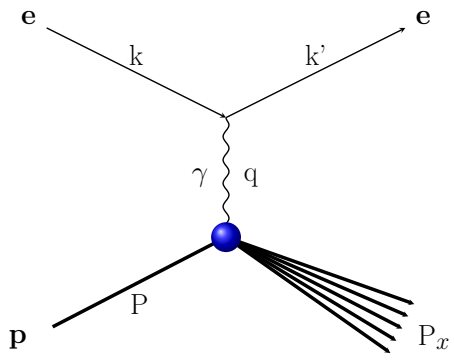

Fig. 1.2: Feynman diagram of deep inelastic electron-proton scattering. $q^2 = -(k - k')^2$ is the squared four-momentum of the exchanged photon and P and P_X represent the target proton and the hadronic final X state four-momenta, respectively.

The kinematics can be characterized by Q^2 as described in Sec. 1.1.1, by the so-called Bjørken scaling variable $x \overset{\text{lab}}{=} \frac{-q^2}{2Mv}$ which is the fraction of the proton momentum carried by the hard-scattered parton and by the squared invariant mass of the target-nucleon – virtual-photon system $W^2 := (P + q)^2 \overset{\text{lab}}{=} M^2 + 2Mv - Q^2$. Combining the latter two variables allows one to determine the mass excitation (change of initial proton mass) caused by the scattering process

$$W^2 - M^2 = 2Mv(1 - x). \tag{1.5}$$

Therefore, the elastic limit corresponds to $x \rightarrow 1$, with $W^2 = M^2$, while $x < 1$ corresponds to the inelastic regime, in which $W^2 > M^2$.
Averaging over all spins in the initial state of the scattering process and summing over the spins in the final state leads to the spin-independent part of the cross section [7, 19]

$$\frac{d^2\sigma^{\text{unpol}}}{d\Omega dE'} = \left(\frac{d\sigma}{d\Omega}\right)_{\text{Mott}} \left[\frac{2}{M} F_1(x, Q^2) \tan^2(\Theta/2) + \frac{1}{v} F_2(x, Q^2)\right], \tag{1.6}$$

where $\left(\frac{d\sigma}{d\Omega}\right)_{\text{Mott}}$ is the Mott cross section, as described earlier. $F_1(x,Q^2) := MW_1(v,Q^2)$ and $F_2(x,Q^2) := vW_2(v,Q^2)$ are the spin-independent structure functions. The deviation from the Mott cross section denoted by the second term of Eq. (1.6) appears due to the composite nature of the proton.
The spin-dependent part of the cross section can be isolated by measuring the difference of the cross sections obtained with two opposite target spin states. In this case the unpolarized components cancel. If both the incident lepton beam and the target protons are longitudinally polarized one obtains [20, 21]

$$\frac{d^3\sigma^{\overrightarrow{\Leftarrow}}}{dxdy} - \frac{d^3\sigma^{\overrightarrow{\Rightarrow}}}{dxdy} = \frac{4\alpha^2}{sxy}\left[\left(2 - y - \frac{\gamma^2 y^2}{2}\right) g_1(x,Q^2) - \gamma^2 y g_2(x,Q^2)\right], \tag{1.7}$$

where $\rightarrow$ indicates the spin orientation of the incoming electron and $\Leftarrow$, $\Rightarrow$ the two different spin states of the target proton. Here $s = (P+Q)^2$ denotes the center of mass energy squared, $y = {}^{P\cdot q}/_{P\cdot k} \overset{\text{lab}}{=} {}^{\nu}/_{E}$ is the fractional energy transfer from the lepton to the nucleon, $\gamma = (2Mx)/Q$, and $g_1(x,Q^2)$ and $g_2(x,Q^2)$ are the polarized structure functions. Figure 1.3 displays the $g_1(x)$ world results for protons, neutrons and deuterons as a function of the Bjørken variable x.
In case of a transverse target polarization with respect to the incoming lepton direction, the polarized cross section becomes

$$\frac{d^3\sigma^{\rightarrow\Downarrow}}{dxdyd\phi_s^l} - \frac{d^3\sigma^{\rightarrow\Uparrow}}{dxdyd\phi_s^l} = \frac{4\alpha^2}{sxy}\gamma\sqrt{1 - y - \frac{\gamma^2 y^2}{4}}\left[\gamma g_1(x,Q^2) + 2g_2(x,Q^2)\right]\cos\phi_s^l, \tag{1.8}$$

where ϕ_s^l is the azimuthal angle of the target spin vector $\vec{S}$ with respect to the lepton beam direction.

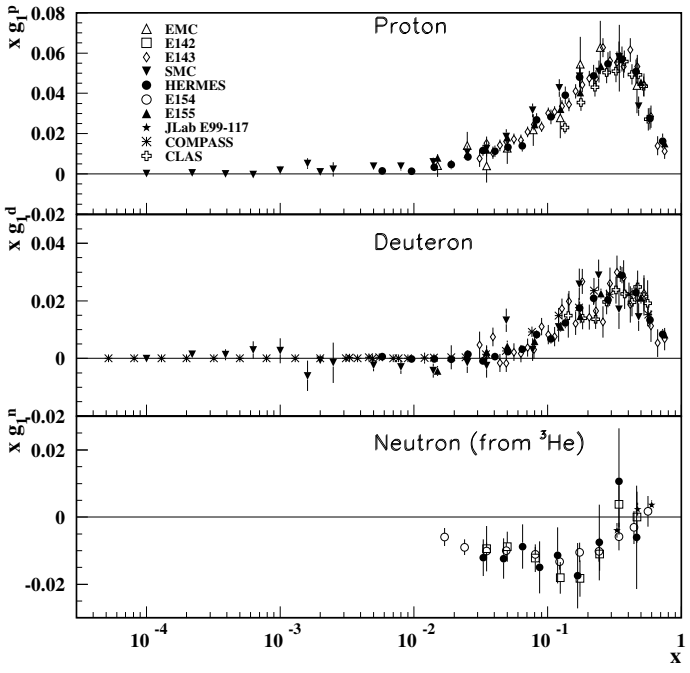

Fig. 1.3.: The spin-dependent structure function $xg_1(x)$ of the proton, deuteron, and neutron (from ^{3}He target), measured in deep inelastic scattering of polarized electrons/positrons [20].

1.1.3. Bjørken Scaling

The nucleon structure has been studied by deep inelastic scattering experiments performed at SLAC [22] and the results show, that the spin-independent structure functions F_1 and F_2 are approximately Q^2-independent in the large momentum transfer region

$$F_2(x, Q^2) \approx F_2(x) \qquad (Q^2 \gg M^2), \tag{1.9}$$

as it was predicted by Bjørken [6]. He reasoned this behavior in the high-energy or Bjørken limit, defined by

$$\lim_{\text{Bj}} = \begin{cases} Q^2 \to \infty \\ v \to \infty \\ x \text{ fixed} \end{cases}, \tag{1.10}$$

in the case that the proton is composed of point-like constituents. F_1 shows the same Q^2-independence, since F_1 and F_2 are related to each other by $F_2(x) = 2xF_1(x)$ according to the Callan-Gross relation [23]. This phenomenon, known as Bjørken scaling or scale invariance is in contrast to the strong Q^2-dependence of the elastic form factors, which stands for an inner structure of the proton, because it implies that the electromagnetic probe (lepton) measures the same proton structure, independent on the spatial resolution as it is the case for scattering from point-like constituents [7]. The Bjørken scaling and the conclusion from other experiments that these constituents are fermions [24], were the first dynamical evidences of the quarks.
With the larger accuracy of the next generation DIS experiments at FNAL[1] [25], at CERN[2] [26, 27], and at the HERA[3] electron-proton collider [28] in conjunction with the broadening of the kinematic regions a noticeable Q^2-dependence appeared (see Fig. 1.4). F_2 increases with Q^2 for low x ($x \leq 0.003$) and decreases for large x ($x \geq 0.6$). The observed violation of the Bjørken scaling was interpreted within the framework of the QCD as the evidence of the dynamical structure of the proton.
As in detail discussed in [11], the sum of the momentum fractions of all the quarks (including antiquarks) can be determined via integration of $F_2(x)$. The extracted value of the momentum carried by quarks is only about 50% of the total momentum of the proton. Since the photon only probes the charged particles, this observation is consistent with about $\frac{1}{2}$ of the nucleon momentum being carried by the exchange particles of the quark interaction, the gluons.

1.1.4. Quark Parton Model

In the QPM, developed by Feynman and Bjørken, the momentum and spin distribution of the quarks inside the proton are characterized at leading twist by three fundamental parton distribution functions (PDF): the quark distribution $q(x, Q^2)$, which is the probability of finding a quark with a fraction x of the longitudinal momentum of the parent hadron; the helicity distribution $\Delta q(x, Q^2)$, which measures the net helicity of a quark in a longitudinally polarized hadron; and the transversity distribution $\delta q(x, Q^2)$ (more usually denoted as $h_1^q(x, Q^2)$), the net transverse polarization in a transversely polarized hadron [29, 30]. They

[1] Fermi National Accelerator Laboratory
[2] European Organization for Nuclear Research
[3] Hadron Electron Ring Accelerator

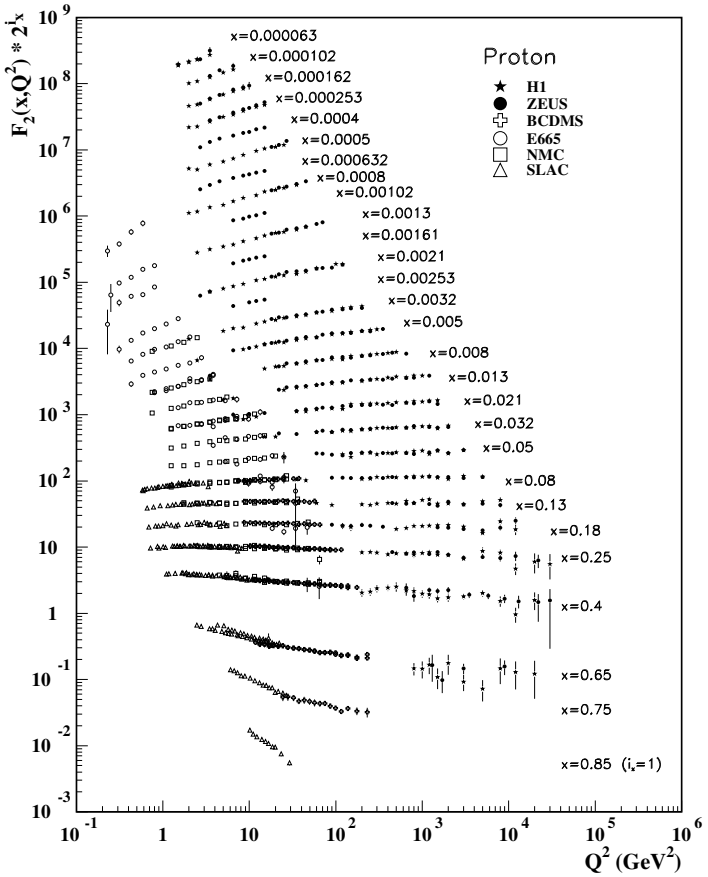

Fig. 1.4.: The proton structure function F_2^p measured in electromagnetic scattering of positrons on protons (collider experiments ZEUS and H1), in the kinematic domain of the HERA data, for $x > 0.00006$, and for electrons (SLAC) and muons (BCDMS, E665, NMC) on a fixed target. The data are plotted as a function of Q^2 in bins of fixed x [20] .

are defined by

$$q_{\mathrm{f}}(x) = q_{\mathrm{f}}^{\overrightarrow{\Rightarrow}}(x) + q_{\mathrm{f}}^{\overrightarrow{\Leftarrow}}(x), \tag{1.11}$$

$$\Delta q_{\mathrm{f}}(x) = q_{\mathrm{f}}^{\overrightarrow{\Rightarrow}}(x) - q_{\mathrm{f}}^{\overrightarrow{\Leftarrow}}(x), \text{ and} \tag{1.12}$$

$$h_1^q(x) = q^{\Uparrow\uparrow}(x) - q^{\Uparrow\downarrow}(x). \tag{1.13}$$

Here $q_{\mathrm{f}}^{\overrightarrow{\Rightarrow}}(x)$ and $q_{\mathrm{f}}^{\overrightarrow{\Leftarrow}}(x)$ are the probability densities to find a quark of flavor f with momentum fraction x and spin parallel or antiparallel to the spin of the longitudinally polarized proton. $q^{\Uparrow\uparrow}(x)$ and $q^{\Uparrow\downarrow}(x)$ are the probability densities to find a quark with its spin aligned or anti-aligned to the spin of a transversely polarized proton.
The spin-independent and spin-dependent structure functions, which can be measured in DIS, can now be interpreted within the QPM as the charge-weighted sums over the quark flavors (including anti-quarks) of the corresponding parton distribution functions (PDF)

$$F_1(x) = \frac{1}{2}\sum_{\mathrm{f}} e_{\mathrm{f}}^2 q_{\mathrm{f}}(x), \tag{1.14}$$

$$g_1(x) = \frac{1}{2}\sum_{\mathrm{f}} e_{\mathrm{f}}^2 \Delta q_{\mathrm{f}}(x), \tag{1.15}$$

where e_{f} is the fractional charge carried by the quarks. Consequently, the first two of these PDFs are well known, whereas the transversity distribution, which describes the quark

transverse polarization inside a transversely polarized proton, is only little-known. Since it is directly measurable by Drell-Yan production $q\bar{q} \rightarrow (\gamma, Z) \rightarrow l^+l^-$ in double polarized $p\bar{p}$ collisions [31], the PAX collaboration proposes a dedicated measurement with polarized antiproton beams [32] at the Facility for Antiproton and Ion Research (FAIR) [33], using the HESR upgraded to a Proton-Antiproton Collider.

1.1.5. Spin Distribution of the Nucleon

The proton is a fermion with spin $1/2$ and, as a composite particle, the question arose how its spin originates from its constituents. 20 years ago, results from deep inelastic muon-proton scattering experiments performed by the European Muon Collaboration (EMC) suggested that the valence quarks intrinsic spin contributes only $25 - 30\%$ to the proton spin [34, 35] instead of 60% predicted by relativistic quark models. As an immediate consequence the question of the additional sources of the spin within the nucleon arises, which inspired a vast program of theoretical activities and new experiments [36]. One goal is the decomposition of the longitudinal spin components [37]

$$\frac{1}{2} = \frac{1}{2}\sum_q \Delta q + \Delta g + L_q + L_g, \tag{1.16}$$

where Δq and Δg denote the longitudinal spin contribution of the quarks (helicity) and gluons, respectively, and L_q and L_g are the orbital angular momentum contributions. A significant part of the spin could be carried by gluons, sea quarks and orbital angular momenta of quarks and gluons. The contribution of the sea quark polarization is consistent with zero as it has been measured by the HERMES experiment at DESY [38, 39]. The solution of this problem, called "spin crisis", was also not found by the COMPASS experiment at CERN or in polarized proton-proton collisions (PHENIX and STAR at RHIC), which determined a gluon polarization much to small to explain the 30% missing according to the theoretical predictions [40–42].

1.2. Polarized Antiproton Experiments

1.2.1. Overview

The HESR storage ring for antiprotons included in the FAIR project is to be build at GSI in Darmstadt/Germany. The machine is planned to provide high luminosity antiproton beams in the momentum range from $1.5\,\mathrm{GeV/c} < p < 15\,\mathrm{GeV/c}$ ($831\,\mathrm{MeV} < T < 14.1\,\mathrm{GeV}$) [1]. In order to study double polarized $p\bar{p}$ collisions proposed by the PAX collaboration, it would need to be upgraded into a collider. This consists of an Antiproton Polarizer Ring (APR) to polarize antiprotons at energies of $50 - 500\,\mathrm{MeV}$ and a Cooler Synchrotron Ring (CSR) to store protons or antiprotons at energies up to $3.5\,\mathrm{GeV}$. As depicted in Fig. 1.5, the polarized antiprotons circulate in the CSR whereas the polarized protons circulate in the HESR.
Polarized antiprotons, produced by spin filtering with an internal polarized gas target, where the beam becomes polarized because of a larger selective removal of one spin state compared to the other (see also Section 2.3), allow a unique access to a number of new fundamental physics observables. This includes a first measurement of the transversity distribution of the valence quarks in the proton, a direct determination of the transverse double spin asymmetry in the $p\bar{p}$ total cross section, and a first measurement of the moduli and the relative phase of the time-like electric and magnetic form factors $G_{\mathrm{E;M}}$ of the proton [1]. The measurement of the transversity is explained in detail in the following.

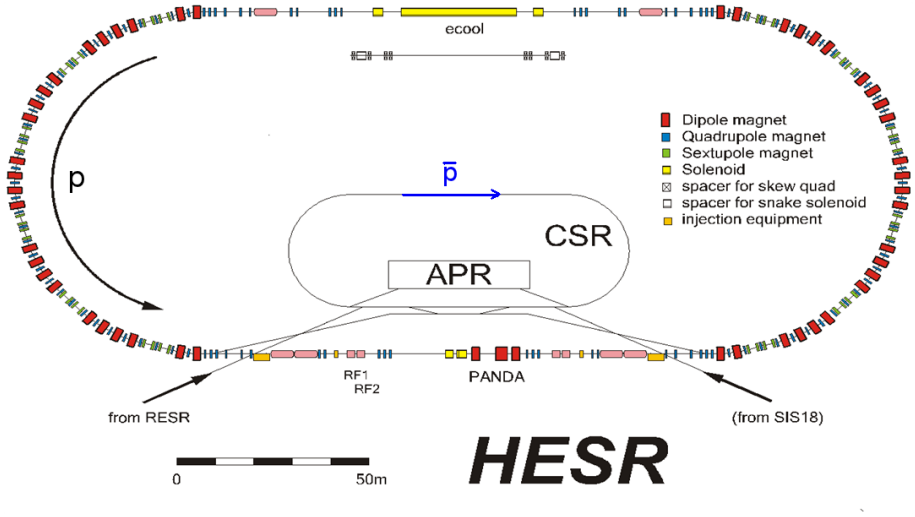

Fig. 1.5.: Proposed HESR upgrade for FAIR. The antiprotons are polarized in the APR by spin filtering. At the PAX interaction point polarized antiprotons from the CSR will collide with polarized protons from the HESR.

1.2.2. Transversity Distribution

The transversity distribution $h_1^q(x)$ is the last missing piece leading-twist of the QCD description of the partonic structure of the nucleon. Unlike the more conventional unpolarized quark distribution $q(x)$ and the helicity distribution $\Delta q(x)$, the transversity $h_1^q(x)$ can neither be accessed in deep inelastic scattering of leptons off nucleons, due to its chiral-odd nature, nor can it be reconstructed from the knowledge of $q(x)$ and $\Delta q(x)$ [43–46]. Since electroweak and strong interactions conserve chirality, $h_1^q(x)$ cannot occur alone, but has to be coupled to a second chiral-odd quantity. This is possible in polarized Drell-Yan processes, where one measures the product of two transversity distributions, and in Semi-Inclusive Deep Inelastic Scattering (SIDIS), where one couples $h_1^q(x)$ to a new unknown fragmentation function, the Collins function [47]. Similarly, one could couple $h_1^q(x)$ and the Collins function in transverse single-spin asymmetries (SSA) in inclusive processes like $p^\uparrow p \to \pi X$ [1].
The HERMES experiment at DESY[1] was the first to measure a nonzero, Collins asymmetry [48, 49], which would allow one to extract the transversity once the Collins function is known. A first extraction of $h_1^q(x)$, based on a global fit of the data from HERMES, COMPASS [50] and BELLE [51, 52] has been reported in [53]. Since the extraction of the transversity uses the projection of the Collins asymmetries measured at BELLE at $Q^2 = 110\,\mathrm{GeV}^2$ to HERMES energies ($\langle Q^2 \rangle = 2.4\,\mathrm{GeV}^2$), the theoretical uncertainties are rather large.
The most direct way to obtain information on transversity is the measurement of the double transverse spin asymmetry A_{TT} in Drell-Yan processes (Fig. 1.6) with both transversely polarized protons and antiprotons

$$A_{\mathrm{TT}} = \frac{d\sigma^{\uparrow\uparrow} - d\sigma^{\uparrow\downarrow}}{d\sigma\uparrow\uparrow + d\sigma^{\uparrow\downarrow}} = \hat{a}_{\mathrm{TT}} \frac{\sum_q e_q^2 h_1^q(x_1, Q^2) h_1^{\bar{q}}(x_2, Q^2)}{\sum_q e_q^2 q(x_1, Q^2) \bar{q}(x_2, Q^2)}, \tag{1.17}$$

where $q = u, d, \ldots$ and $\bar{q} = \bar{u}, \bar{d}, \ldots$, Q is the lepton pair invariant mass and $x_{1,2}$ are the fractional longitudinal momenta of the colliding hadrons, which are carried by the annihilating quark and antiquark. The double spin asymmetry $\hat{a}_{\mathrm{TT}}$ of the QED process

[1] Deutsches Elektronen-Synchrotron

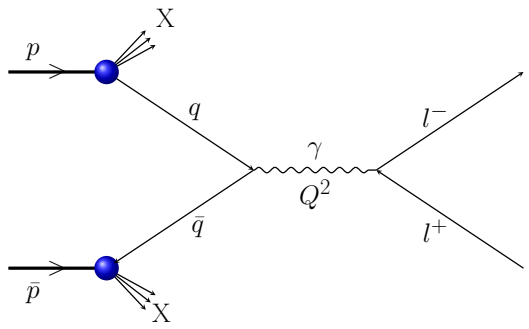

Fig. 1.6: Feynman diagram of the Drell-Yan process $p^\uparrow + \bar{p}^\uparrow \to l^+ + l^- + X$.

$q\bar{q} \to l^+l^-$ is given by

$$\hat{a}_{TT} = \frac{\sin^2\Theta}{1+\cos^2\Theta}\cos 2\phi, \tag{1.18}$$

where Θ is the polar angle of the lepton in the l^+l^- rest frame and ϕ is the azimuthal angle with respect to the proton polarization.
The asymmetry A_{TT} in Drell-Yan processes with transversely polarized protons is at present exclusively measurable at the Relativistic Heavy Ion Collider (RHIC). There, the product of two transversity distributions is measured, one for a quark (h_1^q) and one for an antiquark ($h_1^{\bar{q}}$)(both in a proton). Since they are assumed to be equivalent one basically determines $(h_1^q)^2$. At RHIC energies measurements at $\tau = x_1x_2 = Q^2/s \simeq 10^{-3}$ are expected, which mainly leads to the exploration of the sea quark content of the proton, where the asymmetry A_{TT} is likely to be tiny. Moreover, the QCD evolution of transversity is such that, in the kinematical regions of RHIC data, $h_1^q(x)$ is much smaller than the corresponding values of $\Delta q(x,Q^2)$ and $q(x,Q^2)$. All this makes the double spin asymmetry A_{TT} expected at RHIC very small, of the order of a few percents or less [1, 54, 55].
The golden channel to perform a self-sufficient measurement of A_{TT} is $\bar{p}^\uparrow p^\uparrow \to l\bar{l}X$ as proposed by the PAX collaboration. For typical PAX kinematics in the fixed target mode ($s = 30$ or $45\,\mathrm{GeV}^2$) one has $\tau = x_1x_2 = Q^2/s \simeq 0.2 - 0.3$, which implies that only quarks (from the proton) and antiquarks (from the antiproton) with large x contribute, i.e., valence quarks for which $h_1^q(x)$ is expected to be large. $A_{\mathrm{TT}}/\hat{a}_{\mathrm{TT}}$ is expected to be as large as 30%. When combining the fixed target and the collider operational modes ($s \simeq 30 - 200\,\mathrm{GeV}^2$), the experiment will explore the kinematic regions as shown in the left panel of Fig. 1.7. In the right panel the expected $A_{\mathrm{TT}}/\hat{a}_{\mathrm{TT}}$ as a function of Feynman $x_{\mathrm{F}} = x_1 - x_2$ for $Q^2 = 16\,\mathrm{GeV}^2$ is shown.

While the direct access to transversity is the outstanding, unique possibility offered by the PAX proposal concerning the proton spin structure, there are several other spin observables related to partonic correlation functions. The measurements with a polarized antiproton beam can also provide completely new insights into the understanding of (transverse) single-spin asymmetries or the origin of the unexpected Q^2-dependence of the ratio of the magnetic and electric form factors of the proton, which was illuminated in Sec. 1.1.2.

1.2.3. Production of Polarized Antiprotons

As shown above, polarized antiprotons will provide access to a wealth of single- and double-spin observables. Therefore, the first major goal on the agenda of PAX is to provide polarized antiprotons. Different suggestions, made at workshops in Bodega Bay 1985 [56] and

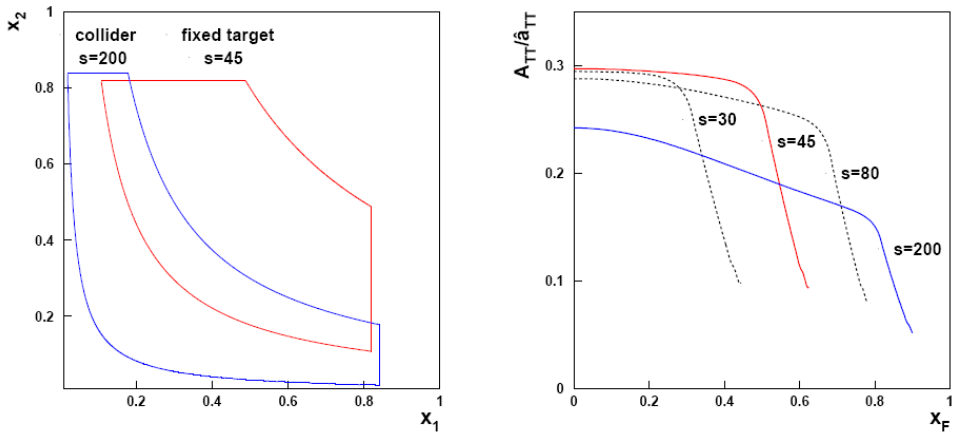

Fig. 1.7.: Kinematic region covered by the $h_1^q(x)$ measurement at PAX. In the asymmetric collider scenario (blue) antiprotons of $3.5\,\mathrm{GeV/c}$ impinge on protons of $15\,\mathrm{GeV/c}$ at c.m. energies of $s \approx 200\,\mathrm{GeV}^2$ and $Q^2 > 4\,\mathrm{GeV}^2$. The fixed target case (red) represents antiprotons of $22\,\mathrm{GeV/c}$ colliding with a fixed polarized target ($\sqrt{s} \approx \sqrt{45\,\mathrm{GeV}}$). Right: The expected asymmetry as a function of Feynman x_F for different values of s, but fixed $Q = 16\,\mathrm{GeV}^2$ [1].

Daresbury 2007 [57], like spin splitting in Stern-Gerlach separation [58] or the production of polarized antiprotons from the decay in flight of $\bar{\Lambda}$ hyperons [59] have not yet been tested or do not allow for efficient accumulation in a storage ring. The production of high luminosity polarized antiproton beams as a crucial prerequisite will be tested in spin-filtering studies at COSY/Jülich [60] and at AD/CERN [61]. The COSY accelerator will be utilized to test and commission the experimental equipment and repeat a spin-filtering experiment with protons in order to confirm our understanding of spin filtering in terms of the machine parameters. Since PAX proposes to build a dedicated Antiproton Polarizer Ring (APR), obtaining a comprehensive knowledge about the experimental boundary conditions is crucial.
Afterwards, a first feasibility test of spin filtering with antiprotons and a measurement of the spin-dependent cross sections σ_1 and σ_2 (see Sec. 2.3.1) in the range from 50 to $450\,\mathrm{MeV}$ is planned to be carried out at the Antiproton Decelerator (AD) at CERN. This data will allow for the definition of the optimum working parameters of the APR.

2. SPIN FILTERING IN STORAGE RINGS

Particle beams provided by accelerators are used in scattering experiments to study the structure and interaction of matter. The focus of current investigations, e.g., extraction of the transversity distribution from Drell-Yan production, requires the use of spin-polarized antiprotons. The spin-filtering method is proposed to pave the way toward such stored polarized antiproton beams.
The idea of spin filtering was first proposed by Csonka [62] in 1968 and can be described as a spin-selective attenuation of the particles circulating in a storage ring. An originally unpolarized beam becomes increasingly polarized by repeated interaction with a nuclear polarized internal gas target. A first feasibility test of polarizing beams of strongly interacting charged particles by spin filtering was carried out with protons at the Test Storage Ring (TSR) at MPIK[1] Heidelberg [63]. The Filter Experiment (FILTEX) from 1992 is described in more detail in Sec. 2.2. The theoretical interpretations, presented in Sec. 2.3, show that the small effective polarizing cross section demands for long filtering times. Consequently, particle beam dynamics and beam loss mechanisms have to be understood properly in order to optimize spin-filtering experiments. These aspects and how beam losses can be minimized by phase-space cooling are described in Sec. 2.1 in order to define the equipment and prerequisites for a spin-filter experiment.

2.1. Beam Dynamics in Storage Rings

One essential ingredient of particle accelerator experiments is the characterization of the particle beam in view of the particle motion and the interactions of the beam particles with each other and with internal targets. For the spin-filtering experiments as well as for the planned polarized antiproton experiments at AD, reasonably high luminosities of the polarized beams are crucial, which makes it indispensable to understand the beam loss mechanisms and how to minimize them.

2.1.1. Linear Beam Optics

The equations of particle motion in a closed orbit can be deduced by the second derivative of the position vector $\vec{r}''(s) = \frac{\vec{F}}{\gamma m}$, where $\vec{F} = q(\vec{v} \times \vec{B})$ is the Lorentz force. For a particle moving in s-direction $\vec{v} = (0, 0, v_s)$ (see Fig. 2.1) and considering only transverse magnetic fields $\vec{B} = (B_x, B_y, 0)$ the betatron oscillations, that characterize the transverse displacement of the orbit with respect to the reference orbit, can be described by the linear equations of motion [64, 65]

[1] Max-Planck-Institut für Kernphysik

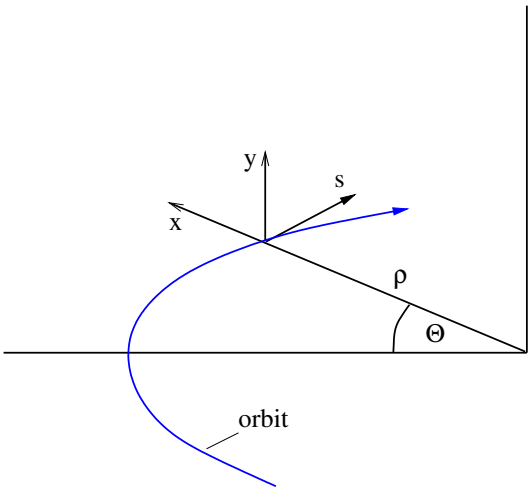

Fig. 2.1: Comoving right-handed coordinate system (s, x, y) for the characterization of particle movement in accelerators, where s points in direction of motion. Θ is the angle of rotation and ρ the orbit curvature.

$$x''(s) + \left(\frac{1}{\rho^2(s)} - k_x(s)\right) x(s) = \frac{1}{\rho(s)} \frac{\Delta p}{p}, \tag{2.1}$$

$$y''(s) + k_y(s) y(s) = 0. \tag{2.2}$$

Here $k_x(s) = \frac{q}{p}\frac{\partial B_y}{\partial x}$ and $k_y(s) = \frac{q}{p}\frac{\partial B_x}{\partial y}$ are the normalized horizontal and vertical focussing strengths induced by a magnetic quadrupole field. $\frac{1}{\rho} = \frac{q}{p}B_y$ is the inverse bending radius due to a vertical magnetic dipole field. These functions are periodical and recur in each turn. For $\frac{1}{\rho} = 0$ and $\frac{\Delta p}{p} = 0$, the general solution of Eq. (2.1) and (2.2) for $z \in \{x, y\}$ is

$$z(s) = \sqrt{\epsilon_z \beta_z(s)} \cos(\psi_z(s) + \psi_{z_0}) \quad \text{with} \quad \psi_z(s) = \int_0^s \frac{d\tilde{s}}{\beta_z(\tilde{s})} + \psi_0 \tag{2.3}$$

being the phase advance of the oscillation, $\beta_z(s)$ the betatron function, and ϵ_z the beam emittance. Hence the position dependent amplitude of the betatron oscillation of a particle is described by $E_z(s) = \sqrt{\epsilon_z \beta_z(s)}$ with the envelope $E_z(s)$. The betatron phase change per revolution $\Delta\psi_z = \psi(s + C) - \psi(s)$ (C is the ring circumference) is of prime importance for the understanding of resonances. The **betatron tune** or working point, that illustrates the number of oscillation per turn is given by

$$Q := \frac{\Delta\psi}{2\pi} = \frac{1}{2\pi} \oint \frac{d\tilde{s}}{\beta(\tilde{s})}. \tag{2.4}$$

The beam lifetime strongly depends on the chosen betatron tunes. Because of the symmetry in a synchrotron like COSY, the magnetic structure after each full turn merges into itself (see Sec. 3.1.1). Consequently, the forces on the beam recur periodically. Therefore the tunes should be irrational numbers, while in practice one tries to stay far from the betatron resonances. The resonance condition is given by

$$mQ_x = nQ_y = l \qquad\qquad m, n, l \in \mathbb{N}. \tag{2.5}$$

Combining Eq. (2.3),

$$z'(s) = -\frac{\sqrt{\epsilon}}{\sqrt{\beta(s)}} \left[\alpha(s) \cos(\psi(s) + \psi_{z_0}) + \sin(\psi(s) + \psi_{z_0})\right], \tag{2.6}$$

and $\gamma(s) := \frac{1+\alpha^2(s)}{\beta(s)}$, where $\alpha(s) := -\frac{\beta'(s)}{2}$, allows for a description of the particle motion in the $z - z'$-plane, which is better known as **transverse phase space**. α, β and γ are also known as Twiss parameters. Here, the trajectory of a particle follows an ellipse described by

$$\boxed{\gamma(s)z^2(s) + 2\alpha(s)z(s)z'(s) + \beta(s)z'^2(s) = \epsilon}, \tag{2.7}$$

which encloses a phase space equal to $F = \pi\epsilon^*$, as depicted in Fig. 2.2. Position and shape of the ellipse change along the orbit due to different Twiss parameters, but the area for a conservative system is invariant according to the Liouville's theorem [67].

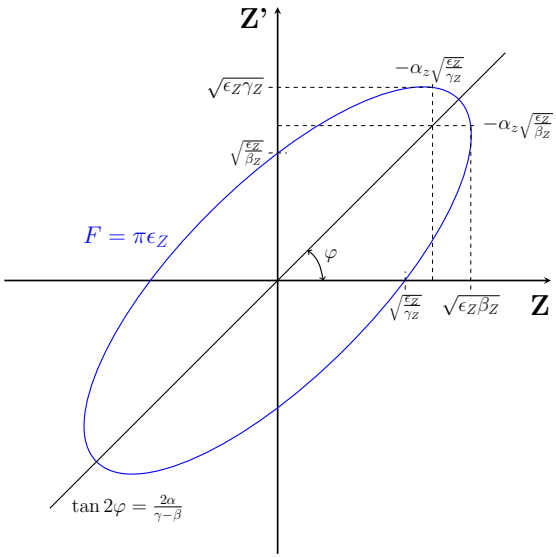

Fig. 2.2: Phase space ellipse of the particle motion in the $z - z'$-plane. The area enclosed by the ellipse is equal to $\pi\epsilon$; α, β and γ are the Twiss functions. The maximum amplitude of the betatron motion is $\sqrt{\beta\epsilon}$, and the maximum divergence (angle) of the betatron motion is $\sqrt{\gamma\epsilon}$ [66].

For a determination of the emittance of a beam, which is an ensemble of particles with each particle having its own phase space ellipse, a Gaussian charge distribution is assumed

$$\rho(x,y) = \frac{Ne}{2\pi\sigma_x\sigma_y} \cdot \exp\left(-\frac{x^2}{2\sigma_x^2} - \frac{y^2}{2\sigma_y^2}\right). \tag{2.8}$$

$\rho(x,y)$ characterizes the transverse charge distribution, with the standard deviations σ_x and σ_y. All particles with a distance of one standard deviation to the beam axis have an **emittance** of

$$\epsilon_{\text{rms}} = \frac{\sigma^2(s)}{\beta(s)}, \tag{2.9}$$

which is defined as the emittance of the beam. The emittance of the particle with the maximum possible phase ellipse equals the **transverse acceptance** of the accelerator (without closed-orbit deviation). It is given as

$$A = \left(\frac{d^2}{\beta}\right)_{\text{min}}, \tag{2.10}$$

where d is the free aperture at the location in the ring where A is minimal. Especially in storage rings a large A/ϵ is crucial to minimize significant beam losses. The acceptance angle

*Here µm is used as the unit of emittance. Accelerator scientist also use mm mrad or even π mm mrad to imply that the emittance as well as the acceptance is related to the area of a phase space ellipse [66].

Θ_{acc} is defined as the maximum allowed angle kick, below which a scattered particle remains in the ring. For decoupled betatron oscillations in both planes it can be determined by [68]

$$\frac{1}{\Theta_{\mathrm{acc}}^2} = \frac{1}{2\Theta_x^2} + \frac{1}{2\Theta_y^2} \quad \text{with} \quad \frac{1}{\Theta_{x,y}^2} = \frac{\beta_{x,y}}{A_{x,y}}. \tag{2.11}$$

In case of a not vanishing momentum dispersion ($\frac{\Delta p}{p} \neq 0$) of the beam particles the beam orbit is manipulated by magnetic dipole components ($\frac{1}{\rho} \neq 0$). For a homogeneous magnetic field without gradients ($k_x = 0$), Eq. (2.1) becomes

$$x'' + \frac{1}{\rho^2} \cdot x = \frac{1}{\rho}\frac{\Delta p}{p}. \tag{2.12}$$

Defining a **dispersion orbit** as

$$D''(s) + \frac{1}{\rho^2} D(s) = \frac{1}{\rho} \tag{2.13}$$

with $\frac{\Delta p}{p} = 1$ and solving the inhomogeneous differential equation, a total displacement from the reference orbit can be calculated

$$x(s)_{\mathrm{tot}} = x(s) + x_D(s) = x(s) + D(s)\frac{\Delta p}{p}. \tag{2.14}$$

A single particle in the beam is not longer moving along the ideal orbit, but oscillates around a dispersion orbit [67]. Thus the path length and the orbit frequency depend on the particle momentum. Since this plays an important role for longitudinal phase focussing the ratio of $\Delta L/L$ to $\Delta p/p$ is defined as **momentum compaction factor**

$$\alpha = \frac{\Delta L/L}{\Delta p/p}. \tag{2.15}$$

The preparation of a closed orbit with minimal distortions is a prerequisite for large beam lifetimes, which are essential for spin-filtering experiments. This includes the choice of a convenient betatron tune in order to prevent betatron resonances and to minimize the dispersion and the betatron function especially at positions with small free aperture.

2.1.2. Beam Loss Mechanisms

Since the polarization build-up rates in spin filtering are rather small, there is a need for long storage times in order to produce intense, polarized proton or antiproton beams with reasonable polarization. Therefore, the dominating particle loss mechanisms have to be understood and minimized. Once the ion beam is injected and circulating in the storage ring, coasting beam condition, various mechanisms give rise to particle losses. In general these are

- Betatron resonances.
- Beam target and/or residual gas Coulomb interactions comprising:
  - energy loss, causing particle losses at the longitudinal acceptance
  - emittance growth due to multiple small-angle scattering, causing losses at the transverse acceptance
  - immediate loss of ions in a single collision where the scattering angle is larger than the transverse acceptance angle.

Energy loss and emittance growth can to a large extent be compensated by electron cooling, the technique applied at COSY for beam cooling at the lower beam energies ($T_p \leq 70\,\mathrm{MeV}$).

- Single intrabeam scattering which is a Coulomb interaction between the beam particles causing emittance growth and possibly large momentum changes (Touschek effect).
- Beam losses due to recombination of beam particles with electrons from the electron cooler are known to be negligible. However, the production of neutral hydrogen atoms (H^0) is large enough to be used as performance monitor [69] (Sec. 3.1.4).
- Hadronic interactions also lead to an immediate particle loss, but this is the effect to be exploited for the polarization build-up.

Betatron resonances
The resonance condition is given in Eq. (2.5). This means that the number of betatron oscillations per turn should be irrational numbers in order to avoid losses of beam particles. Thus, the choice of a suitable working point is mandatory to achieve large beam lifetimes. This procedure is in detail described in Sec. 4.2 (Fig. 4.4).

Energy loss
A charged particle that passes through matter looses energy in proportion to the density of a target through electromagnetic processes. The energy loss per single traversal δT and the knowledge of the stopping power (dE/dx) and the mass of the target atom m allow one to determine the effective target density d_t,

$$d_\mathrm{t} = \frac{\delta T}{(dE/dx)m}. \tag{2.16}$$

In storage rings the energy loss builds up in time due to a large number of circulations and causes a shift in the frequency of revolution f. Therefore the frequency shift in time is a measure of the target density or alternatively of the residual gas contributions [70],

$$d_\mathrm{t} = \left(\frac{1+\gamma}{\gamma}\right)\frac{1}{\eta}\frac{1}{(dE/dx)m}\frac{T_0}{f^2}\frac{df}{dt}. \tag{2.17}$$

Here γ is the Lorentz factor, and η is the frequency slip parameter defined as $\eta = \frac{1}{\gamma^2} - \alpha$. When the shift in frequency and respectively in momentum exceeds the longitudinal acceptance $\delta = \frac{\Delta p_{max}}{p}$ of the accelerator, the particle gets lost,

$$\frac{\Delta f}{f}\frac{1}{\eta} = \frac{\Delta p}{p_0} > \delta. \tag{2.18}$$

The energy loss caused by the polarized gas target, which will be used in spin-filtering experiments, can be balanced by electron cooling. Switching off the electron beam provides a reliable method to determine the target thickness from the observed frequency shift.

Single Coulomb scattering
The Coulomb-loss cross section can be derived by integration of the differential Rutherford cross section, for scattering angles larger than Θ_acc [71],

$$\Delta\sigma_\mathrm{C} = \int_0^{2\pi}\int_{\Theta_\mathrm{acc}}^{\Theta_\mathrm{max}} \frac{d\sigma}{d\Omega} d\phi \sin\Theta d\Theta = 4\pi\frac{Z_\mathrm{gas}^2 Z_i^2 r_i^2}{\beta^4\gamma^2\Theta_\mathrm{acc}^2}. \tag{2.19}$$

Z_gas, Z_i are the atomic numbers of the target (or residual gas) and the ion beam, respectively, and $r_i = r_e m_e/m_i$ is the classical ion radius. Θ_acc is assumed to be small. Consequently, losses due to the residual gas are amplified in regions of small acceptance angles and large

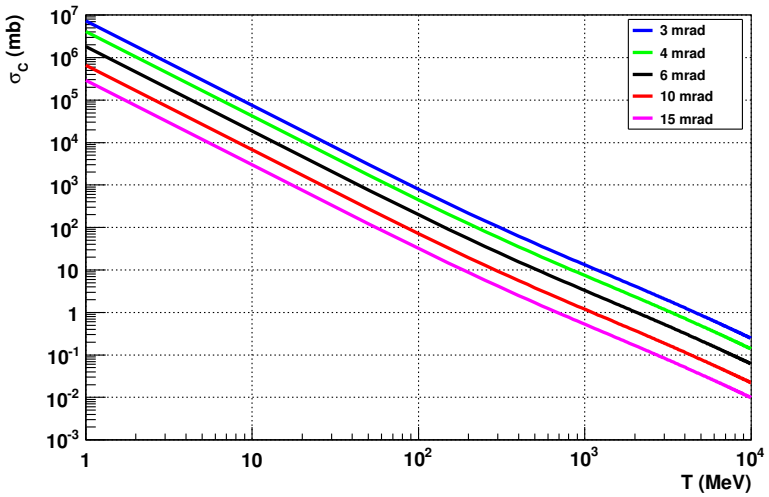

Fig. 2.3.: Coulomb cross section σ_{C} as a function of the kinetic energy T for different acceptance angles Θ_{acc}.

betatron functions. Inserting estimated parameters at COSY ($\Theta_{\mathrm{acc}} \approx 6\,\mathrm{mrad}$, $T = 49.3\,\mathrm{MeV}$) into Eq. (2.19) yields $\Delta\sigma_{\mathrm{C}} \approx 800\,\mathrm{mb}$ (Fig. 2.3). The lifetime due to single Coulomb scattering is given by

$$\tau_{\mathrm{C}} = \frac{1}{\Delta\sigma_{\mathrm{C}} d_{\mathrm{t}} f}, \tag{2.20}$$

where d_{t} is the target areal density and f the revolution frequency.

Touschek effect

Intense ion beams with small emittance as they are created by beam cooling reveal also phenomena of the mutual Coulomb interaction of the individual beam particles, called intrabeam scattering (IBS). Especially at low beam energies, IBS is a further mechanism leading to emittance growth. Large angle intrabeam scattering events known as Touschek effect may change the momentum of a single particle so that it is immediately lost at the longitudinal acceptance of the ring. The Touschek lifetime is given by [72, 73]

$$\tau_{\mathrm{T}} = \frac{4\gamma^3\beta^3 \cdot \langle\sqrt{\beta_z}\rangle \cdot C \cdot \epsilon^{3/2} \cdot \delta^2}{\sqrt{\pi} \cdot I \cdot c \cdot r_0^2}, \tag{2.21}$$

where ϵ_z is the transverse rms beam emittance, I the number of circulating particles, C the ring circumference, β_z the average betatron amplitude in the ring, r_0 the classical particle radius, and δ the longitudinal machine acceptance as defined earlier. If single intrabeam scattering dominates the lifetime in the machine, one has to observe the corresponding dependencies on beam intensity, the beam emittance and momentum acceptance δ. The Touschek effect is an important beam loss factor in electron rings. How far it could be relevant for a proton machine is a topic of the machine studies in this work (see Sec. 4.4).

Hadronic interaction

The total hadronic cross section for pp collisions is shown in Fig. 2.4. For $T = 49.3\,\mathrm{MeV}$ or $p = 308\,\mathrm{MeV/c}$, where the spin-filtering experiment at COSY is planned, the total hadronic cross section amounts to $\sigma_{\mathrm{tot}} \approx 50\,\mathrm{mb}$. The lifetime due to hadronic interactions is given by

$$\tau_{\mathrm{tot}} = \frac{1}{\sigma_{\mathrm{tot}} d_{\mathrm{t}} f}. \tag{2.22}$$

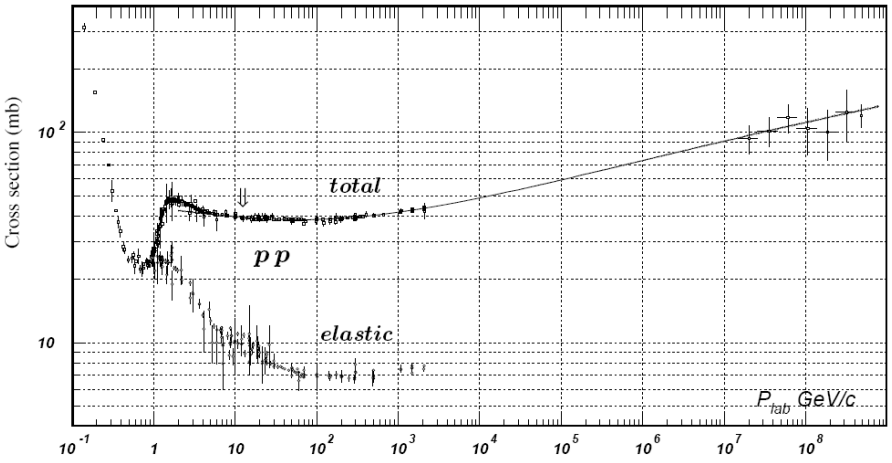

Fig. 2.4.: Hadronic cross section for pp collisions as a function of laboratory beam momentum [20].

2.1.3. Beam Temperature and Beam Cooling

The terms temperature and cooling of a particle beam have been deduced from the kinetic gas theory. The beam temperature $k_{\mathrm{B}}T$ is defined by the mean kinetic energy of the particle beam in the reference system that moves with the mean particle velocity. It is $\frac{3}{2}k_{\mathrm{B}}T = \frac{1}{2}m\langle v^2\rangle$, where k_{B} is the Boltzmann constant. Therewith the transverse and longitudinal beam temperatures become $k_{\mathrm{B}}T_{\perp} = \frac{1}{2m}\langle p_{\perp}^2\rangle \approx \frac{1}{2}mc^2(\gamma\beta)^2\left(\frac{\epsilon_x}{\beta_x}+\frac{\epsilon_y}{\beta_y}\right)$ and $\frac{1}{2}k_{\mathrm{B}}T_{\parallel} = \frac{1}{2m}\langle p_{\parallel}^2\rangle \approx \frac{1}{2}mc^2\beta^2\left(\frac{\sigma_p}{p}\right)^2$, respectively [65].
Scattering processes like those described in Sec. 2.4 cause a beam to change its phase space distribution. Multiple scattering, for example blows up the beam and increases the beam temperature, due to the growth of emittance and momentum distribution. Since those effects lead to intensity losses with time, one has to compensate the "beam heating" by the help of dissipative forces. Thus, different techniques for beam cooling can be applied. At COSY phase-space cooling up to $600\,\mathrm{MeV/c}$ proton-beam momentum is achieved by electron cooling [69] and at larger momenta stochastic cooling is used [74, 75]. In the following electron cooling is described, since this technique is most useful and applicable at spin-filtering energies.

Electron cooling
Electron cooling as "an effective method of damping particle oscillations in proton and anti-proton storage rings" was first proposed by G. I. Budker in 1967 [76], and is an essential tool for many of todays accelerator experiments such as spin-filtering experiments. A first feasibility test of this technique, which shrinks the size, divergence and energy spread of a beam without removing particles, was performed in 1974 [77]. Since the phase space occupied by the stored particles is compressed, it is equivalent to reducing the temperature of the beam [71]. It is achieved by combining a circulating beam with a nearly monochromatic and parallel electron beam over a certain distance, where the "heat" is transfered from the ions to the electrons by Coulomb interaction. The electron beam is renewed and the velocity spread of the ion beam is reduced in all three coordinates.
A "cold", dense electron beam is produced from a thermionic cathode and accelerated electrostatically to the average velocity of the particles in the circulating beam. Guided by the magnetic field of solenoids and toroids the electron beam is directed into the cooling solenoid over a certain length. The dynamics of the cooling process in the interaction region

is conveniently described by the so-called binary collision model in the moving frame of the average electron velocity. The cooling force F, slowing down the ion, is given as a function of the relative velocity between ion and electron $\vec{v}_{\mathrm{rel}} = \vec{v}_{\mathrm{ion}} - \vec{v}_e$ [78]

$$\vec{F}(\vec{v}_{\mathrm{ion}}) = -\frac{4\pi n_e e^2 q^2}{m_e} L_{\mathrm{C}} \int \frac{\vec{v}_{\mathrm{rel}}}{|\ v_{\mathrm{rel}}\ |^3} f(v_e) d^3 v_e. \tag{2.23}$$

Here, n_e is the electron density, m_e is the electron mass, $f(v_e)$ is the velocity distribution, and $L_{\mathrm{C}} = \ln\left({}^{b_{\max}}/_{b_{\min}}\right)$ is the Coulomb logarithm, where $b_{\max}$ and $b_{\min}$ are relevant impact parameters of the collision [79]. The cooling force increases linearly with increasing velocity as long as it is small compared to the velocity spread of the electrons. If the ion velocity is large compared to the velocity spread of the electrons, the cooling force is inversely proportional to the square of the ion velocity due to the shorter interaction time between ion and electron ($F \propto (v_{\mathrm{ion}} - v_e)^{-2}$) [80].
It is important to note that $f(v)$ is not isotropic. Due to the electrostatic acceleration the electron temperature in longitudinal direction is much lower than the cathode temperature of about $0.1\,\mathrm{eV}$. Therefore, the longitudinal cooling force at low relative velocities is expected to be stronger. However, the electrons are not free like in a gas but bounded by cyclotron circles to the longitudinal magnetic field lines. In strong fields the electrons can only move in longitudinal direction because a transverse momentum transfer is retarded. As a consequence, the transverse cooling force is also governed by the longitudinal electron temperature. A detailed theoretical description of these effects is rather complicated. A widely used practical formula is given by Parkhomchuk [81]

$$\vec{F}(\vec{v}_{\mathrm{ion}}) = -\frac{4e^2 q^2 n_e L_C}{m_e} \frac{\vec{v}_{\mathrm{ion}}}{\left(\vec{v}_{\mathrm{ion}}^2 + v_{eff}^2\right)^{3/2}}, \tag{2.24}$$

where $v_{eff} = \sqrt{v_{||}^2 + \Delta v_{\perp}^2}$ describes not only the electron velocity $v_{||}$ but also the transverse components of imperfections of the longitudinal solenoid field $\Delta v_{\perp}$. Figure 2.5 shows qualitatively the cooling force for an effective velocity of $v_{\mathrm{eff}} = 5 \cdot 10^6\,\mathrm{cm/s}$ corresponding to an effective temperature of $k_{\mathrm{B}}T = 0.0142\,\mathrm{eV}$.
Electron cooling is a powerful tool for beam cooling especially at low kinetic proton energies. Thus, as stated before, this technique is applicable for spin-filtering experiments.

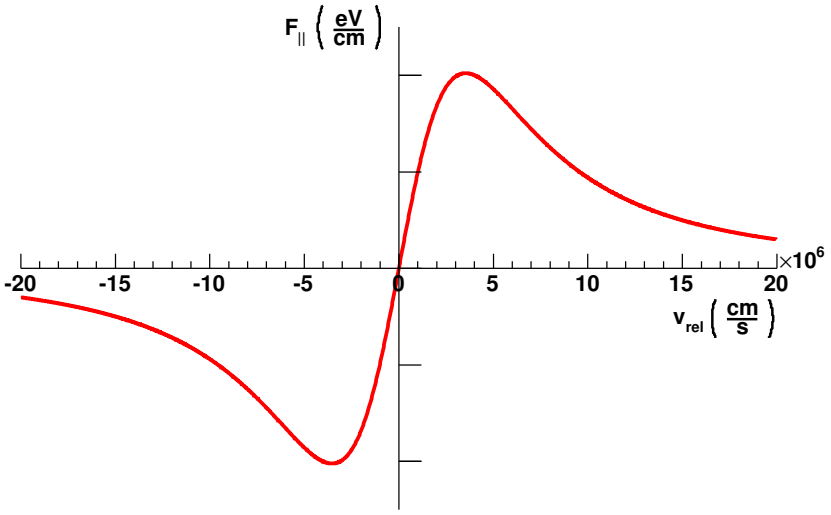

Fig. 2.5.: Qualitative behavior of the cooling force as a function of the relative velocity v_{rel}.

2.2. The Filter Experiment (FILTEX) - Proof of Principle

The build-up of polarization by means of spin filtering was tested for the first time with an initially unpolarized proton beam of kinetic energy $T = 23\,\mathrm{MeV}$ at the Test Storage Ring (TSR) at Heidelberg (Fig. 2.6). Using multiturn stacking injection while reducing the phase space by electron cooling allowed to store a beam of up to $1\,\mathrm{mA}$ in the $55.4\,\mathrm{m}$ long storage ring. The circulating beam passed through a transversely nuclear polarized hydrogen gas target of an areal density of $(5.3\pm0.3)\cdot10^{13}\,\mathrm{H/cm^2}$, provided by atoms from an atomic beam source, which were injected into a $250\,\mathrm{mm}$ long aluminum storage cell tube, cooled to about 100 K. Thereby, the target density compared to room temperature was increased by about a factor $\sqrt{3}$. The target atoms were in a single spin state, i.e., protons and electrons were both polarized. The magnitude of the nuclear target polarization was determined to be $Q = 0.795 \pm 0.024$ using p-α scattering [82, 83].
The beam polarization P is defined by the relative occupation number of protons (antiprotons) with spins parallel and antiparallel to the quantization axis[1]

$$P = \frac{N_\uparrow - N_\downarrow}{N_\uparrow + N_\downarrow}, \tag{2.25}$$

where $N_{\uparrow,\downarrow}$ are the two possible spin-states and $N = N_\uparrow + N_\downarrow$ denotes the total number of particles in the beam. Since in general the total hadronic cross section is different for parallel ($\uparrow\uparrow$) and antiparallel ($\uparrow\downarrow$) orientation of the beam particle spins relative to the direction of the target polarization, one spin direction is depleted faster than the other, so that the circulating beam becomes increasingly polarized, while the intensity decreases with time (Fig. 2.7). This principle can be deduced from the total hadronic cross section [84, 85]

$$\sigma_{\mathrm{tot}} = \sigma_0 + \sigma_1(\vec{P}\cdot\vec{Q}) + \sigma_2(\vec{P}\cdot\hat{k})(\vec{Q}\cdot\hat{k}), \tag{2.26}$$

where $\vec{P}$ and $\vec{Q}$ are the polarization vectors of the beam particle and the target particle, σ_0 is the spin-independent hadronic cross section and σ_1 and σ_2 are the spin-dependent cross sections, describing the effect of the relative orientation of $\vec{P}$, $\vec{Q}$ and the beam direction, given by the unit vector $\hat{k}$. Assuming $|\vec{P}| = |\vec{Q}| = 1$ the cross sections for the transverse and the longitudinal case are

$$\sigma^{\perp}_{\mathrm{tot}\pm} = \sigma_0 \pm \sigma_1 \quad \text{and} \quad \sigma^{\parallel}_{\mathrm{tot}\pm} = \sigma_0 \pm (\sigma_1 + \sigma_2). \tag{2.27}$$

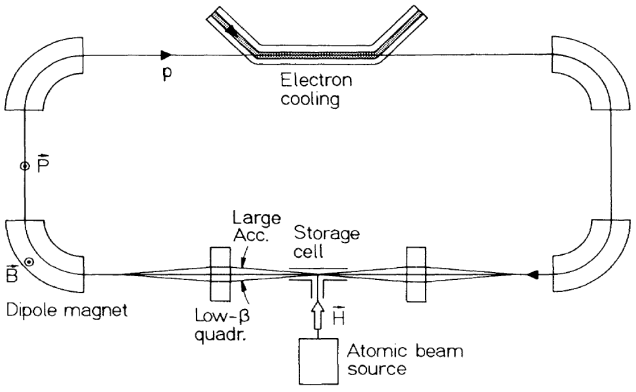

Fig. 2.6: Principle of a spin-filter experiment with a storage ring, a low-β target section, a storage cell, an atomic beam source, and an electron cooler [63].

[1]The quantization axis for the spin orientation of the atoms inside the storage cell is defined by the magnetic holding field orientation.

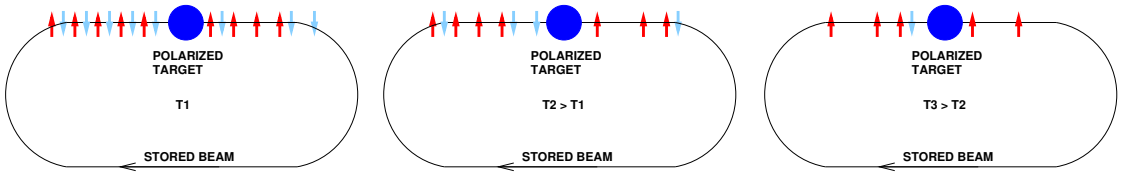

Fig. 2.7.: The three sketches demonstrate the method of spin filtering [86]. The arrows indicate particles with spin up (red) and down (blue). After some time of filtering (T2 and T3) the beam current is reduced and the beam is partially polarized .

Consequently, the intensity of spin-up and spin-down particles each decreases exponentially but with different time constants. This leads to a polarization build-up with time t, which can be expressed in the absence of depolarization as

$$P(t) = \tanh(\mathrm{t}/\tau_1). \tag{2.28}$$

The spin-dependent cross sections σ_1 and σ_2 can be extracted from the time constants for transverse ($\perp$) or longitudinal ($\parallel$) filtering, which are given by

$$\tau_1^{\perp} = \frac{1}{\tilde{\sigma_1} Q d_\mathrm{t} f} \quad \text{and} \quad \tau_1^{\parallel} = \frac{1}{(\tilde{\sigma_1} + \tilde{\sigma_2}) Q d_\mathrm{t} f}, \tag{2.29}$$

respectively. Here, d_t is the target areal density in atoms/cm^2 and f the revolution frequency of the particles in the ring. The polarizing cross sections $\tilde{\sigma_1}$ and $\tilde{\sigma_2}$ are closely related to the spin-dependent total cross sections σ_1 and σ_2, where the difference arises because protons that scatter at a sufficiently small angle remain in the ring ($\tilde{\sigma} = \sigma(\Theta > \Theta_{\mathrm{acc}})$). This is the case if the scattering angle Θ is smaller than the acceptance angle Θ_{acc} of the machine (see Sec. 2.1.1) [60].
At FILTEX, a polarization build-up rate of

$$\frac{dP}{dt} \approx \frac{1}{\tau_1} = 0.0129 \pm 0.0006 \text{ per hour} \tag{2.30}$$

has been observed, as illustrated in Fig. 2.8. This corresponds to a polarizing cross section of $\sigma_{\mathrm{pol}} = (73 \pm 6)$ mb[1] [87]. With positive target polarization, the resulting beam polarization was positive, whereas for a negatively polarized target the beam became negatively polarized.

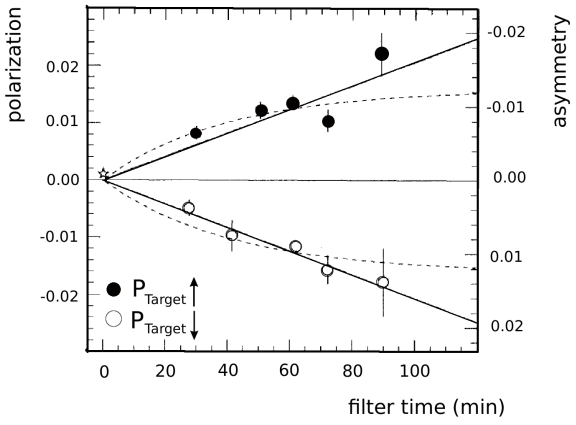

Fig. 2.8: Asymmetry (right-hand scale) and polarization (left-hand scale) measured after filtering the beam in the TSR for different times t. The solid lines are based on an assumed rate of polarization build-up of $1.24 \times 10^{-2} \mathrm{h}^{-1}$, which corresponds to $\tau_1 = 80$ h. The dashed lines are based on the expected build-up rate ($\tau_1 = 42$ h) and an assumed polarization lifetime of $\tau_p = 81$ min [63].

[1] 1 mb = 10^{-27} cm^2 is used in nuclear physics for expressing the cross sectional area.

2.3. Theoretical Foundations of Spin Filtering

2.3.1. Polarization Build-up in a Stored Beam

In view of the planned spin-filtering experiments at COSY and AD a precise calculation of the expected polarization build-up is mandatory. The FILTEX results initiated a multitude of in parts contradictory theoretical calculations which have been discussed repeatedly over the course of the past two decades [88–92]. Especially the question whether, in future, *spin flip* will play a role in polarizing stored beams has been answered in a recent experiment at COSY [93] and will be discussed later on.
For now, two physical processes contribute to polarization build-up in spin filtering, namely spin selective scattering out of the ring acceptance and selective spin flip, where the particles remain in the ring. A derivation of the polarization evolution equations in spin filtering can be carried out using a system of differential equations that model the polarization build-up in a beam by spin filtering in a storage ring. For a given revolution frequency f in a ring with a polarized internal target (PIT) of areal density d_t and polarization Q oriented normal to the ring plane

$$\frac{d}{dt}\begin{pmatrix} N \\ s \end{pmatrix} = -f d_\mathrm{t} \begin{pmatrix} \tilde{\sigma_0} & Q\cdot\tilde{\sigma_1} \\ Q\cdot(\tilde{\sigma_1}+\Delta\sigma_1) & \tilde{\sigma_0}+2\Delta\sigma_0 \end{pmatrix} \cdot \begin{pmatrix} N \\ s \end{pmatrix} \tag{2.31}$$

describes the rate of change of the number of particles N and their total spin $s = N_\uparrow(t) - N_\downarrow(t)$ [94, 95]. The cross sections for the transverse case are

$$\tilde{\sigma_0} = 2\pi \int_{\Theta_\mathrm{acc}}^{\Theta_\mathrm{max}} \left(\frac{d\sigma}{d\Omega}\right) \sin\Theta d\Theta, \tag{2.32}$$

$$\tilde{\sigma_1} = 2\pi \int_{\Theta_\mathrm{acc}}^{\Theta_\mathrm{max}} \left(\frac{A_{00nn}+A_{00ss}}{2}\frac{d\sigma}{d\Omega}\right) \sin\Theta d\Theta, \tag{2.33}$$

$$\Delta\sigma_0 = 2\pi \int_{\Theta_\mathrm{min}}^{\Theta_\mathrm{acc}} \frac{d\sigma}{d\Omega} \left(1 - \frac{1}{2}D_{n0n0} - \frac{1}{2}D_{s'0s0}\cos\Theta - \frac{1}{2}D_{k'0s0}\sin\Theta\right) \sin\Theta d\Theta, \tag{2.34}$$

$$\Delta\sigma_1 = 2\pi \int_{\Theta_\mathrm{min}}^{\Theta_\mathrm{acc}} \frac{d\sigma}{d\Omega} \left(\frac{A_{00nn}+A_{00ss}-K_{n00n}-K_{s'00s}\cos\Theta-K_{k'00s}\sin\Theta}{2}\right) \sin\Theta d\Theta, \tag{2.35}$$

with the double-spin asymmetries $A(\Theta)$, the polarization transfer observables $K(\Theta)$ and the depolarization spin observables $D(\Theta)$, as defined in [84]. $\Delta\sigma_0$ describes the spin flip on an unpolarized target, whereas $\Delta\sigma_1$ stands for the spin flip on a polarized target. Due to azimuthal averaging of observables and cross sections the single-spin observables vanish, for example the analyzing power. Since the Coulomb fields of the proton and the atomic electron screen each other beyond the Bohr radius α_B, it can be assumed that protons flying at impact parameters larger than α_B do not interact with the atom. Therefore, the minimum scattering angle for $T = 23\,\mathrm{MeV}$ is given by

$$\Theta_\mathrm{min} \cong \frac{1}{p\cdot\alpha_\mathrm{Bohr}} = \frac{m_e\alpha_{em}}{\sqrt{2mT}} = 1.795\cdot10^{-2}\,\mathrm{mrad}. \tag{2.36}$$

The coupled evolution equations (Eq. (2.31)) have the solutions $\propto \exp(-\lambda_{1,2} f d_\mathrm{t} t)$ with the eigenvalues

$$\lambda_{1,2} = \tilde{\sigma_0} + \Delta\sigma_0 \pm Q\sigma_3, \qquad \text{where} \tag{2.37}$$

$$Q\sigma_3 = \sqrt{Q^2\tilde{\sigma_1}(\tilde{\sigma_1}+\Delta\sigma_1) + \Delta\sigma_0^2}. \tag{2.38}$$

The polarization and the intensity follow the laws (see also [94, 95])

$$P(t) = -\frac{Q(\tilde{\sigma_1} + \Delta\sigma_1)\tanh(Q\sigma_3 d_t f t)}{Q\sigma_3 + \Delta\sigma_0 \tanh(Q\sigma_3 d_t f t)}, \tag{2.39}$$

$$I(t) = I_0 \cdot \exp\left[-(\tilde{\sigma_0} + \Delta\sigma_0) \cdot \mathrm{d_t} \cdot \mathrm{f} \cdot \mathrm{t}\right] \left(\cosh(\mathrm{Q}\sigma_3 \mathrm{d_t ft}) + \frac{\Delta\sigma_0}{\mathrm{Q}\sigma_3} \sinh(\mathrm{Q}\sigma_3 \mathrm{d_t ft})\right). \tag{2.40}$$

The approximate polarization evolution and the effective polarizing cross sections for sufficiently short times are

$$\frac{dP}{dt} \approx -d_t f Q(\tilde{\sigma_1} + \Delta\sigma_1) \tag{2.41}$$

$$\sigma_\mathrm{P} \approx -Q(\tilde{\sigma_1} + \Delta\sigma_1). \tag{2.42}$$

Upon an extrapolation in detail described in [95], $\Delta\sigma_{0,1}$ are found to be negligible ($\Delta\sigma_1 \approx -6 \cdot 10^{-3}\,\mathrm{mb}$). It is explained by a vanishing interference between the hadronic spin flip and the dominant Coulomb amplitudes. The polarization transfer from polarized electrons to scattered protons is exactly canceled by the electron contribution to the spin-dependent transmission effect. Meanwhile, a measurement of the spin-flip cross section in low-energy electron proton scattering has been carried out at COSY using the electron cooler beam as an electron target. This experiment rules out the option to use comoving polarized positrons to polarize a stored antiproton beam, because the measured cross sections are by many orders of magnitude too small for making spin flip a viable tool [87].
A solution for different sets of differential equations describing the build-up of polarization by spin filtering in different scenarios can be found in [96, 97].

Aiming for an optimal filter experiment dP/dt of Eq. (2.41) has to be maximized. Thus the target density and the target polarization have to be as large as possible. Increasing the revolution frequency in a dedicated accelerator would mean to increase the kinetic energy of the beam and thereby decrease the build-up cross section. For the best compromise $f \cdot \tilde{\sigma}_1$ has to be maximal. Building an accelerator especially for spin filtering could mean to ensure the demanded energy but design the orbit length as short as possible in order to increase the revolution frequency.

2.3.2. Understanding the FILTEX Results

The polarization build-up has been interpreted in terms of the known pp spin-dependent interaction (see, e.g., [94]). The evaluation of the theoretical value for the FILTEX conditions yields

$$-\tilde{\sigma}_1^{\mathrm{theor}} = -2\pi \int_{\Theta_{\mathrm{acc}}}^{\Theta_{\mathrm{max}}} \left(\frac{A_{00nn} + A_{00ss}}{2} \frac{d\sigma}{d\Omega}\right) \sin\Theta d\Theta = (86 \pm 2)\,\mathrm{mb}, \tag{2.43}$$

which is in a good agreement with the experimental value (Sec. 2.2) though differing by about two standard deviations. For the FILTEX experiment, the acceptance angle was measured as $\Theta_{\mathrm{acc}} = (4.4 \pm 0.5)\,\mathrm{mrad}$. The double-spin asymmetries A_{00nn} (A_{yy}) and A_{00ss}(A_{xx}) (Fig. 2.9), the polarization transfer $K(\Theta)$ observables, and the depolarization spin observables $D(\Theta)$ were taken from the SAID database [98]. The theoretical evolution of the polarization with time using Eq. (2.39) is shown in Fig. 2.9 in the bottom right panel. Assuming a linear behavior for short times ($\leq 10\,\mathrm{h}$, black line in Fig. 2.9) the polarization build-up rate results in $dP/dt = 0.0151$ per hour, which is in similar agreement with the measured polarization as the polarizing cross section.

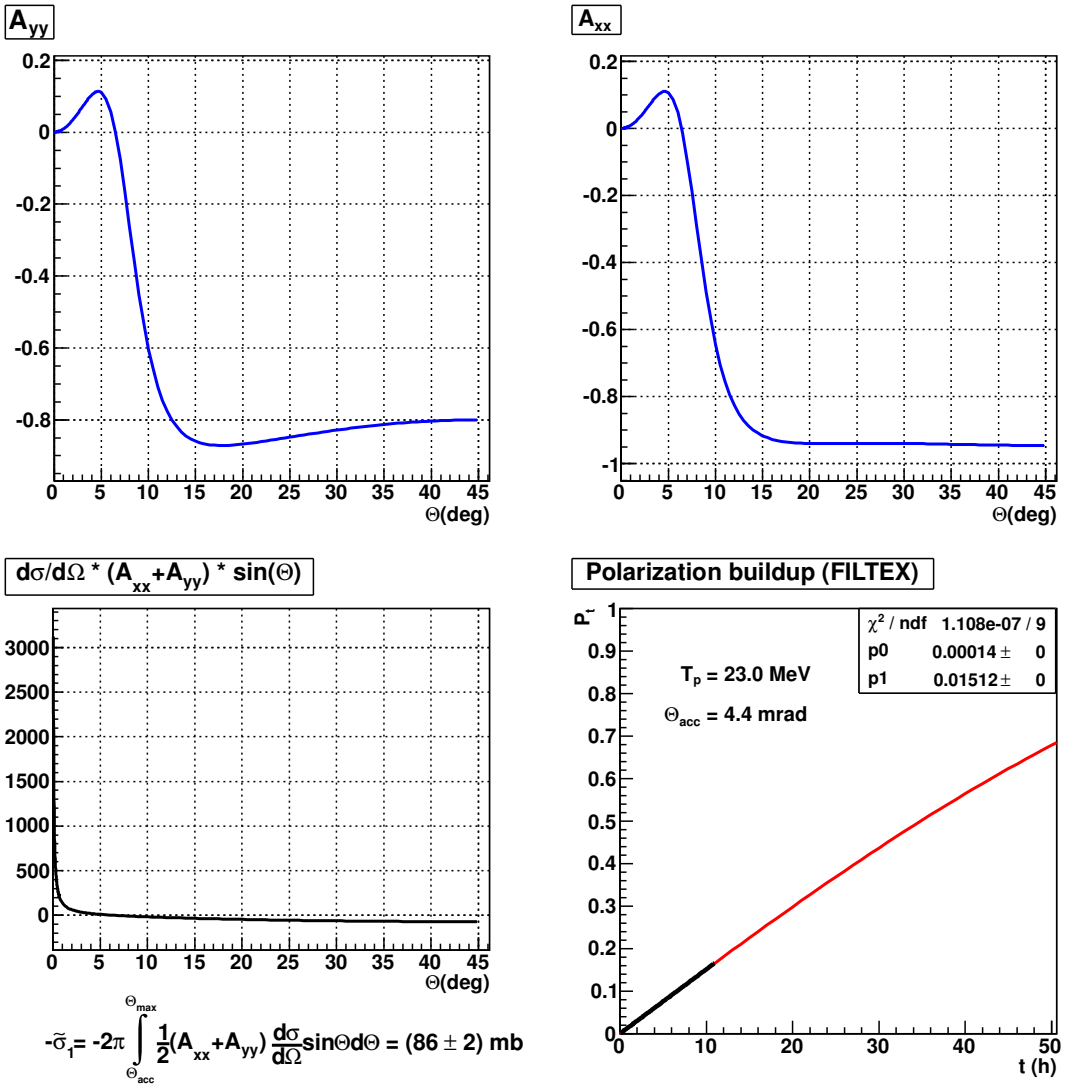

Fig. 2.9.: Top: Double-spin asymmetries A_{yy} (left) and A_{xx} (right) vs laboratory scattering angle Θ for $T = 23\,\mathrm{MeV}$; **Bottom left:** Polarization cross section $\tilde{\sigma_1}$; **Bottom right:** Calculated polarization build-up vs time for FILTEX. The expected polarization build-up rate of $P = 0.01512$ per hour assumes a linear evolution. Thus, the fit belongs only to short times (black curve).

2.4. Beam Lifetime and Figure of Merit

As pointed out above, the polarization build-up at FILTEX was in the order of 0.015 per hour. At COSY this value is expected to be even smaller by about a factor 9 mainly due to the smaller polarizing cross section, the smaller target thickness, and the larger accelerator circumference. Consequently, to achieve a reasonable beam polarization takes hours. Providing large beam intensities after filtering requires beam lifetimes in the same order.

The resulting beam lifetime is composed of the contributions of those particle loss mechanisms, which can not be compensated by electron cooling (see Sec. 2.1.2)

$$\tau = \left(\frac{1}{\tau_\mathrm{C}} + \frac{1}{\tau_\mathrm{tot}} + \frac{1}{\tau_\mathrm{T}} \right)^{-1} = ([\Delta\sigma_\mathrm{C} + \sigma_\mathrm{tot}] \cdot d_\mathrm{t} \cdot f + \frac{1}{\tau_\mathrm{T}})^{-1}, \tag{2.44}$$

where τ_C, τ_tot, and τ_T are the lifetimes due to single Coulomb scattering, hadronic scattering,

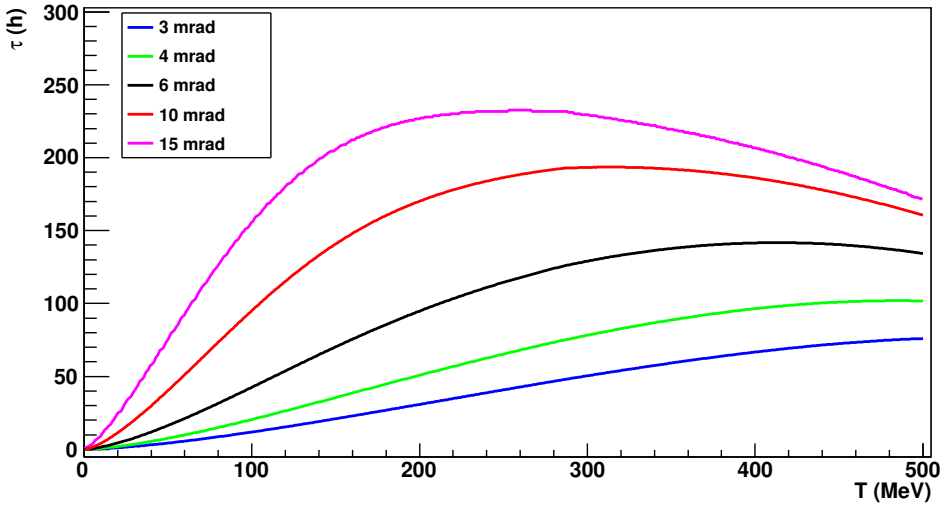

Fig. 2.10.: The calculated beam lifetime τ plotted as a function of the kinetic beam energy T for different acceptance angles Θ. Here only single Coulomb scattering and hadronic interaction are taken into account ($d_\mathrm{t} = 5 \cdot 10^{13}\,\mathrm{atoms/cm^2}$, $f = 500\,\mathrm{kHz}$).

and Touschek effect, respectively. Here the latter two are composed of contributions from the target and the residual gas. A plot of the expected beam lifetime for different acceptance angles as a function of the kinetic energy, considering only single Coulomb scattering and hadronic interaction and using the expected target density at COSY of $5 \cdot 10^{13}\,\mathrm{atoms/cm^2}$, is presented in in Fig. 2.10. The time dependence of the beam intensity based on Eq. (2.40) can now be described by

$$I(t) = I_0 \cdot \exp\left(-\frac{t}{\tau}\right) \cdot \cosh\left(\frac{t}{\tau_\mathrm{P}}\right) \quad \text{with} \quad \tau_\mathrm{P} = \frac{1}{\sigma_\mathrm{P} \cdot d_\mathrm{t} \cdot f}, \tag{2.45}$$

where σ_P is the polarizing cross section (Eq. (2.42)). Since σ_P is known to be very small τ_P becomes almost infinite compared to τ. Thus $\cosh(t/\tau_\mathrm{P})$ in Eq. (2.45) is usually assumed to be one. The deviation due to this approximation is negligible, as discussed in App. A.

The figure of merit provides a measure of the quality of the polarized beam and is given by

$$\mathrm{FOM}(t) = P^2(t) \cdot I(t). \tag{2.46}$$

Its origin is in detail discussed in [99].
Taking into account the trade-off between decreasing beam intensity and increasing beam polarization, maximizing the figure of merit gives the optimum build-up time t_opt. For the present situation $t_\mathrm{opt} = 2\tau$ constitutes a very good approximation [100] as it can be seen in Fig. 2.11. Taking into account a complete experiment consisting of a filtering and a measurement time this number might change. How this develops for a given experiment period is discussed in App. B.

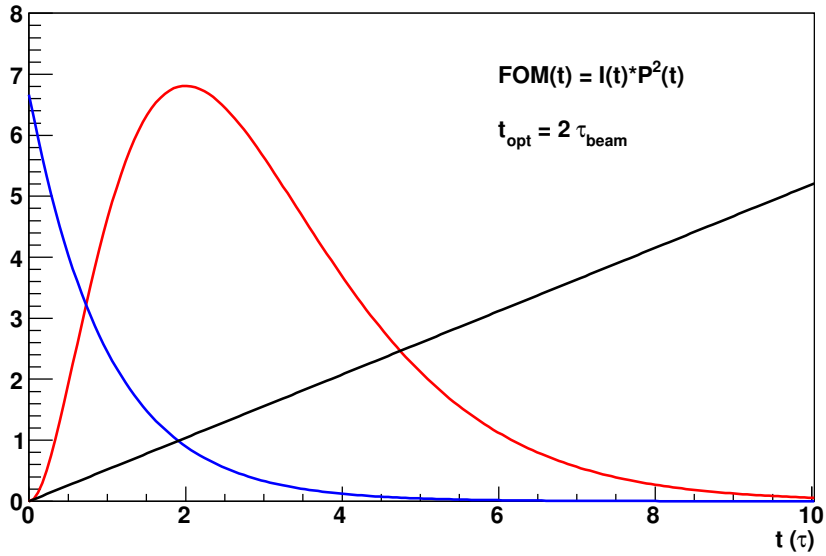

Fig. 2.11.: The figure of merit (red) as defined in Eq. (2.46) as a function of the filtering time t. The blue curve represents the beam intensity, whereas the black one shows the beam polarization. The graphs are scaled to the y-axis, which is given in arbitrary units. The optimal interaction time, where the $\mathrm{FOM}(t)$ reaches the maximum, is $t_{\mathrm{opt}} = 2\tau$. Consequently, one has to filter for two beam lifetimes to provide the maximum usefulness of the beam in later experiments.

3. Experimental Setup for the Spin-Filtering Experiments at COSY

The spin-filtering experiments with protons as a first step toward polarized antiprotons are carried out at the Cooler Synchrotron COSY of the Forschungszentrum Jülich (FZJ). A recent experiment at COSY [87] revealed that $e\vec{p}$ spin-flip cross sections are too small to cause a detectable depolarization of a stored polarized proton beam. This measurement rules out a proposal to use polarized positrons to polarize an antiproton beam by spin-flip interactions [91]. Thus, the method to provide a beam of polarized protons (antiprotons), adopted by the PAX collaboration, is spin filtering using a **P**olarized **I**nternal storage cell **T**arget (PIT). The target density strongly depends on the dimensions of the storage cell. In order to minimize the cell dimensions and thereby maximize the target density, the beam has to be squeezed by additional quadrupole magnets placed around the target. The target will be operated in a weak magnetic guide field of about $1\,\mathrm{mT}$. The orientation of the target polarization can be maintained by weak transverse (x or y) and longitudinal (z) magnetic fields produced by a set of coils.
The accelerator facility COSY is described in Sec. 3.1. In Sec. 3.2, the PAX installation is explained, consisting of a low-β insertion, an atomic beam source (ABS), an openable storage cell and a so-called Breit-Rabi Polarimeter (BRP). The beam polarimeter, which will be used to measure the polarization of the proton beam at the ANKE target position, is described in Sec. 3.3.

3.1. COSY

The synchrotron and storage ring COSY [101, 102] at the Forschungszentrum Jülich is operated by the Institut für Kernphysik (IKP). This accelerator complex, depicted in Fig. 3.1, consists of negative ion sources for unpolarized and polarized H^-/D^- ions[1], the injector cyclotron JULIC that accelerates the H^- ions up to $300\,\mathrm{MeV/c}$ and D^- ions up to $600\,\mathrm{MeV/c}$, and the synchrotron ring with a circumference of $183.4\,\mathrm{m}$. The pre-accelerated ions are stripped off their electrons and the remaining protons or deuterons are injected into COSY (stripping injection) [69], where an acceleration of the particles up to $3.65\,\mathrm{GeV/c}$ can be achieved. The synchrotron contains two cooling systems to shrink the transverse equilibrium phase space and momentum spread. A $100\,\mathrm{keV}$ electron cooler enables beam cooling up to a proton beam momentum of $600\,\mathrm{MeV/c}$ and the stochastic cooling system covers the momentum range above $1.5\,\mathrm{GeV/c}$ [74]. Cooled unpolarized proton beams, required for spin-filtering experiments, have been achieved with intensities up to $2 \cdot 10^{10}$ circulating protons in the ring with single injection and up to $5 \cdot 10^{10}$ protons with stacking injection [103].

[1] Polarized and unpolarized negative ion beams are produced by charge exchange ($\vec{H}^0(\vec{D}^0) + Cs^0 \rightarrow \vec{H}^-(\vec{D}^-) + Cs^+$).

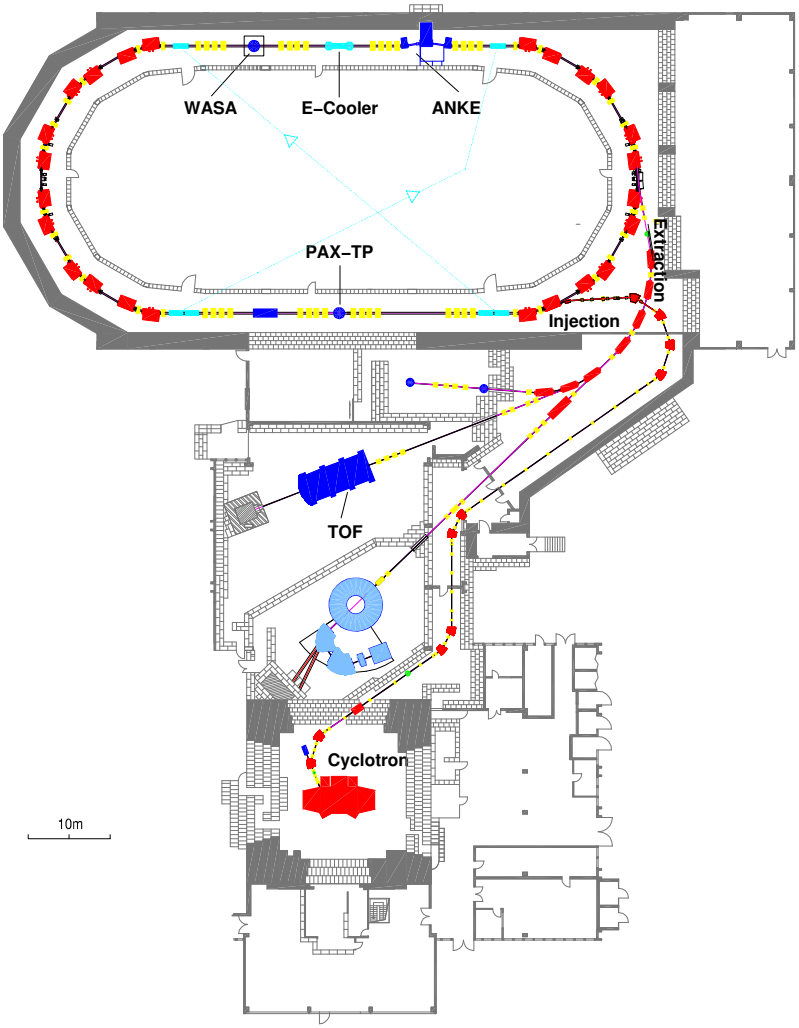

Fig. 3.1.: Floor plan of the COSY facility. The beam is pre-accelerated in the cyclotron JULIC before injection into COSY. Indicated in the straight sections are the internal experiments WASA, ANKE and PAX, as well as the electron cooler. For the external TOF experiment, the beam can be extracted after acceleration to the required energy.

The two $40\,\mathrm{m}$ long straight sections are designated to serve the internal experiments such as WASA (**W**ide **A**ngular **S**hower **A**pparatus) [104], ANKE (**A**pparatus for studies of **N**ucleon and **K**aon **E**jectiles) [105], and the newly implemented PAX target section. For external experiments like TOF (**T**ime **O**f **F**light spectrometer) the beam can be extracted.

3.1.1. COSY Lattice

COSY has a racetrack design with two $180°$ arc sections connected by the straight sections, which can be tuned as telescopes with a $1:1$ imaging with 2π phase advance. Each of the arcs is composed of three mirror symmetrical unit cells consisting of four dipole magnets (O), two horizontally focussing quadrupole magnets (F) and two horizontally defocussing quadrupole magnets (D). Each of the six unit cells has a DOFO-OFOD structure. At COSY the two inner quadrupole magnets of a unit cell (F) are interconnected to the inner pair of the opposite unit cell located in the other arc. Such a group is called a quadrupole family. Since the same is true for the outer quadrupole magnets (D) of each cell, six quadrupole families

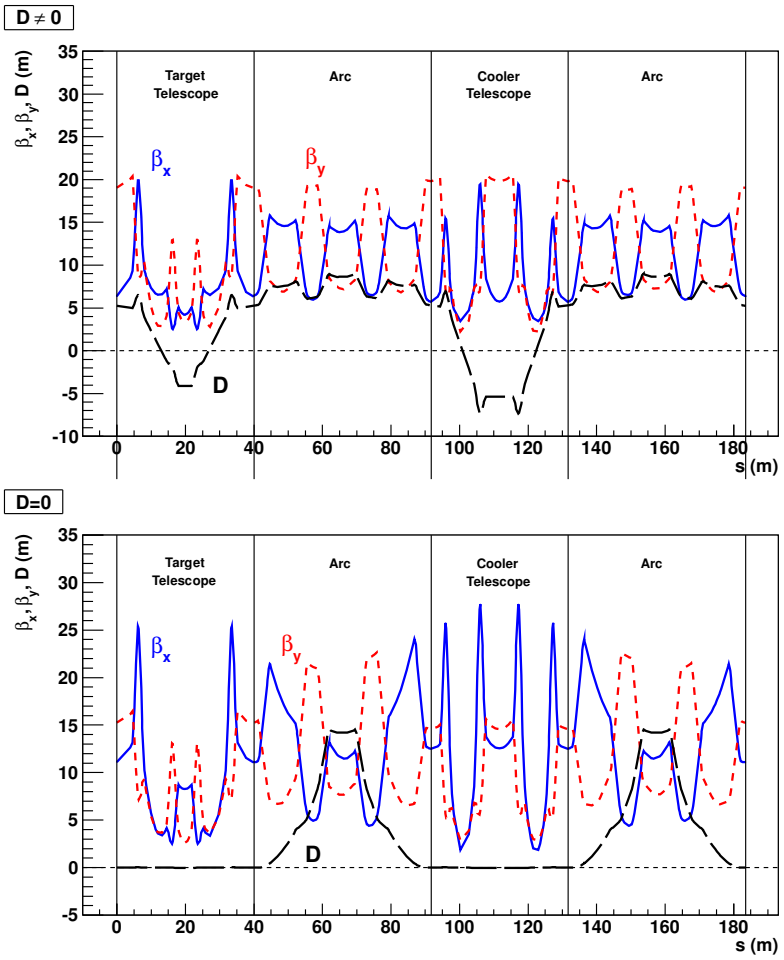

Fig. 3.2.: Top: Optical functions (β_x, β_y) and dispersion D along COSY for a standard setting ($D \neq 0$). In each of the arcs a symmetric behavior due to the 3 similar unit cells is noticeable. **Bottom:** Betatron functions and dispersion for a $D = 0$ setting in the telescopes. The sixfold symmetry breaks and the resulting optical functions show a twofold symmetry.

are formed (QU1-6). A symmetric operation of all unit cells leads to a sixfold symmetry of the betatron functions [106]. Figure 3.2 (top panel) shows the optical functions β_x, β_y and D for a typical setting of COSY which is used for injection.
In the straights, where the target and the electron cooler are located, the dispersion can be made zero by breaking the sixfold symmetry with a specific setting of the six quadrupole families (bottom panel in Fig. 3.2). This so-called $D = 0$ setting is advantageous for the operation of the storage cell and will be used for the spin-filter experiment.

3.1.2. COSY Vacuum System

The expected polarization build-up in spin-filtering experiments at COSY is known to be small and calculations show that it takes $20000\,\mathrm{s}$ at $49.3\,\mathrm{MeV}$ to reach about $1\,\%$ beam polarization (see Sec. 5.1). The long filtering time and the fact that a significant part of the beam is removed on purpose due to interaction with the target atoms lead to the necessity of an ultra-high vacuum in the COSY ring in order to minimize additional losses and to achieve reasonable beam intensities after filtering.
The COSY vacuum system is specified to operate at an average pressure of 10^{-10} mbar [107]. The accelerator ring is divided into eight vacuum sections by gate valves, in a manner

such that each straight section and each bending section is subdivided into two subsections and each subsection forms an independent vacuum system, including different pumps, gas analyzers and pressure gauges. The system is completely remote controlled and provides vacuum safety interlock.
Of special interest is the region around the PAX target point, where the gas load from the atomic beam source would lead to significant beam losses without a dedicated pumping system. This system is in detail described in Sec. 3.2.1.

3.1.3. Electron Cooler

The COSY electron cooler, Fig. 3.4, has been designed for electron energies up to $100\,\mathrm{keV}$, thus enabling phase space cooling up to $183.6\,\mathrm{MeV}$ proton energy. Its design parameters are shown in Table 3.3 [69]. The electron beam is extracted from a thermionic cathode and electrostatically accelerated up to the velocity of the ion beam. The electron beam is guided by the longitudinal magnetic field of toroids and solenoids through the interaction region with the ion beam and, after energy-recovering by electrostatic deceleration, dumped in the collector. Two compensation solenoids with reversed longitudinal field up- and downstream of the cooler device prevent coupling between horizontal and vertical phase space plane as well as distortion of the ion spin direction in the COSY ring. Steerer magnets compensate the orbit distortion caused by the toroids and are serving to match the ion beam in position and angle with the electron beam.
As basic application it was intended to reduce the large emittances and the large momentum spread caused by the stripping injection process before the ion beam is accelerated to a requested experiment energy [101]. The main task of electron cooling for the spin-filtering experiments is to balance emittance growth and energy loss, see Sec 2.1.2. Typical equilibrium emittances at $1\,\mathrm{mA}$ proton beam (corresponding to about 10^{10} circulating protons) are in the range of 0.2 to $0.5\,\mu\mathrm{m}$. Higher beam currents up to $4\,\mathrm{mA}$ could be obtained by a so-called cooling-stacking technique where the principle of the stripping injection allows repeated injections without destroying the already cooled beam [74]. However, at the relatively low proton beam energies of 45 to $49\,\mathrm{MeV}$ such intense and dense ion beams tend to develop coherent betatron oscillations with subsequent beam loss [108, 109]. Therefore, the transverse feedback system of COSY [108, 109] has to be activated to obtain the requested long lifetimes. Once the optimum setting is found, the electron beam can be tilted by steering coils on the drift solenoid to some extent resulting in a slightly reduced cooling force. In such a way it was possible to control the emittance and thereby the lifetime (see Sec 4.4).

Parameter	Design value
Drift solenoid length	2.00 m
Eff. cooling length	1.50 m
Beam tube diameter	0.15 m
Electron beam diameter	0.025 m
Magnetic field	80 ... 165 mT
Electron energy	< 100 keV
Vacuum	$5{\cdot}10^{-9}$ mbar

Fig. 3.3.: Design parameters of the COSY electron cooler [69].

3.1.4. Instrumentation

For the determination of beam and machine related parameters, which have to be carefully studied prior to the actual experiments, a number of diagnostic tools are available at COSY.
While the measurement of the machine acceptance for different optics is important for the understanding of the beam lifetime, the determination of the acceptance angle at the target is a prerequisite to eventually determine experimentally the spin-dependent cross

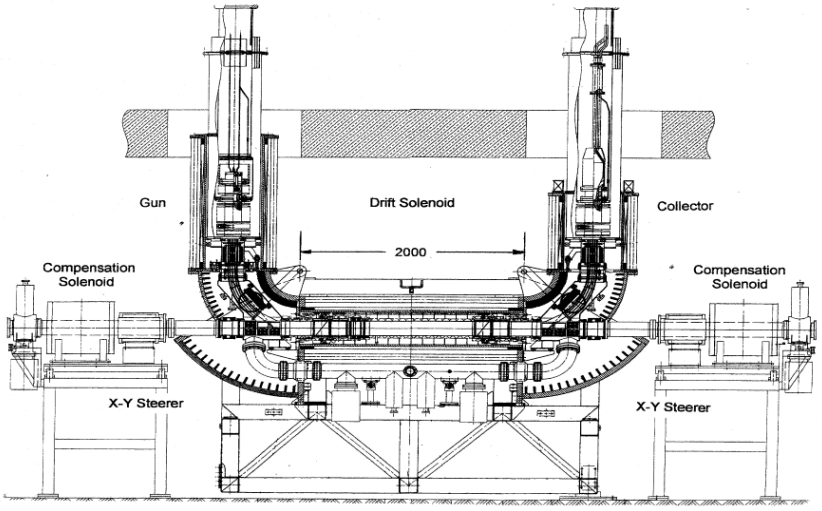

Fig. 3.4.: The COSY electron cooler [108].

section of the proton-proton interaction from the observed polarization build-up after spin filtering (Eq. (2.42)). The machine acceptance can be measured using a fast kicker magnet, or the movable frame system installed in the PAX target chamber [110]. The beam current transformer, the H^0 monitor, the ionization profile monitor and the beam position monitors allow one to measure and further optimize the beam lifetime.

Diagnostic Kicker Magnet: The diagnostic kicker magnet and the stripline unit are used to excite transverse collective oscillations of the beam particles and thereby enable the determination of the machine acceptance and the non-integer part of the betatron tune (Q_x, Q_y) [111]. A short time deflection with the kicker enables a fast measurement of the machine acceptance in horizontal direction. The beam is kicked under a certain angle depending on the applied magnetic field. The beam current is measured as a function of the kick angle. The angle at which the beam gets lost completely, together with the local betatron function yields the machine acceptance (see Sec. 4.5.1).
The stripline unit can be used to enhance horizontal and vertical beam oscillations by RF-excitation. A determination of the exciting frequency, which induces resonant beam oscillations, makes it possible to determine the fractional part of the working point (Q) in both planes (x,y) (see Sec. 4.2).

Movable Frame System: At the target position, where a precise knowledge of the acceptance angle is required, a frame system, shown in Fig. 3.5, has been installed. It consists of three frames ($25\,\mathrm{mm}\times 20\,\mathrm{mm}$) and a tube of $9.6\,\mathrm{mm}$ inner diameter. Allowing the beam to pass each device individually by moving the whole system perpendicular to the beam enables a determination of the acceptance angle at three different positions along the target, i.e., upstream end, center and downstream end of the $400\,\mathrm{mm}$ long storage cell.

Beam Current Transformer: A beam current transformer (BCT) primarily measures the electric current of the circulating ion beam. The BCT electronics is based on the DCCT principle (DC current transformer) [112] and delivers $100\,\mathrm{mV}$ output signal for $1\,\mathrm{mA}$ of beam current I, or alternatively, when a higher sensitivity is required, $100\,\mathrm{mV}$ per $0.1\,\mathrm{mA}$ of beam current. Continuously recorded, the BCT signal forms the basis for the beam lifetime measurements. Combined with the revolution frequency f, the number of ions, e.g., protons in the ring is calculated by

$$N_p = \frac{I}{e \cdot f}. \tag{3.1}$$

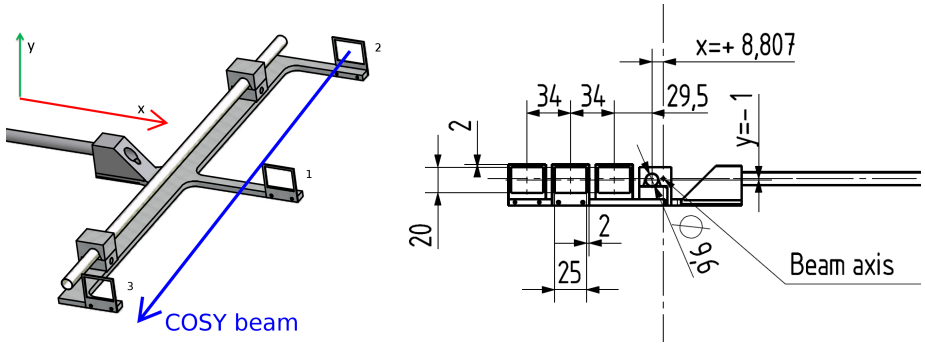

Fig. 3.5.: The movable frame system installed in the PAX target chamber allows for a determination of the acceptance angle and the beam size. **Left:** Drawing of the system consisting of three frames (25 mm×20 mm) and a tube of 9.6 mm inner diameter. The system is movable in horizontal (red arrow) and vertical direction (green) perpendicular to the beam (blue) allowing the beam to pass each device individually. **Right:** Dimensions looking in beam direction.

H^0 Monitor: The performance of the electron cooler can be monitored using the recombination of a small fraction of the protons and the electrons to neutral H^0 atoms. Since those H^0 atoms are not deflected by dipoles, they will immediately get lost at the end of a straight section. For beam diagnostics based on recombination, a so-called H^0 monitor is placed at the end of the cooler straight section in order to optimize electron cooling of protons. This consists of a multiwire proportional chamber, which measures the H^0 profile and scintillators for the determination of the intensity.

Ionization Profile Monitor: An ionization profile monitor (IPM) developed at GSI[1] and operated at COSY, provides a fast and reliable non-destructive beam profile and position measurement [113]. The interaction of the stored beam with the residual gas produces residual gas ions which are guided to a position sensitive detector by transverse electric fields. The ion detection is based on an arrangement consisting of Micro Channel Plates (MCP), where secondary electrons are produced, a phosphor screen to produce light, and a CCD camera for detection. This system enables a high resolution of 0.1 mm [114].
The IPM (Fig. 3.6) was utilized to determine the beam emittance.

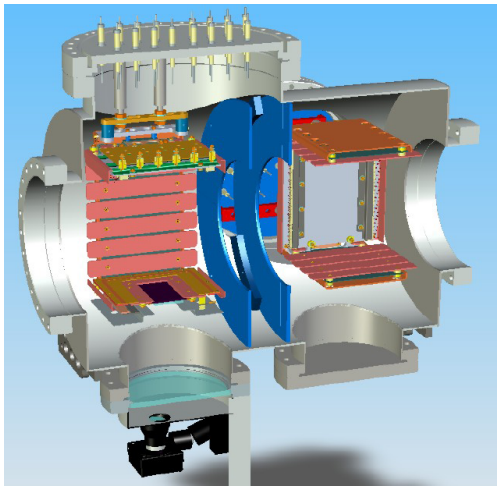

Fig. 3.6: Mechanical design of the ionization profile monitor prototype. It consists of two identical units to enable simultaneous measurements of the horizontal and vertical beam profile. The electric field for ion extraction is provided by high voltage electrodes. For ion detection, a P47 phosphor screen (dark-blue) and a 656 × 494 pixel CCD camera, mounted on the bottom flange, are used. To avoid mutual disturbances a shielding is located between the two IPMs (blue) [113].

[1]Gesellschaft für Schwerionenforschung mbH

Beam Position Monitor: A beam position monitors (BPM) consists of two electrodes placed face to face in x- and in y-direction. A passing bunch of charged particles induces a voltage change in dependence on its distance to the electrode. The difference of the signals at two electrodes $\Delta = U_1 - U_2$ can be used to determine the beam position and transverse components of the beam spectrum. This allows for the determination of the working point in both planes (Q_x, Q_y). The sum signal $\sum = U_1 + U_2$ is a measure of the beam current and it comprises the longitudinal components of the beam spectrum. It is utilized to determine the relative momentum spread of the particles and the shift of the revolution frequency, which is a measure of the beam energy loss. Since this loss is caused by the interaction of the beam with the residual gas and the target, the frequency shift can be used to determine the target density [70].

3.2. PAX Installation

The PAX interaction point (PAX-IP), the place where spin filtering will take place, is located in the straight section opposite to the electron cooler and the ANKE spectrometer (see Fig. 3.1). The experimental setup (fig. 3.7) consists of different components, which are required to enable a measurable polarization build-up of an originally unpolarized proton beam by interaction with a polarized internal target. An atomic beam source (ABS) produces nuclear spin-polarized hydrogen or deuterium atoms. In order to reach target areal densities of up to $5 \cdot 10^{13}\,\mathrm{atoms/cm^2}$ these atoms are injected into a thin-walled storage cell of $10\,\mathrm{mm}$ diameter, which is located below the ABS inside the PAX target chamber. The storage cell is openable which enables beam injection and cooling in open position without beam losses. The cell is closed only after the beam is well prepared for spin filtering. A magnetic guide field system allows to stabilize and to switch the orientation of the target polarization. The polarization of an effusive beam extracted from the cell will be determined by a so-called Breit-Rabi Polarimeter (BRP) and a Target Gas Analyzer (TGA), which are mounted towards the outside of the ring. The gas load into the target chamber and the neighboring sections

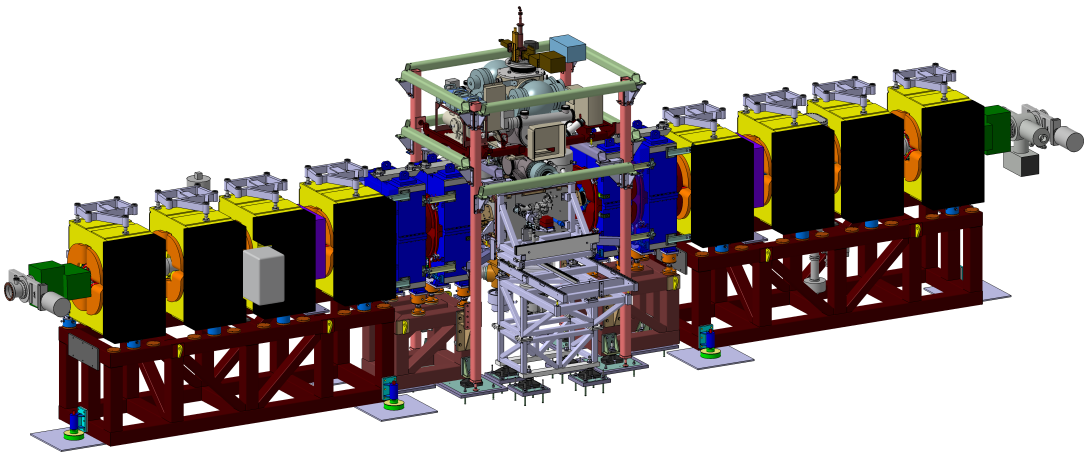

Fig. 3.7.: PAX installation at the Cooler Synchrotron [60]. Shown in yellow are the existing COSY quadrupole magnets and the blue ones are former CELSIUS quadrupole magnets. The atomic beam source is mounted above the target chamber that houses the openable storage cell. Three sets of coils providing magnetic holding fields along x, y, and s are mounted on the edges of the target chamber. The Breit-Rabi target polarimeter and the Target Gas Analyzer are mounted towards the outside of the ring. Fast shutters are used on the target chamber on all four main ports. The beam direction is from left to right.

causes beam losses due to the interaction of beam particles with the residual gas. Thus, a dedicated pumping system is required to minimize these losses. In order to guide the beam through the storage cell without beam losses, a low-β insertion consisting of four additional quadrupole magnets and steerer magnets has been implemented into COSY. In a later stage of the experiment a detector system based on silicon microstrip detectors will be installed into the target chamber.

3.2.1. PAX Vacuum System

A crucial point for beam losses is the region around the PAX target where the atomic beam source with an injected intensity of up to $6.6 \cdot 10^{16}$ H^0/s [115] leads to a significant gas load. Especially in the region up- and downstream of the storage cell, a pressure increase would cause tremendous beam losses due to Coulomb scattering (Sec. 2.1.2) because of the large betatron functions (see Sec. 3.2.2) and consequently small acceptance angles at these positions. In order to minimize losses due to residual gas in the target region and due to the gas flow into adjacent sections, a complex pumping system has recently been installed. It consists of

- flow limiters with an inner diameter of $19\,\mathrm{mm}$ and a length of $80\,\mathrm{mm}$, which are installed at the entrance and exit of the target chamber in order to minimize the target gas flow into the adjacent sections,
- 1 HiPace 1800 turbo pump with a nominal pumping speed of $1200\,\mathrm{l/s}$ for H_2 installed below the target chamber,
- 10 SAES getter pumps GP 500 MK5 (NEG[1] cartridges) providing a nominal pumping speed of $10 \cdot 1900\,\mathrm{l/s}$ for H_2 (see Fig. 3.8),

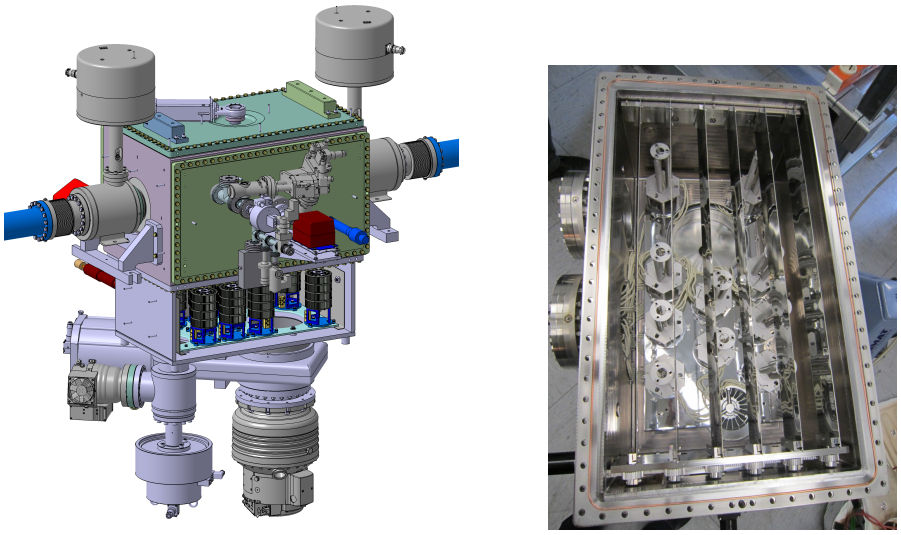

Fig. 3.8.: Left: 3D view of the PAX target chamber with opened NEG box. The target chamber is equipped with two fast shutters (left and right of the chamber), 10 NEG cartridges installed below the chamber and an additional turbo molecular pump, which enables pumping especially before and during NEG activation. **Right:** Photograph of the NEG box. The NEG cartridges (missing in this picture) are mounted on heatable supports, which are needed for the activation process. A jalousie with mirror plates, minimizes heat radiation into the target chamber.

[1]NEG - Non-evaporable getter alloys, after dissolution of their native oxide layer into the bulk, are able to pump most of the gases present in ultra-high vacuum systems.

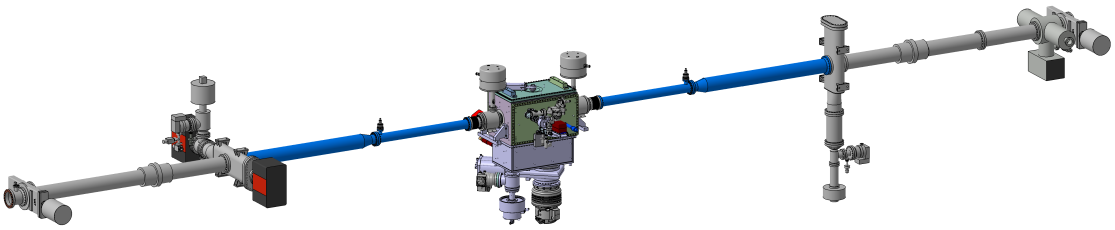

Fig. 3.9.: The complete PAX at COSY vacuum system. The NEG coated beam pipes, shown in blue, are connected to the target chamber. In addition the COSY section valve and ion getter pumps (red) are displayed.

- NEG coating on the beam pipes up- and downstream of the target region with a nominal pumping speed of $2 \cdot 5000\,\mathrm{l/s}$.

The NEG coating and the NEG cartridges have to be activated after saturation by heating them up to $230\,^{\circ}\mathrm{C}$ and $450\,^{\circ}\mathrm{C}$, respectively. Thus the entire low-β section is made bakeable. A jalousie with mirror plates is mounted above the SAES pumps in order to minimize the heat radiation into the target chamber during activation. This is closed during heating and opened for pumping. Assuming a gas flow of about $3.3 \cdot 10^{16}\,\mathrm{H^0/s}$ (one hyperfine state) an activation once per week is required. Additionally, fast shutters have been installed, which will be used to seal the section off from the rest of the ring during bake-out or in case of an emergency such as a sudden increase in pressure. The complete PAX at COSY vacuum section is depicted in Fig. 3.9. Dimensioning of this system was one task on the agenda of the commissioning for spin filtering at COSY.

3.2.2. PAX low-β Section

The operation of the polarized target (Sec. 3.2) requires transportation of the stored beam through the narrow storage cell, which is needed to provide a target areal density of up to $5 \cdot 10^{13}\,\mathrm{atoms/cm^2}$. Taking a storage cell radius of $5\,\mathrm{mm}$ and a minimum possible betatron function at the target position of about $3 - 5\,\mathrm{m}$ for the standard COSY optics, the acceptance would be $A = (5\,\mathrm{mm})^2/3\,\mathrm{m} \approx 8\,\mu\mathrm{m}$ and therewith smaller than the overall COSY acceptance of about $35\,\mu\mathrm{m}$ [111]. This corresponds to a beam emittance of $\epsilon = 0.9\,\mu\mathrm{m}$*, which is smaller than the assumed $10\,\mu\mathrm{m}$ at injection and the $3\,\mu\mathrm{m}$ for a cooled beam. It implies that a significant amount of beam particles would get lost with the regular betatron functions at the target location.
In order to avoid an acceptance limitation due to the cell, a special insertion has been installed, which squeezes the betatron amplitude at the target position to about $0.3\,\mathrm{mm}$. This low-β insertion comprises four additional quadrupole magnets (blue ones in Fig. 3.7), which can be switched on adiabatically, four steerer magnets mounted directly inside the adjacent COSY quadrupole magnets, and two beam position monitors (BPM). The PAX quadrupole magnets are powered pairwise. In the following the outer ones are called PAX1 and the inner pair PAX2 as depicted in Fig. 3.10.
Since a small betatron function enlarges the acceptance angle (Eq. (2.11)), it decreases the spin-independent losses due to single Coulomb scattering and therewith improves the beam lifetime with target as discussed in Sec. 2.1.2. Given that $\tau_{\mathrm{beam}} = (\Delta\sigma_{\mathrm{C}} \cdot d_{\mathrm{t}} \cdot f)^{-1}$ and $\sigma_{\mathrm{C}} \propto \beta$

*Assuming a Gaussian beam intensity distribution, a 3σ beam width was chosen.

the beam lifetime is inversely proportional to the betatron amplitude function at the target. For this reason, a low-β section is mandatory for any spin-filtering experiment either at COSY or at CERN/AD [60, 116]. The calculated optical functions in the COSY low-β insertion at injection energy are shown in Fig. 3.10.

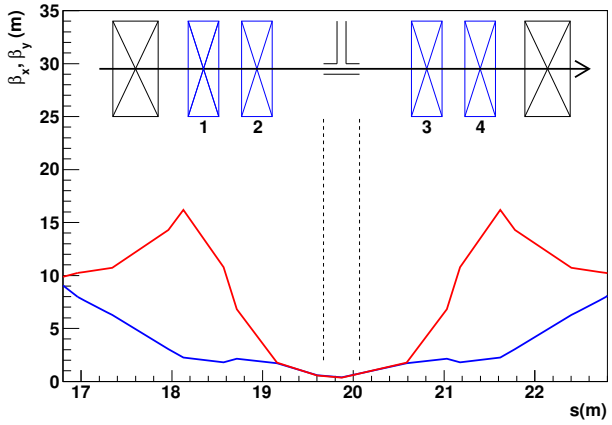

Fig. 3.10: Twiss betatron functions in the low-β insertion for the PAX installation at COSY at injection energy. The blue curve denotes β_x, the red one β_y. The quadrupole magnets numbered from 1 to 4 are the new PAX quadrupoles. They are powered pairwise. In the following, the outer pair $(1+4)$ is called PAX1 and the inner pair $(2+3)$ PAX2.

3.2.3. Atomic Beam Source (ABS)

The ABS, formerly used in the HERMES experiment [117, 118], has been modified for the spin-filtering studies of the PAX experiment. A schematic drawing and a three-dimensional drawing of the PIT is displayed in Fig. 3.11. For differential pumping it mainly consists of four chambers equipped with turbomolecular pumps in order to limit the attenuation of the polarized atomic beam by residual gas and the deflected hyperfine states. The total pumping speed amounts to approximately $10^4\,\mathrm{l/s}$, providing a pressure of $10^{-6}\,\mathrm{mbar}$ in the last chamber close to the target chamber [119].
The dissociator generates atomic hydrogen or deuterium by dissociating molecules in a gas discharge, which is sustained in a microwave induced low ionized plasma. This plasma is contained inside a glass tube at a pressure of 0.5 to $1\,\mathrm{mbar}$ of hydrogen. The dissociation of molecules is caused by the impact with free electrons, which gain energy from an applied electromagnetic field. The working principle is in detail described in [120]. A small fraction of oxygen ($0.1\,\mathrm{vol}\%$) is admitted to the discharge, in order to increase the degree of dissociation. The atomic beam is produced when the dissociated hydrogen/deuterium gas expands through a cooled nozzle into the vacuum of the dissociator chamber. A skimmer and a collimator are used to form a high-brilliance beam with a divergence that matches the acceptance angle of the first sextupole magnet. The admixed oxygen reduces also the recombination in the discharge tube due to the creation of H_2O and HO which forms a water layer on the surface of the glass tube. The recombination coefficient can be reduced by a factor of two compared to the bare glass surface. On the other hand the nozzle, which is cooled to 100 K, gets clogged by ice. Therefore a nozzle regeneration (~ 4 hours), where the ice is evaporated, is required after 3 to 5 days of continuous running.
In order to inject fully nuclear polarized atoms into the cell the ABS has to perform a selection of the different hyperfine states. For hydrogen, the nucleus having a spin $\frac{1}{2}$, the quantum numbers for the total angular momenta are $F = 1, 0$, also corresponding to two energy levels in the ground state ($1S_{1/2}$). This splitting is known as hyperfine structure. The level $F = 1$ is a triplet with $m_F = +1, 0, -1$, and the level $F = 0$ is a singlet with $m_F = 0$ [121]. Without external magnetic field or in a weak magnetic field with $B \ll B_c$, the basis $\{|F, m_F\rangle\}$ is used to describe the four hyperfine states:

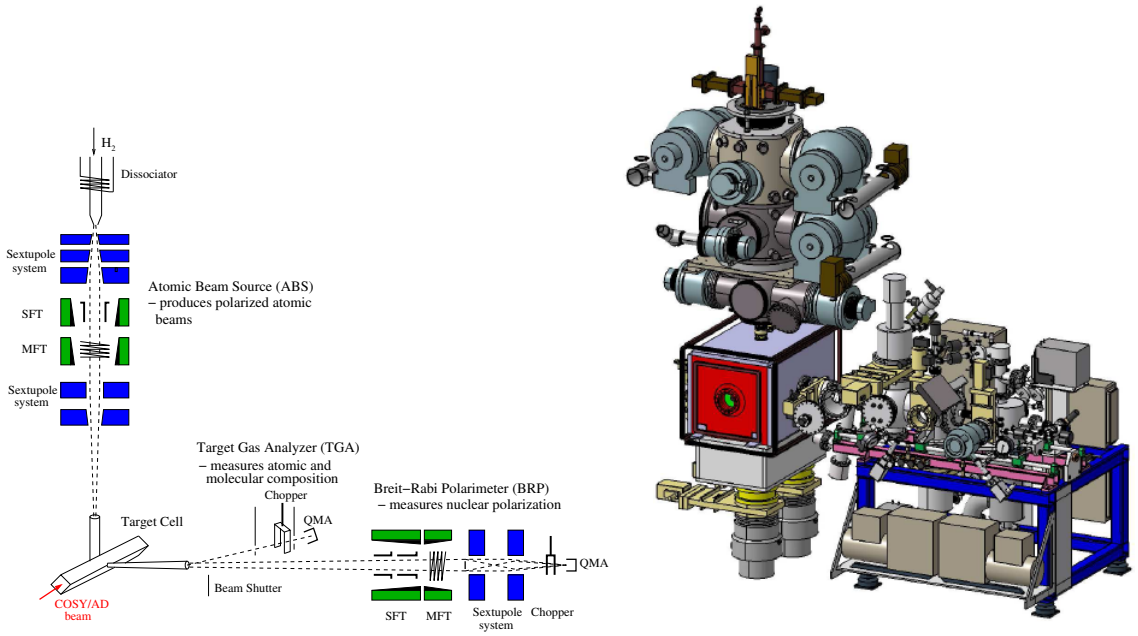

Fig. 3.11.: Left: Schematic drawing of the Polarized Internal Target with the ABS (Sec. 3.2.3) feeding the storage cell (Sec. 3.2.4), the BRP (Sec. 3.2.6), and the Target Gas Analyzer. **Right:** Three dimensional drawing of the ABS and the BRP.

$$
\begin{aligned}
|i\rangle &= |F, m_F\rangle \rightarrow |m_S, m_I\rangle \\
|1\rangle &= |1, +1\rangle = \left| +\frac{1}{2}, +\frac{1}{2} \right\rangle \\
|2\rangle &= |1, 0\rangle = \frac{1}{\sqrt{2}} \cdot \left(\left| +\frac{1}{2}, -\frac{1}{2} \right\rangle + \left| -\frac{1}{2}, +\frac{1}{2} \right\rangle \right) \\
|3\rangle &= |1, -1\rangle = \left| -\frac{1}{2}, -\frac{1}{2} \right\rangle \\
|4\rangle &= |0, 0\rangle = \frac{1}{\sqrt{2}} \cdot \left(\left| +\frac{1}{2}, -\frac{1}{2} \right\rangle - \left| -\frac{1}{2}, +\frac{1}{2} \right\rangle \right).
\end{aligned}
\tag{3.2}
$$

The states $|2\rangle$ and $|4\rangle$ are a mixing of the eigenstates with the quantum numbers m_S and m_I with $-s \leq m_S \leq +s$ and $-I \leq m_I \leq +I$.
The proton (electron) polarization P_z (P_e) is defined by the probability to measure the spin parallel or antiparallel to the magnetic holding field. The expectation value for the nuclear (electron) polarization depends on the individual hyperfine state population of the hydrogen or deuterium atoms. It is defined by [122]

$$P_z = \sum_{i=1}^{4} \langle i | \frac{2}{\hbar} I_z | i \rangle = n_1 - n_3 - (n_2 - n_4) \cos 2\theta \tag{3.3}$$

$$P_e = \sum_{i=1}^{4} \langle i | \frac{2}{\hbar} S_z | i \rangle = n_1 - n_3 + (n_2 - n_4) \cos 2\theta, \tag{3.4}$$

with the mixing angle $\theta = \frac{1}{2} \arctan(B_c^H / B)$ and relative occupation numbers n_i, which are normalized to

$$\sum_{i=1} n_i = 1. \tag{3.5}$$

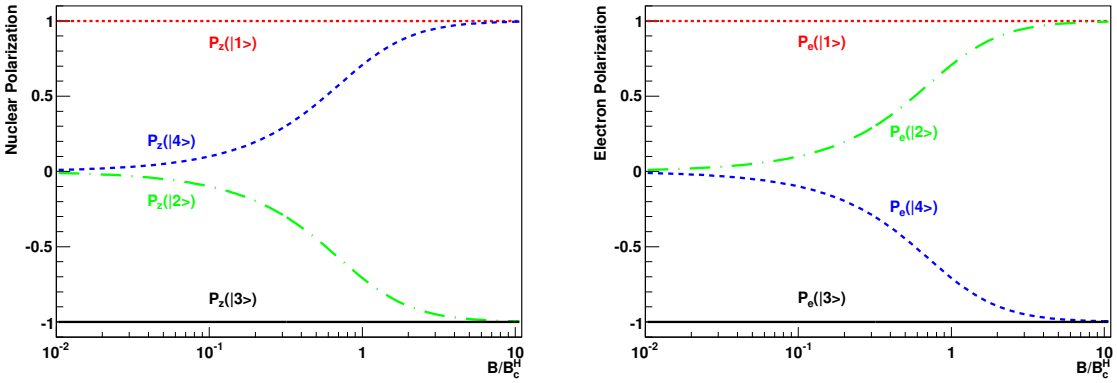

Fig. 3.12.: Nuclear (left) and electron (right) polarization of the hyperfine states of hydrogen versus the external magnetic field normalized to the critical field $B_c^H = 50.7\,\mathrm{mT}$.

Using the mixing coefficients as described in [123], the polarization of the hydrogen hyperfine states can be calculated as a function of B/B_c^H (Fig. 3.12), with $B_c^H \simeq 50.7\,\mathrm{mT}$ the critical field of hydrogen. In a weak magnetic field ($B \ll B_c^H$) as used for the PAX spin-filtering experiment, due to strong spin coupling, the mixed states $|2\rangle$ and $|4\rangle$ do not contribute to the polarization. Therefore the polarized gas target will consist of state $|1\rangle$ only. In this mode of operation, the target polarization can be reoriented using the system of coils around the target chamber, to align the polarization along x, y, and s in short succession. The average dwell time of the atoms in the cell is about a couple of ms.

To perform the selection of the hyperfine states in such a way that only state $|1\rangle$ is injected, the ABS consists of a set of sextupole magnets, followed by two adiabatic rf-transition units and two more sextupole magnets (Fig. 3.11). The first set of sextupole magnets removes states $|3\rangle$ and $|4\rangle$ by deflection, followed by an MFT (medium field transition unit), which in normal operation exchanges the population numbers N_2 and N_3 ($2-3$ transition). As shown in Fig. 3.13, the population of state $|2\rangle$ is almost zero and after removal of state $|3\rangle$ by the second set of sextupole magnets, only hyperfine state $|1\rangle$ is transmitted. This state is finally injected into the storage cell. Different injection modes are used in the calibration procedure of the BRP. The injected states and therewith the polarization are affected by the efficiency of the $2-3$ transition and the transmission efficiency of the sextupole magnets.

The polarized atomic gas is injected into the storage cell, which is traversed by the initially unpolarized particle beam of the accelerator[1]. Since the density and the total polarization of the target affect the polarization build-up, as discussed in Sec. 2.3, an optimal operation of the ABS has to be ensured. In case of hydrogen (hyperfine states $|1\rangle$ and $|2\rangle$ injected) fluxes of $\Phi^{\mathrm{ABS}} \approx 6.6 \cdot 10^{16}\,\mathrm{atoms/s}$ have been observed [115].

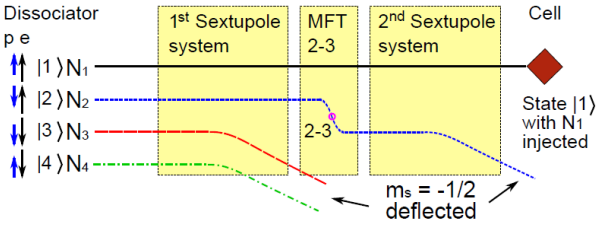

Fig. 3.13: Schematic view of the ABS hyperfine state selection for hydrogen. The sequence of sextupole magnets and rf-transition units separates the hyperfine populations and selects in the ideal case only state $|1\rangle$ for injection into the storage cell.

[1] At COSY protons will interact with the target, whereas at AD spin-filtering studies will be carried out using a beam of stored antiprotons.

3.2.4. Target Chamber and Openable Storage Cell

The target chamber for spin-filtering experiments at COSY was installed at the PAX interaction point (PAX-IP) in 2010 (see Fig. 3.7). It houses the openable storage cell, which is needed to provide target densities of up to $5 \cdot 10^{13}\,\mathrm{atoms/cm^2}$. According to calculations this is not relevant at COSY, but at the AD this function is mandatory. The storage cell target, located inside the target chamber, constitutes the PAX-interaction region. Given that the target chamber is connected to the ABS and the BRP and considering the issue that it will later also contain the silicon detectors, it constitutes the core of the experiment. In addition the target chamber also supports the coil system for the magnetic holding field (see Figures. 3.14 and 3.15). The purpose of the storage cell is to increase the dwell time of the target gas atoms within the area of the beam, and thus to increase the target areal density. An increase of two orders of magnitude is obtained compared to that of a jet target. Since a high areal density is required for spin-filtering experiments the dimensions of the cell have to be optimized. The areal density for a given intensity is proportional to the lengths of the injection and storage tube and inversely proportional to the third power of the diameters. Consequently, the tubes have to be as long as possible and their diameter should be as small as possible, keeping in mind also that the dimensions of the feeding tube are limited by the divergence of the incoming beam.
Since it is planned to use the experimental setup also at the AD for antiproton spin-filtering experiments, where the beam size at the target position after injection is much larger than the $10\,\mathrm{mm}$ diameter of the storage cell, the usage of an openable storage cell (Fig. 3.16) is required. The apertures at the target cell must not restrict the machine acceptance, in particular when the beam is not yet cooled directly after injection. At the AD, a free aperture of $100\,\mathrm{mm}$ diameter is required. Consequently, the beam will be injected with the cell in open position into the AD at $T = 3.57\,\mathrm{GeV}$, ramped down to the energies of interest ($50 - 450\,\mathrm{MeV}$), and finally the machine optics is squeezed by fully powering on the low-β section. Only after this is accomplished ($\approx 100\,\mathrm{s}$) the storage cell will be closed. As a compromise between density and acceptance angle, the closed cell has a square cross section of $10 \times 10\,\mathrm{mm^2}$ and a length of $400\,\mathrm{mm}$ [124]. The cell walls are made of $5\,\mu\mathrm{m}$ Teflon foil which is known to reduce depolarization and recombination and allows in addition to detect low-energy recoil particles.
For the operation at COSY, no restriction of the acceptance due to the cell is expected. Here, the cell will be used for a discrete determination of beam losses due to the target and the target background (see Sec. 4.6.3), and has to be commissioned for operation at the AD. The

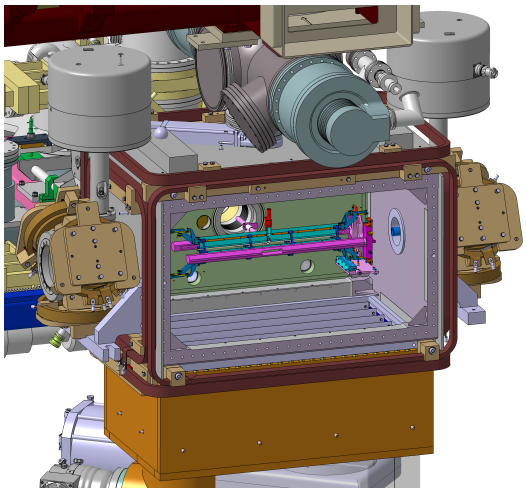

Fig. 3.14: Drawing of the open PAX target chamber, which houses the openable storage cell. The magnetic holding field coils and the compensation coils (brown) are mounted on the chamber and the connected beam tubes. The COSY beam enters the chamber from the left through flow limiter tubes of $19\,\mathrm{mm}$ diameter and $80\,\mathrm{mm}$ length. The NEG box is installed below the target chamber.

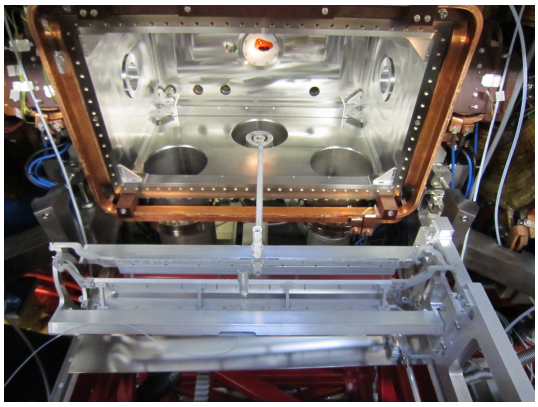

Fig. 3.15: Photograph of the open target chamber. Flow limiters have been installed at the entrance (left) and exit (right) of the chamber. The openable storage cell is shown in the foreground, affixed to a flange on which it slides into the chamber. The vertical tube on top of the storage cell is the feeding tube for the polarized atoms from the ABS. The long horizontal extension tube, connected to cell center, feeds the BRP on the backside of the target chamber.

target background can be determined by measuring the lifetime and target density with open cell. Finally the background can be subtracted from the values with closed cell, leading to the pure target effect.
As soon as the beam is cooled the cell is closed, H^0 atoms in a single hyperfine-state, prepared by the ABS, are injected. As shown in Fig. 3.11, a small sample of the target gas propagates from the center of the cell into the BRP and the TGA, where the atomic polarization as well as the molecular fraction is determined.
In a later stage of the experiment, the storage cell will be surrounded by a detection system based on silicon microstrip detectors. Consisting of 3 layers of different thickness ($300\,\mu\mathrm{m}$, $300\,\mu\mathrm{m}$, $1500\,\mu\mathrm{m}$), it will allow for the detection of particles scattered at the gas target in a wide angular range. The extractable information, like the deposited energy and hit positions, enable vertex reconstruction, particle identification, and consequently a measurement of the beam and target polarization. A description of the detector system is given in Sec. 3.3.2.

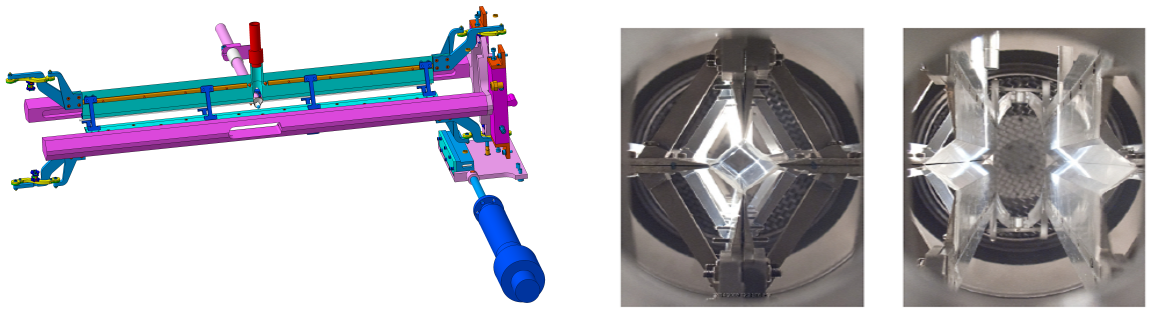

Fig. 3.16.: Left: Technical drawing of the openable storage cell. **Right:** Photograph of the storage cell in beam direction in closed (left) and open (right) position.

3.2.5. Holding Field System

The operation of the polarized target requires a magnetic guide field system providing fields at the storage cell in the order of $1\,\mathrm{mT}$. A system of coils (Fig. 3.17) that provides fields along x-, y-, and s- direction has been developed and built by the Zentralabteilung Technologie (ZAT) of the FZJ [125] and was mounted on the target chamber. It allows one to switch the target polarization in short succession by different powering of the coils. The polarization is known to be fully reversed within about $10\,\mathrm{ms}$ (see [126], Fig. 11). In order to avoid influences on the beam optics in the rest of the ring, the $\int B \cdot ds$ is compensated by additional coils, installed on the beam pipe up- and downstream of the target. A calculation of the magnetic

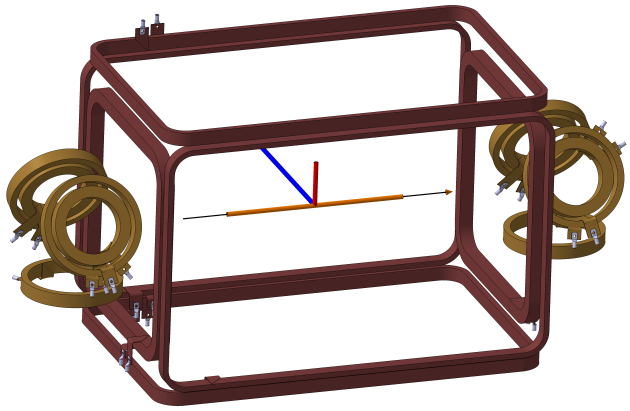

Fig. 3.17: Technical drawing of the magnetic guide field coils. The large coils provide the holding field along the x-, y-, and s-direction. The additional coils up- and downstream of the interaction region compensate the integral $B \cdot ds$ along the beam direction for either the horizontal (x) or the vertical (y) orientations.

field components B_x, B_y, B_s in the target chamber along all three directions is displayed in Fig. 3.18. As one can see, B_x and B_y are compensated along s-direction ($\int B \cdot ds = 0$). The holding field system and the compensation is more detail described in App. C.

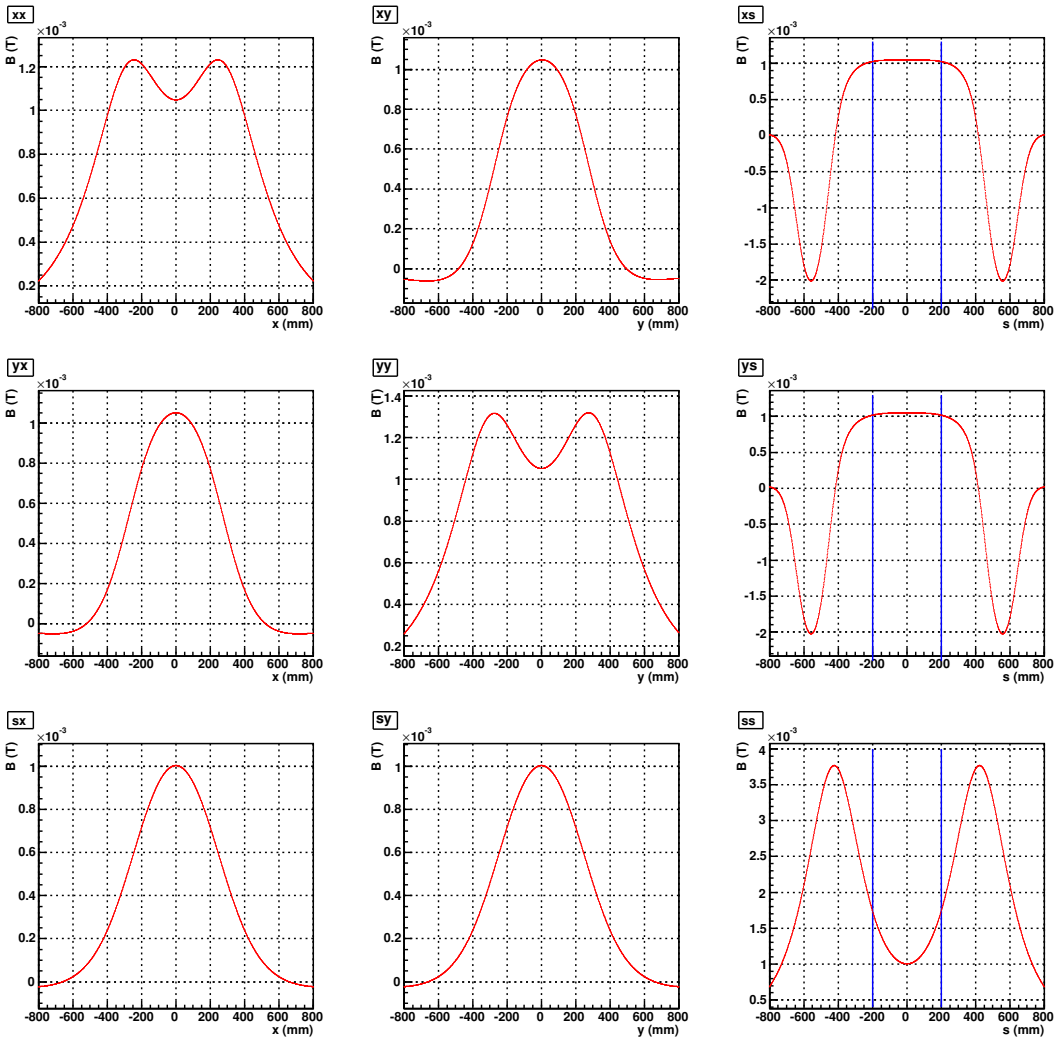

Fig. 3.18.: Calculated magnetic field components B_x, B_y, B_s along x-, y-, and s-direction. The title informs about the plotted component and the direction. For instance graph xs shows B_x along s. The target cell region ($s = -200\,\mathrm{mm}$ to $+200\,\mathrm{mm}$) is indicated in blue.

3.2.6. Target Gas Analyzer and Breit-Rabi Polarimeter

The BRP serves to measure and monitor the target polarization. A feeding tube connected horizontally to the storage cell extracts a small fraction of less than $10\,\%$ of the injected polarized gas toward the BRP, which measures the relative populations n_i of the hyperfine states of hydrogen (or deuterium) atoms, and is therefore capable to determine the polarization of the target atoms. This serves as an important online monitor of the ABS operation, and the performance of the storage cell target. The BRP employed here for the spin-filtering experiments was used previously in the HERMES experiment [118, 127]. It had to be modified due to the use of a storage cell at room temperature [128]. A schematic drawing of the BRP and the Target Gas Analyzer, which measures the relative amount of atoms and molecules coming from the cell, is displayed in Fig. 3.19.

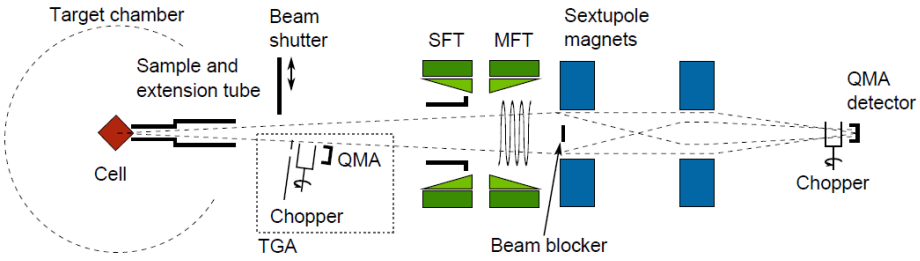

Fig. 3.19.: Schematic drawing of the Breit-Rabi polarimeter and target gas analyzer

The TGA is mounted $7°$ off-axis with respect to the BRP, in order not to interfere with the atomic beam entering the polarimeter. A chopper allows for the subtraction of the background by rotating at $5.5\,\mathrm{Hz}$. Circular beam blockers on the axis to the quadrupole mass analyzer (QMA) ensure that only atoms or molecules from the extension tube can reach the detector. Particles entering the detector are ionized by electrons, mass filtered with the quadrupole mass spectrometer (QMS), and finally detected by the channel electron multiplier (CEM) operated for single ion detection [124, 129].
The BRP mainly consists of the rf transition units, the sextupole magnet system and the Quadrupole Mass Analyzer (QMA). Ultra high vacuum conditions are required to measure beam intensities of the order of $10^{-11}\,\mathrm{mbar}\cdot\mathrm{l/s}$. Thus a differential pumping system with three vacuum chambers, each equipped with more than $2000\,\mathrm{l/s}$ pumping speed, keeps the pressure at $2\cdot10^{-9}\,\mathrm{mbar}$ in the sextupole chamber and at $2.5\cdot10^{-10}\,\mathrm{mbar}$ in the detector chamber. The strong and medium field transition units allow one to exchange the populations between pairs of hyperfine states. The sextupole system, composed of two magnets, spin filters the beam by deflecting atoms with negative electron spin (state $|3\rangle$ and $|4\rangle$) by the Stern-Gerlach force, thereby atoms with positive electron spin are focused into the QMA. The detector stage of the BRP is identical to the one employed in the TGA. Together, BRP and TGA give a value for the target polarization.

3.3. ANKE as a Polarimeter

ANKE serves as a beam polarimeter. The beam polarization after spin filtering will be measured by the existing Silicon Tracking Telescopes (STTs) at the ANKE target place (see Fig. 3.1). As described in detail in Sec. 5.2, the polarization can be determined from the left-right asymmetry in proton-deuteron elastic scattering, where the deuterium is delivered from the ANKE cluster target. After filtering for two beam lifetimes, the PAX polarized gas target will be switched off, and the unpolarized deuterium target at ANKE will be switched on in order to determine the beam polarization.

3.3.1. Deuterium Cluster Target

A deuterium cluster target, developed at the Westfälische-Wilhelms-Universität Münster [130], is available at the internal target position of the ANKE experiment. It provides a target beam of about $10\,\mathrm{mm}$ diameter with a homogeneous density distribution and a small beam target overlap region. The absolute density can be varied over a range of about two orders in magnitude ($10^{13} - 10^{15}\,\mathrm{atoms/cm^2}$), which enables to find a compromise between event rates and beam lifetime.
The clusters of $10^3 - 10^4$ atoms are produced in a Laval-nozzle [131]. Pure hydrogen or deuterium gas is cooled below the vapor pressure curve to a temperature of 20 to $30\,\mathrm{K}$ and pressed through the Laval-nozzle with an opening diameter of $20\,\mu\mathrm{m}$ at a pressure of $15 - 20\,\mathrm{bar}$ (Fig. 3.20). Due to the adiabatic expansion in the nozzle, the gas further cools down and spontaneously condensates into clusters. In the skimmer chamber, the beam is separated from the residual gas by a cone shaped aperture (skimmer). An additional shutter allows one to switch the target on and off in less than $1\,\mathrm{s}$.

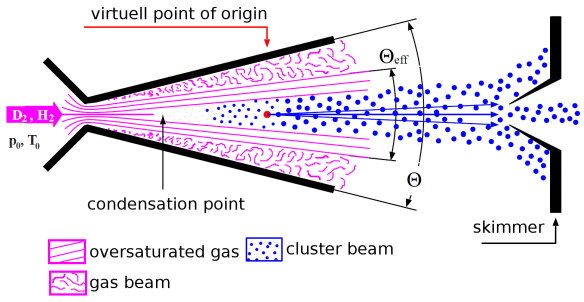

Fig. 3.20: Cluster production at the Laval-nozzle. Adiabatic expansion of the cooled beam (20 K) further cools down the beam and the oversaturated gas spontaneously condensates to clusters. Finally the cluster beam is separated from the residual gas by a skimmer [123].

A differential pumping system (Fig. 3.21) reduces the gas load into the target chamber with the aim to keep the ring vacuum below $10^{-7}\,\mathrm{mbar}$. After crossing the accelerator beam, the cluster beam enters the collector stage, installed below the target chamber. Its differential pumping system consists of three cryopumps and one turbomolecular pump, that ensures a minimum gas load to the adjacent sections of the ring. Since the betatron functions at the ANKE location are of the order of $3 - 5\,\mathrm{m}$, this is essential to provide long beam lifetimes.

3.3.2. Silicon Tracking Telescopes (STTs)

The polarization of the originally unpolarized proton beam after spin filtering will be measured by two Silicon Tracking Telescopes installed in a left-right symmetric arrangement

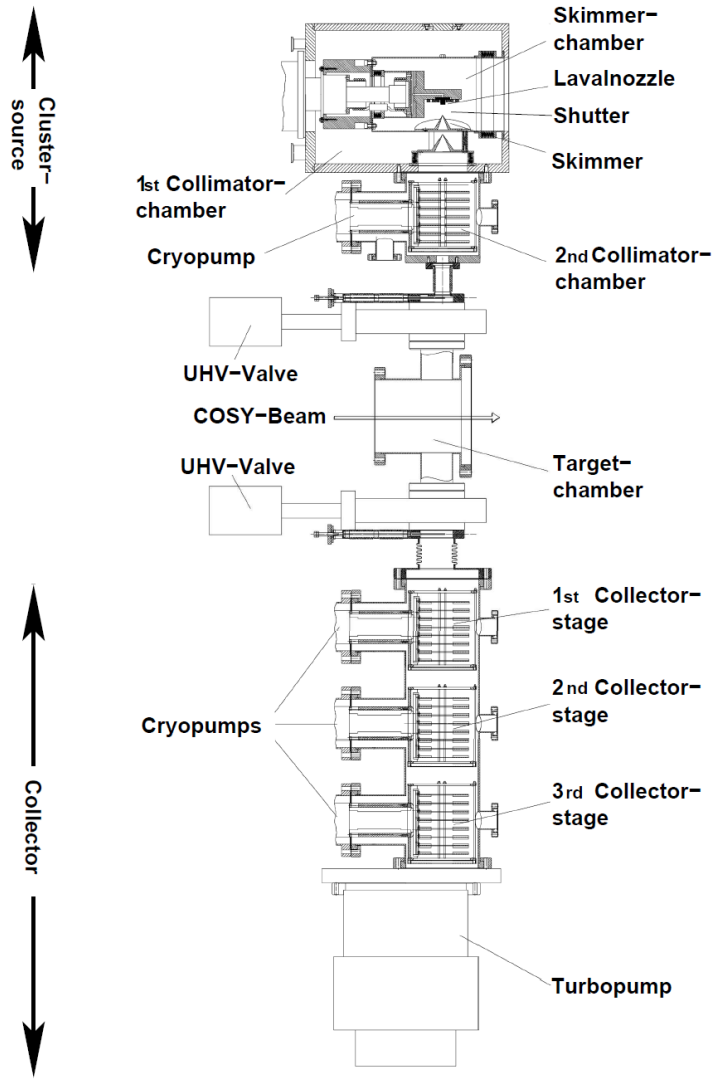

Fig. 3.21.: Schematic view of the cluster target. The cluster source, placed above the COSY beam, produces a well-defined target beam of hydrogen or deuterium clusters. The differential pumping system of the cluster source and the collector stage minimize the degradation of the COSY vacuum [132].

to the beam target overlap region [133]. The determination of the left-right asymmetry in proton-deuteron elastic scattering and the knowledge of the corresponding analyzing power makes it possible to extract the polarization of the proton beam (see Sec. 5.2).
Each STT consists of three individual double-sided silicon strip detectors of different thickness. The basic configuration has a $65\,\mu\mathrm{m}$ (or $300\,\mu\mathrm{m}$) first layer, a $300\,\mu\mathrm{m}$ second layer, and to ensure stopping of protons up to $40\,\mathrm{MeV}$ kinetic energy, a third layer of $5100\,\mu\mathrm{m}$ thickness (Fig. 3.22). The detectors are placed close to the beam target overlap region inside the beam vacuum.
This configuration fulfills the requirement of particle identification together with a precise energy determination ($1-5\,\%$) and tracking with a vertex resolution of $1\,\mathrm{mm}$ over a wide energy range. The combination of the telescope structure with different kinds of detectors, the specially developed front-end electronics, and the technically mature design provides:

- Identification of protons and deuterons via the $\Delta E/E$ method over an energy range

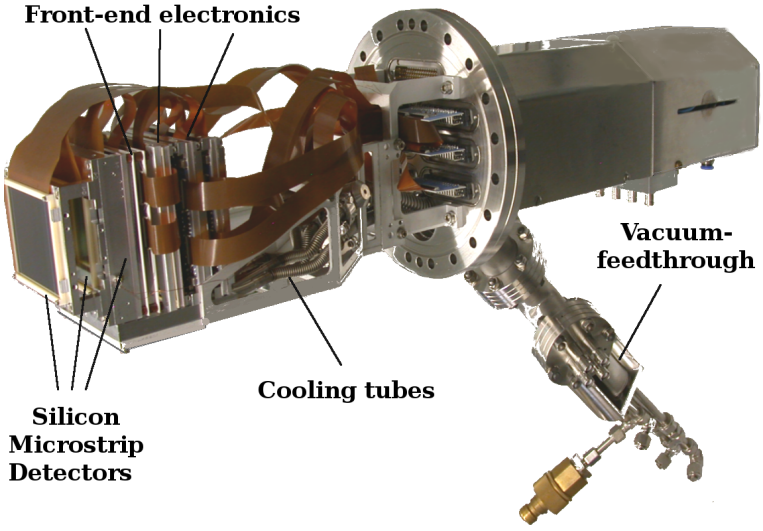

Fig. 3.22.: Setup of one Silicon Tracking Telescope. Each detector side is connected via kapton flat cables to a board equipped with self-triggering front-end chips. Specially developed cooling plates and a vacuum compatible feed-through system allow for efficient cooling of detectors and temperature stabilization of the electronics.

from $2.5\,\mathrm{MeV}$ to $\geq 40\,\mathrm{MeV}$ with a resolution of $\approx 150\,\mathrm{keV}$.

- Particle tracking over a wide energy range, starting from $2.5\,\mathrm{MeV}$ spectator protons up to minimum ionizing particles (MIP) with an angular resolution in the range from 1° to 6° (FHWM). For stopped particles, the resolution depends on angular straggling while for MIPs, it is determined by the strip pitch of the detector.
- Self-triggering within less than $100\,\mathrm{ns}$ after particle passage allows one to use the STTs as a stand alone system and to set timing coincidences with other detectors.
- Maximum modularity gives the opportunity to optimize the detection system according to the needs of each experiment individually. Besides the convenient exchange of detectors and electronics, it is possible to adjust the position with respect to the target and therewith to maximize the acceptance of the detector.
- High rate capability (zero suppression).
- Time resolution of less than $1\,\mathrm{ns}$.

The particle identification, which is crucial for the measurement of the polarization, is based on the so-called $\Delta E/E$-method. Therefore, the energy loss in one layer is plotted against the energy loss in the next layer (see Sec. 5.2). Consequently, the thickness of the first detector layer defines the energy threshold of the measurement. For $65\,\mu\mathrm{m}$ it is about $2.5\,\mathrm{MeV}$ for protons and $4.0\,\mathrm{MeV}$ for deuterons.
The detectors, which will be used for the first two layers of the STT, have been originally designed for the BaBar experiment [134, 135] by the British company Micron Ltd. [136]. They have an active area of $51\,\mathrm{mm} \times 62\,\mathrm{mm}$ and an effective strip pitch of $400\,\mu\mathrm{m}$.
The thick Lithium drifted Silicon detectors Si(Li) [137] with an active area of $64\,\mathrm{mm} \times 64\,\mathrm{mm}$ and a strip pitch of $666\,\mu\mathrm{m}$ (96 strips per side) have been developed in the detector laboratory of the Institut für Kernphysik (IKP) of FZJ. They ensure a stopping of particles up to an energy of about $32\,\mathrm{MeV}$ for protons and $43\,\mathrm{MeV}$ for deuterons.
The signals from the silicon microstrip detectors are transmitted via kapton flat cables to the in-vacuum front-end electronics, which in a first step amplifies the incoming signal. Afterwards, the signal is split into two branches. In the amplitude part the signal is fed

to a slow shaper and once a readout cycle is started the output of each shaper is stored in the sample and hold facility. In the trigger part the signal is shaped with a peaking time of only $75\,\mathrm{ns}$. The comparison of the output signal with a threshold allows one to obtain a trigger signal from the chip. The chip provides a low trigger threshold of $100\,\mathrm{keV}$. More details can be found in [138].
The shaped signals are then further transmitted by additional kapton cable. Each front-end electronics board is controlled via one interface card outside of the vacuum. The interface cards provide power supplies, control signals, trigger pattern threshold, and calibration pulse amplitudes. The read-out chain guarantees a total dead time of less than $50\,\mu\mathrm{s}$.
In order to stabilize the temperature of the front-end electronics at room temperature the electronic boards are mounted on specially developed cooling plates. A connection to vacuum compatible cooling tubes allows one to pump cooling fluid through these aluminum plates (see Fig. 3.22). A second cooling circuit enables a cooling of the detectors down to $-20^{\circ}\mathrm{C}$ in order to reduce the dark current and thereby the noise.
Two Silicon Tracking Telescopes will be installed left and right of the beam-target overlap region opposite to each other, as shown in Fig. 3.23.

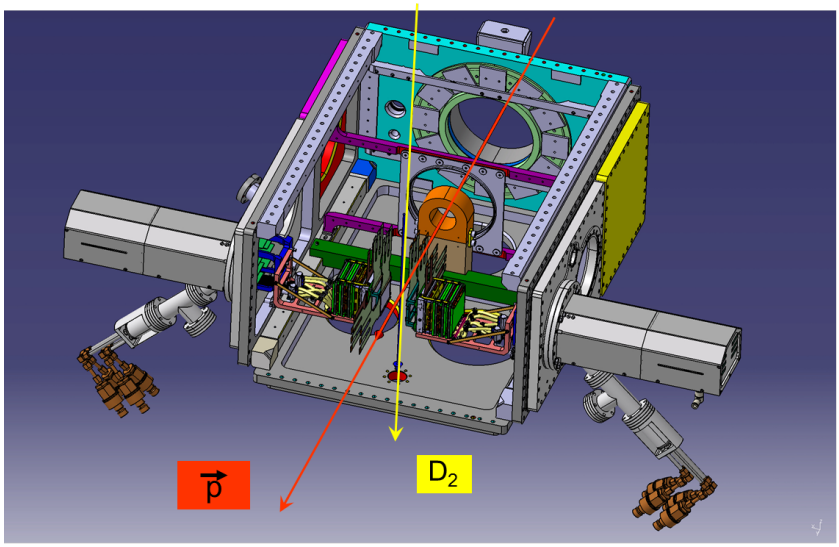

Fig. 3.23.: Drawing of the two Silicon Tracking Telescopes installed close to the beam-target overlap region inside the beam vacuum of the ANKE target chamber. The polarized proton beam (red) enters the chamber through an aperture with an inner diameter of $55\,\mathrm{mm}$, which protects the detectors from a direct hit of the beam, and hits the deuterium cluster target, which is injected from the top (yellow).

4. Commissioning for Spin Filtering at COSY

Sophisticated experiments like the spin-filtering studies require comprehensive understanding of the underlying processes and optimal adjustment of all contributing parameters. Since, especially with protons at COSY, the polarization buildup is expected to be very small, the experiment has to be optimized in view of the maximum reachable beam polarization and its precise determination. This includes detailed knowledge of machine parameters in order to set up the synchrotron, considering a multitude of constraints and to determine the polarization buildup cross section, taking all relevant parameters and possible sources of errors into consideration.
Section 4.1 deals with the commissioning of the low-β insertion. Sections 4.2 - 4.4 describe the adjustment of machine parameters in view of long beam lifetimes, including studies of the contribution to the beam lifetime from single intrabeam scattering. The determination of the machine acceptance and the acceptance angle at the target position is explained in Sec. 4.5. Target related issues like density measurements and holding field commissioning are discussed in Sec. 4.6, and finally, the chapter closes with a description of how to set up the beam for spin-filtering experiments in Sec. 4.7.

4.1. Commissioning of the low-β Section

The commissioning of the low-β insertion at COSY, which mainly consists of two pairs of quadrupole magnets and two steerer magnets, was accomplished during a dedicated beam time in January 2010. It was shown that the installation had no effect on the regular COSY operation. By adjustment of the current of merely two COSY quadrupoles, the proton beam could be stored at injection energy without visible changes compared to the regular COSY settings. PAX1, the outer pair of the new PAX quadrupoles and PAX2, the inner pair (Fig. 3.10), were operated at 184.2 A and 191.4 A, respectively. The horizontal steerer magnets, mounted on the surrounding COSY quadrupoles, have been used to maximize injection intensity.
A simulation of the beam transport along COSY and the calculation of parameters like the working point and the optical functions can be achieved with the MAD8 program[1]. An already existing model of COSY and its magnetic structure allows one to calculate the betatron functions at the PAX-IP, which is an essential input parameter for the calculation of the polarizing cross section, since this affects the machine acceptance angle Θ_{acc} at the target. In order to obtain the betatron functions at the position of the PAX magnets, and therewith check the MAD calculations, the dependence of the betatron tune change on the operating current of the PAX quadrupoles has to be measured. This procedure makes use of the relation between the tune change $\delta Q_{x,y}$ and the change of the focussing strength of a

[1] "MAD" (Methodical Accelerator Design) is a program developed at CERN that provides a standard user interface for solving problems arising in accelerator design [139].

quadrupole $\delta k_{x,y}(s)$

$$\delta Q_{x,y} = -\frac{1}{4\pi} \oint \beta_{x,y}(s)\delta k_{x,y}(s)ds, \tag{4.1}$$

where s is the position along the beam direction.
The matrix formalism, in detail described in [140], affords an opportunity to calculate beam guidance and focussing in analogy to optics. All components such as dipoles, quadrupoles or drift passages are described by a transformation matrix in such a way that the particle movement can be characterized by matrix multiplication. Here one assumes stationary magnetic fields. The application of this formalism on a change of the focussing strength $\Delta k_{x,y}$ of one pair of quadrupoles and the resulting tune shift $\Delta Q_{x,y}$ (see App. D) yields an analytic formula for the local betatron function

$$\beta_{x,y} \approx \frac{4\pi}{l\Delta k_{x,y}} \left(1 + \pi\frac{\Delta Q_{x,y}}{2}\cot(2\pi Q_0)\right) \frac{\Delta Q_{x,y}}{2}. \tag{4.2}$$

Here Q_0 is the unperturbed working point.
Since the four PAX quadrupoles are powered pairwise, only the average betatron function at these two magnets is measurable. The operating current of the outer pair (PAX1) was changed in steps of 0.5 A from 180.7 A to 188.2 A and the current of the inner pair (PAX2) was increased from 181.4 A to 199.4 A in steps of 1 A. The focussing strength $k_x = \frac{q}{p}\frac{\partial B_y}{\partial x}$ can be calculated using the elementary charge e, the known momentum p and a calibration factor which describes the connection between the gradient $\frac{\partial B_y}{\partial x}$ and the current, which has been determined earlier.
For the determination of the revolution frequency, the sum signal of a beam position monitor, described in Sec. 3.1.4, is used. The Schottky noise of this signal shows a periodicity with the revolution frequency and higher harmonics. A Fourier transform allows one to determine the revolution frequency of the beam: $f = 488.85\,\mathrm{kHz}$. The error of this measurement is assumed to be negligible ($\sigma_f \leq 100\,\mathrm{Hz}$).
In order to quantify the betatron tune or working point of the machine, collective transverse oscillations of the beam particles are enhanced by RF-excitation via the stripline unit (Sec. 3.1.4). A sweep over a dedicated excitation frequency range is accomplished. Resonant beam position oscillations occur, if the exciting frequency corresponds to the overlap of betatron frequency and harmonics of f. Thus the fractional part of the working point can be determined by

$$Q_{\mathrm{frac}} = \frac{f_\beta}{f}. \tag{4.3}$$

The analysis of the resulting frequency spectra is performed by a digital spectrum analyzer. The beam deflection as a function of the excitation frequency is plotted and fitted with a Lorentz function. The mean value gives the resonance frequency f_β .
Plotting Q vs Δk (Fig. 4.1) shows an almost linear dependence for changes of the focussing strength that are in the order of $2 - 5\%$. For one pair of quadrupoles, the horizontal and vertical tunes change in opposite directions, which demonstrates that a quadrupole magnet focuses in one direction whereas it defocuses in the perpendicular direction. In addition, the orientation of the tune change is opposite for the inner pair of quadrupoles (PAX2). In case of convergence of Q_x and Q_y the tune change flattens, which is an evidence for coupling in the machine. For larger changes of the quadrupole strength, the tune jumps and continues its linear behavior.
For each point an average betatron function is calculated by Eq. (4.2). Averaging over the individual measurements gives the betatron functions at the position of the PAX quadrupoles as indicated in Tab. 4.1. For these measurements, an electron cooled proton beam at injection energy with dispersion suppression ($D = 0$) in the straight sections was used.

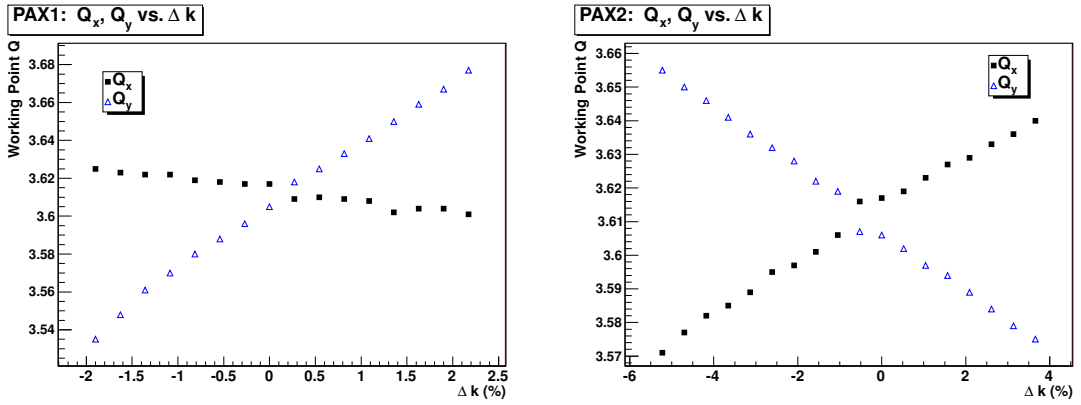

Fig. 4.1.: The change of the betatron tune vs the focussing strength $\Delta k_{x,y}$ of a pair of quadrupoles allows for the determination of the local betatron function. The graphs show the tune change in the horizontal (Q_x) and the vertical (Q_y) plane for the PAX1 (left) and PAX2 (right) quadrupole magnets as a function of the change in focussing strength Δk.

Figure 4.2 displays the model output for this setting in case of PAX magnets switched off (left) and on (right) together with the measured betatron functions, denoted by the crosses of corresponding color. The measurements exhibit a reasonable agreement with the model calculations, therefore betatron functions around the design values of $0.3\,\mathrm{m}$ are expected at the cell center. In addition, it is visible that especially β_x becomes very large in the neighboring regions, which leads to small acceptance angles at this position. If reversing the role of PAX1 and PAX2 can improve the lattice will be tested in the upcoming experiment.

Quadrupole	$\beta_x(m)$	$\beta_y(m)$
PAX1 (outer pair)	3.06	15.17
PAX2 (inner pair)	2.95	3.57
center (COSY model)	0.379	0.361

Table 4.1.: Measured betatron functions β_x and β_y at the position of the PAX quadrupole magnets and expected magnitude of the betatron function at the center of the target from the COSY model.

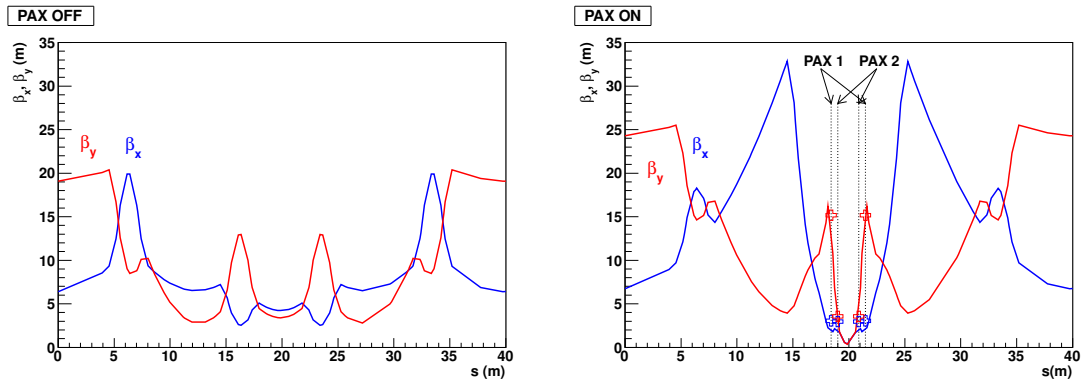

Fig. 4.2.: Model calculation of the betatron functions at the PAX-IP for PAX magnets switched off (left) and on (right). The measured values of β_x and β_y at the magnet positions are indicated in the right panel.

4.2. Working Point Adjustment

In order to increase the beam lifetime a search for the optimal betatron tune has been performed for several machine settings. Betatron resonances (Eq. (2.5)) can lead to an expansion of the beam or even beam losses (Sec. 2.1.1). The creation of a so-called tune map requires a measurement of the beam lifetime for different working points. The lifetime of the particle beam is determined by fitting the beam current signal with an exponential function according to Eq. (2.45). The beam current signal of COSY is delivered via a profibus system and continuously recorded and monitored as displayed in Fig. 4.3. With the properly electron cooled beam, a pure exponential behavior of the beam current has been observed. Therefore, the beam losses are mainly due to single Coulomb scattering.

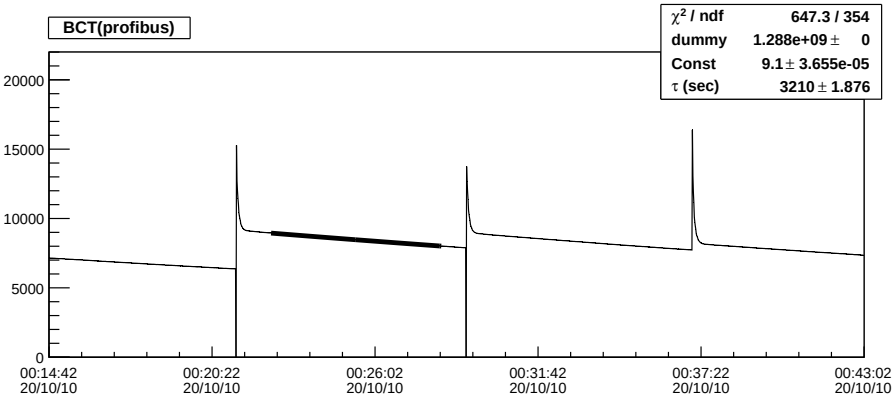

Fig. 4.3.: The beam current of the circulating particle beam in COSY is continuously recorded and monitored allowing for a determination of the beam lifetime τ. The result of the fit ($\tau = 3210 \pm 2\,\mathrm{s}$) is shown in the top right frame. The graph displays three arbitrary cycles of about $8.5\,\mathrm{min}$ length. A cycle starts with an injection peak, followed by fast initial losses ($\approx 25-30\,\%$) until the beam is completely cooled and after about $30\,s$ the intensity drops exponentially.

A common betatron tune of COSY at injection energy is $Q_x \approx Q_y \approx 3.6$. In order to change the working point, the current and thereby the focussing strength in three of the six quadrupole families (QU 1-3-5 or 2-4-6) (see Sec. 3.1.1) was varied after the beam has been stored and cooled. The currents were modified within a range of $\pm 5\%$ starting at $21.6\,\mathrm{A}$ for QU 1-3-5 and $15.7\,\mathrm{A}$ for QU 2-4-6. The tune scans, performed for different optical settings, show a maximum beam lifetime time close to the standard working point of $Q = 3.62$ in both planes for the majority of measurements. The result of a scan with low-β section switched on and dispersion not equal zero is displayed in Fig. 4.4. In addition to this, betatron resonances up to the 10th order are displayed, which obviously shows that the structure of the map can not be easily understood. The observed beam lifetime maxima ($\approx 3200\,\mathrm{s}$) are located symmetrically around $Q_x = Q_y = 3.6$ ($Q_{x(y)} = 3.61$, $Q_{y(x)} = 3.59$). An explanation why they are not located in a resonance free area is still missing. One possible explanation could be, that a small broadening of the beam has a positive effect because of intrabeam scattering. This issue will be discussed further in Sec. 4.4. On the other hand, the effect of 5th order resonances should be rather small.
However, the beam lifetime appears to be very sensitive to the betatron tune. The measurement shows a change of a factor six in beam lifetime for a rather finite region, and therefore the betatron tune is an important parameter that has to be optimized prior to the spin-filtering studies.

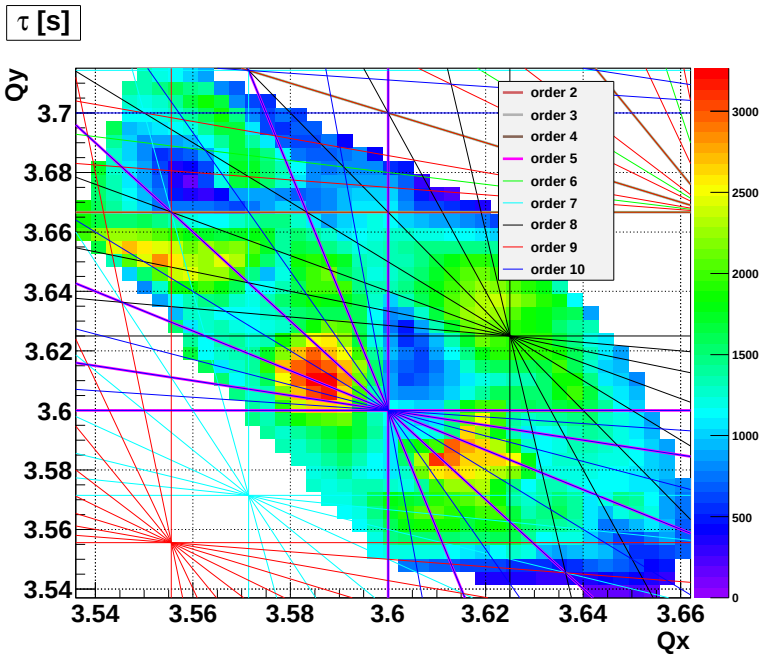

Fig. 4.4.: Lifetime as a function of the betatron tunes Q_x and Q_y. The colors ranging from blue to red indicate the beam lifetime. The lines illustrate betatron resonances of different orders as defined in Eq. (2.5).

4.3. Closed-Orbit Correction Procedure

The trajectories of circulating particles can deviate from the ideal orbit, which is in the center of the beam line, due to different effects such as alignment or field errors of magnets. The orbit deviates, but it remains a closed orbit. These deviations are supposed to cause beam losses especially at positions of large betatron functions. An orbit correction concept based on the orbit response matrix method has been utilized to further improve the beam lifetime. This procedure is in detail described in [141].
The orbit response matrix (ORM) contains the changes of an orbit deviation Δu_d at the beam position monitors at the location d due to changes in the deflection strength $\Delta\Theta'_i$ of orbit correction dipole magnets located somewhere in the machine at location i. The matrix elements are given by

$$R_{d,i} = \frac{\Delta u_d}{\Delta\Theta'_i} = \sqrt{\beta_{u,i}\beta_{u,d}}\frac{\cos(\pi Q_u - \psi_{u,d\to i})}{2\sin(\pi Q_u)}, \tag{4.4}$$

where the phase advance between both locations d and i is denoted by $\psi_{u,d\to i}$. The ORM can either be calculated from a computer model of the accelerator or it can be measured. Thus it can contain measurement errors or deviations between the model and reality. Using the ORM in an iterative process enables an optimization of the closed orbit. For this purpose a vector $\vec{S}$ containing all orbit deviations at the BPMs is given as

$$\vec{S} = R \cdot \vec{\Theta}, \tag{4.5}$$

where $\vec{\Theta}$ describes the deflection strengths of the orbit correction dipole magnets.
One way how to correct the orbit is to vary $\vec{\Theta}$ in order to reproduce the measured deviations, e.g., with a χ^2 minimization. In this case $-\vec{\Theta}$ contains the appropriate settings of the correction dipole magnets to minimize the closed orbit deviations.

Another possibility would be to apply the inversion of the ORM and calculate the settings by $\vec{\Theta} = R^{-1}\vec{S}$. The second method is usually faster, though an inversion of the matrix R is not always possible.
The orbit correction procedure for COSY has been tested for the first time in January of 2009 within the framework of a PAX beam time and was further optimized since then, hoping to allow for longer lifetimes at injection energy. The measurement of the ORM during the last PAX beam time makes use of up to 17 orbit correction dipole magnets for the measurement of the vertical orbit response matrix and 20 horizontal orbit correction dipole magnets, two horizontal back-leg-windings on the ANKE dipole magnets, and both compensation dipole magnets next to the electron cooler toroid magnets for the horizontal ORM. Depending on their reliability, up to 29 beam position monitors along COSY can be utilized to record the ORM. As the measurements show, the phase-space coupling can be neglected for the measurement of the ORM. The procedure is to deflect the beam in both transverse planes by changing the current of the particular magnet by approximately 5% if no beam losses occur. The orbit changes at the BPMs normalized to the variation of the current correspond to the entries of the ORM, which now can be utilized to perform an orbit correction. In spite of the longer computation time the χ^2 minimization was used since it is faster to set up.
An example of a successful orbit correction with two iterations is displayed in Fig. 4.5 for the horizontal and vertical orbit. Initial deviations of up to $35\,\mathrm{mm}$ (horizontal) could be decreased to less than $10\,\mathrm{mm}$. Including the steerer magnets of the electron cooler, which was not the case for the demonstrated measurement, enables further improvement. Recent closed-orbit corrections show resulting deviations of less than $3\,\mathrm{mm}$. It has been discovered that, depending on the starting conditions, the reduction of orbit distortions can significantly increase the machine acceptance ($A_{x,y} = 14\,\mu\mathrm{m}$ to $A_{x,y} = 25\,\mu\mathrm{m}$), and therewith substantially improve the beam lifetime. It was also recognized that in general the vertical orbit is much better than the horizontal orbit. Additionally, the orbit correction procedure allows one to set boundary conditions such as the beam position at the target or the electron cooler.
In view of a routine for the machine development prior to spin-filtering experiments a satisfactory correction of the closed orbit is essential.

4.4. Single Intrabeam Scattering

Investigations in January 2010 have shown that the beam lifetime remained stable ($\approx 4000\,\mathrm{s}$) in spite of drastic changes of the machine acceptance. As reported in [142], the acceptance has been measured with two different machine settings, with normal polarity of the quadrupoles in the electron cooler straight section, and with reversed polarity in the horizontal and vertical plane. The resulting acceptance difference of about a factor five in both planes caused no significant change of the beam lifetime. This surprising result indicates that other effects are limiting the beam lifetime.
As explained in Sec. 2.1.2, single intrabeam scattering (IBS) outside the longitudinal machine acceptance can be considered to cause particle losses. This effect is known to be limiting in case of electron machines, but has not been reported for proton machines. For an estimation of this effect at COSY injection energy of $45\,\mathrm{MeV}$ the following parameters can be inserted into the Touschek formula (Eq. 2.21): $\beta = 0.30$, $\gamma = 1.05$, $C = 184\,\mathrm{m}$, $\beta_\mathrm{z} = 10\,\mathrm{m}$, $r_0 = 1.535 \cdot 10^{-18}\,\mathrm{m}$, $I = 5 \cdot 10^9$, $\epsilon = 0.5\,\mu\mathrm{m}$, and an assumed $\Delta p/p = 0.001$. The resulting lifetime of $\tau \approx 4100\,\mathrm{s}$ is close to the value which has been observed for different settings. According to the Touschek formula

$$\tau_\mathrm{T} = \frac{4\gamma^3\beta^3 \cdot \langle\sqrt{\beta_\mathrm{z}}\rangle \cdot C \cdot \epsilon^{3/2} \cdot \left(\frac{\Delta p}{p}\right)^2}{\sqrt{\pi} \cdot I \cdot c \cdot r_0^2}, \tag{4.6}$$

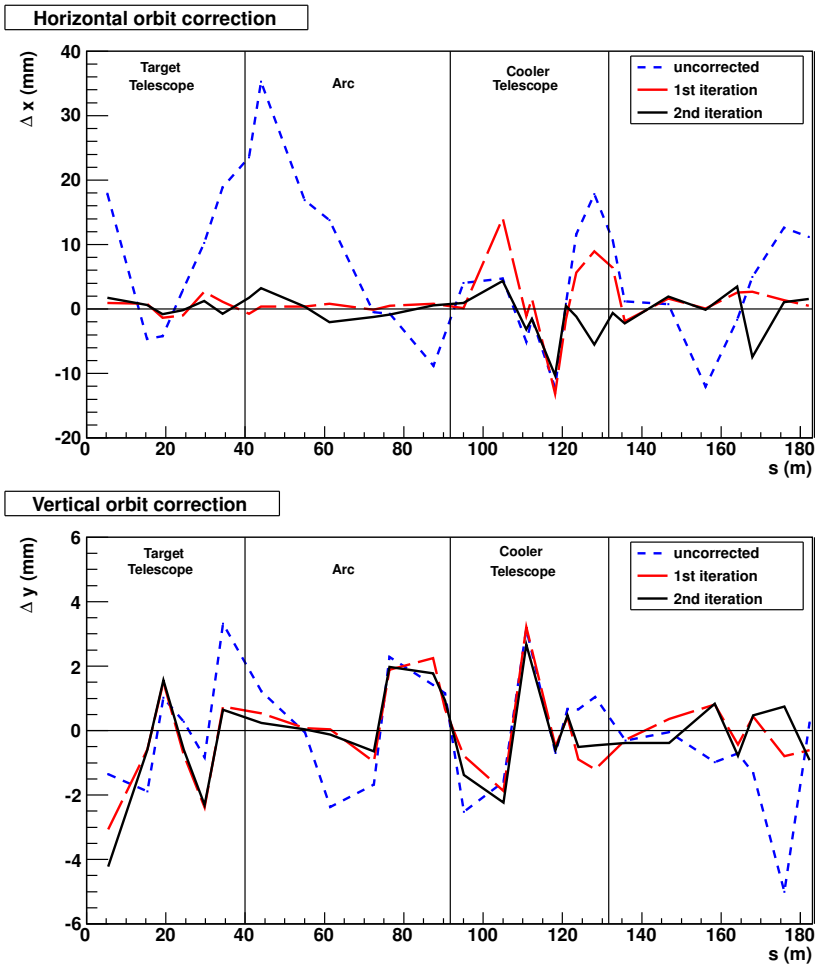

Fig. 4.5.: Horizontal (top) and vertical (bottom) closed-orbit correction for COSY at injection energy. The vertical orbit deviations are in general smaller.

a study of this effect can be accomplished by changing the beam emittance ϵ, the beam intensity I, or the energy. These actions should change the beam lifetime in a predictable way. The following studies were carried out with low-β section switched off and $D \neq 0$.
An investigation of the intensity dependence was achieved using a micro-pulsing system in the injection beam line. Here, the beam intensity can be controlled by chopping the injection pulse length [69]. Since the number of particles affects the beam emittance the intensity has to be normalized to the beam emittance. Thus, the beam lifetime is studied as a function of $I/\epsilon^{3/2}$. The determination of the beam emittance makes use of the ionization profile monitor, described in Sec. 3.1.4. The measured distribution of ions, produced by the interaction of the stored beam with the residual gas, is fitted by a Gaussian, as shown in Fig. 4.6. The resulting beam widths $\sigma_{x,y}$ in both directions are used to calculate the beam emittance as

$$\epsilon = \sqrt{\epsilon_x^2 + \epsilon_y^2} \qquad \text{with} \qquad \epsilon_{x,y} = \frac{\sigma^2}{\beta_{x,y}}. \tag{4.7}$$

According to Eq. (4.6) the lifetime should be inversely proportional to the normalized beam intensity. As displayed in Fig. 4.7, the measurement shows no clear indication for the expected intensity dependence.
In a next step, the beam lifetime was studied as a function of the beam emittance, where the beam intensity was kept constant. Here, both the horizontal and vertical electron beam

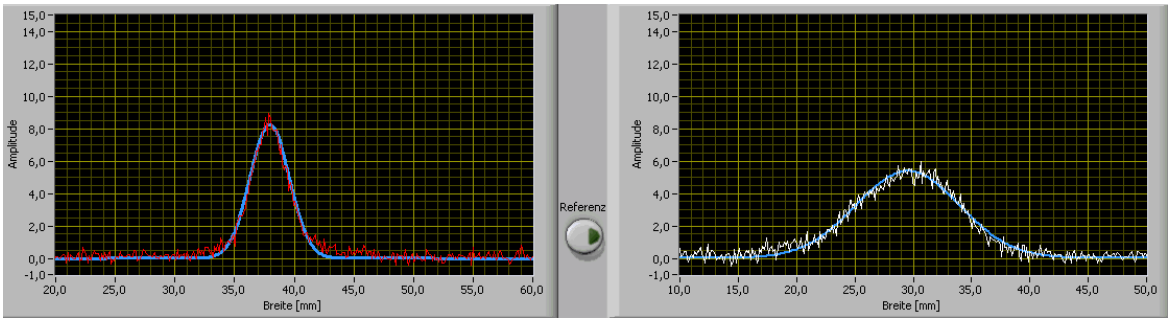

Fig. 4.6.: Measurement of the beam widths using the ionization profile monitor. The spatial ion distribution in horizontal (left) and vertical (right) direction is fitted by Gaussians, which yields the beam widths σ_x and σ_y.

steerers at the cooling solenoids were used to tilt the electron beam relative to the proton beam, thus decreasing the cooling performance. A test showed that a controllable increase and stabilization of the beam emittance is achievable. The beam widths $\sigma_{x,y}$ were measured by the help of the IPM. As shown in Fig. 4.8, the beam was completely cooled to widths of about $\sigma_x = 1.6\,\mathrm{mm}$ (white) and $\sigma_y = 1.2\,\mathrm{mm}$ (red) and then expanded by tilting the electron beam. The graph shows that the beam size could be stabilized afterwards. The beam emittance was calculated according to Eq. (4.7). The result of a first measurement is depicted in Fig. 4.9, which shows that the beam lifetime increases with increasing beam emittance. For large emittances ($\epsilon > 1\,\mu\mathrm{m}$) corresponding to large electron beam tilt angle, the cooling performance is too poor. Therefore, these two points are ignored in the analysis. A fit to the curve using $\tau \sim \epsilon^{\frac{3}{2}}$ according to Eq. 4.6 roughly describes the measured values. However, this emittance dependence can not be a consequence of the pure Touschek effect, because a subsequent measurement of the longitudinal ring acceptance revealed a $\frac{\Delta p}{p} = 0.003$, which would predict a ten times longer lifetime. At the AD, where the specified acceptance is roughly ten times larger [143] the effect of single IBS is beyond any relevance.

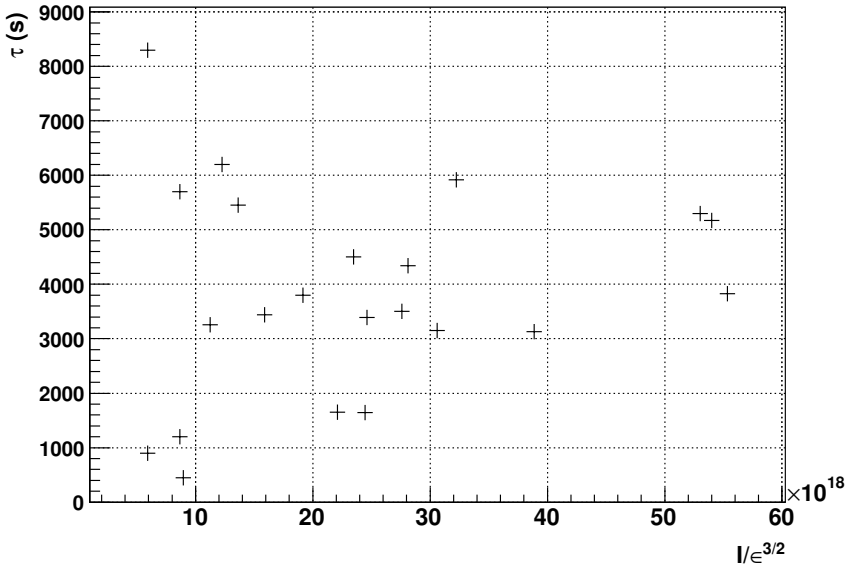

Fig. 4.7.: Beam lifetime as a function of the beam intensity. According to the Touschek effect τ should be inversely proportional to the intensity, which is not clearly visible.

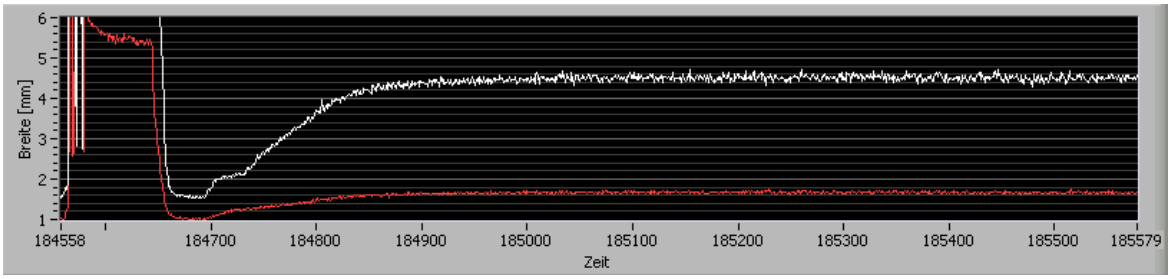

Fig. 4.8.: Adjustment and stabilization of the beam size. After injection the electron cooling shrinks the vertical (red) and horizontal (white) size to about $1.0\,\mathrm{mm}$ and $1.6\,\mathrm{mm}$, respectively. A tilt of the electron beam with respect to the proton beam allows one to increase and stabilize the beam size of the proton beam. The shown manipulation to $\sigma_x = 4.5\,\mathrm{mm}$ and $\sigma_y = 1.65\,\mathrm{mm}$ increased the lifetime by about $3000\,\mathrm{s}$.

Summing up, by this procedure the COSY beam lifetime could be increased by 50% from $6000\,\mathrm{s}$ to $9000\,\mathrm{s}$, which was a main result of these investigations. For spin-filtering experiments at COSY the optimization of the electron cooling has to include the tilting of the electron beam in order to adjust the proton beam emittance in view of the maximum beam lifetime. A complete understanding of the beam lifetime limitations is still missing and asks for further studies.

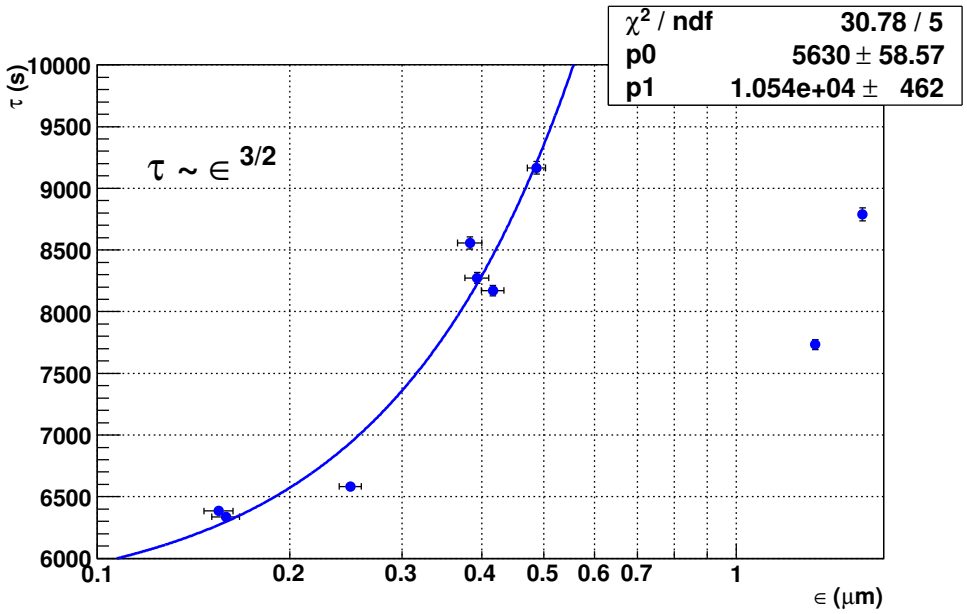

Fig. 4.9.: The beam lifetime increases with increasing beam emittance until an optimum. Following the Touschek formula the resulting curve is fitted with $\tau = p0 + p1 \cdot \epsilon^{\frac{3}{2}}$, which roughly describes the measurement.

4.5. Machine Acceptance and Beam Size

As already discussed in Sec. 2.1.1, the acceptance of a storage ring, which is determined by ion optics and the size of the vacuum enclosure, is preferred to be as large as possible to minimize beam losses. The dominating beam loss mechanism arises from single Coulomb scattering from atoms in the target or the imperfect ring vacuum. The machine acceptance and acceptance angle are given by

$$A = \left(\frac{d^2}{\beta}\right)_{\min}, \qquad \Theta_{x,y} = \sqrt{\frac{A_{x,y}}{\beta_{x,y}}}, \tag{4.8}$$

where the dispersion is assumed to be zero. A measurement of the machine acceptance allows one to evaluate different optics settings and to detect possible sources of beam loss. For small beam emittance ϵ and small acceptance angle Θ_{acc}, the beam lifetime is in proportion to the acceptance A according to Eqs. (2.19) and (2.20). A relatively fast measurement of A uses pulsed magnets, so-called kickers. In addition, a precise determination of the acceptance angle exactly at the position of the forthcoming measurements is important because it plays a crucial role in the interpretation of the observed polarization buildup (see Sec. 2.3.1). A movable frame system (Sec. 3.1.4) developed in particular for these measurements and installed in the target chamber was utilized for the determination of the acceptance angle, the beam position, and the beam width at the position of the target [110].

4.5.1. Kicker Measurement for Different Ion Optics

The geometrical magnitude of the machine acceptance excluding possible dynamic effects can be determined using the kicker magnet (described in Sec. 3.1.4). It enables a fast comparison of different machine settings in view of the machine acceptance. The circulating stored beam gets kicked under a certain angle by applying a magnetic field. The kick angle, at which the complete beam gets lost, together with the local betatron function yields the machine acceptance. This measurement was accomplished for various settings. At COSY only a horizontal kicker magnet is available.
The following analysis of this technique concentrates on the comparison of the acceptance with and without powered PAX quadrupoles. The results of the kicker measurements are displayed in Fig. 4.10. The fractional beam intensity is plotted versus the acceptance, where the acceptance is calculated using the applied kick angle and $\beta_x = 5.586\,\text{m}$ at the location of the kicker,

$$A_x = \beta_x \cdot \Theta_{\text{acc}}^2 = \beta_x \cdot \left(\int Bds\right)^2. \tag{4.9}$$

The beam was kicked twice and the ratio of the beam current before and after the kick was recorded. A fit to the data allows one to extract the angle at which the beam gets lost, which already defines the machine acceptance. The resulting machine acceptances are

$$A_x = 91.94\,\mu\text{m} \tag{4.10}$$

without PAX optics and

$$A_x = 86.74\,\mu\text{m} \tag{4.11}$$

with PAX optics. Consequently the horizontal acceptance drops by $\approx 5.7\,\%$ if the PAX low-β section is switched on. An observation of the lifetime with PAX optics switched on and off at the time of the acceptance measurement showed a reduction in the lifetime of about

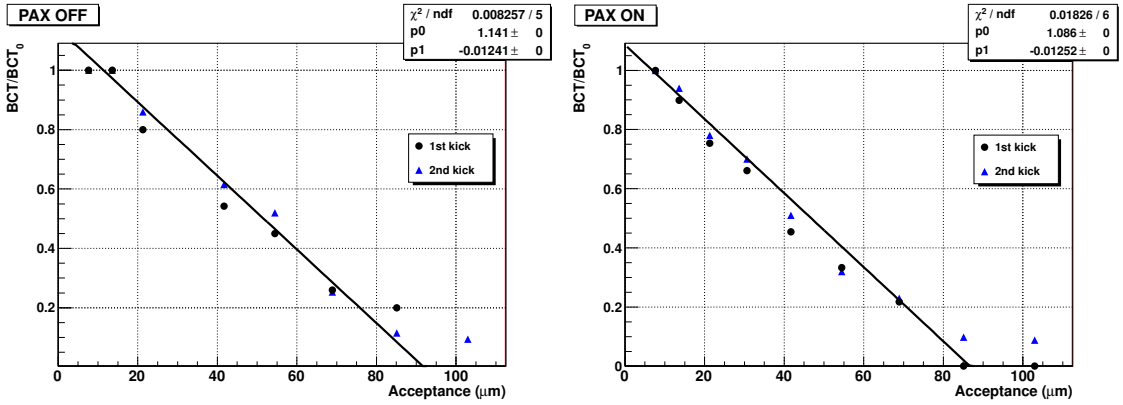

Fig. 4.10.: The kick angle, applied by the fast kicker magnets, plotted against the acceptance. The angle at which the intensity reduces to zero defines the machine acceptance. The measurement was carried out with a cooled proton beam at injection energy without (left) and with (right) powered PAX magnets.

40% ($7500\,\mathrm{s} \rightarrow 4500\,\mathrm{s}$) when the PAX magnets are on. Since the restriction of the horizontal acceptance due to the PAX optics can not explain this change of the lifetime, other effects have to be considered. At first, the vertical machine acceptance can change as well due to the low-β optics. This is unfortunately not detectable with the available kicker system. Nevertheless, an observation of the beam positions in vertical direction shows only small deviations ($\approx 2 - 3\,\mathrm{mm}$) from the reference orbit, which makes additional beam losses due to a restriction of the vertical acceptance less probable. Another explanation of the beam losses are possible dynamic effects, which are not detectable by the kicker measurement either. For example, a shift of the beam at the interaction region with the electron beam of the electron cooler can significantly decrease the beam lifetime due to a worse cooling performance without changing the geometrical acceptance. In addition, switching on the PAX quadrupoles changes the betatron tune. As described in Sec. 4.2, the beam lifetime is very sensitive to the choice of the working point. Consequently, the magnet settings of COSY have to be readjusted to the tunes (Q_x, Q_y) after switching on the PAX magnets.
Summing up, the kicker measurement allows one to compare different optic settings at COSY in view of the horizontal acceptance. As it turns out, this alone does not afford a direct conclusion on the beam lifetime, since it neglects dynamical effects and changes of the betatron tune.

4.5.2. Acceptance Angle and Beam Position at the PAX Target Place

Using a storage cell target of $10\,\mathrm{mm} \times 10\,\mathrm{mm}$ and $400\,\mathrm{mm}$ length requires an accurate orientation of the proton beam along the cell in order to avoid a limitation of the machine acceptance or even a destructive contact. In addition, it is foreseen to install an aperture at the entrance and exit of the target chamber that limits the target gas flow into the adjacent sections, where the betatron functions are large (see Fig. 4.2, right panel). Thus the acceptance angle and the beam positions along s have to be studied and optimized carefully.
Equation (4.8) states that an object, placed at a horizontal distance of less than d from the equilibrium orbit, will lower the machine acceptance causing a decrease of the beam lifetime [144]. This fact is utilized in the determination of the acceptance angle at the target place by moving the system of the three rectangular frames (Fig. 3.5) into the machine acceptance and observing the resulting lifetime. The arrangement allows one to measure at three positions along the beam direction, namely at the entrance of the storage cell ($-0.2\,\mathrm{m}$), at

the center (0 m), and at the exit (+0.2 m). Using all four edges of the three frames in separate measurements allows one to determine as well the horizontal and vertical beam position along the storage cell.

How to Correctly Determine the COSY Machine Acceptance

Preparative to the data analysis, a simulation that concentrates on how to correctly extract the COSY machine acceptance has been accomplished. For this purpose, realistic phase space distributions at the PAX target position based on the calculated Twiss functions (α, β, γ), the measured beam emittances (ϵ_x, ϵ_y), and assumed machine acceptances (A_x, A_y) have to be generated. The correct procedure should return these assumed acceptances. Figure 4.11 (left) displays the generated vertex distribution in horizontal direction assuming a normal distribution with $\sigma_x = \sqrt{\epsilon_x \cdot \beta_x} = 0.355\,\mathrm{mm}$. This value was chosen on the basis of an earlier analysis of the beam width measurement, which was improved in the meantime. However, the result should be independent on the beam width. In combination with the corresponding momentum distribution a phase space ellipse as shown in the right panel of Fig. 4.11 is generated. In conjunction with the accordant vertical phase space the N-particle system can be described at the target position. The input parameters are listed in Tab. 4.2.

Direction	$A(\mu\mathrm{m})$	$\epsilon_{1\sigma}(\mu\mathrm{m})$	$\beta(\mathrm{m})$	$\gamma(\mathrm{m}^{-1})$	$\sigma(\mathrm{mm})$	$\sigma_p(\mathrm{mrad})$
x	20.0	0.229	0.549	1.821	0.355	0.646
y	15.0	0.251	0.376	2.660	0.307	0.817

Table 4.2.: Input parameters for the acceptance angle simulations.

The boundary of a particle in phase space is either defined by the maximum extension of the phase space ellipse (see Fig. 4.12) or an external restriction moved into the acceptance, depending on which of the two is smaller. The developed Monte-Carlo-Simulation now extracts the average acceptance angle by applying positive and negative angle kicks $\delta x'$ and $\delta y'$ to each particle and recognizing for which angle this particle leaves its boundary. One half of the particles is kicked in positive the other half in negative direction. The result of this procedure in the x-plane for a realistic case at COSY without additional restriction is shown on the right-hand side of Fig. 4.12. It is a normal distribution for positive and negative kick angles located at about $|\delta x'| \approx 6\,\mathrm{mrad}$. Averaging $|\delta x'|$ and $|\delta y'|$ over all generated particles

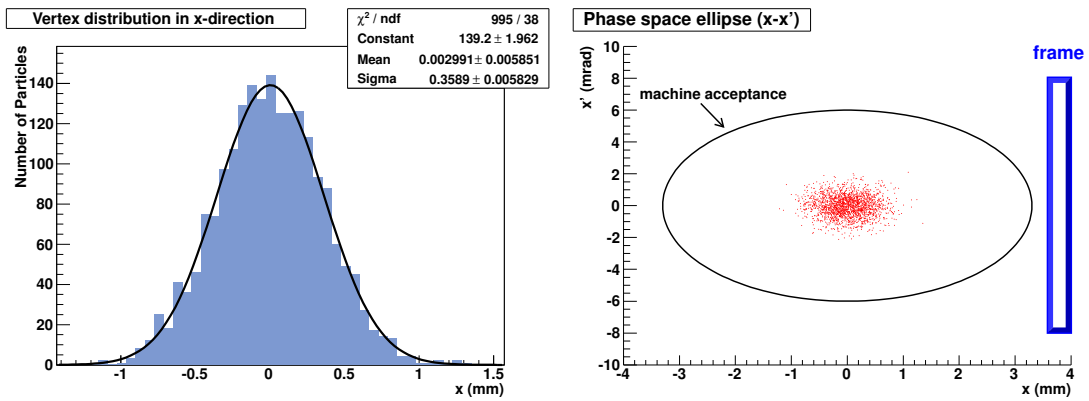

Fig. 4.11.: Left: Generated vertex distribution in horizontal direction for a beam width of $\sigma = 0.359\,\mathrm{mm}$ (2000 events). **Right:** Generated horizontal phase space distribution in the cell center. A realistic machine acceptance at COSY is indicated by the black ellipse. Moving a frame (blue) into the machine acceptance ($x < x_{\max}$) decreases the beam lifetime and allows one to determine A_x and Θ_x.

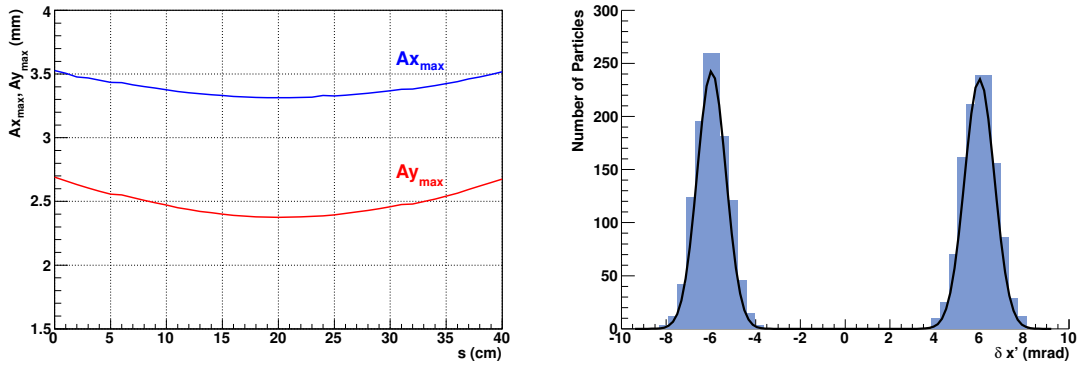

Fig. 4.12.: Left: Horizontal (x) and vertical (y) maximum extension of phase space ellipse along the storage cell. The center of the cell is located at 20 cm. **Right:** Acceptance angle distribution for the simulated realistic case at COSY. One half of the generated particles is kicked in positive direction ($\delta x' > 0$) the other half in negative direction ($\delta x' < 0$) resulting in two peaks with the same $|\delta x'|$.

and calculating Θ_{acc} for the uncoupled case results in

$$\Theta_{\mathrm{acc}} = \sqrt{\left[\frac{1}{2}\left(\frac{1}{\langle|\delta x'|\rangle^2} + \frac{1}{\langle|\delta y'|\rangle^2}\right)\right]^{-1}} = (6.19 \pm 0.53)\,\mathrm{mrad}. \tag{4.12}$$

In order to generate a plot of the lifetime as a function of the frame position, which will be measured during the experiment, an additional restriction has to be implemented. Moving this restriction (frame) into the acceptance reduces the maximum allowed x and leads to a smaller beam lifetime. Since the simulation is foreseen to qualitatively characterize the behavior of τ as a function of the frame position, only single Coulomb scattering is considered.

Disregarding the constant factors (see Eq. (2.19)), the beam lifetime is calculated as

$$\tau \sim \Theta^2. \tag{4.13}$$

To ensure that the analysis works properly, the simulations have been carried out for three different beam emittances (see Fig. 4.13) and at two different positions along the target (cell center and cell entrance). The resulting machine acceptance should be independent of ϵ and s. As depicted in Fig. 4.13 the lifetime remains stable until the frame cuts into the machine acceptance. At this edge of the distribution a slight dependence on the beam emittance can be observed. The smaller the beam emittance the sharper the edge. This can be explained using the right panel of Fig. 4.12. A larger beam emittance causes a wider acceptance angle distribution, which means that some particles get already lost at smaller angles. In case of a small emittance the distribution is more narrow such that first losses occur at larger angles, but the decay is faster. The average acceptance angle should nevertheless remain constant.

An analytic formula that describes the beam lifetime τ as a function of the frame position x can be deduced using the beam lifetime due to single Coulomb scattering

$$\tau \approx \tau_{\mathrm{C}} = \frac{1}{\Delta\sigma_{\mathrm{C}} d_{\mathrm{t}} f} = \frac{\beta^4\gamma^2\Theta_{\mathrm{acc}}^2}{4\pi Z_{\mathrm{gas}}^2 Z_i^2 r_i^2 \cdot d_{\mathrm{t}} \cdot f} \approx \Theta_{\mathrm{acc}}^2, \tag{4.14}$$

assuming a constant effective target density and stable machine settings. The acceptance angle is given as

$$\Theta_{\mathrm{acc}}^2 = \left[\frac{1}{2\Theta_x^2} + \frac{1}{2\Theta_y^2}\right]^{-1} \qquad \text{with} \qquad \Theta_{x,y}^2 = \frac{A_{x,y}}{\beta_{x,y}}. \tag{4.15}$$

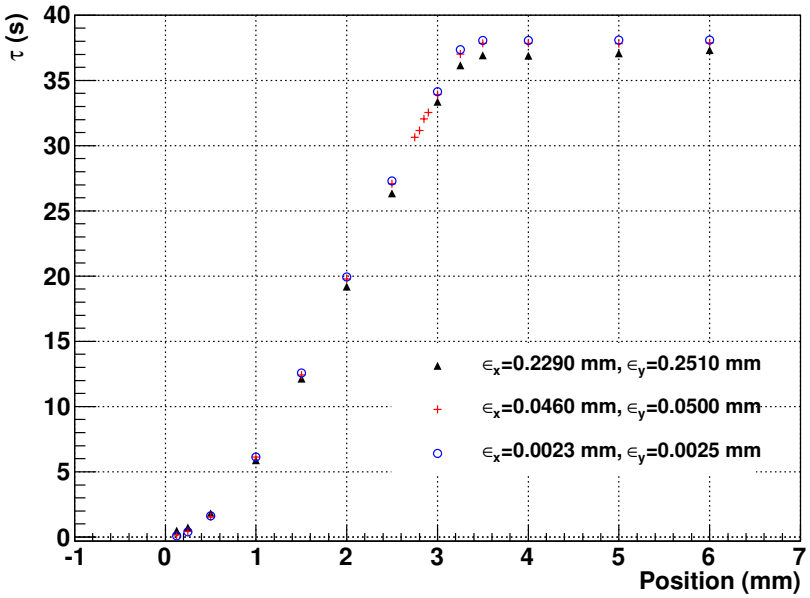

Fig. 4.13.: Behavior of the beam lifetime as a function of the frame position for three different beam emittances ($\epsilon_{x,y}$). At about $3.5\,\mathrm{mm}$, the frame cuts into the machine acceptance which leads to the observation of shorter beam lifetimes.

Thus it follows

$$\tau \approx \left(\frac{\beta_x}{2A_x} + \frac{\beta_y}{2A_y} \right)^{-1}. \tag{4.16}$$

In the following, the acceptance angle determination in x-direction is discussed exemplary. Thus A_y is assumed to be constant whereas A_x changes due to the movement of the frame in x-direction. Inserting A_x as given in Eq. (2.10) results in

$$\tau(x) \approx 2 \cdot \left(\frac{\beta_x^2}{x^2} + \frac{\beta_y}{A_y} \right)^{-1}. \tag{4.17}$$

This equation already implies that a measurement of the acceptance in x-direction additionally allows one to extract A_y from the fit. As one can see in Fig. 4.14, the fit function $\tau(x)$ is well in accordance with the simulated data. Furthermore, it is visible that the simulated beam lifetime remains constant at some point, whereas the calculation shows a further increase. This is because the simulation does not consider the restriction due to the machine but only due to the frame. Thus the intersection point of the two fit functions (blue and red in Fig. 4.14) defines x which is used to derive the machine acceptances. The extraction of the acceptance uses

$$A_{x,y} = \frac{(x,y)^2}{\beta_{x,y}}. \tag{4.18}$$

The results of the described simulations for three different emittances and at two positions are displayed in Tab. 4.3. The upper table represents the measurement in x-direction, whereas the lower table shows results for a measurement in y-direction.
The developed procedure of the acceptance determination shows no dependence on the beam emittance and the position along the target. Except for a few points, the results are in good agreement with each other and with the input parameters of $A_x = 20\,\mu\mathrm{m}$ and $A_y = 15\,\mu\mathrm{m}$. As side effect it allows one to determine the acceptance in one direction by the frame movement in perpendicular direction.

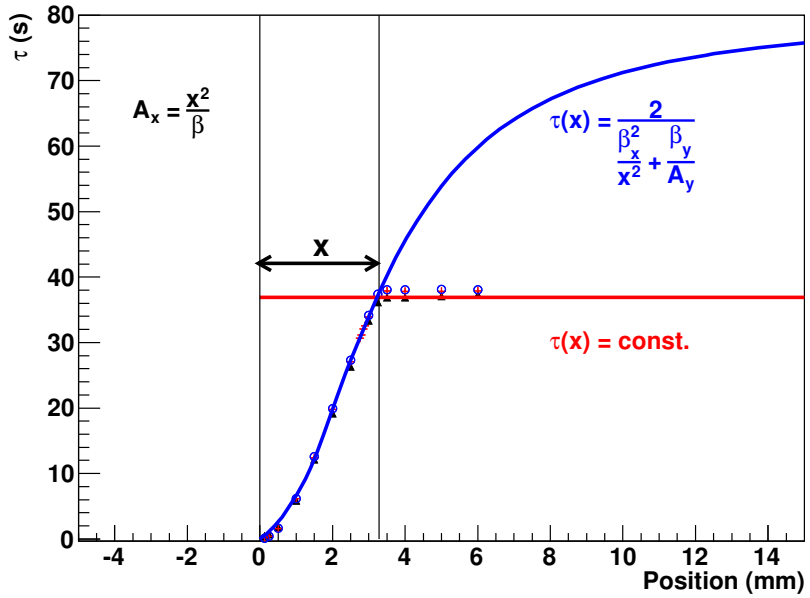

Fig. 4.14.: The half width of free aperture x is defined by the distance between the frame position where the beam lifetime starts to decrease and where it is 0. The edge is given by the intersection of the two fitted curves (blue and red). The fit functions are in good agreement with the simulated data.

Movement in x-direction

Input Parameters		**Output Parameters**			
		Target Center		**Target Entrance**	
$\epsilon_x(\mu m)$	$\epsilon_y(\mu m)$	$A_x(\mu m)$	$A_y(\mu m)$	$A_x(\mu m)$	$A_y(\mu m)$
0.229	0.2514	19.683 ± 0.517	15.850 ± 0.376	19.500 ± 0.695	15.473 ± 0.475
0.046	0.050	19.859 ± 0.260	15.162 ± 0.148	18.182 ± 0.499	15.164 ± 0.366
$2.29 \cdot 10^{-3}$	$2.51 \cdot 10^{-3}$	19.880 ± 0.264	15.005 ± 0.083	19.399 ± 0.172	15.015 ± 0.104

Movement in y-direction

Input Parameters		**Output Parameters**			
		Target Center		**Target Entrance**	
$\epsilon_x(\mu m)$	$\epsilon_y(\mu m)$	$A_x(\mu m)$	$A_y(\mu m)$	$A_x(\mu m)$	$A_y(\mu m)$
0.229	0.2514	21.266 ± 0.096	15.091 ± 0.198	22.467 ± 0.176	14.323 ± 0.121
0.046	0.050	20.820 ± 0.063	14.937 ± 0.067	20.613 ± 0.104	14.542 ± 0.088
$2.29 \cdot 10^{-3}$	$2.51 \cdot 10^{-3}$	20.184 ± 0.085	15.028 ± 0.010	20.193 ± 0.014	14.607 ± 0.013

Table 4.3.: Results of the acceptance determination from simulated events for 3 different emittances and at 2 different positions. The upper table shows the results of the movement in x-direction whereas the lower one comprises the results for a movement in y-direction. The input machine acceptances are $A_x = 20\,\mu m$ and $A_y = 15\,\mu m$.

Acceptance Measurement

The acceptance measurement by the help of the movable frame system was accomplished for all four edges of the three frames. In addition, one measurement was carried out with the ANKE cluster target switched on during the measurement. Thus, a substantial dataset enables a precise determination of the machine acceptance and the acceptance angle in horizontal and vertical direction and of the total acceptance angle Θ_{acc}. The beam intensity was in the range of $7.5 - 10 \cdot 10^9$ circulating unpolarized cooled protons at injection energy. The PAX optics was switched on and the initial beam lifetime was around $2500\,\mathrm{s}$. During the measurement, which took about two days, the lifetime increased up to $4000\,\mathrm{s}$ due to the vacuum improvement after the installation of the frame system. This change of the lifetime is neglected in the analysis, since the change during one of the twelve separate measurements was small. During every injection the frame was centered on the beam to avoid a restriction of the acceptance. After injection and cooling, the frame was moved in horizontal (vertical) direction and the resulting lifetime was measured. This procedure was repeated for each frame position. An example plot of the measurement with frame 1, which is located at the target center, is displayed in Fig. 4.15. The beam lifetime is plotted as a function of the horizontal (left) and vertical (right) displacement of the frame. As one can see, the edges of the $x-$measurement are smoother than those in $y-$direction, which leads to larger errors for the fit. This behavior is caused by a non-Gaussian particle distribution within the beam. The uncertainties of τ have been scaled by a factor to yield a reduced χ^2 of approximately unity. Half of the width of the plateau subtracted from the half width of the frame ($w_x \approx 25\,\mathrm{mm}$, $w_y \approx 20\,\mathrm{mm}$), which has been precisely determined for each frame, results in x (y). Using Eq. (4.15) and (4.18) gives the results for A_x, A_y, Θ_x, Θ_y and Θ_{acc} as listed in Tab. 4.4.

Frame	Pos (m)	$A_x(\mu\mathrm{m})$	$A_y(\mu\mathrm{m})$	$\Theta_x(\mathrm{mrad})$	$\Theta_y(\mathrm{mrad})$	$\Theta_{\mathrm{acc}}(\mathrm{mrad})$
1	0.0	26.70 ± 3.02	12.48 ± 1.71	6.97 ± 0.53	5.76 ± 0.49	6.28 ± 0.37
2	-0.2	24.21 ± 2.74	16.62 ± 2.06	6.24 ± 0.47	5.87 ± 0.47	6.05 ± 0.33
3	0.2	22.93 ± 2.54	19.55 ± 2.27	6.09 ± 0.45	6.40 ± 0.49	6.24 ± 0.33
1 (tgt)	0.0	21.53 ± 2.32	12.33 ± 1.47	6.26 ± 0.46	5.73 ± 0.45	5.98 ± 0.32
Average		23.49 ± 1.31	14.33 ± 0.90	6.35 ± 0.24	5.93 ± 0.24	6.13 ± 0.17

Table 4.4.: Results of the acceptance determination with the movable frame system.

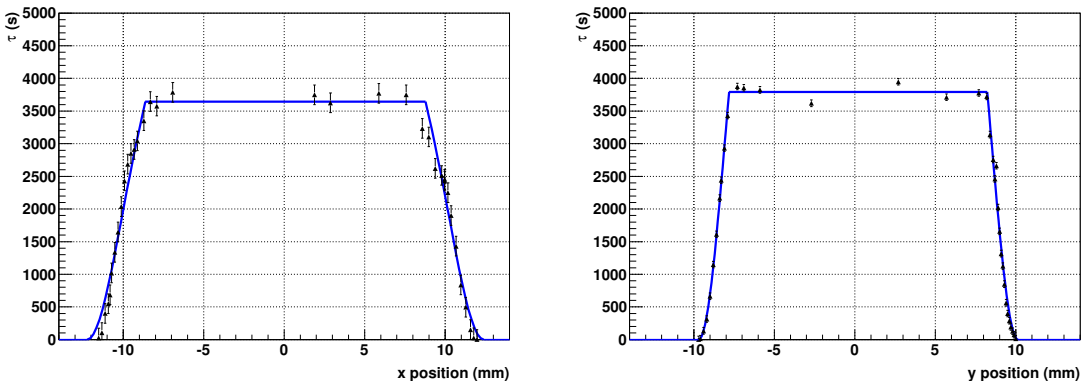

Fig. 4.15.: Frame scan and fit at the center of the PAX target place (frame 1) in x- (left) and y-direction (right).

Thus the total acceptance angle at the target position was determined as

$$\Theta_{\mathrm{acc}} = (6.13 \pm 0.17)\,\mathrm{mrad}, \tag{4.19}$$

which is in good agreement with the predictions. The developed procedure makes it possible to precisely determine the acceptance angle, which is crucial for the understanding of the polarization buildup. Thus it has to be carried out for the present optics prior to the spin-filtering experiment.

The center of a trapezoid from a frame scan is a measure of the center of the beam. Consequently, the beam positions and inclination along the target are detectable. The results are displayed in Tab. 4.5 and Fig. 4.16. In x-direction a kink is visible. This behavior is difficult to explain since the PAX target region is a drift region without any forces on the beam, as long as the holding field is switched off. The observed behavior in y-direction is similar. Here an inclination of about $1\,\mathrm{mm}$ over the length of the storage cell of $0.4\,\mathrm{m}$ was detected. The only reasonable explanation of the kink in the orbit is a deformation of the phase space ellipse and consequently a shift of the center of gravity of the ellipse, while the ellipse rotates. The position measurement with cluster target switched on indicates a large displacement in y-direction.
The position measurement with the frame system enables an improvement of the beam trajectory by the help of correction magnets and consequently makes it possible to avoid a restriction due to the storage cell and the flow limiters installed at the entrance and the exit of the target chamber. Finally $2 \cdot 10^{10}$ protons could be injected and stored through a tube of $10\,\mathrm{mm}$ diameter and $400\,\mathrm{mm}$ length.

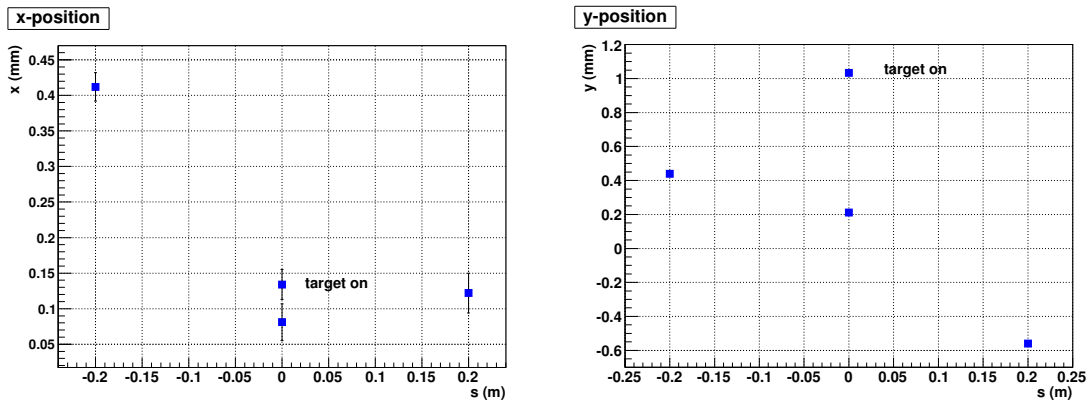

Fig. 4.16.: Horizontal (left) and vertical (right) beam positions along the target region. At the center of the target an additional measurement with cluster target switched on was carried out. The determined beam position with cluster target shows a large deviation of $0.8\,\mathrm{mm}$ compared to the measurement without target.

Frame	$x(\mathrm{mm})$	$y(\mathrm{mm})$
1 (target off)	0.081 ± 0.026	0.212 ± 0.012
2 (target off)	0.412 ± 0.020	0.439 ± 0.008
3 (target off)	0.122 ± 0.028	-0.560 ± 0.010
1 (target on)	0.134 ± 0.021	1.034 ± 0.006

Table 4.5.: Beam positions along the target region.

4.5.3. Measurement of the Beam Width at the Target Position

A measurement of the beam width at the center of the low-β section, i.e., the PAX target position was carried out by the help of the frame system as well. For this purpose the frame has to be moved through the proton beam in one action. The resulting intensity dependence is recorded with the BCT (see Sec. 3.1.4). Assuming no coupling in the machine, a properly aligned scraper moving along $x(y)$ direction will only remove particles from the x-x' (y-y') phase space with betatron amplitudes larger than the distance from the beam center to the scraper edge. This fact together with the assumption that the cooled and stored beam exhibits a two dimensional Gaussian distribution in transverse phase space, which yields a density distribution of the betatron amplitude ρ_β in the x-x' plane of [145]

$$\rho_\beta(x) = \frac{I_0}{\sigma_x^2} \cdot x \cdot \exp\left(-\frac{x^2}{2\sigma_x^2}\right), \tag{4.20}$$

allows one to write the inverted beam intensity as a function of the frame position [110]

$$I(x) = \int_0^{x-\mu_x} \rho_\beta(x) \cdot dx = I_0 \left[1 - \exp\left(-\frac{(x-\mu_x)^2}{2\sigma_x^2}\right)\right]. \tag{4.21}$$

Here I_0 is the beam intensity with the frame in nominal position, μ_x is the beam center, and σ_x the beam width in x-direction. This function is fitted to the beam intensity distribution in order to determine $\sigma_{x,y}$. The measurement was carried out with all three frames. In horizontal direction it was realized twice by moving the frames in positive and negative direction, whereas the measurement of the vertical beam size was only feasible by moving the frame upward. In case of the downward movement the beam was not fully destroyed.
An example plot of the BCT signal over time during the frame movement is depicted in Fig. 4.17. Fitting the curve yields a beam width σ in units of time. In order to transform this number into a beam width, the speed of the frame movement has to be inserted. This has been determined to

$$v_x = v_y = (1.65 \pm 0.02)\,\mathrm{mm/s}. \tag{4.22}$$

The resulting 1σ beam widths for each measurement are listed in Tab. 4.6. The given errors are those of the fit. An observation of the collected data shows significant distortions of the BCT curve for a few measurements (Fig. 4.18). Possible origins are oscillations of the beam or the frame system and a non-Gaussian density distribution within the beam. This is an explanation of deviations between the different measurements, which are nevertheless in rather good agreement with each other. The measured beam widths clarify that the storage cell with a diameter of about $10\,\mathrm{mm}$ should not restrict the cooled COSY beam.
Taking the calculated betatron functions at the PAX-IP (Tab. 4.6) and assuming that the dispersion is zero enables a determination of the beam emittance. The weighted averages yield

$$\epsilon_x = \frac{\sigma_x^2}{\beta_x} = (0.450 \pm 0.002)\,\mu\mathrm{m} \qquad \text{and} \qquad \epsilon_y = \frac{\sigma_y^2}{\beta_y} = (0.778 \pm 0.006)\,\mu\mathrm{m}. \tag{4.23}$$

Thus, the total beam emittance is

$$\epsilon = \sqrt{\epsilon_x^2 + \epsilon_y^2} = (0.899 \pm 0.006)\,\mu\mathrm{m}. \tag{4.24}$$

For a comparison of the determined values, a measurement of the beam widths using the ionization profile monitor (Sec. 3.1.4) was accomplished. Taking the betatron functions at the position of the IPM ($\beta_x = 16.61\,\mathrm{m}$, $\beta_y = 7.30\,\mathrm{m}$) yields the beam emittances

$$\epsilon_x^{\mathrm{IPM}} = 0.518\,\mu\mathrm{m} \qquad \text{and} \qquad \epsilon_y^{\mathrm{IPM}} = 0.824\,\mu\mathrm{m}. \tag{4.25}$$

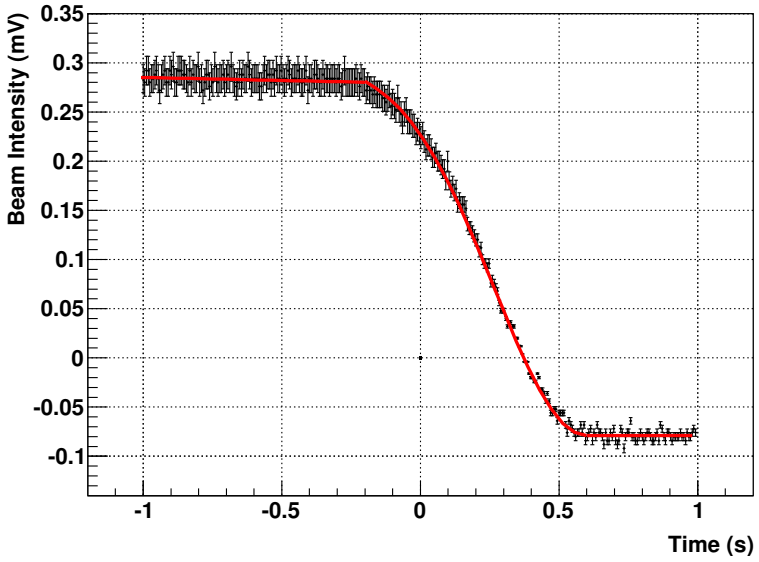

Fig. 4.17.: Measurement of the beam width using the movable frame system.

Thus the total emittance (from Eq. (4.24)) is $\epsilon = 0.973\,\mu\mathrm{m}$.
Given the fact, that the errors of the frame measurement are optimistic values and that the ion distribution at the IPM shows not always a Gaussian distribution, the measured emittance with the frame system and the ionization profile monitor are comparable with each other.

4.6. Target Related Issues

The performance of the polarized gas target is essential for the spin-filtering experiment in view of the achievable polarization and the remaining intensity after filtering. After the installation of the polarized internal target in 2010 consisting of the target chamber, the ABS, the BRP, the storage cell, and the holding field coil system (Sec. 3.2) a first commissioning at the position of the later experiment was carried out. This includes the commissioning

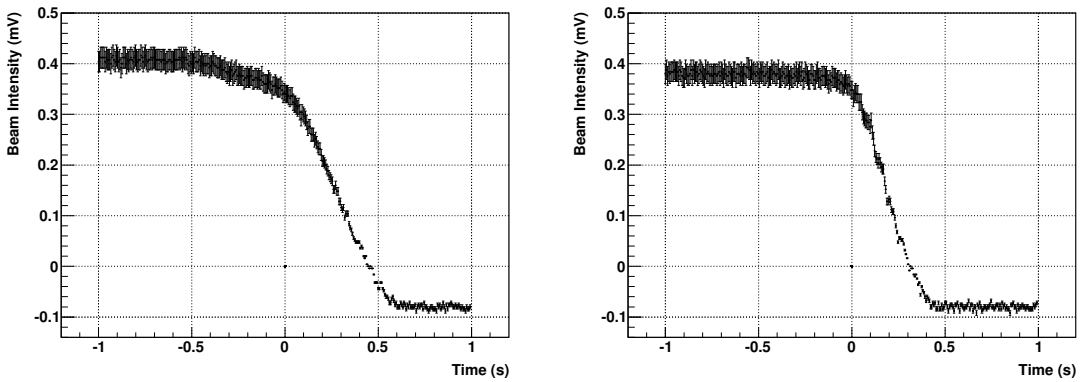

Fig. 4.18.: The BCT curves of the fast frame scans show distortions in a few cases. The left plot displays the measurement in $y-$direction for frame 1, which has a bump at the upper edge and the right plot is the fast scan using frame 3, which shows small oscillations.

Frame	$\sigma_{+x}(\mathrm{mm})$	$\sigma_{-x}(\mathrm{mm})$	$\sigma_{+y}(\mathrm{mm})$	$\beta_x(m)$	$\beta_y(m)$
1	0.549 ± 0.004	0.589 ± 0.009	0.593 ± 0.002	0.549	0.376
2	0.533 ± 0.001	0.513 ± 0.002	0.544 ± 0.004	0.622	0.482
3	0.554 ± 0.010	0.571 ± 0.010	0.521 ± 0.018	0.622	0.482

Table 4.6.: Measured beam widths along the target region and calculated betatron functions.

of the holding field system and the newly developed openable storage cell, as well as the measurement of the achieved target density, provided by the ABS in combination with the storage cell. Since a flux of $\Phi^{ABS} \approx 3.3 \cdot 10^{16}\,\mathrm{atoms/s}$ from the ABS into the target chamber for one hyperfine state is expected, a dedicated pumping system is foreseen to avoid significant beam losses due to target background. A study on the lifetime contributions of the target using different pumping equipment allows one to design an adequate pumping system for the target chamber.

4.6.1. Holding Field Commissioning

The holding field system, explained in Sec. 3.2.5, allows one to fix and to switch the orientation of the target polarization. For this purpose it is possible to power the holding field coils in different ways, in order to enable transverse (x, y) or longitudinal (s) target polarization. Due to time constraints prior to the commissioning beam time, the cabling of the system only allowed to switch on the magnetic field in x-direction (B_x) without compensation and in y-direction (B_y) with compensation. A measurement of B_y in the center of the target chamber using a Hall probe yielded $10.8\,\mathrm{gauss} = 1.08\,\mathrm{mT}$ ($y \downarrow$) and $11.0\,\mathrm{gauss} = 1.1\,\mathrm{mT}$ ($y \uparrow$). This is in very good agreement with the expected field of about $1.0 - 1.1\,\mathrm{mT}$ (see Fig. 3.18) even without considering the rough positioning of the Hall probe.
In order to quantify how good the calculations of the magnetic fields fit to the existing setup and to show that the magnetic field flips as expected, a measurement of the beam position and its change in the center of the target chamber is appropriate. These investigations would also be possible with the planned PAX detector system, which is presently under development. Therewith one could easily measure the change of asymmetries in double polarized pp scattering due to a flip of the target polarization. Also the shift of the beam position would be measurable by vertex reconstruction [126].
Integrating the vertical magnetic field B_y along s yields the deflection angle Θ, as displayed for both polarities in the left panel of Fig. 4.19. According to the Lorentz force $F_x = q(v_s \times B_y)$ the beam is deflected in horizontal (x) direction (Fig. 4.19 right panel). Because of the compensation of the holding field by the compensation coils the beam deflection at the exit of the target chamber should be zero. The maximal displacement of the beam of $\pm 0.143\,\mathrm{mm}$ (depending on the direction of B_y) is reached at the center of the target. Thus, a measurement of the beam position at the target center using the movable frame system allows one to cross-check the strength of B_y. The measured displacements for both polarities of B_y yield

$$\begin{aligned} B_y \uparrow: &\qquad x_\uparrow = (0.381 \pm 0.030)\,\mathrm{mm}, \\ B_y \downarrow: &\qquad x_\downarrow = (0.052 \pm 0.029)\,\mathrm{mm}. \end{aligned} \tag{4.26}$$

The resulting shift of the beam between both holding field polarities is $\Delta x = x_\uparrow - x_\downarrow = (0.329 \pm 0.0417)\,\mathrm{mm}$. Since this is in good agreement with the expectations ($0.286\,\mathrm{mm}$) it confirms that the magnetic holding field system achieves the required $1\,\mathrm{mT}$. Thinking about the direction of the beam deflection one has to keep in mind, that the first deflection is caused by the compensation coils, which deflect the beam in opposite direction to the holding field

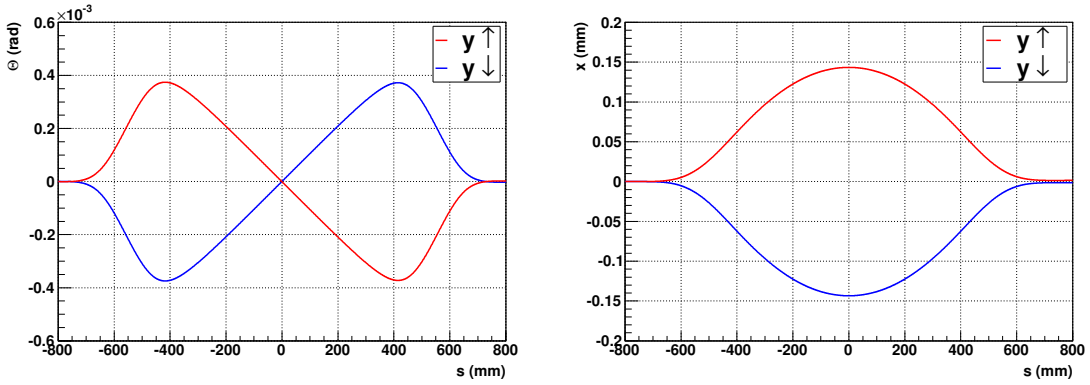

Fig. 4.19.: Deflection angle and deflection in x-direction due to B_y for both holding field polarities ($y\uparrow$: red, $y\downarrow$: blue).

coils. In addition to this, no noticeable changes of the beam positions along COSY were detectable with the BPMs. Thus the target holding field was fully compensated.
Also important to mention is, that the lifetime did not change due to switching of the holding field by the up- and downstream compensation coils. Since the magnetic field in horizontal direction could not be compensated at the time of the investigations, a measurement of the resulting orbit change in the vertical direction along COSY was accomplished by the help of the BPMs and compared to calculations. For the MAD calculations of the orbit deviations an angle kick of $1.8\,\mathrm{mrad}$ at the cell center was assumed. The measured displacements range from $+1.8\,\mathrm{mm}$ to $-2.5\,\mathrm{mm}$ which perfectly follows the calculations, as displayed in Fig. 4.20. Thus, the target holding field system works as expected.

Prior to the spin-filtering experiment the cabling of the holding field coil system has been finalized.

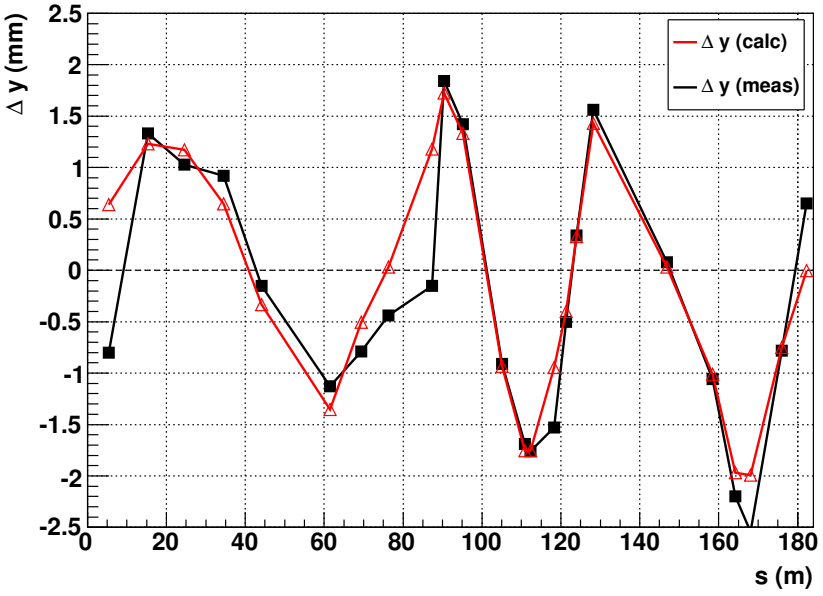

Fig. 4.20.: The plot shows the change of the beam orbit in vertical direction due to the uncompensated holding field in x-direction with respect to the reference orbit without holding field. The red curve displays the calculated displacements assuming an angle kick of $1.8\,\mathrm{mrad}$ at the center of the target and the black curve are the measured values.

4.6.2. Openable Storage Cell Commissioning and Target Density Measurement

The openable storage cell was installed into the PAX target chamber after the completion of all measurements that required the frame system. Since the correct opening and closing was already tested in the laboratory, the main issue was to commission the cell under experiment conditions. This includes a check of the alignment along the beam axis, the proper connection of the feeding tubes to the ABS and the BRP, and a measurement of the achieved target density.
Prior to the installation at COSY the cell position and the alignment with respect to the vacuum flange has been precisely measured with a dedicated measuring device. A proper alignment of the $400\,\mathrm{mm}$ long storage cell along the beam axis basically means that the beam and its lifetime should not be affected by the cell, especially when the cell is closed. For this test the beam was injected and cooled with opened cell. A slow manual closing of the cell showed no detectable change of the beam lifetime. Further tests, where the cell was opened and closed automatically, also showed no influence on the beam lifetime (Fig. 4.21).

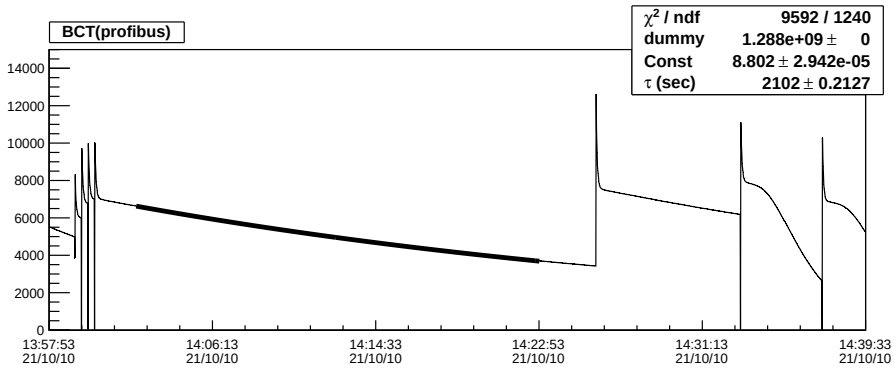

Fig. 4.21.: Closing the storage cell in the middle of the shown cycle did not affect the beam lifetime ($\tau = 2102\,\mathrm{s}$).

Switching the atomic beam source on with the cell in open position immediately decreased the lifetime from $2100\,\mathrm{s}$ to about $1200\,\mathrm{s}$. Hence the ABS injected an atomic beam into the target chamber. In order to quantify the target density, a dedicated measurement using the Schottky method was carried out. This method is based on the energy loss of the coasting beam due to the interaction with the target atoms, as described in Sec. 2.1.2. The shift of the revolution frequency is a measure of the target density (see Eq.(2.17)). How the measurement in detail works, can be described by the help of Fig. 4.22. From top to bottom the BCT signal, the H^0 signal and the revolution frequency are plotted as a function of the time. Shown is one cycle of about $10\,\mathrm{min}$ duration with electron cooling switched on (start at $12:54$) and one short cycle where the electron cooler is switched off after $30\,\mathrm{s}$ (start at $13:04$). As one can see, the BCT signal in the second cycle drops very fast in comparison to the cycle with electron cooling. The H^0 signal in the second panel in principle monitors the working state of the electron cooler. As long as the cooler is switched on, a small fraction of the protons and the electrons recombine to neutral H^0 atoms which are detected by a H^0 monitor (see Sec. 3.1.4). Consequently, the H^0 signal characterizes the performance of the electron cooler. And finally, the revolution frequency is displayed in the lower panel. During the long cycle with electron cooling no significant frequency shift Δf is visible because the cooling compensates the energy losses. In the second cycle f immediately starts to decrease after switching of the electron cooler. A fit to the decreasing slope yields the $\Delta f/\Delta t$, which can then be inserted into Eq. (2.17) in order to calculate d_t.

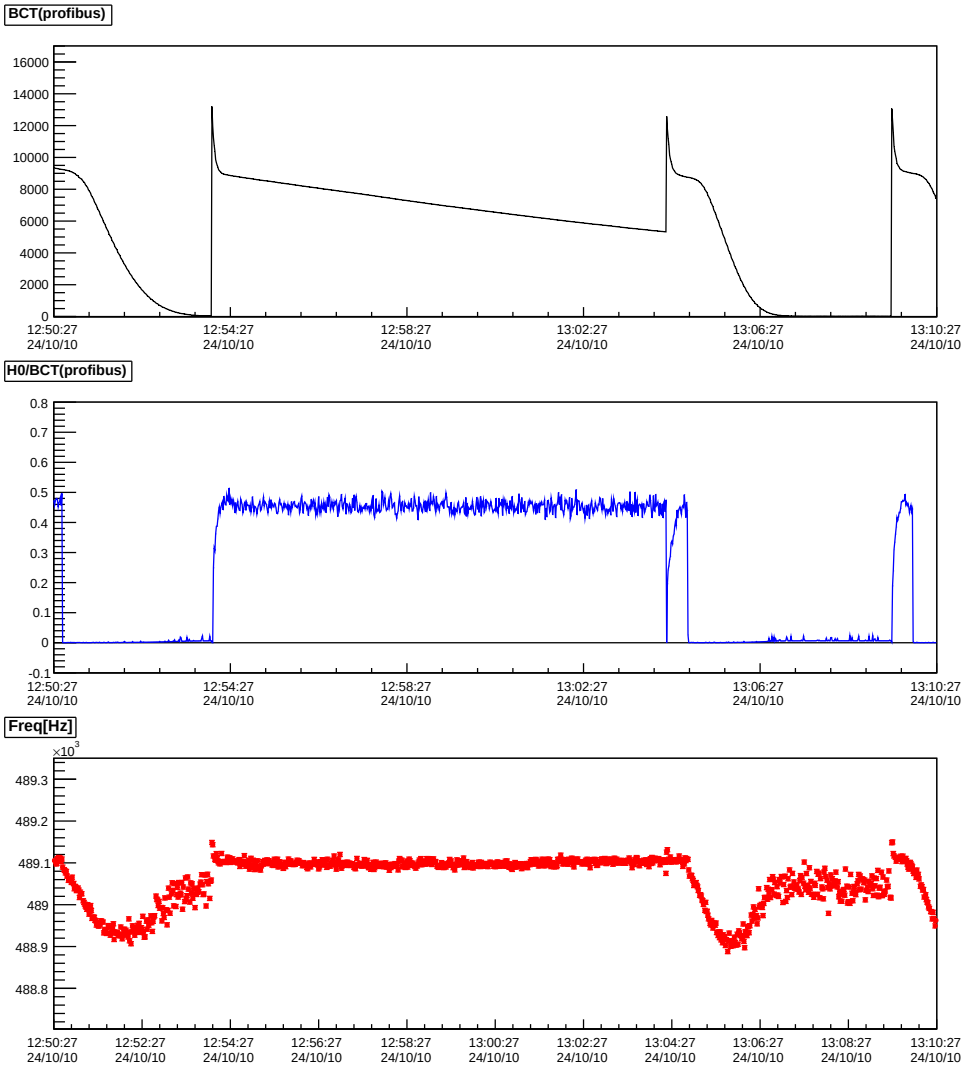

Fig. 4.22.: Online analysis window. In the upper panel the beam current is shown. The middle panel monitors the H^0 rate. In the lower panel, the revolution frequency of the beam, which has been measured using a Schottky pickup, is shown. Using this tool, the change of the revolution frequency when the electron cooler is switched off, can be observed, and therefore the target density can be calculated.

Closing the cell for the first time with atomic beam source switched on, showed no relevant change of the lifetime or the frequency shift. Thus it did not increase the target density. Dismounting and examination showed, that the cell did not close perfectly and therefore had to be adjusted mechanically. After reassembly the movement worked and enabled a determination of the target density. At first the frequency shift was measured without atomic beam, in order to quantify the effect of the residual gas inside COSY. The measured frequency shift corresponds to a density of the residual gas $d_{\mathrm{t}}^{\mathrm{residual}} = (2.2 \pm 0.3) \cdot 10^{12}\,\mathrm{atoms/cm^2}$. The target density determination uses Δf with ABS switched on for the storage cell in open and closed position. The frequency shift for the open cell is used for an approximation of the target background and thus has to be subtracted from the shift with closed cell. The determined values are listed in Tab. 4.7.
Due to further mechanical problems the cell was fixed in closed position afterwards and the measurement was repeated. At that time the background could be estimated using an additional gas inlet system by injecting hydrogen directly into the target chamber (not into the

cell), until the pressure reaches the same value as with ABS switched on ($p = 2.5 \cdot 10^{-7}\,\mathrm{mbar}$). For the injection of one hyperfine state a density of $d_\mathrm{t} = (2.09 \pm 0.07) \cdot 10^{13}\,\mathrm{atoms/cm^2}$ was measured in case of the openable cell and $d_\mathrm{t} = (2.52 \pm 0.09) \cdot 10^{13}\,\mathrm{atoms/cm^2}$ after fixing the cell in closed position. The increase of about $20\,\%$ is an indication that the cell did not close completely during the first measurement.
An estimation of the expected target density at COSY that uses the actual storage cell dimensions including the ABS feeding tube, the cell tube, and the extraction tube to the BRP, can be found in App. E. Using a recently measured flux of $\Phi = (3.05 \pm 0.15) \cdot 10^{16}\,\mathrm{atoms/s}$ coming from the ABS for the injection of one hyperfine state [146] the expected target density is $d_\mathrm{t} = (4.1 \pm 0.2) \cdot 10^{13}\,\mathrm{atoms/cm^2}$. Since this is $60\,\%$ larger than the measured value a specific checkup of the target became necessary. This was done after a mechanical upgrade of the cell during a shutdown period in May 2011. An additionally installed capacitive baratron gauge enables a measurement of the pressure directly in the center of the cell and confirms that the ABS delivers the full intensity and that the openable storage cell is leak tight [146]. The determined pressure is equivalent to an areal density of $d_\mathrm{t} = (4.35 \pm 0.1) \cdot 10^{13}\,\mathrm{atoms/cm^2}$. Since this is in good agreement with the theoretical value we assume that this target density can be achieved during the spin-filtering experiment. The reason for the reduced density during the beam time was an incomplete closed cell due to forces on the BRP feeding tube. This problem was solved in the meantime.

4.6.3. Lifetime Contributions of the Polarized Target

A fundamental aspect of the accomplished machine studies is the minimization of beam losses in order to achieve reasonably long filtering times. Since scattering of the beam with the residual gas plays a crucial role, the accelerator vacuum has to be as good as possible. On the other hand, a maximal target density is preferred in order to increase the polarization buildup rate. A high flux injected into the cell causes an increase of the background pressure in the target chamber and the adjacent sections. Thus a dedicated pumping system is needed to avoid substantial beam losses. The proper dimensioning of this system requires testing of the components. Therefore, the improvement of the beam lifetime in dependence on different vacuum components was examined. The values of the beam lifetime for different setups are listed in Tab. 4.8. As contributions to the lifetime add up reciprocally, the individual contributions to the total beam lifetime can be calculated. In detail three setups were tested.

Turbomolecular Pump: One turbomolecular pump (see Sec. 3.2.1) with a pumping speed of $1200\,\mathrm{l/s}$ was connected to the target chamber via a gate valve and a tube with a total conductance of about $1200\,\mathrm{l/s}$. Thus, the resulting pumping speed is assumed to be $600\,\mathrm{l/s}$. The individual contributions from COSY, from the background due to the

Target Status	movable		fixed	
	$\Delta f/\Delta t$ (Hz/s)	d_t (atoms/cm^2)	$\Delta f/\Delta t$ (Hz/s)	d_t (atoms/cm^2)
ABS off, cell closed	-0.21 ± 0.03	$(0.22 \pm 0.03) \cdot 10^{13}$		
ABS on, cell closed	-3.83 ± 0.06	$(2.09 \pm 0.07) \cdot 10^{13}$	-2.90 ± 0.08	$(2.52 \pm 0.09) \cdot 10^{13}$
ABS on, cell open	-1.85 ± 0.03		-0.51 ± 0.01	

Table 4.7.: Measurement of the target density utilizing the revolution frequency shift of the beam due to energy loss on the target. Movable means the measurement with working openable cell and fixed stands for the measurement after the cell movement broke and the cell was fixed in closed position.

Target Status	1 Turbo only	+1 NEG	+ Flow Limiters
ABS off, cell closed	2200 s	3200 s	3500 s
ABS on, cell closed	746 s	1273 s	1882 s
ABS on, cell open	767 s		

Table 4.8.: Beam lifetime for three different vacuum setups. The first measurement was carried out using one turbo molecular pump installed at the target chamber, for the second measurement one additional NEG cartridge was activated, and for the third measurement flow limiters of 19 mm diameter were installed in order to minimize gas load into the adjacent sections.

target, and from the target gas in the storage cell can be calculated using the measured numbers.

- Lifetime from the ring: $\tau_{\mathrm{COSY}} = 2200\,\mathrm{s}$.
- Lifetime from the target background: $\tau_{\mathrm{back}} = \left(\frac{1}{767\,\mathrm{s}} - \frac{1}{2200\,\mathrm{s}}\right)^{-1} = 1178\,\mathrm{s}$.
- Lifetime from the target gas in the cell: $\tau_{\mathrm{target}} = \left(\frac{1}{746\,\mathrm{s}} - \frac{1}{2200\,\mathrm{s}} - \frac{1}{1178\,\mathrm{s}}\right)^{-1} = 27246\,\mathrm{s}$.

Consequently, the lifetime is mainly restricted by the background of the target. This is already an evidence that a powerful pumping system around the PAX-IP is required to achieve a total lifetime of at least 3000 s.
A theoretical calculation of the target lifetime using the determined acceptance angle of $\Theta_{\mathrm{acc}} = (6.13 \pm 0.17)\,\mathrm{mrad}$ and the target density of $d_{\mathrm{t}} = (2.09 \pm 0.07) \cdot 10^{13}\,\mathrm{atoms/cm^2}$ yields 106600 s. The calculation takes into account losses due to Single Coulomb scattering and hadronic interaction as described in Sec. 2.1.2 and 2.4

$$\tau = \frac{1}{(\Delta\sigma_{\mathrm{C}} + \sigma_{\mathrm{tot}}) \cdot d_{\mathrm{t}} \cdot f}. \tag{4.27}$$

A cross check of the calculations using the parameters for FILTEX shows a reasonable agreement between theory ($\tau_{\mathrm{target}} = 2113\,\mathrm{s}$) and the observed value of $\tau_{\mathrm{total}} = (1800 \pm 60)\,\mathrm{s}$ [82].
Summing up, the theoretical lifetime due to the target is almost a factor four larger than the measured value. Since we believe in the measurement of the acceptance angle and the target density these parameters should not cause this discrepancy. A target lifetime of about 10^5 s would change the total lifetime of 767 s by only 6 s. Therefore, the exponential fit to the BCT curve of this measurement has been repeated using slightly different fit ranges. This investigation shows, that the measured lifetime can easily fluctuate from 743 s to 770 s. Consequently, the measurement is not sensitive to the large target lifetimes as long as the lifetime due to the machine and the background are so small.
For the following calculations the lowest measurable lifetime will be used in order to determine a lower limit of the expected total lifetime. Taking the 743 s, the lifetime due to the target becomes $\tau_{\mathrm{target}} = 23745\,\mathrm{s}$. Nevertheless, it is supposed that the calculated value of 10^5 s is reasonable.

+ 1 NEG: The measurement was repeated after the activation of one already installed NEG cartridge (Sec. 3.2.1), which provides in the optimal case a pumping speed of 1900 l/s, depending on the activation. Due to the mentioned mechanical failure, the storage cell was in closed position for all subsequent measurements. As no measurement with an open cell was possible, the target contribution to the lifetime is estimated as $\tau_{\mathrm{target}} = 23745\,\mathrm{s}$, scaled to the actual target density. The results of the following calculations will also be presented later for the calculated lifetime due to the target of $\tau_{\mathrm{target}} = 106600\,\mathrm{s}$. The individual contributions are:

- Lifetime from the target: $\tau_{\mathrm{target}} = 23745\,\mathrm{s} \cdot \frac{2.08}{2.53} = 19522\,\mathrm{s}$.
- Lifetime from the machine: $\tau_{\mathrm{COSY}} = 3200\,\mathrm{s}$.
- Lifetime from the target background: $\tau_{\mathrm{back}} = \left(\frac{1}{1273\,\mathrm{s}} - \frac{1}{3200\,\mathrm{s}} - \frac{1}{19522\,\mathrm{s}}\right)^{-1} = 2371\,\mathrm{s}$.

The activation of one NEG pump increased the lifetime from the target background from $1178\,\mathrm{s}$ to $2371\,\mathrm{s}$ by 50% ($1193\,\mathrm{s}$).

+ Flow Limiters: According to the calculations of the betatron functions (see Fig. 4.1), the acceptance angle is significantly decreased in the region $10\,\mathrm{m}$ up- and downstream of the target. Thus the flow of the target gas into the adjacent sections has to be minimized. Therefore the entrance and the exit of the chamber have been equipped with cylindrical flow limiter tubes with an inner diameter of $19\,\mathrm{mm}$ and a length of $80\,\mathrm{mm}$. For this setup the individual contributions are:

- Lifetime from the target: $\tau_{\mathrm{target}} = 19522\,\mathrm{s}$.
- Lifetime from the machine: $\tau_{\mathrm{COSY}} = 3500\,\mathrm{s}$.
- Lifetime from the target background: $\tau_{\mathrm{back}} = \left(\frac{1}{1882\,\mathrm{s}} - \frac{1}{3500\,\mathrm{s}} - \frac{1}{19522\,\mathrm{s}}\right)^{-1} = 5144\,\mathrm{s}$.

The flow limiter tubes improve the lifetime due to the target background by a factor 2.17. For the estimations of the lifetime for the spin-filtering experiment it is assumed that every additional NEG pump increases the lifetime due to the target background by $2.17 \cdot 1193\,\mathrm{s} = 2589\,\mathrm{s}$. This is reasonable, since only losses due to target gas background are discussed and one simply adds pumping speed. Assuming a constant flux into the target chamber, the pressure reduces inversely proportional to the pumping speed S and consequently in first order the lifetime due to single Coulomb losses increases in proportion to S. This improvement per NEG pump becomes smaller in case of higher fluxes into the chamber.

Conclusion for the Spin-Filtering Experiment: Collecting all numbers, enables an extrapolation of the beam lifetime with the completely installed PAX vacuum equipment. As a starting point the lifetime of COSY alone of

$$\tau_{\mathrm{COSY}} = 6000\,\mathrm{s} \tag{4.28}$$

has been observed after a machine development (Fig. 4.23). The contribution of the target to

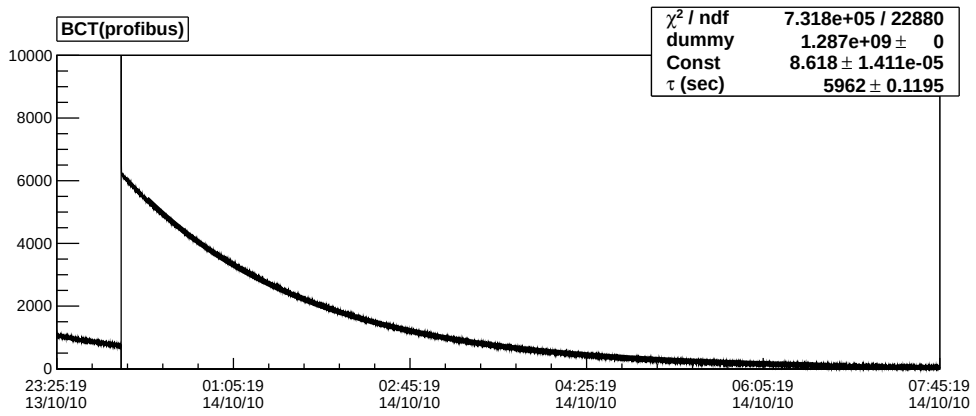

Fig. 4.23.: Long cycle with a duration of six hours and a beam lifetime of $6000\,\mathrm{s}$. The PAX optics is switched on.

the lifetime is $\tau_{\mathrm{target}} = 19522\,\mathrm{s}$ at a target density of $2.53 \cdot 10^{13}\,\mathrm{atoms/cm^2}$. At the expected target density of $4.35 \cdot 10^{13}\,\mathrm{atoms/cm^2}$, the target lifetime is

$$\tau_{\mathrm{target}} = 11354\,\mathrm{s}. \tag{4.29}$$

Since a dedicated pumping system, consisting of 10 NEG pumps (described in Sec. 3.2.1), has recently been installed below the target chamber, an improvement in the lifetime of the target background will be achieved. Recent measurements showed that the flux from the ABS stays constant and the lower observed target density was just because of the incomplete closed cell [146]. Thus the lifetime contribution of the target residual gas becomes

$$\tau_{\mathrm{back}} = 5144\,\mathrm{s} + 9\,\mathrm{pumps} \cdot 2589\,\mathrm{s/pump} = 28443\,\mathrm{s}. \tag{4.30}$$

Finally, the beam lifetime including all contributions is

$$\tau_{\mathrm{totalexp}} = \left(\frac{1}{\tau_{\mathrm{COSY}}} + \frac{1}{\tau_{\mathrm{target}}} + \frac{1}{\tau_{\mathrm{back}}} \right)^{-1} = 3449\,\mathrm{s}. \tag{4.31}$$

Obviously the largest contribution to the lifetime comes from COSY. It is therefore important, to make an attempt to improve the beam lifetime during the beam development beyond the already achieved $6000\,\mathrm{s}$. Both the lifetime of COSY and of the residual gas due to the target can be increased further by activating the NEG-coating in the adjacent beam pipes. These NEG pumps provide an additional pumping speed of about $1000\,\mathrm{l/s}$ in each of the up- and downstream sections, where before only a few $100\,\mathrm{l/s}$ of pumping speed were available and where the acceptance angle is small (see Fig. 4.2). Also a different optical setting, which was tested once, could allow for smaller betatron functions and thereby larger Θ_{acc} in this region. Disregarding a possible improvement on the COSY lifetime τ_{COSY}, an improvement on the lifetime caused by the target background τ_{back} of a factor 10 due to the NEG-coating would result in a total lifetime of

$$\boxed{\tau_{\mathrm{total}} = 3872\,\mathrm{s}.} \tag{4.32}$$

This is the expected lower limit of the achievable lifetime with a polarized gas target of an areal density of $d_{\mathrm{t}} = 4.35 \cdot 10^{13}\,\mathrm{atoms/cm^2}$. As already mentioned, the determined target lifetime is a rather imprecise input parameter. Taking the theoretical value of $106600\,\mathrm{s}$, which is believed to be reasonable, and repeating the calculations yields a total lifetime of

$$\tau_{\mathrm{total}} = 5239\,\mathrm{s}. \tag{4.33}$$

4.7. How to Set Up the Beam for Spin-Filtering Experiments

One major achievement of the commissioning beam time is the development of a routine which enables spin-filtering experiments in terms of the beam lifetime. This procedure is described below:

1. Provide very good vacuum conditions ($p < 3 \cdot 10^{9}\,\mathrm{mbar}$).
2. Injection of unpolarized protons with an intensity as large as possible ($I > 1 \cdot 10^{10}$). 1-2 weeks of running Ti-getter pumps prior to the beam time should be mandatory.
3. The COSY setting should be $D = 0$ and the PAX optics is switched off.

4. The experiment requires an experiment energy of $T = 49.3\,\mathrm{MeV}$, since known analyzing powers at this energy [147] enable a beam polarization determination. Consequently an acceleration is required, which was not done during the machine studies in 2010.
5. Adjustment of the electron cooler, i.e., alignment and electron current.
6. The beam polarization will be measured by the left-right asymmetry in $\vec{p}d$ elastic scattering. Thus the beam has to be positioned properly on the ANKE cluster target.
7. Orbit correction in horizontal and vertical direction.
8. Optimization of the electron cooler in terms of the electron beam angle and the feedback for different targets.
9. Working point adjustment.
10. Switching to PAX optics.
11. Orbit correction in horizontal and vertical direction.
12. Readjust the working point to the value measured without PAX optics.

This procedure is known to provide an intense stored unpolarized proton beam with a beam lifetime of more than $6000\,\mathrm{s}$. Since long beam lifetimes are a prerequisite for spin-filtering investigations at COSY and the AD, the development of this routine is an essential achievement on the way toward polarized antiprotons.

5. Outline of the COSY Spin-Filtering Experiment

The results of the PAX commissioning period at COSY enable estimations for the first spin-filtering experiment at COSY, scheduled in the second half of 2011. This includes the calculation of the expected polarization build-up and the valuation how well the spin-dependent cross section $\tilde{\sigma}_1$ (Eq. (2.42)) in pp elastic scattering can be determined. This settles the framework requirements for this experiment. The main requirements for the spin-filtering experiments are a low kinetic energies, where the polarizing cross section is large, and the possibility to measure the beam polarization. Thus, the COSY accelerator will be operated at an energy of $T = 49.3\,\mathrm{MeV}$, which is slightly above injection energy, since here precise analyzing powers for a polarization analysis are available [147].
A typical spin-filtering cycle starts with the injection and ramping of the unpolarized proton beam to experiment energy. As soon as the beam is cooled, the storage cell closes and the polarized gas from the ABS is injected into the cell. The originally unpolarized beam becomes polarized during a spin-filtering time that lasts for two beam lifetimes (Sec. 2.4). Subsequently, the polarized internal target and its holding field are switched off, and the ANKE deuterium cluster target is switched on in order to determine the beam polarization. The asymmetry in $\vec{p}d$ elastic scattering, detected with the STTs at ANKE, is a measure of the beam polarization. A scheme of COSY and the main components used for the spin-filtering experiments are shown in Fig. 5.1.
The expectations for the polarization build-up using the results of the COSY machine studies are discussed in Sec. 5.1. The determination of the beam polarization and possible sources of errors are presented in Sec. 5.2.

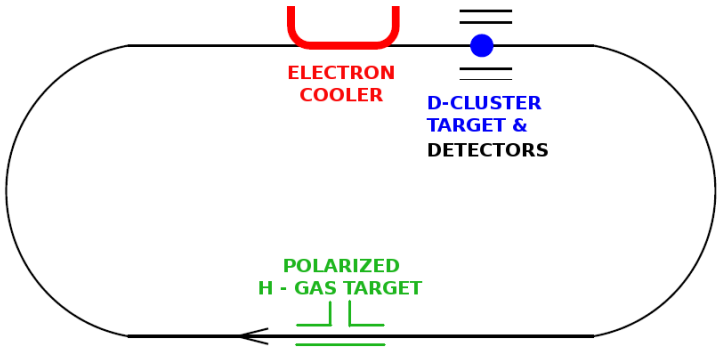

Fig. 5.1.: Sketch of the spin-filtering setup at COSY. The electron cooler ensures large beam lifetimes. During spin filtering, the polarized internal target at the PAX-IP builds up polarization in the proton beam, which will afterwards be measured using the ANKE cluster target and the Silicon Tracking Telescopes.

5.1. Polarization Build-up

In order to predict the polarization build-up rate, the relevant parameters of the machine and those which contribute to the spin-dependent cross section have to be well known. The COSY accelerator has a circumference of $183.4\,\mathrm{m}$ and will be operated at an energy of $T = 49.3\,\mathrm{MeV}$. According to Eq. (2.39), the polarization build-up depends on the target polarization Q, the target density d_t, the revolution frequency f, the acceptance angle at the target position Θ_acc, and the polarizing cross section $\tilde{\sigma}_1$. The used input parameters are

$$\begin{aligned} Q &= 0.8, \\ d_\mathrm{t} &= 4.35 \cdot 10^{13}\,\mathrm{atoms/cm^2}, \\ f &= 510032\,\mathrm{Hz}\ \ (\mathrm{T} = 49.3\,\mathrm{MeV}), \\ \Theta_\mathrm{acc} &= 6.13\,\mathrm{mrad}. \end{aligned} \tag{5.1}$$

In order to calculate the rate of polarization build-up according to Eqs. (2.41), (2.33), and (2.35) the double-spin asymmetries A_{00nn} (A_{yy}) and A_{00ss}(A_{xx}) (Fig. 5.2), the polarization transfer observables, and depolarization spin observables, which contribute to the polarizing cross section (see Sec. 2.3.1), were taken from the SAID database at $T = 50\,\mathrm{MeV}$ [98].
Consequently, with the given boundary conditions at COSY a polarization build-up rate of

$$\frac{dP}{dt} \approx 0.0019\,/\mathrm{h} \tag{5.2}$$

is expected, as displayed in Fig. 5.2 (bottom right panel). The optimal spin-filtering time of two beam lifetimes is a result of maximizing the gained statistics as discussed in detail in Sec. 2.4. Consequently, after filtering for $t = 2 \cdot \tau = 7744\,\mathrm{s}$ (Sec. 4.6.3), the expected beam polarization is

$$P = 0.0041. \tag{5.3}$$

Since the beam lifetime represents a lower limit, as described in Sec. 4.6.3, the same is true for the resulting polarization. Taking the total beam lifetime of $\tau = 5239\,\mathrm{s}$, which is based on the target lifetime calculations, the resulting beam polarization after filtering for 2τ would be $P = 0.0056$.
Either way, the beam polarization after filtering will be well below 0.01. Therefore, an appropriate strategy to determine this small polarization is required.

5.2. Beam Polarization Measurement at ANKE

The measurement of the proton beam polarization after spin filtering makes use of the left-right asymmetry in $\vec{p}d$ elastic scattering. The transverse polarization P of the beam made of spin-$\frac{1}{2}$ particles leads to an azimuthal dependence of the differential cross section, given by [99, 148]

$$\frac{d\sigma}{d\Omega}(\Theta, \phi) = \frac{d\sigma_0}{d\Omega}(\Theta) \cdot \left[1 + P A_y(\Theta) \cos(\phi)\right], \tag{5.4}$$

with the unpolarized differential cross section $\frac{d\sigma_0}{d\Omega}$, the scattering angle Θ in the laboratory system, the azimuthal angle ϕ, and the analyzing power A_y. The scattering angle Θ is measured from the outgoing beam direction, and the azimuthal angle ϕ from the horizontal direction. Consequently, a nonzero A_y causes a left-right asymmetry for the scattering of a polarized beam on an unpolarized target. The used technique and most of the equipment was already utilized in a recent experiment within the framework of PAX [149]. Therefore, in the following just the major issues of the setup, the polarimetry, and systematic effects will be discussed.

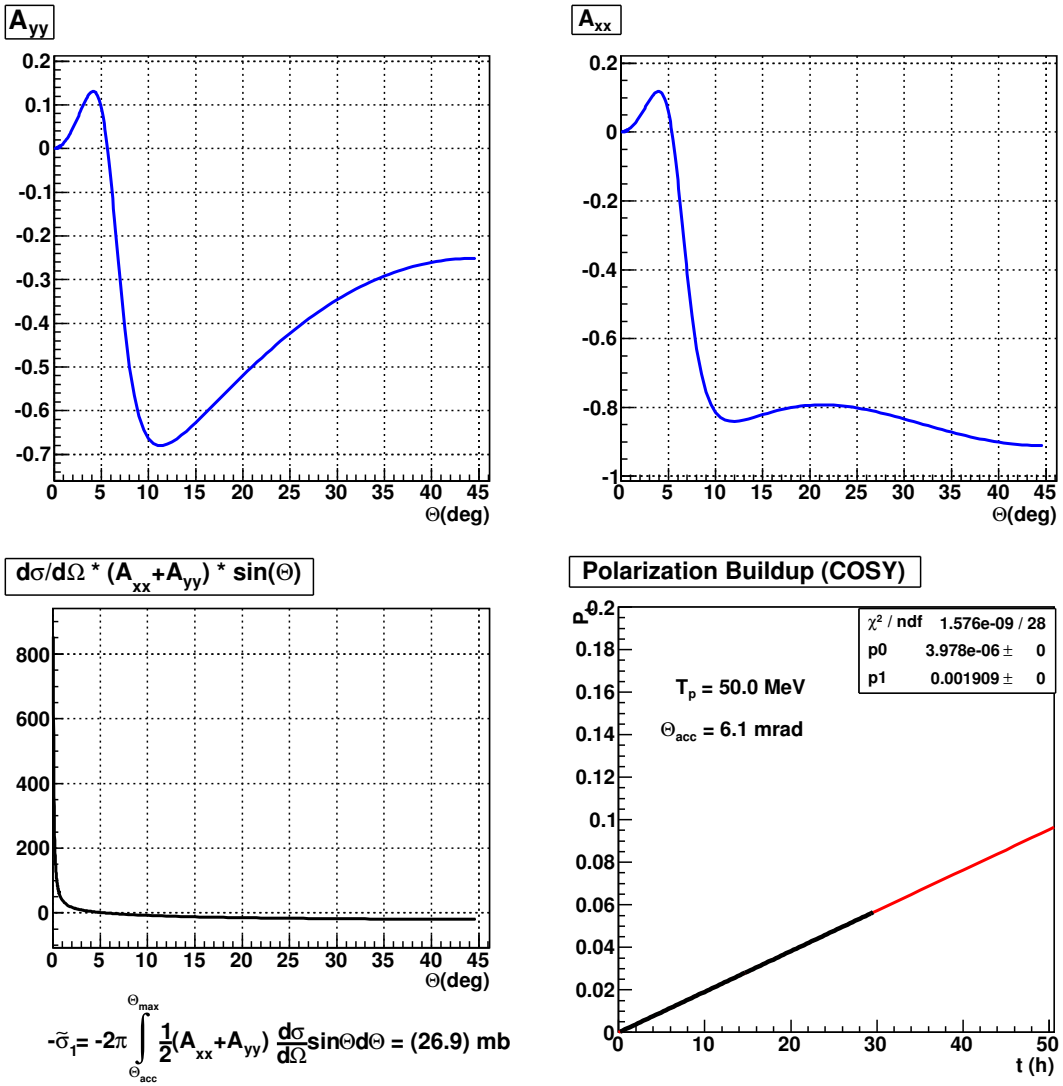

Fig. 5.2.: Top: Double-spin asymmetries A_{yy} (left) and A_{xx} (right) for $T = 50\,\mathrm{MeV}$ in pp elastic scattering as a function of laboratory scattering angle Θ; **Bottom left:** Polarizing cross section $\tilde{\sigma}_1$; **Bottom right:** Expected polarization build-up for spin filtering at COSY as a function of time. A build-up rate of $P = (0.001909 \pm 0.00001)$ per h is expected from the fit (black line), assuming a linear evolution.

5.2.1. Setup for Polarization Measurement

The polarimeter consists of the ANKE cluster target and the Silicon Tracking Telescopes (see Sec. 3.3). Two STTs will be installed left and right of the beam target overlap region opposite to each other, as shown in Fig. 3.23. The modularity of the telescopes allows one to choose a detector of $65\,\mu\mathrm{m}$ or $300\,\mu\mathrm{m}$ thickness as first layer, and enables an adjustment of the detector position along the beam direction. The center of the detector can be positioned in a range from $s = -42.5\,\mathrm{mm}$ up to $s = +17.5\,\mathrm{mm}$ with respect to the center of the cluster target. The observable scattering angle interval or geometrical acceptance depends on the exact positioning of the detectors, but ranges from 44° to 133° in the laboratory frame. In order to optimize the setup in view of the position and the thickness of the first layer, and to derive information about the achievable precision, a Monte-Carlo-Simulation for the experiment was carried out.
The asymmetry determination is mainly based on the identification of deuterons, which are

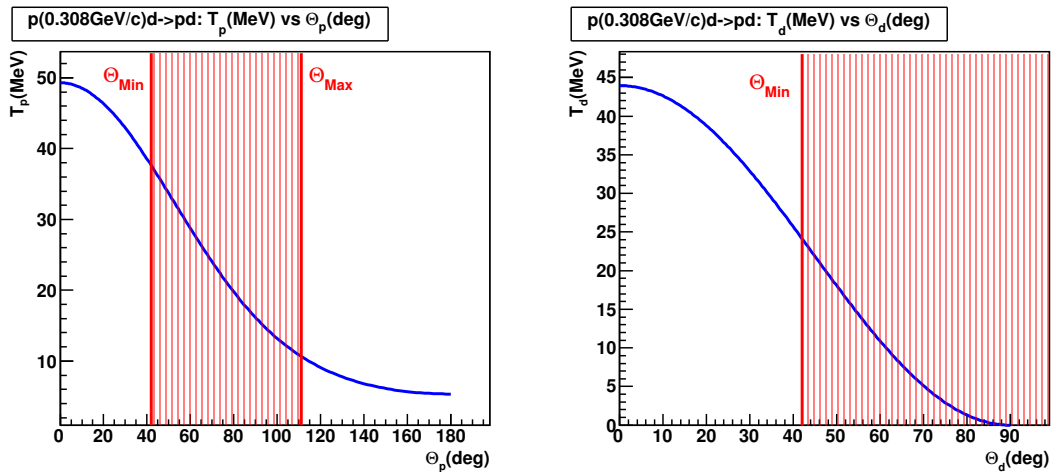

Fig. 5.3.: Kinematics of pd elastic scattering for $T = 49.3\,\mathrm{MeV}$ ($p = 0.308\,\mathrm{GeV/c}$) and geometrical acceptance of the STTs for two layers. **Left:** Proton energy T_p vs proton scattering angle Θ_p in laboratory frame. **Right:** Deuteron energy T_d vs deuteron scattering angle Θ_d.

stopped in the second or third detector layer. According to the kinematics of pd scattering (Fig. 5.3), the detectable deuterons within the geometrical acceptance of the detector are low energetic. Since these particles have to pass the first layer to produce a track, it is easy to understand, that this layer should be the $65\,\mu\mathrm{m}$ thin detector in order to decrease the energy threshold of particle identification.
The detector positioning has been optimized considering the following aspects:

- The statistical error of the beam polarization measurement has to be minimal.
- The detector setup has to be build in a ϕ-symmetric (left-right) arrangement to make use of the double ratio method (Sec. 5.2.3).
- Protection of the detectors from radiation damage requires placing the detectors at least $25\,\mathrm{mm}$ away from the orbiting beam.
- Events with proton and deuteron tracks should be in the detector acceptance, in order to align the setup and monitor the beam target overlap region.

The accomplished Monte-Carlo-Simulations do not only consider the differential cross section but also the analyzing power (Fig. 5.4). The simulations show that the STTs should be placed as far as possible downstream in the available range. Since the largest possible

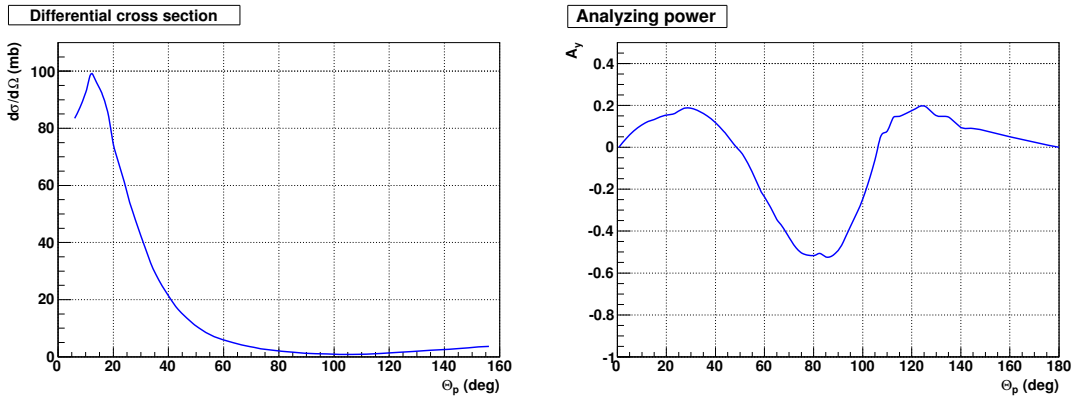

Fig. 5.4.: Left: Differential cross section $d\sigma/d\Omega$ vs the proton laboratory scattering angle Θ for $\vec{p}d$ elastic scattering ($T = 49.3\,\mathrm{MeV}$) [150]. **Right:** Analyzing power A_y vs scattering angle Θ [147].

deuteron scattering angle in the laboratory system is $90°$, which is anyway covered by the STTs, a shift downstream increases the geometrical acceptance for deuteron detection and for the detection of two track events (Fig. 5.5). The resulting geometrical acceptance with respect to the center of the target is $44.7° \leq \Theta \leq 105.8°$ for the second layer and $50.9° \leq \Theta \leq 103.4°$ for the third layer. Taking into account the dimensions of the cluster target ($s = \pm 5\,\mathrm{mm}$) the geometrical acceptance increases to $41.9° \leq \Theta \leq 111.1°$ for the second layer and $48.2° \leq \Theta \leq 107.7°$ for the third layer. A schematic view of the planned detector geometry is given in Fig. 5.6.
Major changes of the setup, in comparison to the polarization measurement described in [86], are the usage of a $65\,\mu\mathrm{m}$ first layer instead of $300\,\mu\mathrm{m}$ and the analysis of the data provided by the third layer.

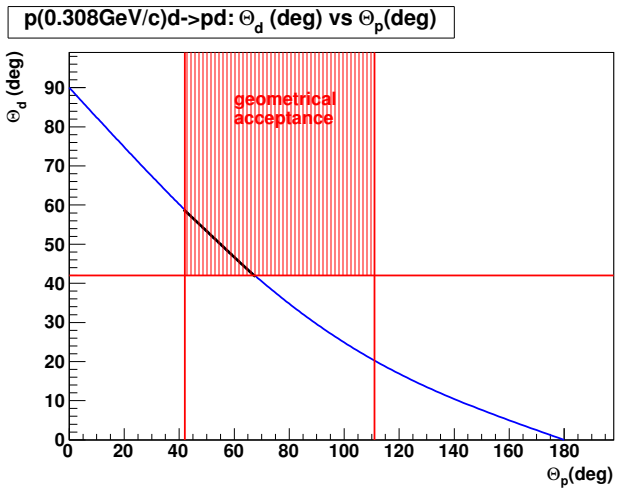

Fig. 5.5.: Proton laboratory scattering angle Θ_p vs deuteron laboratory scattering angle Θ_d. In addition, the geometrical acceptance of the detection of one proton and one deuteron in coincidence is indicated (red).

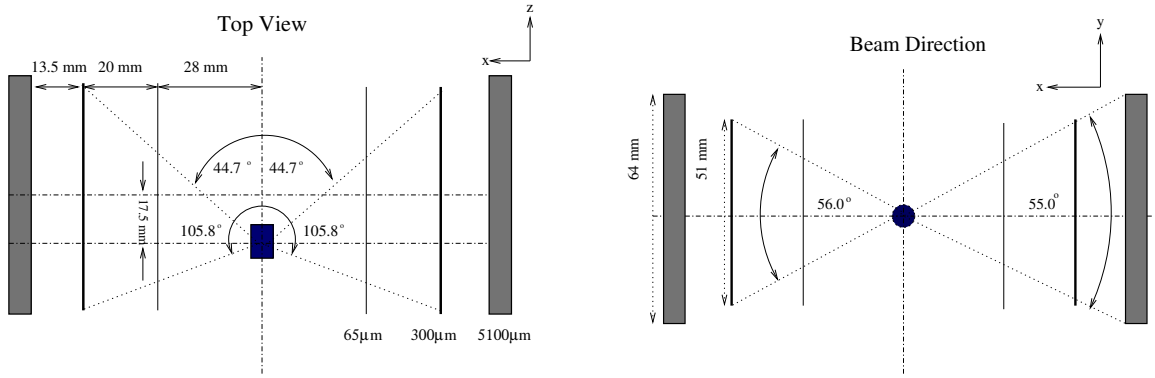

Fig. 5.6.: **Left:** Schematic view of the detection setup looking from the top. The proton beam direction is pointing along the s-axis and the polarization is aligned along the y-axis. The given angles indicate the geometrical acceptance for the scattering angle Θ if a particle is detected within the first two layers. **Right:** Schematic view of the detection setup looking in beam direction. Here the azimuthal acceptance angle ϕ is indicated for the second and third detector layer.

5.2.2. Event Selection

The event selection for the polarization measurement mainly follows that of earlier experiments [86]. The task is to reconstruct $\vec{p}d$ elastic events with low background. Since the data are taken below the pion-production threshold, an identified deuteron ensures that elastic scattering took place. Thus the first step is to identify tracks in the data which are produced by a deuteron. According to the Bethe-Bloch formula

$$-\frac{dE}{dx} = \frac{4\pi n Z^2}{m_e v^2} \cdot \left(\frac{e^2}{4\pi\epsilon_0}\right)^2 \cdot \ln\left(\frac{2m_e v^2}{I}\right), \tag{5.5}$$

the energy loss of a particle in matter depends on its mass. Here v is the particle velocity, ϵ_0 is the vacuum permittivity, m_e is the electron mass, and the material related values are: n the electron density, Z the atomic number, and I the average ionization energy. A simple linear cut in the plot of the deposited energy in the first layer vs the energy loss in the second layer (Fig. 5.7) allows one to identify deuterons. The upper band belongs to deuterons, whereas the lower band are protons. A particle that passes the first layer and generates a signal above threshold in the second layer causes a trigger and appears in the dE vs dE plot. With increasing energy, the energy deposit in the first layer decreases, whereas that in the second layer increases. If the energy further increases, the particle penetrates the second layer leading to a smaller energy deposit in both detectors. The same method of identification can also be applied for particles stopped in the third layer.

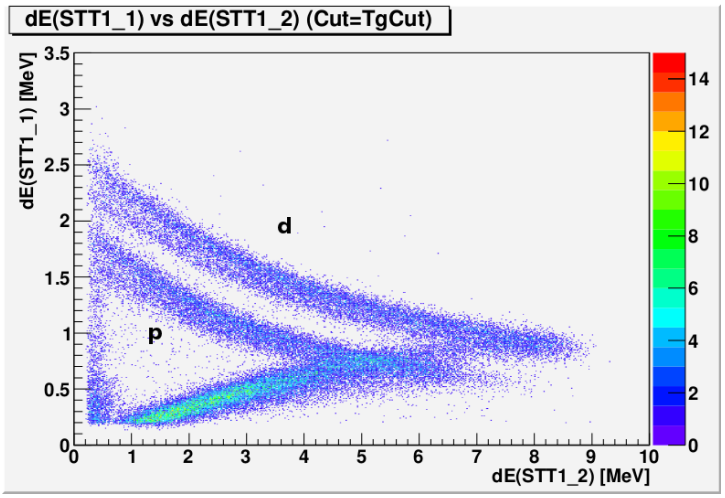

Fig. 5.7.: Deuteron identification with the $\Delta E/E$ method. The energy deposit in the first layer is plotted vs the one in layer two. The two visible bands allow us to clearly distinguish between protons and deuterons.

Additional deuterons, whose locus in the $\Delta E/E$ plot overlaps with the proton locus, can also be identified, provided that they are accompanied by a coincident proton in the other telescope, that the two tracks are co-planar with the beam axis, and that the respective polar angles are consistent with the kinematics of pd elastic scattering [87].
Since a detected proton can originate from pd elastic or pd breakup reactions, the correlation of the scattering angle and the particle energy in elastic scattering has to be used (Fig. 5.3), to identify elastically scattered protons. In this case the STTs have to measure the absolute energy and the scattering angle of the detected particle. Since the protons within the geometrical acceptance have a kinetic energy of $10\,\mathrm{MeV} \leq T_p \leq 36\,\mathrm{MeV}$, they will be stopped

in the third detector layer. The identification of the protons from pd elastic scattering would increase the statistics by about a factor two.
Even without a precise energy determination with the third layer there is an option to use these events without identification of the underlying reaction. For this purpose one has to measure the analyzing powers of this sample of events once with a beam of known polarization. The measured analyzing powers could then later be used to determine the unknown polarization of the proton beam from this sample of events.
Taking into account the geometrical acceptance of the detection system, the energy thresholds of the detectors, and the event selection, yields the detectable scattering angles and energy ranges as listed in Tab. 5.1. By the detection of the different particles, different proton scattering angles Θ_p can be observed, as indicated in Fig. 5.8. This graph shows the figure of merit, defined as

$$\mathrm{FOM}(\Theta_p) = A_y^2(\Theta_p) \cdot \frac{d\sigma}{d\Omega}(\Theta_p), \tag{5.6}$$

as a function of Θ_p. In total, the three different Θ_p-ranges, which can be observed by the detection of deuterons stopped in the second and third layer and of protons stopped in the third layer, cover almost the complete figure of merit. The lower threshold is defined by the thickness of the first layer. If a deuteron identification would be possible for particles, which are stopped in the first layer, this threshold could be further decreased. This subject is presently under investigation.

events	$\Theta(^\circ)$	$T(\mathrm{MeV})$	corresponding Θ_p
d stopped in layer 2	$61.0 - 75.0$	$2.9 - 10.2$	$19.8 - 38.9$
d stopped in layer 3	$48.2 - 61.0$	$10.2 - 19.4$	$38.9 - 58.0$
p stopped in layer 3	$48.2 - 107.7$	$11.4 - 34.6$	$48.2 - 106.5$

Table 5.1.: Geometrical acceptance and energy ranges for the detection of different particles. The last column displays the laboratory scattering angle of the corresponding proton of each reaction.

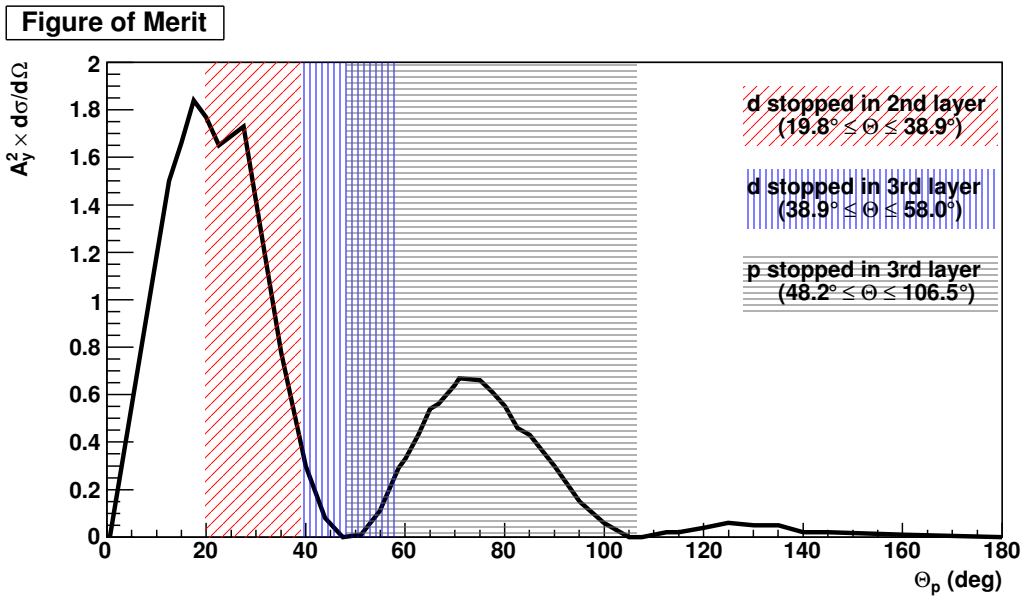

Fig. 5.8.: Figure of merit vs scattering angle for $\vec{p}d$ elastic scattering at $T = 49.3\,\mathrm{MeV}$. Different regions of the proton scattering angle Θ_p can be investigated by the detection of stopped deuterons in the second (red) and the third layer (blue) and by detecting stopped protons (gray).

5.2.3. Determination of the Beam Polarization

The actual number of recorded counts in a detector, the yield $\mathrm{Y}(\Theta, \phi)$, may be written as [99]

$$\mathrm{Y}_{\mathrm{L,R}}(\Theta, \phi) = n \cdot d_{\mathrm{t}} \cdot \Delta t \cdot \Delta\Omega_{\mathrm{L,R}} \cdot \varepsilon_{\mathrm{L,R}} \frac{d\sigma}{d\Omega}(\Theta, \phi). \tag{5.7}$$

Here n is the number of particles incident on the target, d_{t} is the target areal density, Δt is the measurement time, $\Delta\Omega_{\mathrm{L,R}}$ is the solid angle covered by the left (L) and right (R) detector, $\varepsilon_{\mathrm{L,R}}$ are the detector efficiencies, and $\frac{d\sigma}{d\Omega}(\Theta, \phi)$ is the differential cross section as defined in Eq. 5.4. This count number is recorded for the left (L) and right (R) detector and for runs with beam polarization pointing up and down ($\uparrow$, $\downarrow$), resulting in four yields $\mathrm{Y}_{\mathrm{L}\uparrow}$, $\mathrm{Y}_{\mathrm{R}\uparrow}$, $\mathrm{Y}_{\mathrm{L}\downarrow}$, $\mathrm{Y}_{\mathrm{R}\downarrow}$.
Now, one can define the fraction

$$\delta = \sqrt{\frac{\mathrm{Y}_{\mathrm{L}\uparrow} \cdot \mathrm{Y}_{\mathrm{R}\downarrow}}{\mathrm{Y}_{\mathrm{L}\downarrow} \cdot \mathrm{Y}_{\mathrm{R}\uparrow}}} = \frac{1 + P A_y(\Theta)}{1 - P A_y(\Theta)}, \tag{5.8}$$

where $\Delta\Omega$, ε, and the integrated luminosity $n \cdot d_{\mathrm{t}} \cdot \Delta t$ cancel out and $\frac{d\sigma}{d\Omega}(\Theta, \phi)$ is inserted according to Eq.(5.4). Consequently, the detected asymmetry

$$\epsilon = \frac{\delta - 1}{\delta + 1} = P \cdot A_y \tag{5.9}$$

allows one to determine the beam polarization for a known A_y. This method is called cross-ratio method [151]. It allows one to determine the beam polarization independent of relative detector efficiencies, of solid angles, of relative integrated charge, and of target thickness variations. Time fluctuations in the beam current n or the target thickness are of no consequence since they are common to both detectors. However,

$$\delta' = \sqrt{\frac{\mathrm{Y}_{\mathrm{L}\uparrow} \cdot \mathrm{Y}_{\mathrm{L}\downarrow}}{\mathrm{Y}_{\mathrm{R}\uparrow} \cdot \mathrm{Y}_{\mathrm{R}\downarrow}}} = \frac{\Delta\Omega_L \cdot \varepsilon_L}{\Delta\Omega_R \cdot \varepsilon_R} \tag{5.10}$$

must not vary with time.
Commonly the events are sorted into angle bins Θ_i. For each bin i, the analyzing power that represents the data is calculated resulting in a beam polarization for each bin $P_i = \epsilon_i / \bar{A}_{y,i}$, where $\bar{A}_{y,i}$ is the event weighted average of A_y over that bin. The weighted average yields the overall beam polarization.
Taking into account the dependence of the analyzing power on the azimuthal angle Eq. (5.9) has to be corrected for the average of the azimuthal coverage of the detector. Finally, the beam polarization is given by

$$P = \frac{\epsilon}{A_y \cdot \langle \cos\phi \rangle}. \tag{5.11}$$

5.2.4. Systematic Errors

In order to reduce the systematic errors of the polarization build-up measurement different parameters have to be under control. These are the polarization lifetime, the detector stability, the spin-flip efficiency and a stable position of the interaction region.

Polarization Lifetime: Depolarizing resonances arise when the horizontal and the vertical tune, the orbit frequency, and the synchrotron frequency, or combinations thereof, are related in a simple way to the spin tune, which is the net precession angle of the magnetic moment of a particle during one turn in the machine. A finite value of the

polarization lifetime τ_{Pol} reduces the resulting beam polarization. Thus a dedicated measurement of the polarization lifetime is needed in order to quantify this effect and enable a correction.

An optimized cycle to measure the polarization lifetime starts with the injection of a polarized proton beam from the polarized source of COSY ($P \approx 0.8$). Then the polarization is measured using $\vec{p}d$ elastic as described earlier. After measuring for about $100\,\mathrm{s}$ the cluster target is switched off for about $1200\,\mathrm{s}$ in order to decrease the beam loss during a waiting period, and finally it is switched on again for approximately $1100\,\mathrm{s}$ (Fig. 5.9, left panel). The time periods are optimized to yield the smallest relative errors in τ_{Pol}. The measured beam polarizations before and after waiting allow one to determine the polarization lifetime. The statistical error of both measurements, before and after waiting, is equal.

Using the described cycle, one day of data taking is sufficient, and for an anticipated polarization lifetime of $\tau_{\mathrm{Pol}} = 10^5\,\mathrm{s}$, the expected error is $\Delta\tau_{\mathrm{Pol}} \approx 10^3\,\mathrm{s}$. Assuming a polarization lifetime of $10^5\,\mathrm{s}$ the loss in beam polarization during filtering (assuming a filtering time of $7000\,\mathrm{s}$) would be about $7\,\%$. Thus, an error of $10\,\%$ in the polarization lifetime would translate into an error of $0.7\,\%$ for the polarization.

Detector Stability: The cross-ration method combines the detector yields from $p_\uparrow d$ and $p_\downarrow d$ scattering. In the later analysis the geometrical acceptance of the left and right detector is reduced to the stable part of the system. To ensure a stable fraction $\frac{\Delta\Omega_L \cdot \epsilon_L}{\Delta\Omega_R \cdot \epsilon_R}$, as discussed in Sec. 5.2.3, the detector setup has to give a stable response over the integration time. Thus, a spin-flipper which is able to reverse the beam polarization of the coasting beam will be utilized in each cycle in order to reduce the integration time.

Spin-Flip Efficiency: During the measurement, the beam polarization will be flipped every $200 - 400\,\mathrm{s}$ to enable the application of the cross-ratio method within each cycle.

The spin flips are generated using a so-called Froissart-Stora scan induced with an RF-solenoid [152]. The RF-frequency is swept over the precession frequency of the proton spin and flips resonantly at the precession frequency. Such a scan needs roughly $1\,\mathrm{s}$, and therefore the effect on the duty cycle is negligible.

In order to fulfill the assumption of identical polarizations for polarization up and down a spin-flip efficiency of $\varepsilon_{\mathrm{flip}} \geq 0.99$ is required. According to the simulations, a cycle to determine the spin-flip efficiency with the smallest relative error in $\varepsilon_{\mathrm{flip}}$ starts with the injection and ramping of a polarized proton beam, followed by a polarization measurement for a time period of about $50\,\mathrm{s}$. Then the cluster target is switched off and about 100 spin flips are performed within a time period of $100\,\mathrm{s}$. Finally, the beam polarization is measured again for about $60\,\mathrm{s}$ (Fig. 5.9, right panel). About six hours of data taking are sufficient to reach an error of the spin-flip efficiency of about of $\Delta\varepsilon_{\mathrm{flip}} \approx 8 \cdot 10^{-5}$ for a spin-flip efficiency of $\varepsilon_{\mathrm{flip}} = 0.99$.

False Asymmetry: A systematic shift of the beam target overlap region causes a false asymmetries, which could probably be interpreted as a beam polarization. Although, there is no obvious reason for a systematic shift, this problem was examined. A tool to monitor the position of the beam target overlap region is the analysis of events where a proton and a deuteron is detected, as described in Sec. 5.2.2. The vertex position can be reconstructed with a precision of approximately $20\,\mu\mathrm{m}$ [86].

In addition, the asymmetry due to a systematic shift is constant over the scattering angle and does not follow the functional dependence of the analyzing power. Consequently, a shift of the beam target overlap region does not affect the polarization measurement.

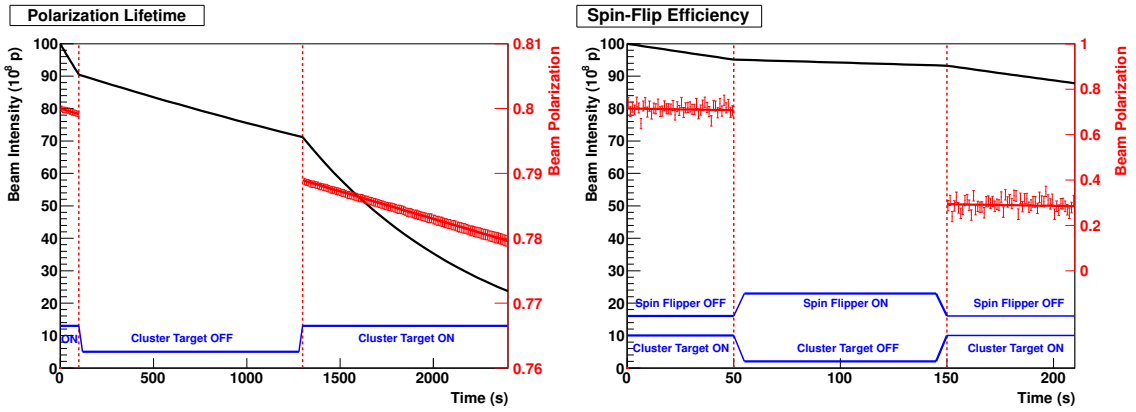

Fig. 5.9.: Left: Cycle for the measurement of the beam polarization lifetime. A polarized proton beam is injected and stored into COSY. The beam polarization (red) is measured for 100 s at the beginning of the cycle, then the ANKE cluster target is switched off for 1200 s, and finally the beam polarization is measured again for 1100 s at the end of the cycle. **Right**: Cycle for the measurement of the spin-flip efficiency. Between the measurement of the beam polarization at beginning (50 s) and the end of the cycle (60 s) the beam polarization is flipped about 100 times (100 s). Assuming $\varepsilon = 0.99$ and $P_0 = 0.8$ the beam polarization after 100 flips is $P = P_0 \cdot \varepsilon^{100} = 0.293$.

Dead Time: In addition, dead time effects which are not equal for both detectors have to be corrected, since they lead to a decrease of the measured asymmetry. A correction of the effect due to the data acquisition dead time, which is about $80 \cdot 10^{-6}$ s, can be achieved by counting the number of "lost" events, which cause a trigger signal in the detector, during the read-out process of one event. Additionally, a determination of the dead time is possible by the help of test pulses, which are sent to the detection system with a certain frequency. The ratio between sent (TP_{sent}) and detected (TP_{det}) test pulses allows for a direct measurement of the dead time and thus for a correction of the number of recorded counts (Eq. 5.7)

$$\mathrm{Y_L} = \sum_i L_i \cdot CL_i \qquad \text{and} \qquad \mathrm{Y_R} = \sum_{\mathrm{i}} \mathrm{R_i} \cdot \mathrm{CR_i}, \tag{5.12}$$

where L_i and R_i are the detected events in the left and right detector and $CL = {}^{TP^{\mathrm{l}}_{\mathrm{sent}}}/_{TP^{\mathrm{l}}_{\mathrm{det}}}$ and $CR = {}^{TP^{\mathrm{r}}_{\mathrm{sent}}}/_{TP^{\mathrm{r}}_{\mathrm{det}}}$ are the correction factors for the left for the right detector, respectively.

The read-out of the Silicon Tracking Telescopes is arranged such, that in case of a trigger, independent in which detector, the whole detection system (all 12 sides) is read out. Consequently, the dead time is exactly the same for both telescopes and thus the correction factors in the left and right telescope are equal.

Summing up, due to the read-out of the detection system an effect on the measured beam polarization due to dead time is prevented.

5.2.5. Results

A typical spin-filtering super cycle consists of two separate cycles with inversed target polarization (Fig. 5.10). After injection and ramping of the unpolarized proton beam to $T = 49.3\,\mathrm{MeV}$ ($I \approx 2 \cdot 10^{10}$ circulating protons) spin filtering with target polarization $+y$ takes place for two beam lifetimes. The beam polarization increases and after about $t_\mathrm{F} = 2\tau$, the polarized internal target is switched off. In order to measure the beam polarization, the ANKE cluster target is switched on, and the beam polarization is determined using the STTs, as described earlier.
The subsequent cycle is similar, only the target polarization is reversed (-y). The optimal measurement time t_M depends on the beam lifetime during filtering τ_F and during data taking τ_M. A detailed calculation of the optimal cycle as a function of τ_F and τ_M can be found in App. B.
A simulation of the experiment shows the achievable precision of the polarization determination. This simulation was verified with data from an earlier experiment [149], where a similar system of STTs was used to determine the beam polarization from $\vec{p}d$ elastic scattering with the ANKE cluster target. For the simulations an initial beam intensity of $1{\cdot}10^{10}$ stored protons, a target density of $4.35 \cdot 10^{13}$ atoms/cm^2, and a beam lifetime with cluster target of $1000\,\mathrm{s}$ was assumed. Within four weeks of data taking, the final beam polarization of $P = 0.0041$ can be measured with a relative precision of $15\,\%$.
The expected polarizing cross section at $T = 50\,\mathrm{MeV}$ assuming an acceptance angle of $6.1\,\mathrm{mrad}$ and the achievable precision are shown in Fig. 5.11. In addition the FILTEX result at $T = 23\,\mathrm{MeV}$ is indicated.

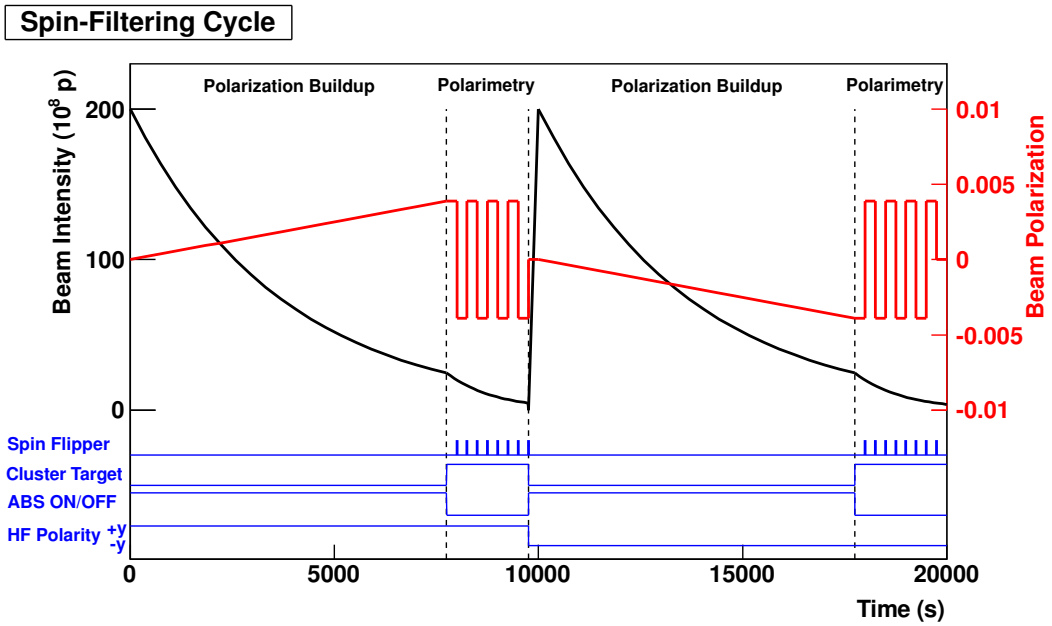

Fig. 5.10.: Spin-filtering cycle. After injection and cooling of the unpolarized proton beam, the polarized H-target at PAX is switched on (ABS on, $+y$). After two beam lifetimes ($> 6000\,\mathrm{s}$) the polarized H-target is switched off (ABS off) and the ANKE-Deuterium Cluster target is switched on. During additional roughly two beam lifetimes, $\vec{p}d$ elastic events are detected using the ANKE-STTs. The spin flipper will switch the beam polarization between 5 and 9 times during this measurement period. In the subsequent cycle the holding field polarity (HF) of the polarized H-target is reversed ($-y$).

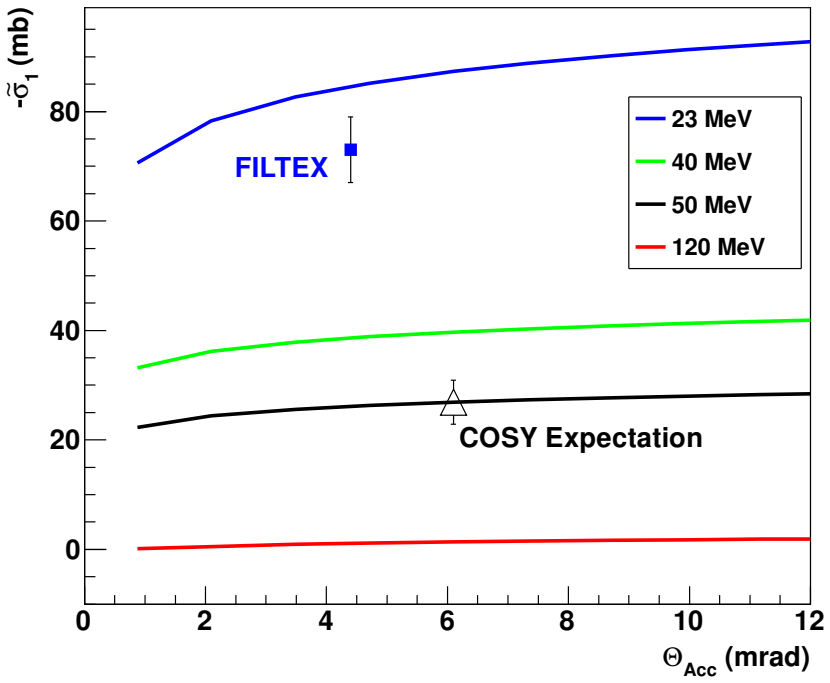

Fig. 5.11.: The polarizing cross section $\tilde{\sigma}_1$ vs acceptance angle for different beam energies. Indicated is the TSR measurement of FILTEX (blue) and the expected theoretical value for spin-filtering at COSY (black triangle).

6. PERSPECTIVES AND SUMMARY

The scientific objectives of the spin-filtering experiments at COSY are twofold. Firstly, to prove our present understanding of spin-filtering processes in storage rings by the determination of the well-known spin-dependent total cross sections in pp scattering, and secondly the commissioning of the experimental setup, which will be used for the experiments with antiprotons at AD (CERN). Thus, the anticipated experimental program of PAX does not only comprise transverse spin filtering, but also at a later stage the installation and commissioning of a Siberian Snake, which enables experiments with longitudinal polarization, the commissioning of the CERN/AD detector at the PAX-IP, and the absolute calibration of the BRP.

The anticipated time plan of PAX at COSY mainly consists of four different phases, as listed in Tab. 6.1. A successful spin-filtering experiment with transverse beam polarization will complete phase II[1]. The summary of this work, which mainly includes phase I and II, is given in Sec. 6.1. Section 6.2 gives an outlook of the subsequent phases, including the already accomplished experiment simulations.

Since the preparations for spin-filtering experiments with antiprotons at the CERN/AD take place in parallel, a short overview of these activities is presented in Sec. 6.3. The planned measurement of the spin-dependent total cross sections in $\bar{p}p$ scattering at AD and the involved machine studies will allow to define a future, dedicated large-acceptance Antiproton Polarizer Ring (APR), intended to feed a double-polarized asymmetric $\bar{p}p$ collider at FAIR with polarized antiprotons.

Phase	Beam Time / Installation	Description
I		COSY proposal submitted
	completed	Installation of the Low-β section
		Commissioning of the Low-β section
II	completed	Installation of the target chamber, the ABS, the BRP
	completed	Machine studies on the beam lifetime dependences (single intra-beam scattering)
	completed	Measurement of the acceptance angle at the target position
	completed	Test of the openable storage cell and ABS commissioning
	completed	Pumping speed upgrade
	2011	Spin filtering at COSY with transverse beam polarization
III	2012	Siberian Snake installation at ANKE
		Commissioning of the Siberian snake
IV		Commissioning of the CERN/AD detector
	2013	Absolute calibration of the BRP
		Longitudinal spin filtering

Table 6.1.: PAX Anticipated time plan.

[1]The corresponding beam time is already scheduled to take place in August and September of 2011.

6.1. Summary

The PAX low-β section, consisting of four additional quadrupole magnets and four steerer magnets, mounted directly on the surrounding COSY quadrupoles, was implemented into COSY in summer of 2009. The commissioning exhibited a reasonable agreement with the model calculations. Therefore, betatron functions around the design values of $0.3\,\mathrm{m}$ were achieved at the cell center. In addition, it was shown that the closed storage cell did not affect the beam lifetime. Consequently, phase I of the PAX time plan as prerequisite to achieve target densities of up to $5 \cdot 10^{13}\,\mathrm{atoms/cm^2}$ was successfully accomplished in early 2010.
During a shutdown period in 2010, the PAX target consisting of the ABS, the BRP, and the target chamber, equipped with holding field coils, was installed. The subsequent commissioning of these components, including the openable storage cell was carried out in a dedicated beam time in 2010, which also comprised studies on the acceptance angle and the improvement of the beam lifetime, e.g., intra-beam scattering effects.
The experimental setup was shown to work as expected. The target chamber equipped with one turbo pump and one NEG cartridge already allowed for pressures below $1 \cdot 10^{-9}\,\mathrm{mbar}$ without gas load. Studies on the beam lifetime and pressure performance with an ABS flux of $3.05 \cdot 10^{16}\,\mathrm{atoms/s}$ and different pumping systems enabled the dimensioning of the required vacuum equipment, consisting of 10 NEG pumps, NEG coating on the beam pipe, and flow limiters installed between the target chamber and the adjacent beam tubes. In addition, an estimation of the total beam lifetime and the individual contributions from the target, the target background, and the machine was carried out. The commissioning of the openable storage cell revealed mechanical weak spots, which have been re-engineered in the meantime. A recent measurement showed that a target areal density of $4.35 \cdot 10^{13}\,\mathrm{atoms/cm^2}$ can be achieved. The target holding field system provides the required magnetic field of about $1\,\mathrm{mT}$ at the center of the target chamber as it was measured by a Hall probe, and by the observed displacement of the beam in the target region. Since no noticeable displacement of the beam in the ring was observed, the compensation system of the holding field also works properly.
The installation of a movable frame system enables a measurement of the beam size and the beam position, which is necessary to perfectly align the beam to the cell, and thereby to avoid beam losses. As an important input parameter for the calculation of the polarizing cross section, the acceptance angle with electron cooled beam was precisely determined at the target position.
An improvement of the beam lifetime to about $6000\,\mathrm{s}$ without target is indispensable for the spin-filtering experiments at COSY. This goal could be achieved as a result of various machine studies. These studies included an improvement of the COSY vacuum environment, the adjustment of the machine tune, closed orbit corrections, adjustment of the electron cooler performance, and studies on single intra-beam scattering effects. Finally, the reached beam lifetime without target and the expected beam lifetime with polarized internal target enable a measurement of the polarizing cross section in pp scattering at $T = 49.3\,\mathrm{MeV}$ at COSY.
Simulations yield a necessary time of data taking of four weeks to measure the final beam polarization of $P = 0.0041$ with a relative precision of about $15\,\%$.
These four weeks of beam time and additional three weeks for machine development, prior to the actual spin-filtering experiment, were requested by the PAX collaboration and approved by the COSY Program Advisory Committee. Thus, the spin-filtering experiment with transverse polarization will be carried out in the second half of 2011.

6.2. Status and Outlook

After completion of phase II with the spin-filtering measurements with transverse polarization at $T = 49.3\,\mathrm{MeV}$, it is foreseen to install the AD Siberian Snake at the ANKE target position in phase III. This will be used as a spin rotator providing a longitudinal invariant spin axis at the PAX-IP. It enables a transfer of the vertical polarization into the horizontal plane and thereby provides longitudinal polarization at the symmetry point of the snake, which is located at the opposite side of the snake in the ring [153]. The commissioning has to be accomplished prior to the installation at AD [61].
Phase IV of the PAX time plan comprises the installation and commissioning of the CERN/AD detector, which is currently in the designing phase, the absolute calibration of the BRP, and finally longitudinal spin filtering. The latter two points require a detection system placed at the PAX-IP.
The actual design of the AD detector is based on simulations which have been carried out in order to design and optimize a common detector to measure the polarization observables in pp and $\bar{p}p$ elastic scattering. These simulations are in detail described in [154]. The detector had to be optimized to detect the scattered particles in the energy range of $40 \leq T_{p(\bar{p})} \leq 500\,\mathrm{MeV}$. Three types of $\bar{p}$ interactions have been considered, namely elastic scattering ($\bar{p}p \to \bar{p}p$), inelastic scattering ($\bar{p}p \to X$), and charge-exchange ($\bar{p}p \to \bar{n}n$). The proposed detector setup consists of four quadrants placed at azimuthal angles of $\phi = 45°$, $135°$, $225°$, and $315°$ (Fig. 6.1). Every quadrant has two layers, each equipped with three double-sided silicon strip detectors of $300\,\mu\mathrm{m}$ thickness. They are based on the TIGRE design of Micron Ltd. [136] with an active area of $97.3 \times 97.3\,\mathrm{mm}^2$ and a strip pitch of $0.758\,\mathrm{mm}$. In addition to detectors which have formerly been used at the HERMES experiment [155, 156], new detectors are already in production.
Recent simulations revealed that this system is also suitable to measure the spin dependence of proton deuteron breakup at 30 and $49\,\mathrm{MeV}$ proton beam energy. Thus, a proposal for this experiment has been submitted to the COSY Program Advisory Committee [157] and was approved. The breakup measurement, which is foreseen after phase IV of the PAX time plan, requires an additional third detector layer of $1500\,\mu\mathrm{m}$ thickness. The realizability of this system is currently under investigation. The actual design of the detector system, consisting of three layers is presented in Fig. 6.1.

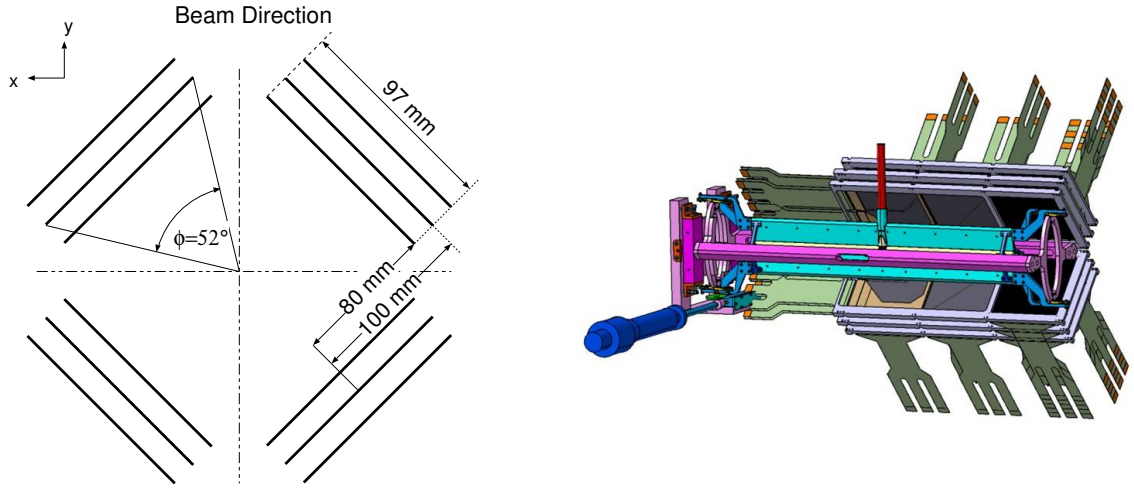

Fig. 6.1.: Left: Schematic drawing of the PAX detector looking in beam direction. The system provides a ϕ-coverage of about 57%. **Right:** The complete system with openable storage cell and silicon detectors (with two quadrants removed).

In addition to the simulations for spin filtering at COSY, which are described in this work, further simulations on the measurement of the polarization observables in $\vec{p}\vec{p}$ elastic scattering with the PAX detector were carried out (see App. G). These simulations show that the estimated detector geometry is well suited to determine the beam and the target polarization by pp elastic scattering using the known analyzing powers and double-spin asymmetries. Using A_{xx} or A_{yy} in double polarized $\vec{p}\vec{p}$ scattering enables a five to six times faster measurement of the beam polarization P compared to the measurement which uses the left-right asymmetry in $\vec{p}d$ elastic scattering and the ANKE polarimeter. Here only events with two protons in coincidence in opposite detectors were taken into account. First of all the acceptance of about 28% is larger than the corresponding one in $\vec{p}d$ elastic scattering and secondly the double-spin asymmetries are larger. A sophisticated method to deduce the polarization from the measured yields of the four different quadrants is the so-called diagonal scaling method. This is in detail described in [158]. It also allows one to extract the detector efficiencies and the luminosity.
Once the PAX detector is assembled and installed at COSY, it can be commissioned by the measurement of the proton beam polarization in $\vec{p}\vec{p}$ elastic scattering. A comparison of the extracted value with that of a simultaneous determination of the beam polarization using the conventional ANKE polarimeter ($\vec{p}d$ scattering) ensures a proper functioning of the detector system and a correct analysis of the collected data.
A properly working detector installed at the PAX-IP enables a determination of the target polarization Q for targets with H or D injected, and thereby an absolute calibration of the BRP. In case of a polarized hydrogen target, $\vec{p}\vec{p}$ scattering shall be used to measure the target polarization if the beam polarization is measured simultaneously with the ANKE polarimeter using $\vec{p}d$ elastic scattering. By measuring the target polarization with the Breit-Rabi polarimeter, the latter is calibrated to deliver absolute target polarizations during the spin-filtering experiments with a precision of about 0.01, and also later during the studies at AD.
Phase IV of the PAX experiments at COSY will be completed by spin filtering with longitudinally polarized target at $T_p = 130\,\mathrm{MeV}$.

6.3. Spin-Filtering Experiments at AD

The PAX collaboration proposed to measure the polarization build-up in an antiproton beam at CERN/AD (Fig. 6.2) by spin filtering at beam energies of $50 - 450\,\mathrm{MeV}$ [61]. According to the expectations from different models for the spin dependence of the $\bar{p}p$ interaction, antiproton beam polarizations in the range of $15 - 20\%$ are achievable with filtering for two beam lifetimes. Recent calculations based on $\bar{N}N$ interaction models developed at Jülich show that the maximum polarization is expected at kinetic energies above $200\,\mathrm{MeV}$ for longitudinal polarization (Fig. 6.3) [159]. As one can see, the predicted polarization strongly depends on the chosen interaction model. The available models are the $\bar{N}N$ models A [160] and D [161]. The filtering experiment at AD would allow one to determine for the first time the two total spin-dependent $\bar{p}p$ cross sections σ_1 and σ_2 (Sec. 2.3).
At the same time, when spin-filtering experiments and commissioning of the experimental setup is carried out at COSY, the preparations for the proposed measurement of the polarization build-up in an antiproton beam at the CERN/AD will be accomplished. This includes the installation and commissioning of a low-β insertion consisting of additional quadrupole magnets (Fig. 6.4), which is required to transport the stored beam through the narrow storage cell of the internal polarized target. The betatron function at the storage cell target should be about $\beta_x = \beta_y = 0.3$. Since one AD quadrupole magnet has to be removed

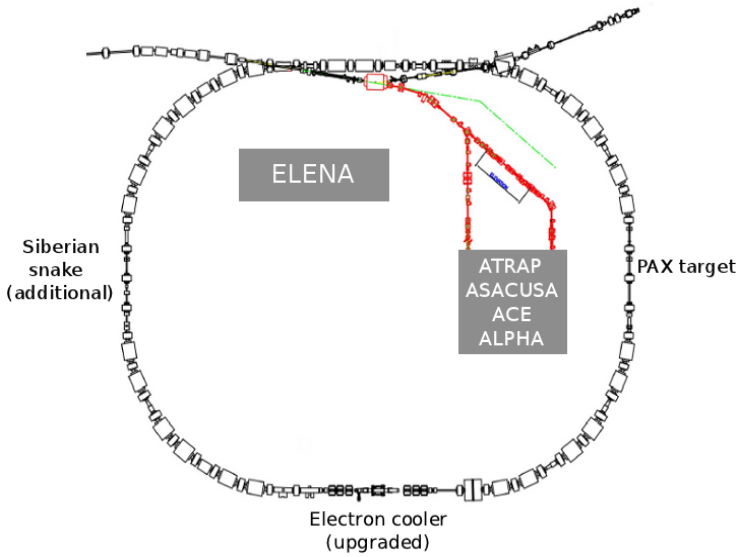

Fig. 6.2.: Schematic drawing of the Antiproton Decelerator AD at CERN. The injected and decelerated antiproton beam is cooled by an electron cooler, which will be upgraded to 300 keV at a later stage. The polarization build-up in the circulating beam is based on the interaction with the polarized H or D target. Spin filtering with longitudinal polarization requires the installation of a Siberian Snake in the opposite straight section of the target.

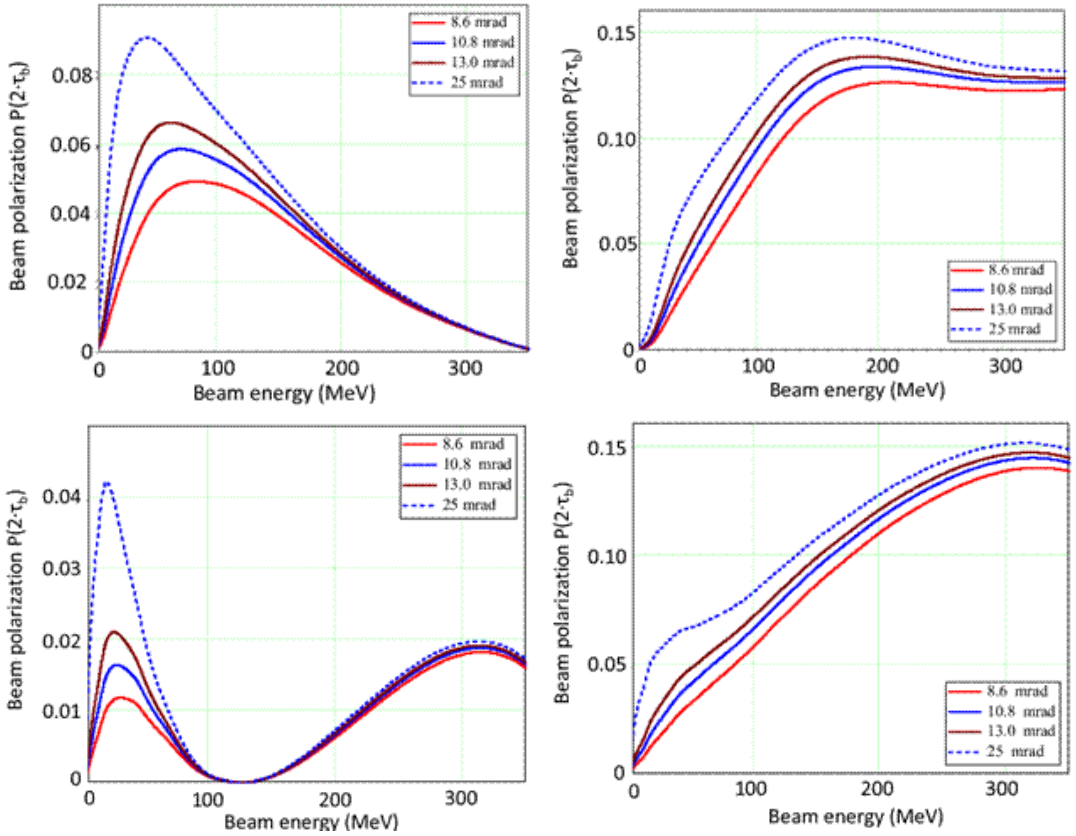

Fig. 6.3.: Estimated beam polarizations at AD after filtering for two lifetime as a function of the beam energy [61]. The panels on the left and on the right are for transverse and longitudinal polarization, respectively. The panels in the top row are for model A [160] and in the bottom for model D [161].

prior to the installation of the target chamber, the machine development shall ensure that all regular AD operations can be accomplished without this magnet.
Phase II of the anticipated program at AD starts with the installation of the target chamber, which together with an implemented frame system as used at COSY (Sec. 3.1.4) allows one to determine the machine acceptance, and the machine acceptance angle at the target position. In addition, studies on the increase of the beam intensity will be carried out using stacking of antiprotons into the AD. Subsequently the polarized internal target consisting of an ABS, a BRP, and the openable storage cell will be installed together with the PAX detector system in the straight section between injection and electron cooling. All components shall be tested and commissioned at COSY.
After a measurement of the target polarization with H or D injected into the storage cell, a first spin-filter measurement using the existing electron cooler at AD is planned at energies below $T_{\bar{p}} = 70\,\mathrm{MeV}$ for transverse polarization. An upgrade of the electron cooler from $30\,\mathrm{keV}$ to $300\,\mathrm{keV}$ makes it possible to expand the energy range for spin-filtering studies up to $450\,\mathrm{MeV}$. A measurement of σ_1 up to this energy is planned afterwards.
For a determination of σ_2 the stable spin direction has to be longitudinal at the target position. Thus, a solenoidal Siberian snake is going to be implemented in the opposite straight section (Fig. 6.2). Finally, spin-filtering studies will be carried out with longitudinally polarized target.

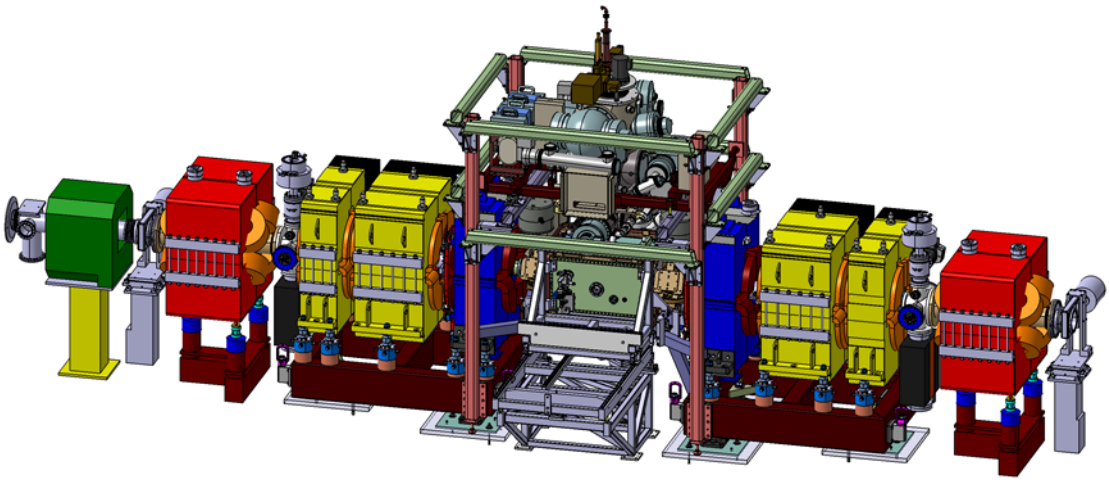

Fig. 6.4.: Complete PAX installation foreseen at the AD. The antiproton beam moves from left to right. Displayed are the already existing AD quadrupole magnets (red), the COSY quadrupole magnets (yellow) and quadrupole magnets recaptured from the CELSIUS ring (blue). The target chamber that houses the detector system is connected to the ABS (above) and the BRP (backside).

Appendices

A. Approximations for Intensity and Figure of Merit

This appendix deals with the question how good the approximations, made in Sec. 2.4, describe the behavior of the beam intensity, the beam polarization and the figure of merit. Definition of parameters:

- I_0 initial beam intensity,
- Q target polarization,
- P beam polarization,
- d_t target density,
- f_rev revolution frequency,
- σ_sum total spin-independent cross section, including single Coulomb, hadronic scattering, as well as Touschek effect,
- $\tilde{\sigma}_1$ spin-dependent cross section

The beam lifetime τ and the polarization build-up time τ_P are defined as

$$\tau = (d_\mathrm{t} \cdot f_\mathrm{rev} \cdot \sigma_\mathrm{sum})^{-1} \tag{A.1}$$

$$\tau_\mathrm{P} = (d_\mathrm{t} \cdot f_\mathrm{rev} \cdot \tilde{\sigma}_1 \cdot Q)^{-1} \tag{A.2}$$

The beam intensity is given as

$$I(t) = I_0 \cdot \exp\left(-\frac{t}{\tau}\right) \cdot \cosh\left(\frac{t}{\tau_\mathrm{P}}\right). \tag{A.3}$$

The polarization growth with time is

$$P(t) = \tanh\left(\frac{t}{\tau_\mathrm{P}}\right). \tag{A.4}$$

The figure of merit which describes the degree of usefulness of a beam of intensity I and polarization P is defined as

$$\mathrm{FOM}(t) = P(t)^2 \cdot I(t). \tag{A.5}$$

The solution of $\frac{d}{dt}\mathrm{FOM}(t) = 0$ defines the filtering time when the polarized beam obtained from spin filtering comprises the maximal information.

A.1. Exact Calculations

The beam intensity and polarization build-up are used as in Eq. (A.3) and (A.4). Thus the derivative is

$$\begin{aligned}\frac{d}{dt}\mathrm{FOM}(t) = & I_0 \cdot \frac{1}{\tau_\mathrm{P}} \cdot \sinh\left(\frac{t}{\tau_\mathrm{P}}\right) \cdot \tanh\left(\frac{t}{\tau_\mathrm{P}}\right)^2 \cdot \exp\left(-\frac{t}{\tau}\right) \\ & - I_0 \cdot \frac{1}{\tau} \cdot \cosh\left(\frac{t}{\tau_\mathrm{P}}\right) \cdot \tanh\left(\frac{t}{\tau_\mathrm{P}}\right)^2 \exp\left(-\frac{t}{\tau}\right) \\ & - 2I_0 \cdot \frac{1}{\tau_\mathrm{P}} \cdot \cosh\left(\frac{t}{\tau_\mathrm{P}}\right) \cdot \tanh\left(\frac{t}{\tau_\mathrm{P}}\right) \cdot \exp\left(-\frac{t}{\tau}\right) \cdot \left(\tanh\left(\frac{t}{\tau_\mathrm{P}}\right)^2 - 1\right) \\ & = 0.\end{aligned} \tag{A.6}$$

Reducing and dividing by $\cosh\left(\frac{t}{\tau_\mathrm{P}}\right)$ results in

$$0 = -\frac{1}{\tau_\mathrm{P}} \cdot \tanh\left(\frac{t}{\tau_\mathrm{P}}\right)^2 - \frac{1}{\tau} \cdot \tanh\left(\frac{t}{\tau_\mathrm{P}}\right) + \frac{2}{\tau_\mathrm{P}}. \tag{A.7}$$

Therefore, the optimal filtering time t_opt solves the following equation

$$\boxed{0 = \tanh\left(\frac{t_\mathrm{opt}}{\tau_\mathrm{P}}\right)^2 + \frac{\tau_\mathrm{P}}{\tau} \cdot \tanh\left(\frac{t_\mathrm{opt}}{\tau_\mathrm{P}}\right) - 2}. \tag{A.8}$$

A.2. Approximate Calculations

Since $\tilde{\sigma}_1$ is expected to be small in comparison to σ_sum and thus τ_P is large, the following approximations are reasonable:

$$\cosh\left(\frac{t}{\tau_\mathrm{P}}\right) = 1 \tag{A.9}$$

$$\tanh\left(\frac{t}{\tau_\mathrm{P}}\right) = \frac{t}{\tau_\mathrm{P}}. \tag{A.10}$$

Thus it follows

$$I(t) = I_0 \cdot \exp\left(-\frac{t}{\tau}\right) \qquad \text{and} \tag{A.11}$$

$$P(t) = \frac{t}{\tau_\mathrm{P}}. \tag{A.12}$$

The optimal filtering time t_opt can now be calculated as

$$\frac{d}{dt}\mathrm{FOM}(t) = \left(\frac{t}{\tau_\mathrm{P}}\right)^2 I_0 \cdot \exp\left(-\frac{t}{\tau}\right) = \frac{2I_0 \cdot t \cdot \exp\left(-\frac{t}{\tau}\right)}{\tau_\mathrm{P}^2} - \frac{I_0 \cdot t^2 \cdot \exp\left(-\frac{t}{\tau}\right)}{\tau \cdot \tau_\mathrm{P}^2} = 0, \tag{A.13}$$

which leads to

$$\boxed{t_\mathrm{opt} = 2 \cdot \tau}. \tag{A.14}$$

A.3. Comparison of Results

In order to evaluate how well the approximations work, measured values for FILTEX and realistic parameters for the spin-filtering experiment at COSY can be inserted (Tab. A.1).
Since τ_P for FILTEX is significantly smaller than at COSY, the deviation between exact calculations (Eqs. (A.3), (A.4), and (A.8)) and approximations (Eqs. (A.11), (A.12), and (A.14)), if there are some, should be larger for FILTEX. Therefore, the intensity over time as well as the polarization and the figure of merit are displayed in Fig. A.1 for the exact and approximate calculations. The exact curves are plotted in color, whereas the approximation is displayed in black. As on can see, there is no visible deviation for all three curves.

Experiment	$I_0(p)$	$\tau(\mathrm{s})$	$f_\mathrm{rev}(\mathrm{Hz})$	$d_\mathrm{t}(\mathrm{atoms/cm^2})$	Q	$\tilde{\sigma}_1(\mathrm{mb})$	$\tau_\mathrm{P}(\mathrm{s})$
FILTEX	$2 \cdot 10^{10}$	1800	$1.1767 \cdot 10^6$	$5.3 \cdot 10^{13}$	0.795	73.0	$2.763 \cdot 10^5$
COSY	$2 \cdot 10^{10}$	3600	$5.1059 \cdot 10^5$	$4.35 \cdot 10^{13}$	0.7	26.9	$2.400 \cdot 10^6$

Table A.1.: Simulation input parameters for spin-filtering at FILTEX [87] and COSY.

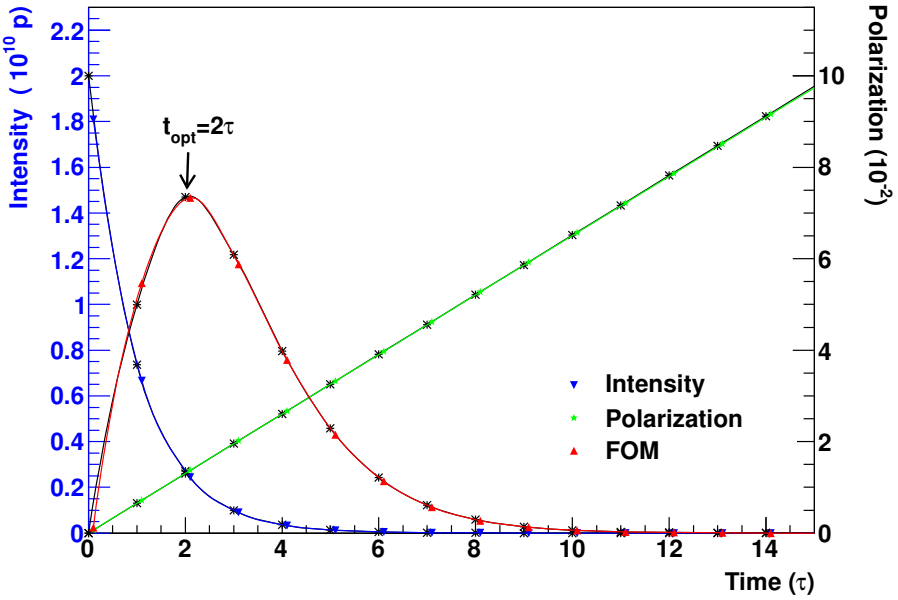

Fig. A.1.: Comparison of exact (blue,green, and red) and approximate (black) calculations for the beam intensity, the polarization and the FOM. Here the FOM is scaled in order to be displayed together with I and P.

For this reason the ratio $I_\mathrm{exact}/I_\mathrm{approx}$ is displayed in Fig. A.3 (left) for the assumed parameters at COSY and FILTEX. As one can see the intensity deviation increases with increasing lifetime does not exceed $1\,\%$ (for FILTEX) even if spin filtering would be carried out for 20 beam lifetimes. Since the filtering time is usually about 2τ, this deviation can be neglected. In case of COSY the deviation does not even exceed $1\,‰$ after 20τ.
In addition the optimal filtering time has been calculated precisely for both experiments. The graph on the right hand side of Fig. A.3 displays $t_\mathrm{opt}/2\tau$, where 2τ is the optimal filtering time for the approximate calculation, as a function of the beam lifetime. At FILTEX the relative shift of the optimal filtering time would be about $3 \cdot 10^{-5}$ for the observed lifetimes of $1800\,\mathrm{s}$. For the spin-filtering experiments at COSY a deviation of 1% would be reached in case of

$\tau \approx 300000\,\mathrm{s}$. Even in an optimal case the lifetime for none of these experiments is larger than $10000\,\mathrm{s}$ which makes $t_{\mathrm{opt}} = 2\tau$ a very reasonable approximation.

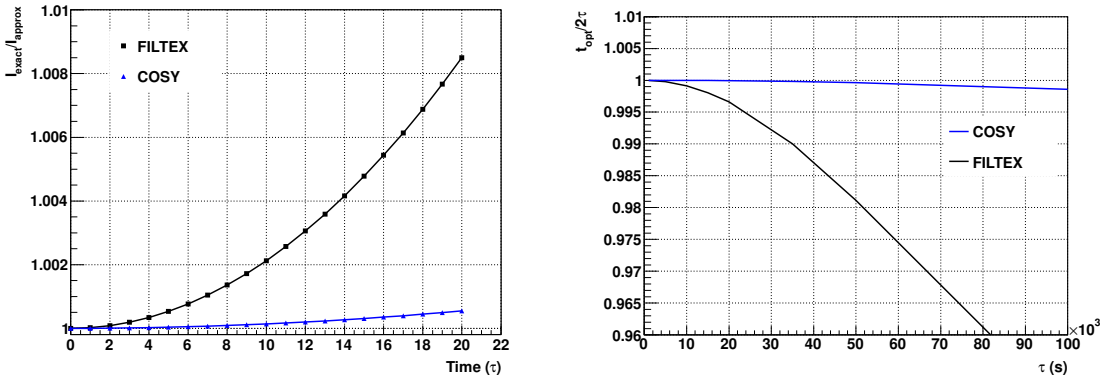

Fig. A.2.: Left: $I_{\mathrm{exact}}/I_{\mathrm{approx}}$ as a function of the filtering time for FILTEX (black) and COSY (blue). **Right:** Optimal filtering time t_{opt} (in units of τ) as a function of the beam lifetime τ.

B. Determination of the Optimal Cycle

As explained in Sec. 2.4, the maximum figure of merit ($FOM(t) = P^2(t) \cdot I(t)$) is reached after filtering for two beam lifetimes ($t_\mathrm{F} = 2\tau_\mathrm{F}$). Thus the quality of the polarized beam in terms of a measurement of the beam polarization or a subsequent application is optimized. Taking into account a complete spin-filtering cycle consisting of a filtering time t_F and a measurement time t_M changes the situation. An exemplary calculation of the optimal cycle based on experiment simulations, using the expected conditions at COSY is given below.
The general goal of the experiment is to measure the beam polarization after filtering with highest possible precision. Thus $\Delta P/P$ as a function of the filtering time and the measurement time has to be minimal.
The following parameters for the beam lifetimes with polarized gas target τ_F, with cluster target τ_M, and the initial beam intensity I_0 are assumed:

$$I_0 = 1 \cdot 10^{10} \qquad \tau_\mathrm{F} = 5000\,\mathrm{s} \qquad \tau_\mathrm{M} = 1500\,\mathrm{s}. \tag{B.1}$$

According to the calculations in Sec. 5.1 the expected polarization as a function of the time is

$$P(t) = \begin{cases} \frac{0.0019}{3600\,\mathrm{s}} \cdot t & \text{for } t < t_\mathrm{F} \\ P(t_\mathrm{F}) & \text{for } t > t_\mathrm{F} \end{cases}$$

Here the polarization is supposed to grow linear with time during filtering (with the initial polarization $P(t=0) = P_0 = 0$) and remains constant during the measurement period. The beam intensity follows

$$I(t) = \begin{cases} I_0 \cdot \exp\left(\frac{-t}{\tau_\mathrm{F}}\right) & \text{for } t < t_\mathrm{F} \\ I_0 \cdot \exp\left(\frac{-t_\mathrm{F}}{\tau_\mathrm{F}}\right) \cdot \exp\left(\frac{-(t-t_\mathrm{F})}{\tau_\mathrm{M}}\right) & \text{for } t > t_\mathrm{F}. \end{cases}$$

The complete cycle time is given as

$$T_\mathrm{cycle} = t_\mathrm{F} + t_\mathrm{M} = n_\mathrm{F} \cdot \tau_\mathrm{F} + n_\mathrm{M} \cdot \tau_\mathrm{M}, \tag{B.2}$$

where the filtering and the measurement time are given in numbers of the lifetime during filtering and measurement respectively. Assuming a beam time of 30 days defines the number of cycles n_cycles in dependence of n_F and n_M for given lifetimes.
The accomplished simulations described in Sec. 5 yield an error ΔP of about 0.02 for a $60\,\mathrm{s}$ measurement assuming $d_\mathrm{t} = 5 \cdot 10^{13}$ and $I_0 = 1 \cdot 10^{10}$. These ingredients enable an estimation of the total error in dependence on the cycle structure. The measurement time is divided into intervals i with $\Delta T = 10\,\mathrm{s}$ and the error per interval is calculated by

$$\Delta P_i(t_i, t_\mathrm{F}, t_\mathrm{M}, \tau_\mathrm{F}, \tau_\mathrm{M}) = \frac{0.02 \cdot \sqrt{\frac{60\,\mathrm{s}}{\Delta T}} \sqrt{\frac{I_0}{I(t_i, t_\mathrm{F}, t_\mathrm{M}, \tau_\mathrm{F}, \tau_\mathrm{M})}}}{\sqrt{n_\mathrm{cycles}}}. \tag{B.3}$$

Calculating the weighted average of the beam polarization

$$P_{\mathrm{av}} = \frac{\sum_i \left[\frac{1}{(\Delta P_i)^2} \cdot P_i\right]}{\sum_i \frac{1}{(\Delta P_i)^2}} \tag{B.4}$$

and the error

$$\Delta P = \frac{1}{\sqrt{\sum_i \left[\frac{1}{(\Delta P_i)^2}\right]}} \tag{B.5}$$

allows one to calculate $\Delta P/P$ for different filtering and measuring times. The resulting $\Delta P/P$ as function t_{F} and t_{M}, which are given in numbers of the corresponding lifetimes, is plotted in Fig. B.1. The rather flat minimum is located at about $t_{\mathrm{F}} = 1.5 \cdot \tau_{\mathrm{F}}$ and $t_{\mathrm{M}} = 2.5 \cdot \tau_{\mathrm{M}}$ for the lifetimes as assumed above.

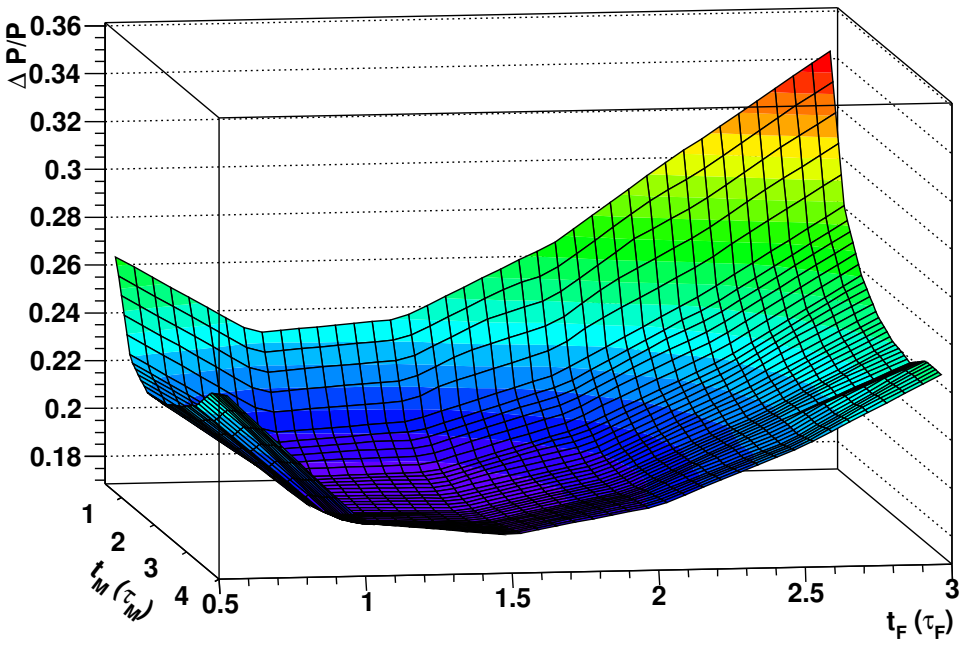

Fig. B.1.: Expected $\Delta P/P$ as a function of the filtering time and the measurement time. The optimal cycle is defined by the minimum of $\Delta P/P$.

C. Holding Field System

The magnetic holding field system of the PIT provides magnetic fields of about $1\,\mathrm{mT}$ in beam direction (s) and transverse to the circulating beam (x, y). In addition to the requirements to the magnetic field, the $\int B \cdot ds$ has to be compensated in $x-$ and $y-$ direction, which requires additional coils. The coils providing the holding field are mounted directly on the target chamber. A special geometry of three compensation coils mounted on the beam tubes up- and downstream of the target chamber (see Fig. 3.17) is the best solution to fulfill the mentioned requirements and fit to the spatial frame conditions [125].

The working modes for target polarization pointing in $x-$, $y-$, and $z-$ direction are described in the following.

$x-$direction: The magnetic field is applied by the coils mounted left and right of the target chamber (looking in beam direction). This field is compensated by powering the two upper coils of each compensation group in the correct way (see Fig. C.1). The vertical magnetic component evoked by each compensation coil is compensated by its partner, since they point in opposite directions. The horizontal components add up and compensate the horizontal component evoked by the holding field coils. A calculation that shows the horizontal magnetic field along s is given in the top right panel of Fig. 3.18.

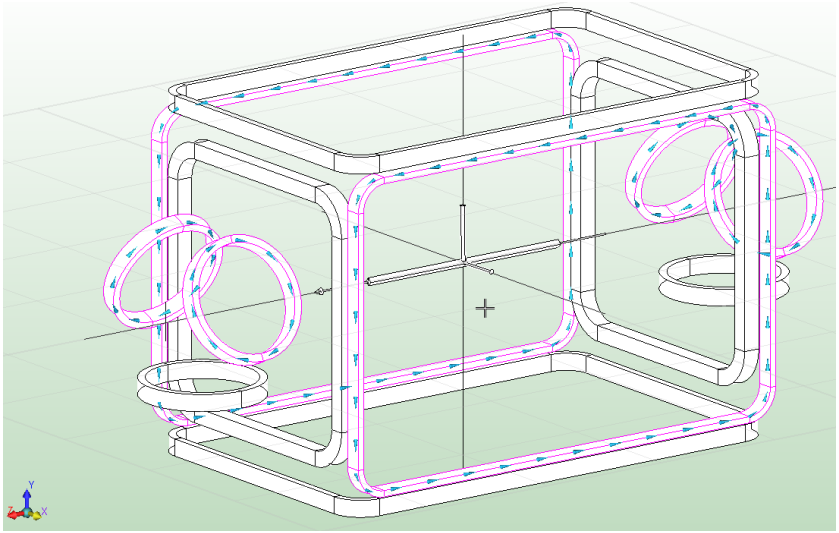

Fig. C.1.: Setting for holding field in $+x$-direction. The beam is moving from left to the right side. The magnetic field applied by the coils left and right of the moving beam is compensated by powering the two upper coils of each compensation coil group in the correct way.

$y-$direction: The magnetic field is applied by the coils mounted above and below the target chamber. It is compensated by powering all three coils of each compensation group in the correct way (see Fig. C.2). The horizontal magnetic component evoked by each of the two upper compensation coils is compensated by its partner, since they point in opposite directions. The vertical components of all three coils add up and compensate

the vertical magnetic field evoked by the holding field coils. A calculation that shows the vertical magnetic field along s is given in the middle right panel of Fig. 3.18.

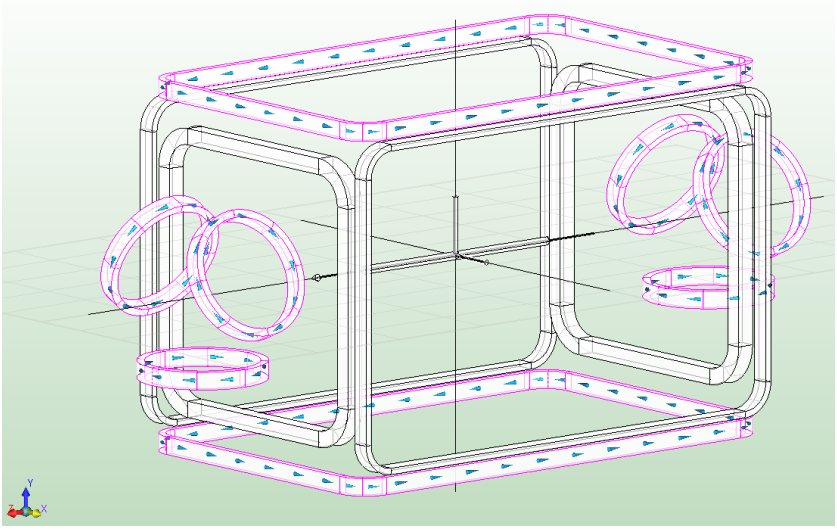

Fig. C.2.: Setting for holding field in $+y$-direction. The magnetic field applied by the coils above and below the target chamber is compensated by powering all three coils of each compensation coil group in the correct way.

$s-$**direction:** The magnetic field is applied by the coils mounted in front and behind the target chamber (looking in beam direction). Since the longitudinal magnetic field has not to be compensated in this case since $\vec{v} \times \vec{B} = 0$ the compensation coils are not powered (see Fig. C.3).

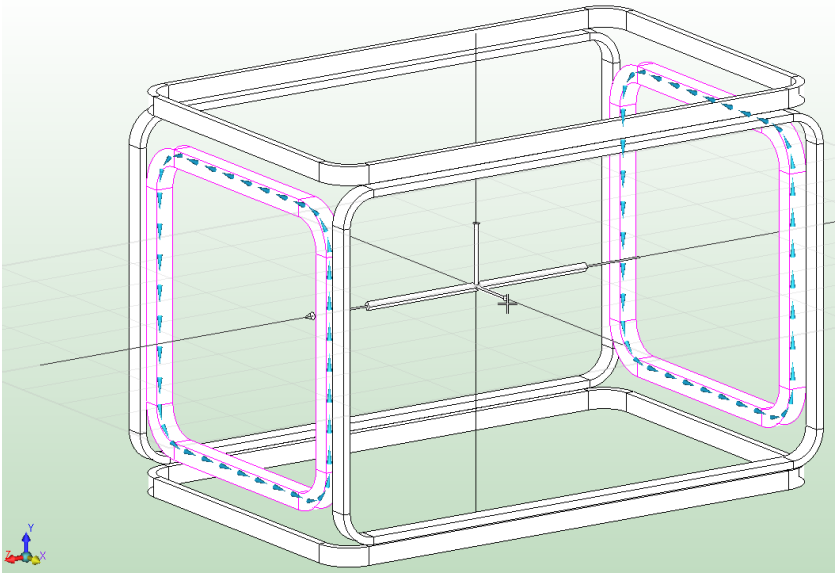

Fig. C.3.: The magnetic field is applied by the coils in front and behind the target chamber (in beam direction). the compensation coils are not powered.

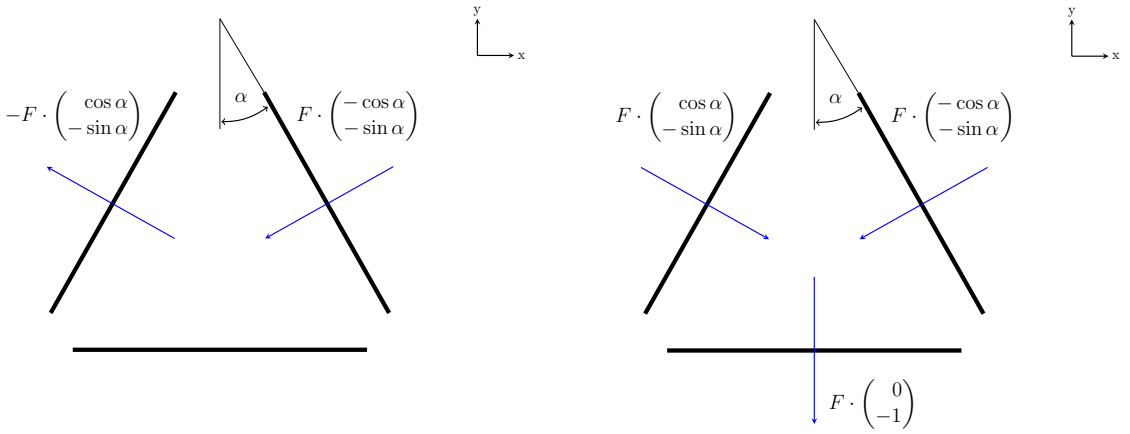

Fig. C.4.: Compensation field components for the compensation of a horizontal (left) and vertical (right) magnet holding field. F is the field integral of the compensation coils.

The optimal angle α and the magnetic field integral F of the three compensation coils is defined by the applied magnetic field $B_{x,y}$, which has to be compensated. Using G_x and G_y as magnetic field integral of the horizontal and vertical holding field, it can be calculated as follows.
Compensation of the horizontal magnetic field (x) (see Fig. C.4 left):

$$\vec{0} = \begin{pmatrix} G_x \\ 0 \end{pmatrix} + 0 \cdot \begin{pmatrix} 0 \\ -1 \end{pmatrix} - F \cdot \begin{pmatrix} \cos\alpha \\ -\sin\alpha \end{pmatrix} + F \begin{pmatrix} -\cos\alpha \\ -\sin\alpha \end{pmatrix}. \tag{C.1}$$

Compensation of the vertical magnetic field (y) (see Fig. C.4 right):

$$\vec{0} = \begin{pmatrix} 0 \\ G_y \end{pmatrix} + F \cdot \begin{pmatrix} 0 \\ -1 \end{pmatrix} + F \cdot \begin{pmatrix} \cos\alpha \\ -\sin\alpha \end{pmatrix} + F \begin{pmatrix} -\cos\alpha \\ -\sin\alpha \end{pmatrix}. \tag{C.2}$$

Thus, the system of equations, which has to be solved is

$$0 = G_x - 2F \cdot \cos\alpha, \tag{C.3}$$
$$0 = G_y - F - 2F \cdot \sin\alpha. \tag{C.4}$$

The resulting field integral and angle of the compensation coils are given as

$$\alpha = \arctan\left(\frac{G_y - F}{G_x}\right), \tag{C.5}$$
$$F = \frac{1}{3}\left(\sqrt{4G_y^2 + 3G_x^2} - G_y\right). \tag{C.6}$$

Inserting the expected magnetic field integrals $G_x = 0.85256$ and $G_y = 0.87611$ yields a compensation field integral of

$$F = 0.472, \tag{C.7}$$

and optimal angle for the coils of

$$\alpha = 25.373°. \tag{C.8}$$

Additional coils mounted inside the compensation coils even allow for a compensation of holding fields under $45°$. The technical parameters are displayed in Fig. C.5.

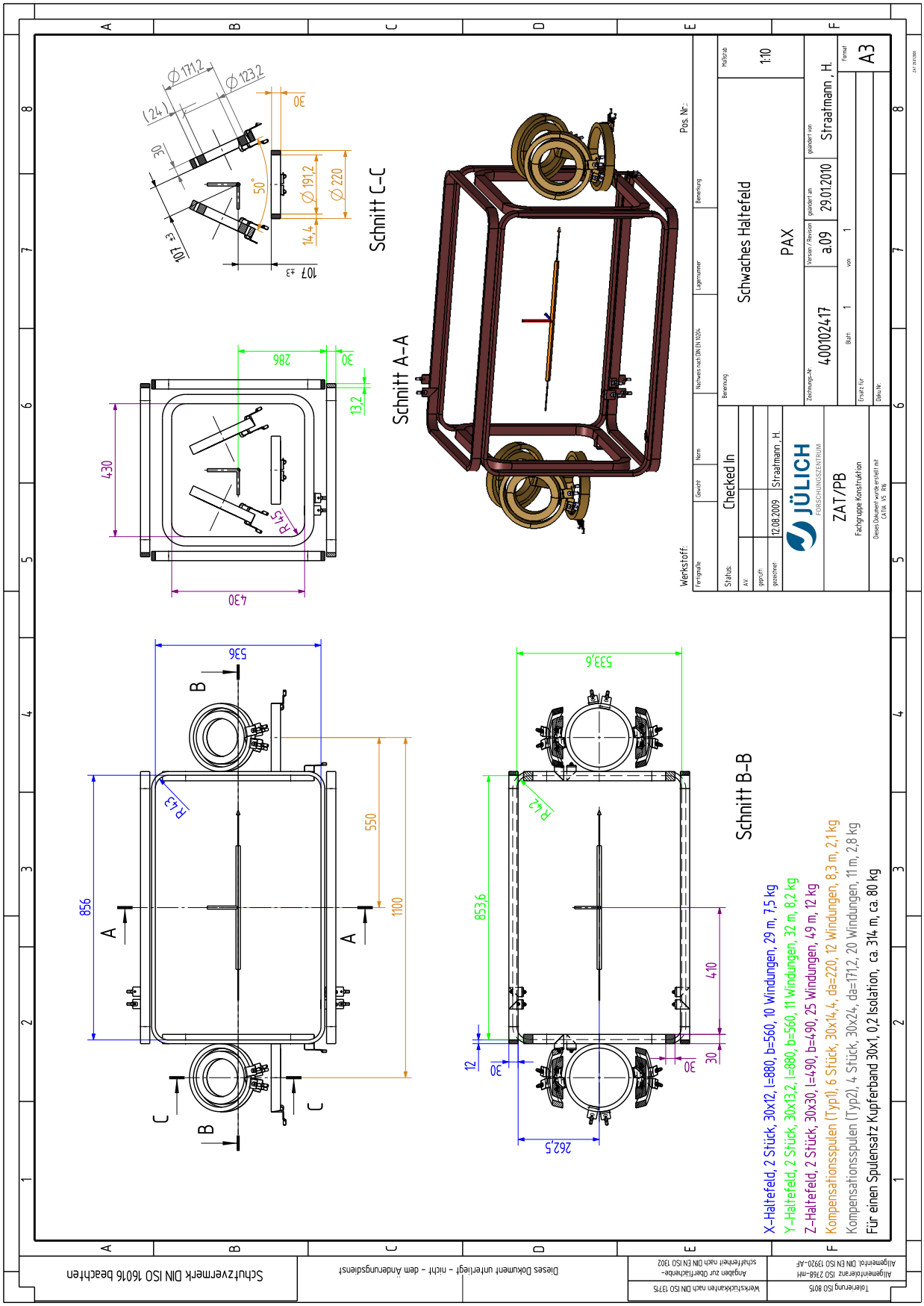

Fig. C.5.: Technical drawing of the magnetic holding field system.

D. Matrix Formalism and Measurement of the β Function

The betatron oscillations of a particle can be described by the linear equations of motion (Sec. 2.1.1)

$$x''(s) + \left(\frac{1}{\rho^2(s)} - k_x(s)\right) x(s) = \frac{1}{\rho(s)} \frac{\Delta p}{p}, \tag{D.1}$$

$$y''(s) + k_y(s) y(s) = 0. \tag{D.2}$$

For $\frac{\Delta p}{p} = 0$ a general form is [140]

$$z'' - K(s) \cdot z = 0, \tag{D.3}$$

where z represents either the horizontal or the vertical displacement ($z \in \{x, y\}$), and where $K(s)$ satisfies the periodicity relation

$$K(s + C) = K(s). \tag{D.4}$$

Here C is the circumference of the equilibrium orbit. The general solution of such linear second order differential equations has the form

$$z(s) = a z(s_0) + b z'(s_0), \tag{D.5}$$

$$z'(s) = c z(s_0) + d z'(s_0), \tag{D.6}$$

or in matrix notation,

$$Z(s) = \begin{bmatrix} z(s) \\ z'(s) \end{bmatrix} = M(s|s_0) Z(s_0) = \begin{bmatrix} a & b \\ c & d \end{bmatrix} \begin{bmatrix} z(s_0) \\ z'(s_0) \end{bmatrix}. \tag{D.7}$$

One feature of this transfer matrix formalism is, that the matrix describing any interval made up of sub-intervals is just the product, calculated by the usual rules of matrix multiplication, of the matrices for the sub-intervals, that is,

$$M(s_2|s_0) = M(s_2|s_1) M(s_1|s_0). \tag{D.8}$$

In the particular case of a constant K, it follows:

- for a focussing quadrupole ($K = k_z < 0$)

$$M_{\text{foc}} = \begin{pmatrix} \cos(\sqrt{|k_z|}s) & \frac{1}{\sqrt{|k_z|}} \sin(\sqrt{|k_z|}s) \\ -\sqrt{|k_z|} \sin(\sqrt{|k_z|}s) & \cos(\sqrt{|k_z|}s) \end{pmatrix}, \tag{D.9}$$

- and for a defocussing quadrupole ($K = k_z > 0$)

$$M_{\text{def}} = \begin{pmatrix} \cosh(\sqrt{k_z}s) & \frac{1}{\sqrt{k_z}}\sinh(\sqrt{k_z}s) \\ \sqrt{k_z}\sinh(\sqrt{k_z}s) & \cosh(\sqrt{k_z}s) \end{pmatrix}, \tag{D.10}$$

- for a dipole ($K = {}^{1}\!/_{\rho^2}$)

$$M_{\text{dip}} = \begin{pmatrix} \cos\left(\frac{s}{\rho}\right) & \rho\sin\left(\frac{s}{\rho}\right) \\ -\frac{1}{\rho}\sin\left(\frac{s}{\rho}\right) & \cos\left(\frac{s}{\rho}\right) \end{pmatrix}, \tag{D.11}$$

- for a drift region without forces ($K = 0$) has the matrix

$$M_{\text{drift}} = \begin{pmatrix} 1 & s \\ 0 & 1 \end{pmatrix}. \tag{D.12}$$

In order to reconstruct the particle movement along one turn in the ring, the N transfer matrices $M_1, M_2, ..., M_N$ of all contributing elements have to be multiplied in the correct order

$$M = M_N \circ ... \circ M_2 \circ M_1 = \prod_{1 \le i \le N} M_i. \tag{D.13}$$

The general form of the one turn matrix (Twiss matrix) that describes the particle motion is given (see [140]) by

$$M = \begin{pmatrix} \cos\Delta\psi + \alpha\sin\Delta\psi & \beta\sin\Delta\psi \\ -\gamma\sin\Delta\psi & \cos\Delta\psi - \alpha\sin\Delta\psi \end{pmatrix}, \tag{D.14}$$

where α, β and γ are the already known Twiss parameters and $\Delta\psi$ is the phase advance.

For the **determination of the local β-function** at the position of a quadrupole a small interval of length ds_1 near s_1 is considered. The corresponding transfer matrix of this quadrupole in the limit $\sqrt{k_0}ds_1 \ll 1$ is

$$m_0 = \begin{pmatrix} 1 & ds_1 \\ -k_0(s_1)ds_1 & 1 \end{pmatrix}. \tag{D.15}$$

Changing the quadrupole strength by a small amount $k(s_1)$ gives the new matrix

$$m = \begin{pmatrix} 1 & ds_1 \\ -[k_0(s_1) + k(s_1)]ds_1 & 1 \end{pmatrix}. \tag{D.16}$$

The modified general matrix M can now be defined by multiplying m and m_0^{-1} from the left to M. In case of small changes, quadratic terms are allowed to be neglected ($(ds_1)^2 \approx 0$). Therefore it follows

$$mm_0^{-1} = \begin{pmatrix} 1 & 0 \\ -k(s_1)ds_1 & 1 \end{pmatrix}. \tag{D.17}$$

Equalizing the trace of the new transfer matrix ($mm_0^{-1}M$) and the general transfer matrix M results in the following correlation

$$\text{tr}M = 2\cos\Delta\psi = 2\cos\Delta\psi_0 - (\beta\sin\Delta\psi_0)k(s_1)ds_1, \tag{D.18}$$

which, by insertion of the phase advance $\Delta\psi = 2\pi \cdot Q$ (Eq. 2.4), the length l, and the quadrupole strength Δk, allows one to extract β

$$\beta = -\frac{2}{l \cdot \Delta k} \frac{\cos(2\pi Q) - \cos(2\pi Q_0)}{\sin(2\pi Q_0)}. \tag{D.19}$$

Here Q_0 is the unperturbed working point. Since the changes of k and therewith of Q are small, a Taylor expansion of the β-function for $Q = Q_0$ up to the second order can be applied [162]

$$\beta \approx \frac{4\pi}{l\Delta k}(1 + \pi\Delta Q \cot(2\pi Q_0))\Delta Q. \tag{D.20}$$

Consequently a change of the quadrupole strength causes a change of the working point, which, by measuring both parameters, allows one to determine β.

E. Estimation of the Target Density from the Cell Dimensions

The spin-filtering experiment requires a high areal target density of up to $5 \cdot 10^{13}\,\mathrm{atoms/cm^2}$. For a given intensity of the injected beam I, the areal density d_t (atoms/cm^2) depends on the length of the storage cell tube l_t and the total conductance of the cell C_tot [163]:

$$d_\mathrm{t} = \frac{1}{2} \cdot \frac{l_\mathrm{t} \cdot I}{C_\mathrm{tot}}. \tag{E.1}$$

As a consequence of this formula, it is already clear that the length of the cell and the injected intensity have to be maximized in order to reach highest target densities. The total conductance of the storage cell system can be calculated by

$$C_\mathrm{tot} = 2 \cdot C_\mathrm{halftube} + C_\mathrm{feed} + C_\mathrm{extract}, \tag{E.2}$$

with C_halftube the conductance of one arm of the cell, C_feed the conductance of the feeding tube from the ABS, and C_extract the conductance of the extraction tube to the BRP. The dimensions of the cell are shown in Fig. E.1 and E.2.
The conductance of a tube with rectangular cross section can be calculated by (Eq. [3.110] in [163])

$$C = 9.71 \cdot 10^{-2} \cdot \sqrt{\frac{T}{M}} \frac{a^2 b^2 \cdot K}{[(a+b) \cdot l_\mathrm{t} + 2.66 \cdot a \cdot b]}. \tag{E.3}$$

Here $T(\mathrm{K})$ is the temperature, $M(\mathrm{amu})$ is the molecular mass, $a(\mathrm{mm})$ and $b(\mathrm{mm})$ are the side lengths, and K is an experimental correction factor ($K = 1.108$ for $a = b$).
The conductance of a short tube with uniform circular cross section such as the feeding and the extraction tube is given by (Eq. [3.108] in [163])

$$C = 3.81 \cdot 10^{-2} \cdot \sqrt{\frac{T}{M}} \frac{d_\mathrm{e,f}^3}{l_\mathrm{e,f} + 1.33 \cdot d_\mathrm{e,f})}. \tag{E.4}$$

Since the extraction tube consists of two tubes of different dimensions connected in series, the total conductance of the extraction tube can be calculated as reciprocal of the inverse sum of the individual conductances:

$$C_\mathrm{extract} = \left(\frac{1}{C_\mathrm{e1}} + \frac{1}{C_\mathrm{e2}} \right)^{-1}. \tag{E.5}$$

For the calculation of the conductances the dimensions as given in the figures E.1 and E.2 are used together with the temperature $T = 300\,\mathrm{K}$, and the molecular mass $M = 1\,\mathrm{amu}$.
Combining the individual conductances

$$C_\mathrm{halftube} = 3.892\,\mathrm{l/s}, \tag{E.6}$$
$$C_\mathrm{feed} = 5.807\,\mathrm{l/s}, \tag{E.7}$$
$$C_\mathrm{extract} = 1.259\,\mathrm{l/s}, \tag{E.8}$$

as in Eq. (E.2), yields the total conductance of the storage cell system of

$$C_{\text{total}} = 14.85\,\text{l/s}. \tag{E.9}$$

Using $I = (3.05 \pm 0.15) \cdot 10^{16}\,\text{atoms/s}$ for 1 state injected from the ABS [146] the expected target density for the given geometry is

$$\boxed{d_{\text{t}} = \tfrac{1}{2} \cdot \tfrac{l_{\text{t}} \cdot I}{C_{\text{tot}}} = (4.1 \pm 0.2) \cdot 10^{13}\,\text{atoms/cm}^2}. \tag{E.10}$$

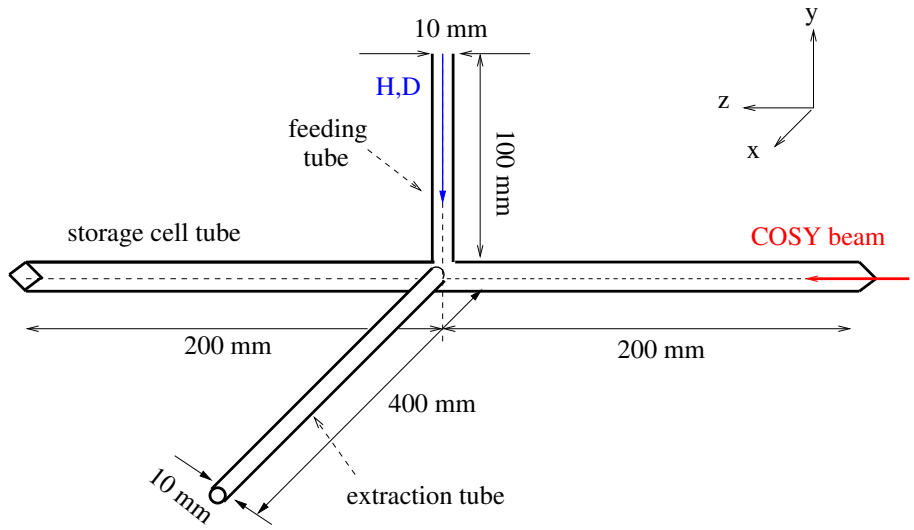

Fig. E.1.: Side view of the storage cell. The polarized atomic beam is focused by the last sextupole magnet of the ABS and is injected from the top. A small fraction of the atoms leave the cell through the extraction tube into the BRP which measures the polarization of that sample. Coming from the cell, the first 20 mm of the extraction tube have a diameter of just 6 mm (not drawn).

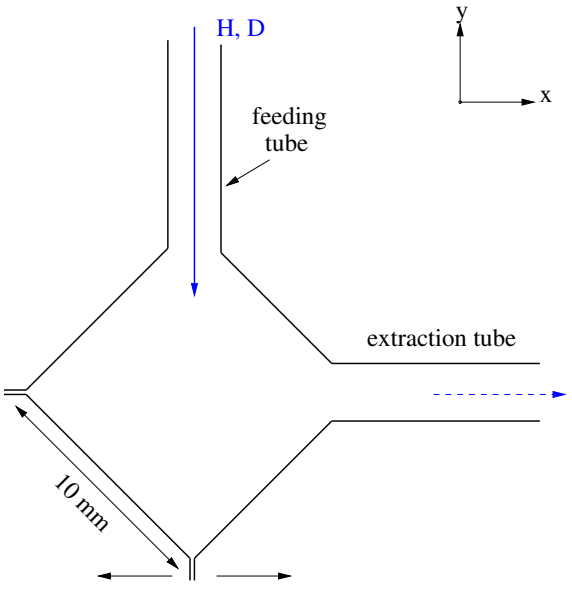

Fig. E.2: Cut through the center of the storage cell. The cell walls, made from 5 µm teflon foil, are separately fixed for each quarter. The left-hand and right-hand halves of the cell are moved to open the cell.

F. PAX SEQUENCER

The sequencing for the spin-filtering experiment at COSY is presented in Fig. F.1. The cycle for detector commissioning and calibration of the BRP are shown in Fig. F.2 and F.3, respectively. The details of each cycle are in detail described in the corresponding captions.

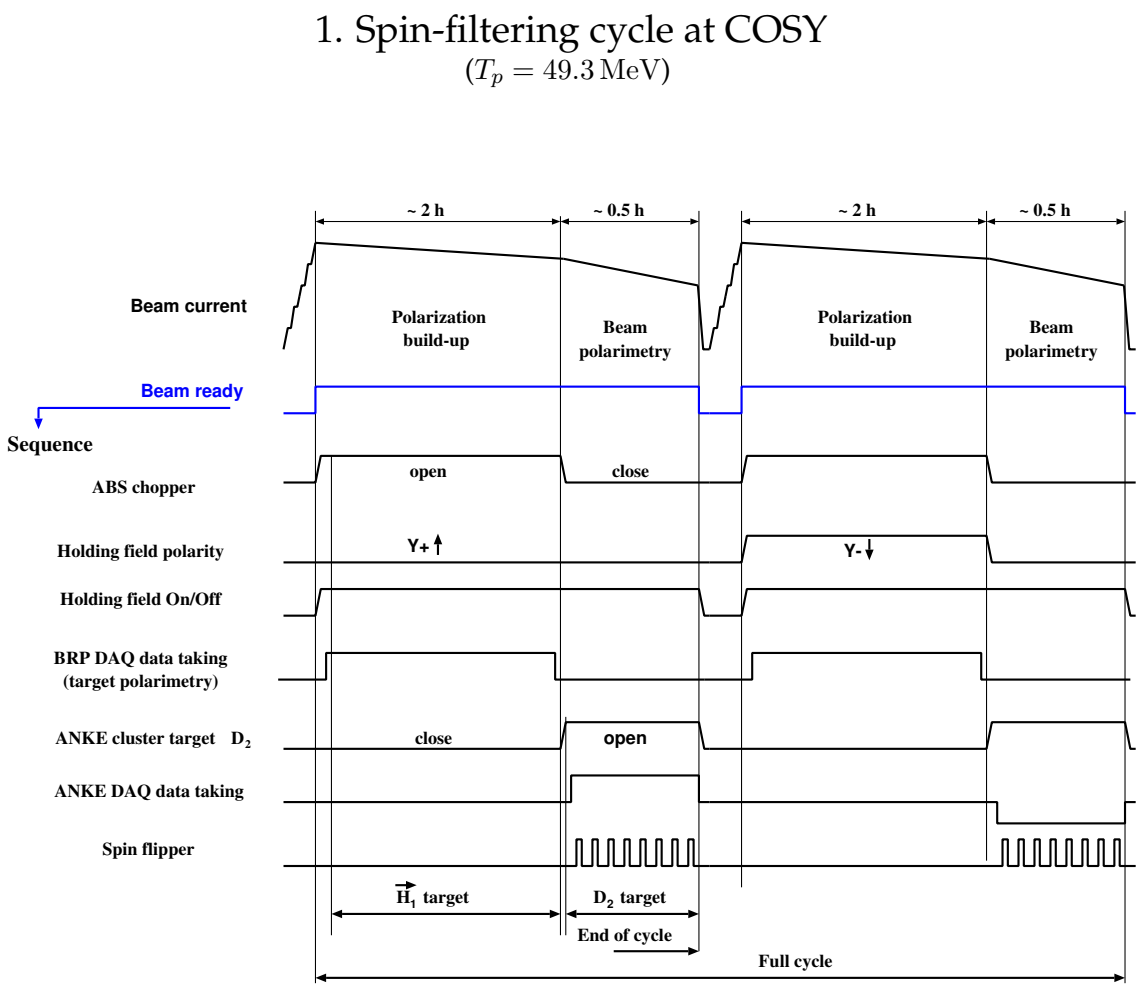

Fig. F.1.: Sequence of one spin-filtering cycle. During the polarization build-up the polarized internal target and its holding field is switched on (ABS chopper, Holding field). The BRP measures the target polarization. After filtering the ABS chopper is closed and the ANKE cluster target together with the ANKE DAQ is switched on in order to measure the p-beam polarization. During the measurement the polarization is flipped $5-8$ times in order to minimize systematic effects (Sec. 5.2.4). Subsequently the holding field polarity is reversed during polarization build-up.

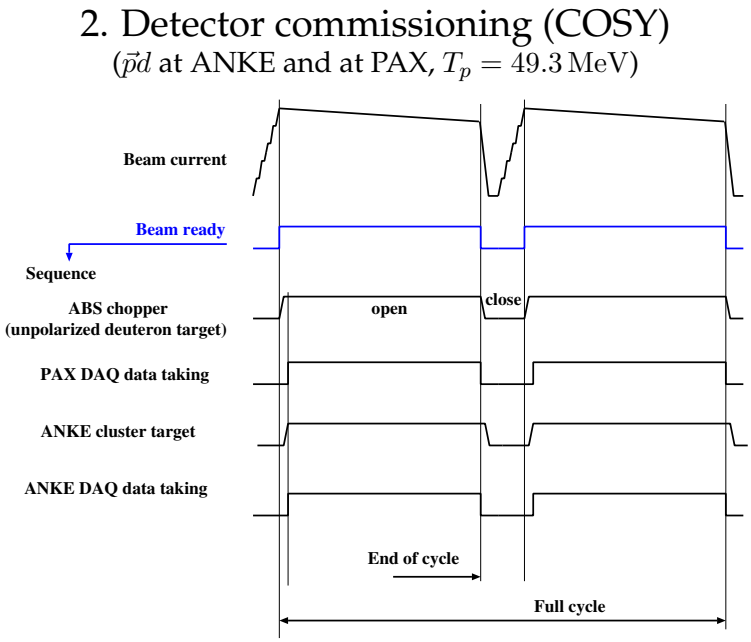

Fig. F.2.: The PAX detector will be commissioned by a measurement of the p-beam polarization in $\vec{p}d$ elastic scattering at ANKE and at PAX. A comparison of both measurements ensures that the new system work properly.

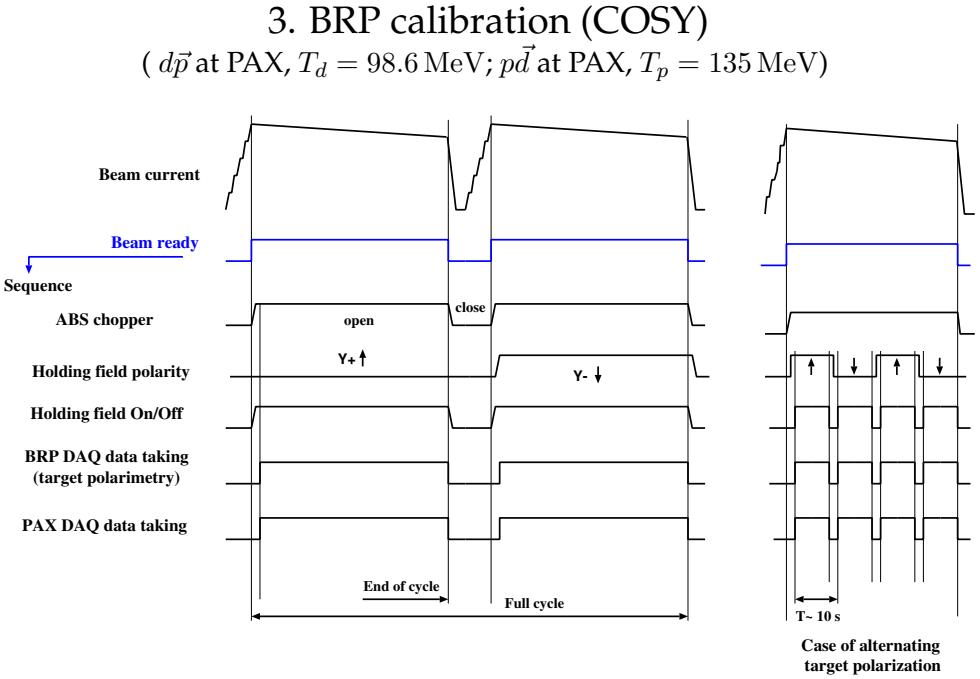

Fig. F.3.: The BRP will be absolutely calibrated by $d\vec{p}$ elastic scattering at PAX. The polarization of the polarized hydrogen gas target is measured with the PAX silicon strip detector using an unpolarized deuteron beam. The polarization of the deuterium gas target can be measured using the unpolarized proton beam at $T_p = 135\,\mathrm{MeV}$.

G. Summary of Experiment Simulations for the PAX Detector

The new PAX detector is well suited to measure all polarization observables in $\vec{p}\vec{p}$ and $\vec{\bar{p}}\vec{p}$ elastic scattering. Simulations of the proton beam polarization measurement using an internal polarized hydrogen gas target and the new detection system have been carried out. In the following the results are summarized.
The spin-dependent cross section for a polarized beam (spin $^1/_2$ particles) and a polarized target (spin $^1/_2$ particles) in units of the unpolarized cross section is given by [164]

$$\begin{aligned} X = \frac{\sigma}{\sigma_0} = 1 &+ A_y \left[(P_y + Q_y)\cos\phi - (P_x + Q_x)\sin\phi\right] \\ &+ A_{xx}\left[P_x Q_x \cos^2\phi + P_y Q_y \sin^2\phi + (P_x Q_y + P_y Q_x)\sin\phi\cos\phi\right] \\ &+ A_{yy}\left[P_x Q_x \sin^2\phi + P_y Q_y \cos^2\phi - (P_x Q_y + P_y Q_x)\sin\phi\cos\phi\right] \\ &+ A_{xz}\left[(P_x Q_z + P_z Q_x)\cos\phi + (P_y Q_z + P_z Q_y)\sin\phi\right] \\ &+ A_{zz} P_z Q_z . \end{aligned} \tag{G.1}$$

Here the analyzing power A_y and the double-spin asymmetries A_{mn} in terms of the nucleon-nucleon scattering matrix M are defined as in Eqs.(5.31) and (6.3) of Ref. [148]. $P_{x,y,z}$ and $Q_{x,y,z}$ are the components for beam and target polarization, respectively. The comoving coordinate system is defined as in Fig. 2.1 ($s \equiv z$).
The double-spin asymmetries A_{xx} (C_{xx}) and A_{yy} (C_{yy}) in pp elastic scattering for different energies are plotted in Fig. G.1 [165]. The figure of merit for the analyzing power and the double-spin asymmetries, defined by

$$FOM(\Theta) = A_{mn}^2 \cdot \frac{d\sigma}{d\Omega}, \tag{G.2}$$

is shown in Fig. G.2.

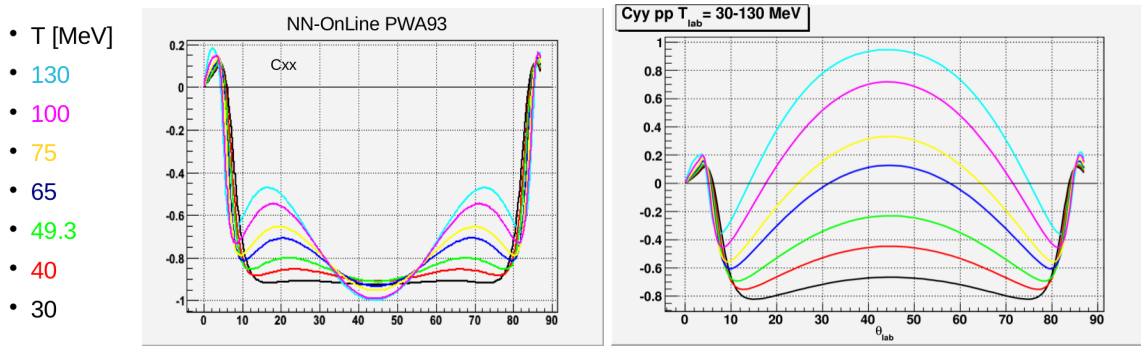

Fig. G.1.: The double-spin asymmetries A_{xx} and A_{yy} in pp elastic scattering as a function of the scattering angle for different kinetic energies [165].

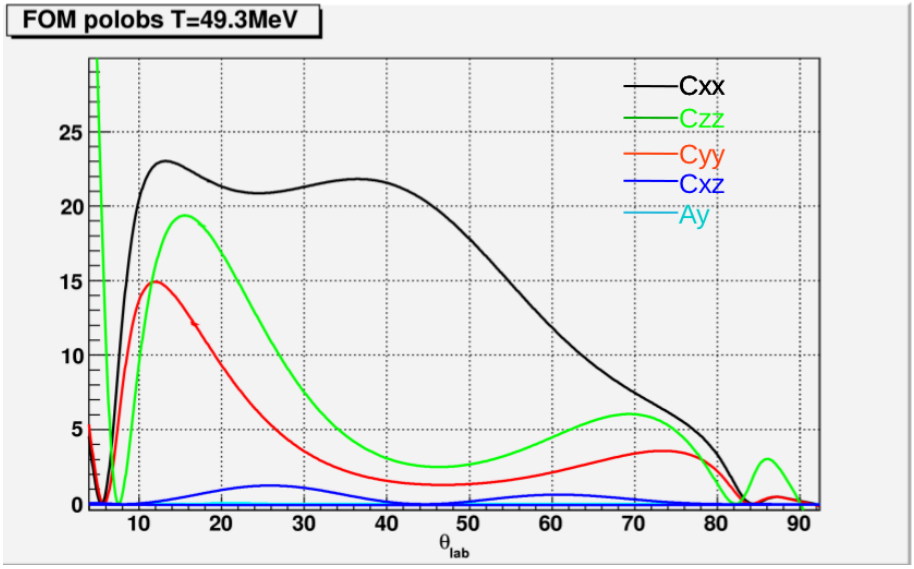

Fig. G.2.: Figure of merit in pp elastic scattering at $T = 49.3\,\mathrm{MeV}$ for the analyzing power A_y and the main double-spin asymmetries A_{mn} (C_{mn}).

G.1. Event Generation

Besides generation of the reaction vertex using the dimensions of the beam and the target, the scattering angles Θ and ϕ of the protons were generated according to the complete differential cross section and including all relevant analyzing powers and double-spin asymmetries. The resulting asymmetries were calculated according to Eq. (G.1) assuming a target polarization of $Q = 0.7$ and $P = 0.005$. Figure G.3 shows the rate $^{d\sigma}/_{d\sigma_0}$ as a function of the azimuthal angle ϕ for a beam polarized in $y-$direction and a target polarized in $x-$ (left panel) and $y-$ (right panel) direction. For displaying reasons $P = 0.5$ is used in order to increase the effect of rate changes. As it is visble in Fig. G.4, there is no ϕ dependence if beam and target are longitudinal polarized (P_z, Q_z).
For further analysis, it is assumed that the beam and the target are vertically polarized (P_y, Q_y).

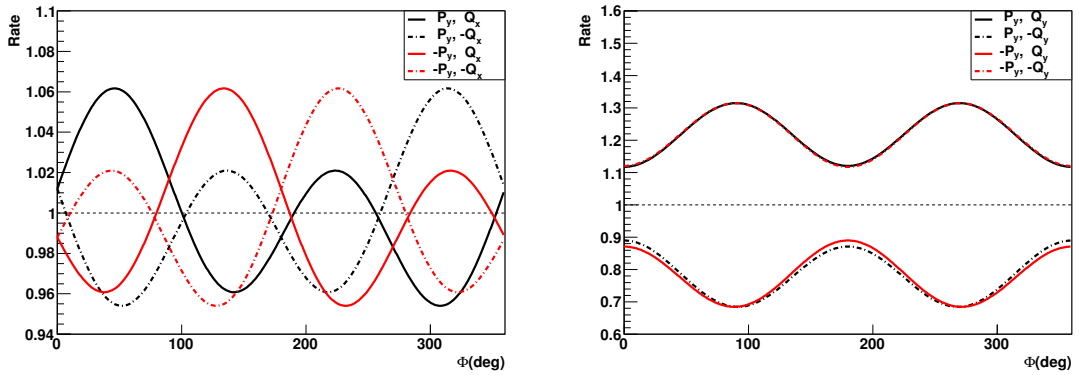

Fig. G.3.: Rates in pp elastic scattering at $\Theta = 40°$ for $P_y = 0.5$ and $Q_{x,y} = 0.7$ vs azimuthal angle ϕ.

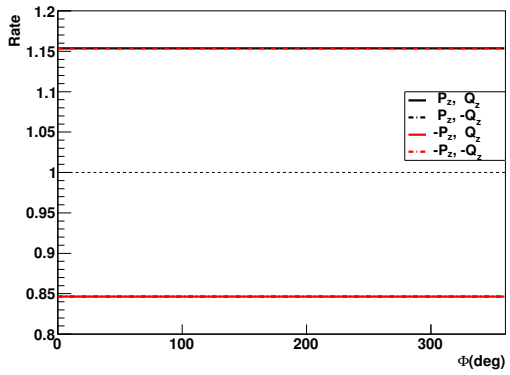

Fig. G.4: Rates in pp elastic scattering at $\Theta = 40°$ for $P_z = 0.5$ and $Q_z = 0.7$ vs azimuthal angle ϕ. The rates change in case of polarization reversal, but they do not show a ϕ dependence.

G.2. Event Detection

Asking for two protons (one hit in each layer above threshold) in coincidence in opposite detectors the ϕ-symmetric detector arrangement (see Fig. 6.1) placed from $z = -40...260\,\mathrm{mm}$ ($z = 0$ at the center of the storage cell) accepts roughly 28% of the generated events. This is about a factor four larger than for $\vec{p}d$ scattering with the ANKE STTs (Sec. 5.2.1). Figure G.5 illustrates the azimuthal scattering angle distribution of generated (blue) and reconstructed events (red) in the left panel and the vertex distribution along the target ($z-$direction) in the right panel.

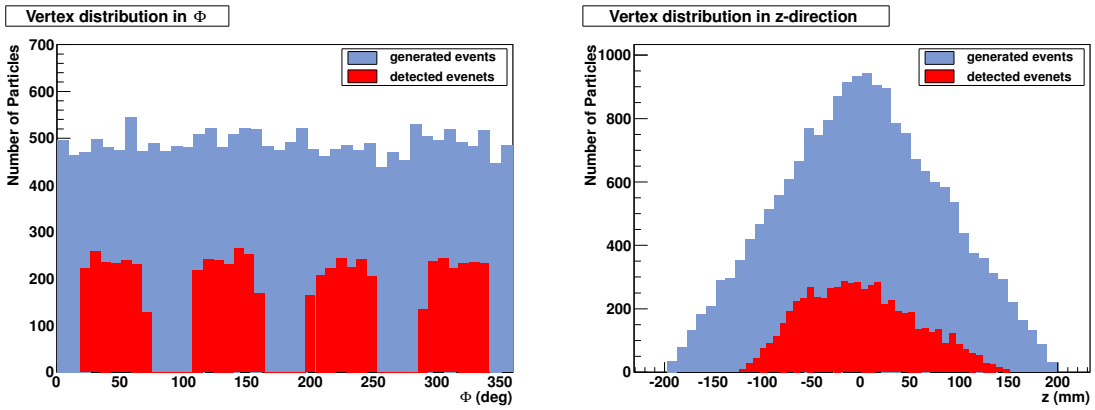

Fig. G.5.: left: Distribution of the azimuthal angle ϕ for generated (blue) and reconstructed (red) events. The four detectors provide a ϕ coverage of about 57%. **right:** Vertex reconstruction for generated (blue) and reconstructed (red) events. The acceptance of the PAX detetor for pp elastic scattering is 28% including energy thresholds.

G.3. Diagonal Scaling

To deduce the polarizations from the measured yields the so called diagonal scaling method, which is in detail described in [158], will be used. A given yield matrix Y of rank four comprises the measured yields of all four detector quadrants (rows) for all four possible

polarization combinations ($\uparrow\uparrow, \uparrow\downarrow, \downarrow\uparrow, \downarrow\downarrow$) of beam and target:

$$Y_{i,j} = \begin{pmatrix} Y_{0,0} & Y_{0,1} & Y_{0,2} & Y_{0,3} \\ Y_{1,0} & Y_{1,1} & Y_{1,2} & Y_{1,3} \\ Y_{2,0} & Y_{2,1} & Y_{2,2} & Y_{2,3} \\ Y_{3,0} & Y_{3,1} & Y_{3,2} & Y_{3,3} \end{pmatrix}. \tag{G.3}$$

Each row and each column of this matrix shall be multiplied by a constant in such a way that the new matrix X,

$$X = \alpha Y \beta \tag{G.4}$$

satisfies the following conditions with respect to its row sums r_i and column sums c_k,

$$r_i = \sum_k x_{ik}, \tag{G.5}$$

$$c_k = \sum_i x_{ik}. \tag{G.6}$$

The task is to simultaneously solve all three equations to find the matrices α, β and X, where the latter contains the pure polarization informations. By correctly adding the components together and inserting the known polarization observables A_y, A_{mn} one can extract the target polarization if the beam polarization is known or vice versa. In addition it allows one to extract all flipping and non-flipping polarization components, as well as luminosities and detector efficiencies.

G.4. Results

Analyzing the reconstructed $\vec{p}\vec{p}$ elastic events with the diagonal scaling method shows that approximately $(5.5 - 6) \cdot 10^6$ events are needed to reach an absolute accuracy of $\Delta P = 0.001$. Besides the larger geometrical acceptance (factor four) of the PAX detector the double-spin asymmetries of $\vec{p}\vec{p}$ elastic scattering are larger compared to A_y in $\vec{p}d$ scattering. Assuming a target areal density of $d_\mathrm{t} = 4.8 \cdot 10^{13}/cm^2$ and $1 \cdot 10^{10}$ injected protons the required measurement time is about a factor 5.5 shorter than for the polarization measurement using $\vec{p}d$ scattering with the STTs. For the determination of the optimal detector position in $z-$direction, the sum of the figure of merit of all events has been maximized ($FOM = \sum_i d\sigma d\Omega \cdot A_{xx}^2 + \sum_i d\sigma d\Omega \cdot A_{yy}^2$).

List of Figures

List of Tables

BIBLIOGRAPHY

[1] P. Lenisa and F. Rathmann for the PAX Collaboration, *Technical Proposal for Antiproton-Proton Scattering Experiments with Polarization* (2005); available from the PAX website http://www.fz-juelich.de/ikp/pax.

[2] J. J. Thomson, Phil. Mag. **44**, 293 (1897).

[3] E. Rutherford, Phil. Mag. **21**, 669 (1911).

[4] H. Geiger and E. Mardsen, Proc. Roy. Soc. **A82**, 495 (1909).

[5] E. Rutherford, Phil. Mag. **ser6 XXXIV**, 537 (1919).

[6] J. Bjørken, Phys. Rev. **179**, 1547 (1969).

[7] J. Bjørken and E. Paschos, Phys. Rev. **185**, 1975 (1969).

[8] R. Feynman, Phys. Rev. Lett. **23**, 1415 (1969).

[9] M. Gell-Mann, Phys. Lett. **8**, 214 (1964).

[10] G. Zweig, CERN preprints **TH-401, TH-412**, (1964).

[11] D. Perkins, *Proceedings of the 16th Int. Conf. on High Energy Physics,* Batavia, Illinois, 6-13 Sep. 1972, Vol. **4** (NAL, Batavia) p. 189.

[12] D. Griffiths, *Introduction to Elementary Particles*, 2nd ed. (Wiley-VCH, 2008).

[13] M. Rosenbluth, Phys. Rev. **179**, 615 (1950).

[14] J. Murphi *et al.*, Phys. Rev. C **9**, 2125 (1974).

[15] O. Gayou *et al.*, Phys. Rev. Lett. **88**, 092301 (2002), arXiv:nucl-ex/0111010.

[16] M. Jones *et al.*, Phys. Rev. Lett. **84**, 1398 (2000), arXiv:nucl-ex/9910005.

[17] A. V. Afanasev *et al.*, Phys. Rev. **D72**, 013008 (2005), arXiv:hep-ph/0502013.

[18] N. H. Buttimore and E. Jennings, Eur. Phys. J. **A31**, 9 (2007), arXiv:hep-ph/0607227.

[19] M. Breidenbach *et al.*, Phys. Rev. Lett. **23**, 935 (1969).

[20] K. Nakamura, (Particle Data Group), J. Phys. G **37**, 075021 (2010).

[21] L. L. Pappalardo, *Transverse spin effects in polarized semi inclusive deep inelastic scattering*, PhD thesis, Univ. degli Studi di Ferrara, 2008, DESY-THESIS-2008-032.

[22] L. Whitlow *et al.*, Phys. Lett. **B282**, 475 (1992), and refs. therein.

[23] C. Callan and D. Gross, Phys. Rev. Lett. **33**, 156 (1969).

[24] R. P. Feynman, Science **183**, 601 (1974).

[25] M. R. Adams *et al.*, (Fermilab E665 Collaboration), Phys. Rev. D **54**, 3006 (1996).

[26] A. Benvenuti *et al.*, (BCDMS Collaboration), Phys. Lett. B **223**, 485 (1989).

[27] M. Arneodo *et al.*, (New Muon Collaboration), Nucl. Phys. B **483**, 3 (1997).

[28] HERA, H1 and ZEUS Collaborations (2009), arXiv:hep-ex/0911.0884.

[29] V. Barone *et al.*, Physics Reports **359**, 1 (2002).

[30] J. Collins and D. Soper, Nuclear Physics B **194**, 445 (1982).

[31] S. D. Drell and T.-M. Yan, Phys. Rev. Lett. **25**, 316 (1970).

[32] P. Lenisa and F. Rathmann for the PAX Collaboration, *Antiproton-Proton Scattering Experiments with Polarization* (2005), arXiv:hep-ex/0505054.

[33] FAIR, Baseline Technical Report (Darmstadt 2006); http://www.gsi.de/fair/ reports/btr.html .

[34] J. Ashman *et al.*, Phys. Lett. **B206**, 364 (1988).

[35] S. J. Brodsky, J. R. Ellis, and M. Karliner, Phys. Lett. **B206**, 309 (1988).

[36] S. D. Bass, Mod. Phys. Lett. **A24**, 1087 (2009), arXiv:hep-ph/0905.4619.

[37] S. D. Bass, Rev. Mod. Phys. **77**, 1257 (2005).

[38] A. Airapetian *et al.*, Phys. Rev. Lett. **92**, 012005 (2004), arXiv:hep-ex/0307064.

[39] A. Airapetian *et al.*, Phys. Rev. **D71**, 012003 (2005), arXiv:hep-ex/0307064.

[40] E. Ageev *et al.*, Phys. Lett. **B612**, 154 (2005), arXiv:hep-ex/0501073.

[41] S. D. Bass and C. A. Aidala, Int. J. Mod. Phys. **A21**, 4407 (2006), arXiv:hep-ph/0606269.

[42] G. K. Mallot, *Proceedings of the 17th International Spin Physics Symposium (SPIN 2006),* Kyoto, 2006, Vol. **915** (AIP, New York, 2007) p. 325, arXiv:hep-ex/0612055.

[43] R. Jaffe and X. Ji, Nucl. Phys. B **375**, 527 (1992).

[44] J. Ralston and D. Soper, Nuc. Phys. B **152**, 109 (1979).

[45] V. Barone *et al.*, Physics Letters B **639**, 483 (2006).

[46] X. Artru and M. Mekhfi, Z. Phys. C **45**, 669 (1990).

[47] J. Collins, Nuclear Physics B **396**, 161 (1993).

[48] M. Diefenthaler, HERMES Collaboration (2007) , arXiv:hep-ex/0706.2242.

[49] A. Airapetian *et al.*, Phys. Rev. Lett. **94**, 012002 (2005).

[50] E. Ageev *et al.*, Nucl. Phys. **B765**, 31 (2007), arXiv:hep-ex/0610068.

[51] R. Seidl *et al.*, Phys. Rev. **D78**, 032011 (2008), arXiv:0805.2975.

[52] R. Seidl *et al.*, Phys. Rev. Lett. **96**, 232002 (2006), arXiv:hep-ex/0507063.

[53] M. Anselmino *et al.*, Phys.Rev. **D75**, 054032 (2007), arXiv:hep-ph/0701006.

[54] J. L. Rosner, *Proceedings of the XXV International Conference on Physics in Collision,* Praque, CR, 5-9 Jul 2005, Vol. **815** (AIP, New York, 2006) p. 218, arXiv:hep-ph/0508155.

[55] X.-G. He, X.-Q. Li, and J. Ma, Phys. Rev. **D71**, 014031 (2005), arXiv:hep-ph/0407083.

[56] A. Krisch, A. Lin, and O. Chamberlain, *Proceedings of the Workshop on Polarized Antiproton Sources,* Bodega Bay, CA, 18-21 Apr 1985, Vol. **145** (AIP, New York, 1986) p. 1.

[57] S. Chattopadhyay *et al.*, *Proceedings of the International Workshop,* Daresbury, UK, 29-31 Aug 2007, Vol. **1008** (AIP, New York, 2008) p. 133.

[58] T. O. Niinikoski and R. Rossmanith, Nucl. Instrum. Meth. A **255**, 460 (1987).

[59] D. P. Grosnick *et al.*, Nucl. Instrum. Meth. **290**, 269 (1990).

[60] M. Nekipelov and C. Weidemann for the PAX Collaboration, *Spin-Filtering Studies at COSY* (2009); available from the PAX website http://www.fz-juelich.de/ikp/pax.

[61] P. Lenisa and F. Rathmann for the PAX Collaboration, *Measurement of the Spin-Dependence of the $\bar{p}$ Interaction at the AD-Ring* (2009); available from the PAX website http://www.fz-juelich.de/ikp/pax.

[62] P. Csonka, Nucl. Instrum. Meth. **63**, 247 (1968).

[63] F. Rathmann *et al.*, Phys. Rev. Lett. **71**, 1379 (1993).

[64] E. Courant, M. Livingston, H. Snyder, and J. Blewett, Phys. Rev. **91**, 202 (1953).

[65] A. Lehrach, *Strahl- und Spindynamik von Hadronenstrahlen in Mittelenergie-Ringbeschleunigern* Habilitationsschrift Universität Bonn, 2008, ISBN 978-3-89336-548-7 (2008).

[66] S. Lee, *Accelerator physics* World Scientific, 2nd edition, (1999).

[67] K. Wille, *Physik der Teilchenbeschleuniger und Synchrotronstrahlungsquellen* Teubner Studienbücher, 1. Auflage, (1992).

[68] N. Madsen, S. Maury, and D. Möhl, Nucl. Instrum. Meth. **A441**, 54 (2000).

[69] H. Stein *et al.*, *Proceedings of the XVIII Conference on Accelerators of Charged Particles, RUPAC-2002,* Obninsk, Russia, (2004), arXiv:1101.5963.

[70] H. J. Stein *et al.*, Phys. Rev. ST Accel. Beams **11**, 052801 (2008).

[71] H. Poth, Phys. Rept. **196**, 135 (1990).

[72] A. Lehrach *et al.*, Nucl. Instrum. Meth. **A561**, 289 (2006), arXiv:physics/0511165.

[73] A. Piwinski, DESY 98 - 179, (1998), arXiv:physics/9903034.

[74] D. Prasuhn *et al.*, Nucl. Instrum. Meth. **441**, 167 (2000).

[75] D. Möhl, G. Petrucci, L. Thorndahl, and S. Van Der Meer, Phys. Rept. **58**, 73 (1980).

[76] G. I. Budker *et al.*, Sov. Atom. Energ. **22**, 438 (1967).

[77] G. I. Budker *et al.*, Part. Accel. **7**, 197 (1976).

[78] V. V. Parkhomchuk and A. N. Skrinsky, Reports on Progress in Physics **54**, 919 (1991).

[79] J. D. Jackson, *Classical Electrodynamics Third Edition* Wiley, 3rd edition, (1998).

[80] K. Rathsman, *Modeling of electron cooling*, PhD thesis, Uppsala Universitet, 2010.

[81] V. Parkhomchuk, Nucl. Instrum. Meth. **A441**, 9 (2000).

[82] K. Zapfe *et al.*, Nucl. Instrum. Meth. **A 368**, 293 (1996).

[83] K. Zapfe *et al.*, Rev. Sci. Instrum. **66**, 28 (1995).

[84] J. Bystricky, F. Lehar, and P. Winternitz, J. Phys. (France) **39**, 1 (1978).

[85] S. Bilenky and R. Ryndin, Physics Letters **6**, 217 (1963).

[86] D. Oellers, *Polarizing a stored proton beam by spin-flip?*, PhD thesis, Universität zu Köln, 2010.

[87] D. Oellers *et al.*, Phys. Lett. **B 674**, 269 (2009), arXiv:nucl-ex/0902.1423.

[88] H. O. Meyer, Phys. Rev. E **50**, 1485 (1994).

[89] C. Horowitz and H. Meyer, Phys. Rev. Lett. **72**, 3981 (1994), arXiv:nucl-th/9403004.

[90] W. MacKay and C. Montag, Phys. Rev. **E73**, 028501 (2006).

[91] T. Walcher *et al.*, Eur. Phys. J. **A34**, 447 (2007), arXiv:physics.acc-ph/0706.3765.

[92] A. Milstein, S. Salnikov, and V. Strakhovenko, Nucl. Instrum. Meth. **B266**, 3453 (2008), arXiv:hep-ph/0802.3766.

[93] D. Oellers and F. Rathmann for the PAX Collaboration, *Measurement of the depolarizing p(pol)e cross section using co-moving electrons* (2007); available from the PAX website http://www.fz-juelich.de/ikp/pax.

[94] A. Milstein and V. Strakhovenko, Phys. Rev. **E72**, 066503 (2005), arXiv:physics/050418.

[95] N. Nikolaev and F. Pavlov, *Proceedings of the 17th International Spin Physics Symposium (SPIN 2006)*, Kyoto, 2006, Vol. **915** (AIP, New York, 2007) p. 932, arXiv:hep-ph/0601184.

[96] N. H. Buttimore and D. O'Brien, Eur. Phys. J. **A35**, 47 (2008), arXiv:hep-ph/0707.2065.

[97] D. O'Brien, *AIP Conference Proceedings*, Dublin, Ireland, 2008, Vol. **1008** (AIP, New York, 2008) p. 24, arXiv:hep-ph/0711.4819.

[98] SAID, *Nucleon Nucleon scattering database*, available from Center for Nuclear Studies, Department of Physics, George Washington University, USA, at website gwdac.phys.gwu.edu/analysis/nnanalysis.html.

[99] G. Ohlsen and P. Keaton, Nucl. Instrum. Meth. **109**, 41 (1973).

[100] F. Rathmann *et al.*, Phys. Rev. Lett. **94**, 014801 (2005), arXiv:physics/0410067.

[101] R. Maier, Nucl. Instrum. Meth. **A390**, 1 (1997).

[102] D. Prasuhn *et al.*, *Proceedings of the IEEE Particle Accelerator Conference (PAC2001)*, Chicago, Illinois, 18-22 Jun 2001.

[103] B. Lorentz *et al.*, *Proceedings of the 9th European Particle Accelerator Conference (EPAC 2004)* Lucerne, Switzerland, 5-9 Jul 2004.

[104] Adam, H. H. for the WASA-at-COSY Collaboration, *Proposal for the Wide Angle Shower Apparatus (WASA) at COSY-Juelich - 'WASA at COSY'* (2004).

[105] S. Barsov *et al.*, Nucl. Instrum. Meth. **462**, 364 (2001).

[106] A. Lehrach *et al.*, Nucl. Instrum. Meth. **A439**, 26 (2000).

[107] H. Stechemesser and V. Vau, Vacuum **46**, 867 (1995).

[108] V. Kamerdzhiev, *Untersuchung und Verbesserung des Stabilitätsverhaltens eines intesiven elektronengekühlten Teilchenstrahls in COSY,* PhD thesis, Universität Dortmund, 2003.

[109] V. Kamerdzhiev *et al.*, Nucl. Instrum. Meth. **A532**, 285 (2004).

[110] K. Grigoryev *et al.*, Nucl. Instrum. Meth. **A599**, 130 (2009).

[111] R. Maier *et al.*, *Proceedings of the 2nd European Particle Accelerator Conference (EPAC 90),* Nice, France, 1990.

[112] K. Unser, IEEE Trans. Nucl. Sci. **28**, 2344 (1981).

[113] C. Böhme *et al.*, *Proceedings of the 9th European Workshop on Beam Diagnostics and Instrumentation for Particle Accelerators (DIPAC09)* Basel, Switzerland, 25-27 May 2009.

[114] P. Forck, *Proceedings of the 1st International Particle Accelerator Conference (IPAC 10),* Kyoto, Japan, 23-28 May 2010.

[115] G. Ciullo *et al.*, J. Phys. Conf. Ser. **295**, 012150 (2011).

[116] A. Garishvili *et al.*, *Proceedings of the 11th European Particle Accelerator Conference (EPAC 2008),* Genoa, Italy, 23-27 Jun 2008.

[117] A. Nass *et al.*, Nucl. Instrum. Meth. **505**, 633 (2003).

[118] A. Airapetian *et al.*, Nucl. Instrum. Meth. **A540**, 68 (2005), arXiv:physics/0408137.

[119] A. Nass *et al.*, *Proceedings of the 17th International Spin Physics Symposium (SPIN 2006),* Kyoto, 2006, Vol. **915** (AIP, New York, 2007) p. 1002.

[120] N. Koch, *A study on the production of intense cold atomic beams for polarized hydrogen and deuterium targets,* PhD thesis, Universität Erlangen-Nürnberg, 1999, DESY-THESIS-2008-032.

[121] W. Demtröder, *Experimentalphysik 3*, 3. Auflage (Springer, 2005).

[122] S. Gasiorowicz and I. Paschen, *Quantenphysik*, (Oldenbourg, 2001).

[123] C. Barschel, *Calibration of the Breit-Rabi Polarimeter for the PAX Spin-Filtering Experiment at COSY/Jülich and AD/CERN* diploma thesis, Universität Aachen, 2010.

[124] P. Lenisa and F. Rathmann for the PAX Collaboration, *Measurement of the Spin-Dependence of the $\bar{p}p$ Interaction at the AD-Ring* (2009); available from the PAX website http://www.fz-juelich.de/ikp/pax.

[125] Dr. H. Soltner, private communication.

[126] F. Rathmann *et al.*, Phys. Rev. **C 58**, 658 (1998).

[127] C. Baumgarten *et al.*, Nucl. Instrum. Meth. **A 482**, 606 (2002).

[128] Stancari, M. , *Modifying the HERMES Breit-Rabi Polarimeter for experiments at Juelich* (2006), University of Ferrara, PAX-Note-6/2006.

[129] C. Baumgarten *et al.*, Nucl. Instrum. Meth. **A 508**, 268 (2003).

[130] H. Dombrowski *et al.*, Nucl. Instrum. Meth. **A 386**, 228 (1997).

[131] A. Khoukaz *et al.*, Eur. Phys. J. **D 5**, 275 (1999).

[132] T. Mersmann, *Untersuchung der Wechselwirkung zwischen η-Mesonen und ^{3}He-Kernen am Experimentaufbau ANKE* PhD thesis, Westfälische Wilhelms-Universität Münster, 2007.

[133] R. Schleichert *et al.*, IEEE Trans. Nucl. Sci. **50**, 301 (2003).

[134] C. Bozzi *et al.*, Nucl. Instrum. Meth. **A 447**, 15 (2000).

[135] C. Bozzi *et al.*, Nucl. Instrum. Meth. **A 473**, 7 (2001).

[136] Micron Semiconductor Ltd., http://www.micronsemiconductor.co.uk.

[137] D. Protic, T. Krings, and R. Schleichert, IEEE Trans. Nucl. Sci. **49**, 1993 (2002).

[138] A. Musgiller, Ph.D. thesis, University of Cologne, 2006.

[139] F. Iselin, *The MAD Program (Methodical Accelerator Design)*, 1985.

[140] E. Courant and H. Snyder, Annals Phys. **3**, 1 (1958), also reprinted in 'The Development of Coliders', N.Y., AIP, 1995. pp. 23-70.

[141] D. Welsch, *Investigation and Optimization of Transverse Non-Linear Beam Dynamics in the High-Energy Storage Ring HESR* PhD thesis, Rheinische Friedrich-Wilhelms-Universität Bonn, 2009.

[142] M. Nekipelov and C. Weidemann for the PAX Collaboration, *Status Report and Beam-Time Request for COSY experiment 199* (2010); available from the PAX website http://www.fz-juelich.de/ikp/pax.

[143] P. Belochitskii *et al.*, *Proceedings of IEEE Particle Accelerator Conference (PAC 01)*, Chicago, Illinois, 18-22 June 2001.

[144] M. Ross *et al.*, Nucl. Instrum. Meth. **326**, 424 (1993).

[145] F. Hinterberger and D. Prasuhn, Nucl. Instrum. Meth. **A279**, 413 (1989).

[146] A. Nass, *Determination of the target density inside the openable storage cell*, PAX Note 2/2011 ; available from the PAX website http://www.fz-juelich.de/ikp/pax.

[147] N. King *et al.*, Phys. Lett. **69 B**, 151 (1977).

[148] G. G. Ohlsen, Rept. Prog. Phys. **35**, 717 (1972).

[149] D. Oellers and F. Rathmann for the PAX Collaboration, *Measurement of the depolarizing p(pol)e cross section using co-moving electrons* (2007); available from the PAX website http://www.fz-juelich.de/ikp/pax.

[150] S. Bunker *et al.*, Nucl. Phys. **A 113**, 461 (1968).

[151] R. Hanna, *Proceedings of the 2nd Int. Symp. on Polarization Phenomena of Nucleons*, Karlsruhe, Germany, 1965.

[152] M. Froissart and R. Stora, Nucl. Instrum. Meth. **7**, 297 (1960).

[153] Lehrach, A. and Maier, R., *Siberian Snake for the Cooler Synchrotron COSY* (2001); available from www2.fz-juelich.de/ikp//spin@cosy/.

[154] G. Macharashvili, *Detector for Spin-Filtering Experiments*, PAX Note 7/2007 ; available from the PAX website http://www.fz-juelich.de/ikp/pax.

[155] A. Borysenko, Nuclear Physics B (Proc. Suppl.) **125**, 189 (2003).

[156] J. Stewart, Nucl. Instr. Meth. A **511**, 271 (2003).

[157] P. Thörngren Engblom for the PAX Collaboration, *Measurement of Spin Observables in the $\vec{p}\vec{d}$ Breakup Reaction* (2011); available from the PAX website http://www.fz-juelich.de/ikp/pax.

[158] H. Meyer, Phys. Rev. **C56**, 2074 (1997).

[159] Y. Uzikov and J. Haidenbauer, Phys. Rev. **C 79**, 024617 (2009), arXiv:nucl-th/0810.3997.

[160] T. Hippchen, J. Haidenbauer, K. Holinde, and V. Mull, Phys. Rev. C **44**, 1323 (1991).

[161] V. Mull and K. Holinde, Phys. Rev. C **51**, 2360 (1995).

[162] J. Kuhs, *Bestimmung der mittleren Betafunktion an den Quadrupolfamilien des Kühlersynchrotron COSY,* Bachelor thesis, RWTH Aachen, 2010.

[163] A. Roth, *Vacuum Technology*, 3rd ed. (Elsevier Science Ltd, 1990).

[164] W. Haeberli *et al.*, Phys. Rev. **C55**, 597 (1997).

[165] NN-Online, *Nucleon nucleon interaction*; available from Theoretical High Energy Physics Group of the Radboud University Nijmegen, Netherlands, at website http://nn-online.org/.

ACKNOWLEDGMENTS

I would like to thank those persons whose help made this thesis possible and who made working in the IKP a very interesting and enjoyable time full of experiences.

My first thanks go to Prof. Dr. H. Ströher for giving me the opportunity to work on this challenging and important project within the motivating atmosphere of his institute.

I want to thank Prof. Dr. J. Jolie for acting as the co-referee of this work.

I am very grateful to Dr. Ralf Schleichert for acting as my supervisor and for his continuous support at all times especially during the preparation of the experiment. I also owe my gratitude to Dr. Frank Rathmann for all the small and large advices and especially for his help during the experiment analysis and for prove reading this work. I thank both for all the fruitful discussions and for sharing their knowledge with me.

Special thanks to Dr. Hans-Joachim Stein for his comprehensive support and his patience in explaining me valuable details of electron cooling and accelerator physics in general. My thanks to Dr. Paolo Lenisa for his explanations on the theoretical background, to Dr. Dieter Oellers and Dr. Mikhail Nekipelov for the good collaboration during the preparation and execution of the experiments and for helpful and good discussions related to physics or not. For prove reading special subjects of my thesis and for answering all my questions I thank Dr. Alexander Nass and PD Dr. Andreas Lehrach.

Furthermore, I am grateful to the STT group Dr. Sergey Mikirtychiants, Dr. Sergey Trusov, Dr. Sergey Merzliakov and Andreas Erben for sharing their expertise on electronics and silicon detectors with me. For the beautiful drawings and the permanent support, especially by mounting the target chamber on Friday evening, I thank Heidi Straatmann.

Thanks to the COSY group Dr. Dieter Prasuhn, Dr. Bernd Lorentz, Dr. Ralf Gebel for their patience in improving the beam conditions and their advices and help on accelerator subjects. For the motivating and enjoyable working atmosphere I would like to thank all my colleagues from the IKP and the Italian group in the collaboration, especially Dr. Detlev Gotta, Dr. Hellmut Seyfarth, Dr. Ralf Engels, Martin Gaisser, Dr. Maxim Mikirtychiants, Dr. Kirill Grigoryev, Guido D'Orsaneo, Dirk Spöllgen, Ilhan Engin, Peter Wieder, Norbert Dolfus, Gisela Roes and all other people who contributed to this work by ideas and advices, by technical support, by help on the administrative things and by taking shifts during the beam time.

I was lucky to share the office with two great guys (disregarding their favorite football teams). Special thanks to Dr. Thomas Strauch for his help and support during my starting time at the IKP and to Léonard Kröll for proof reading this thesis and for becoming a really good friend.

Finally, I would like to thank my parents Frank and Heike Weidemann for guiding me the correct way and for the continuous support even over this long distance, my sister, my grandparents, my aunt and my friends for motivating me and for the energy I gained every time was at home.

Steffi Reinartz I thank for believing in me at any time, for the unreserved support especially during the stressful experiment periods, and for her love.

ERKLÄRUNG

Ich versichere, dass ich die von mir vorgelegte Dissertation selbständig angefertigt, die benutzten Quellen und Hilfsmittel vollständig angegeben und die Stellen der Arbeit - einschließlich Tabellen, Karten und Abbildungen -, die anderen Werken im Wortlaut oder dem Sinn nach entnommen sind, in jedem Einzelfall als Entlehnung kenntlich gemacht habe; dass diese Dissertation noch keiner anderen Fakultät oder Universität zur Prüfung vorgelegen hat; dass sie - abgesehen von unten angegebenen Teilpublikationen - noch nicht veröffentlicht worden ist sowie, dass ich eine solche Veröffentlichung vor Abschluss des Promotionsverfahrens nicht vornehmen werde.
Die Bestimmungen der Promotionsordnung sind mir bekannt. Die von mir vorgelegte Dissertation ist von Herrn Prof. Dr. H. Ströher betreut worden.

Christian Weidemann

Veröffentlichung

- C. Weidemann, J. Phys. Conf. Ser. **295**, 012127 (2011).